The crust and upper mantle structure of the UAE-Oman mountains: Insights from new gravity and seismological data

Brook Keats

Thesis submitted to the University of Oxford
for the degree of Doctor of Philosophy
in
Geophysics



Department of Earth Sciences
and Worcester College,
University of Oxford

Trinity, 2019

Supervised by Prof. Tony Watts *and* Prof. Mike Searle

Declaration

I declare that the contents of this thesis, including all figures, are my own work, except where explicitly stated. I also confirm that no part of this thesis has been submitted or accepted for consideration for any other degree, diploma or qualification.

Citation: Brook Keats (2019), The crust and upper mantle structure of the UAE-Oman mountains: Insights from new gravity and seismological data, D.Phil. Thesis, University of Oxford, Department of Earth Sciences, Oxford, UK.

Keywords: United Arab Emirates, UAE, Semail, ophiolite, receiver functions, gravity, gravity modelling.

This thesis has been typeset using LaTeX and references were compiled using BibTeX. The majority of Figures have been produced using Generic Mapping Tools (*GMT*), and the python package *matplotlib*.

Copyright ©, by Brook Keats, 2019.
All rights reserved.

No part of the material protected by this copyright notice may be reproduced or utilised in any form or by any means, electronic or mechanical, including photocopying, recording or by any information storage and retrieval system, without written permission from the copyright owner.

Abstract

The crust and upper mantle structure of the UAE-Oman mountains: Insights from new gravity and seismological data

Brook Keats
Worcester College, Oxford

Trinity, 2019

The UAE-Oman mountains are a $\sim$ 700 km long mountain belt located on the north-eastern margin of the Arabian plate, extending from the Musandam peninsula in the north, through the United Arab Emirates (UAE) and Oman to terminate at the eastern tip of Arabia. These mountains contain a series of stacked thrust sheets that incorporate a full "half ocean" sequence, including: deep ocean sediments and volcanoclastic exotics; shelf and slope sediments; and an obducted slab of oceanic crust and upper mantle known as the Semail ophiolite. The obduction of these thrust sheets emplaced a significant load on the Arabian margin, and the resulting flexure and subsidence led to the formation of a foreland basin inland from this load. Significant sedimentation has also occurred on the seaward side of the ophiolite since its obduction, with up to 10 km of deposition since the end of the Cretaceous, concealing the eastern termination of the ophiolite, and the present day transition from continental to oceanic crust.

This thesis utilises passive seismic and gravity data acquired across two east-west profiles. We aim to constrain the thickness and subsurface geometry of this ophiolite, investigate its offshore extent, constrain the crustal thickness of the underlying Arabian margin, and investigate the transition from continental to oceanic crust offshore in the Gulf of Oman.

Receiver functions and gravity modelling across these profiles revealed: a $\sim$ 15 km sedimentary sequence and a $\sim$ 36 km Moho in the foreland basin to the west, suggesting a stretching factor for the rifted Arabian margin of 1.49; a $\sim$ 10 km flexural root beneath the UAE-Oman mountains, offset $\sim$ 20 km landwards from the primary ophiolite load; that the Semail ophiolite dips eastwards at $\sim$ 30°, increasing from $5 - 10$ km depth near Masafi to $\sim$ 25 km depth near the Gulf of Oman coastline; that

high ophiolite densities ($\sim$ 3120 $kg\,m^{-3}$) are required to reproduce the $\sim$ 160 $mGal$ Bouguer anomalies observed across the ophiolite, implying minimal bulk serpentinisation ($< 30\%$); that the ophiolite extends offshore below the hinterland sediments in the Gulf of Oman in a steep normal fault; and that the Moho thins rapidly east of Masafi to transition from thinned continental crust of the Arabian margin to in situ oceanic crust of the Gulf of Oman $\sim$ 30 km offshore.

Extended Abstract

The crust and upper mantle structure of the UAE-Oman mountains: Insights from new gravity and seismological data

Brook Keats

Worcester College, Oxford

Trinity, 2019

The UAE-Oman mountains are a $\sim$ 700 km long mountain belt located on the north-eastern margin of the Arabian plate, extending from the Musandam peninsula in the north, through the United Arab Emirates (UAE) Oman to terminate at the eastern tip of Arabia. These mountains contain a series of stacked thrust sheets that incorporate a full "half ocean" sequence, including: deep ocean sediments and volcanoclastic exotics; shelf and slope sediments; and an obducted slab of oceanic crust and upper mantle known as the Semail ophiolite. This ophiolite formed between $96.5 - 95.5$ Ma above an intra-oceanic subduction zone in the Neo-Tethys ocean, and was subsequently obducted onto the Arabian margin (with its associated sedimentary thrust sheets) over the next $\sim$ 25 Ma. The obduction of these thrust sheets emplaced a significant load on edge of the Arabian plate, and the resulting flexure and subsidence led the formation of a foreland basin to the west. Significant sedimentation has also occurred on the seaward side of the ophiolite since its obduction, with up to 10 km of deposition since the end of the Cretaceous, concealing the eastern termination of the ophiolite and the

present day transition from continental to oceanic crust.

The Semail ophiolite and its associated allochthonous blocks have been the subject of numerous studies. However, there are still many questions remaining around its formation, emplacement, thickness, internal structure, and offshore extent. This thesis forms part of a broader project, formed as a collaboration between the Petroleum Institute (now Khalifa University) and the University of Oxford, that aims to address some of these questions. Specifically, this thesis aims to: constrain the thickness and subsurface geometry of the ophiolite in the UAE, and investigate its offshore extent; examine the nature of the underlying continental crust by constraining Moho depths; and investigate the transition from continental to oceanic crust offshore in the Gulf of Oman.

A large geophysical dataset was acquired for the project, with the majority coming from a marine geophysical survey undertaken by the M/V *Hawk Explorer* from the 25^{th} of June to the 29^{th} of July in 2014. This cruise acquired $\sim 925\ km$ of offshore reflection seismic, 2 onshore-offshore refraction profiles across the ophiolite, continuous marine gravity data, and $\sim 770\ km$ of magnetic data. This marine dataset was supplemented by a network of 25 seismometers, deployed along two east-west profiles to record these refraction profiles. The majority of this network remained in place for up to 2.4 years following the cruise, and recorded passive seismic data continuously during this time. These seismometer profiles were designed to be coincident with a set of vibroseis surveys undertaken by WesternGeco on behalf of the Ministry of Energy of the UAE in 2003-2004. The two east west profiles of these Ministry of Energy surveys were termed D1 and D4 for the southern and northern profile respectively, and we retain these names for our study.

We compute receiver functions across this passive seismic network to obtain Moho depths and constrain the deeper crustal structure along these profiles. Earthquakes for receiver function analysis were selected from the USGS global earthquake catalogue by

taking all $M_w > 5.5$ events between $30 - 98$ from a central point in our array ($25.5\,N$, $56.0\,E$) that occurred between June 2014 and November 2016. Our catalogue included 382 events, with limited coverage over all back azimuths. There was a significant bias towards events originating in the east however, with a large number of events recorded in the subduction zones of Java, Sumatra, and the Western Pacific. Receiver functions computed from these earthquakes varied in quality, and a significant amount of testing, optimisation, and quality control was required to produce a set of good quality results to interpret. These results exhibited a large degree of variation with back azimuth and epicentral distance at many stations, suggesting that the underlying crustal structure is highly heterogeneous. Moho conversions were generally weak or absent entirely, and results were dominated by mid-crustal conversions at most stations. Results at each station were subdivided by back-azimuth and epicentral distance to create a set of consistent subsets, and depth conversions for these subsets were obtained via $H - k$ stacking.

Along the southern line D1, a strong mid-crustal conversion is dominant in the foreland between $14 - 16\,km$ depth, and we interpret this to be a conversion from basement to the base of the foreland sedimentary sequence. Moho conversions are observed at $\sim 36\ km$ in the western foreland, and again at $\sim 40\ km$ at the western edge of the UAE-Oman mountains. Eastwards of the Semail thrust Moho signals are more difficult to identify, as numerous deep crustal conversions are observed. Tracing the deeper results suggests the Moho may flex down to $\sim 48\ km$ below Masafi, before rapidly shallowing eastwards. East of Masafi a strong negative polarity signal is observed. This signal begins at $< 10\ km$ depth and dips eastwards at $\sim 30°$ to $\sim 25\ km$ depth at Gulf of Oman the coastline. Along the northern profile D4 a coherent Moho is also observed beneath the allocthonous sedimentary blocks in the western mountains. Depth increases from $\sim 36\ km$ at the western edge of these mountains to a maximum of $\sim 44\ km$ below the Masafi window, before decreasing again eastwards. Beyond the

Semail thrust where peridotite outcrops become dominant these deeper signals disappear and a strong, negative polarity (slow to fast) signal again becomes dominant. This phase begins $\sim 5\ km$ east of the Semail thrust at a depth of $\sim 10\ km$ and deepens slightly eastwards, before stepping down to $\sim 25\ km$ depth near the Gulf of Oman coastline. We interpret these negative polarity signals to be conversions from the 'slow' Arabian continental margin below to the 'fast' oceanic crust and upper mantle of the Semail ophiolite, and therefore mark the base of these obducted thrust sheets.

The marine gravity data acquired by the M/V *Hawk Explorer* is processed to a free-air gravity anomaly dataset, and checked for internal consistency by analysing shiptrack crossovers. The dataset was found to be highly consistent, with a mean crossover error of $-0.22\ mGal$. Two onshore gravity profiles were acquired along D1 and D4 during fieldwork in early 2016, comprising 78 and 71 additional onshore gravity data points along each respective profile. This data was processed to terrain corrected Bouguer anomalies along both profiles. The regional trend was removed from both datasets by subtracting the EGM2008 model to degree and order 12, and the datasets merged to create a consistent regional gravity grid.

The processed gravity datasets reveal gravity lows of $-80\ mGal$ in the Arabian Gulf decreasing to $-110\ mGal$ as we move onshore into the western UAE foreland. Along the southern gravity profile D1 the anomalies begin to increase by $\sim 6\ mGal\,km^{-1}$ as we approach the mountains (and ophiolite), this trend eases, then reverses briefly, as we approach Masafi, before increasing steadily again to level out at $\sim 160\ mGal$ at the Gulf of Oman coastline. Along the northern gravity profile D4 the trend is slightly different, with the $-110\ mGal$ low of the foreland rapidly increasing by $\sim 60\ mGal$ as we move into the allocthonous sedimentary units of the Sumeini and Hawasina. A gradual positive trend continues eastwards until we reach the Semail thrust and transition from allocthonous sediments to dense obducted peridotites, resulting in a steep $\sim 12\ mGal\,km^{-1}$ gradient that levels out at $\sim 160\ mGal$ near the Gulf of Oman

coastline. Offshore in the Gulf of Oman the gravity anomaly rapidly falls off again at $-7\ mGal\,km^{-1}$ to reach a minimum of about $-10\ mGal$ about 30 km offshore. It then gradually increases back to 20 $mGal$ at the eastern edge of our dataset.

Utilising this gravity dataset, and constraints provided by the reflection seismic, refraction profiles, receiver functions, surface geology, and previously published data, we build two 2D onshore-offshore gravity models along profiles D1 and D4. We model the entire crustal structure, including the Moho, against a reference section consisting of a 31.2 km crustal column of density 2754 $kg\,m^{-3}$ above a 3290 $kg\,m^{-3}$ mantle. This reference section was constructed to be in isostatic balance with a mid ocean ridge. Reflection seismic data revealed up to 10 km of sediments and significant extensional/transpressional deformation in the hinterland basin offshore in the Gulf of Oman. Refraction modelling in this basin suggested seismic velocities increases rapidly below these sediments in a manner consistent with typical oceanic crust. Onshore no refractions from below $\sim 10\,km$ could be reliably modelled however, meaning we were entirely reliant on receiver function results to constrain the lower crustal structure. The original D1 and D4 vibroseis lines and models associated with them provide constraints on the upper crustal structure onshore, providing excellent constraints on the sedimentary structure in the foreland. A high degree of scattering was evident across the ophiolite however, making interpretations based on this section of the lines less reliable.

The D1 gravity model extends 160 km east-southeast, beginning 30 km offshore in the Arabian Gulf and linking up with the onshore passive seismic and gravity profile at the coastline. It continues across the foreland and mountains to Fujairah city and finishes 35 km offshore in the Gulf of Oman. We model the gravity lows in the foreland with a ~ 15 km thick sedimentary sequence and a slightly thickened (relative to our reference section) $36\,km$ crust. Across the mountains the observed gravity highs are modelled with a ~ 8 km thick folded ophiolite overlying obducted sedimentary wedges.

As we move eastwards our ophiolite thickens and deepens rapidly, dropping down below the Cenozoic sediments in the hinterland basin offshore in the Gulf of Oman. This low density offshore sedimentary sequence causes a rapid drop-off in the modelled gravity anomaly. This is counteracted by a rapidly thinning Moho, as we transition from $\sim 48\ km$ thick continental crust below Masafi to $20\ km$ thick oceanic crust offshore in the Gulf of Oman, resulting in a near zero gravity anomaly offshore similar to that observed.

The D4 gravity model starts $6\ km$ north of D1 on the western coastline of the foreland, and extends $130\ km$ due east to the edge of our offshore gravity dataset some $55\ km$ offshore in the Gulf of Oman. The gravity anomalies observed along D4 in the foreland are similar to D1, and are modelled in the same fashion. Across the mountains we model the gravity anomalies with a $\sim 10\ km$ thick, eastward dipping obducted sedimentary wedges with a slight negative density contrast. From the Semail thrust onwards this transitions into a $15 - 20\ km$ thick, high density, steeply dipping ophiolite block to reproduce the $\sim 160\ mGal$ gravity high observed near the Gulf of Oman coastline. The gravity anomaly falls off rapidly as we move offshore in a manner similar to D1, and this is modelled again with a thick sedimentary package. Our Moho exhibits a slightly smaller root compared to D1, extending down to $44\ km$ depth west of the Semail thrust and rapidly thinning eastwards to oceanic levels offshore in the Gulf of Oman to counteract the effect of the sedimentary package and give us the near zero anomaly that we observe.

The data that we have acquired, and the results of our modelling suggest that the Semail ophiolite must be both very dense ($\sim 3120\ kg\,m^{-3}$) and very thick ($\sim 20\ km$), particularly near the Gulf of Oman coastline. This implies bulk serpentinisation must be minimal ($< 30\%$), and is potentially restricted to surficial processes. The obduction of such a large, dense load onto the Arabian margin has resulted in significant flexure. The ~ 10 km flexural root that we observe below the mountains, offset $\sim 20\ km$ west-

wards from the primary ophiolite load, is too deep to be accounted for by topographic compensation alone, and is likely a direct result of this loading. This flexural down-warping has also created the accommodation space for the formation of a thick foreland basin inland of the ophiolite load, where we obtain crustal thicknesses of $\sim 36\ km$, with a $\sim 15\ km$ sedimentary sequence. If we assume the Arabian margin was originally at typical continental values ($31.2\ km$), this would imply a stretching factor(β) of ~ 1.49. Gravity modelling suggests crustal thickness thins rapidly east of Masafi, and transitions from extended, down-warped, continental to oceanic crust $\sim 30\ km$ offshore in the Gulf of Oman. A thick hinterland sedimentary basin has also formed here, concealing the suture zone that must mark the transition from the obducted oceanic crust of the Semail ophiolite, to the in situ present day oceanic crust of the Gulf of Oman.

Acknowledgements

This thesis represents the results of my work over the last four years. However, science is a collaborative pursuit, and this thesis has benefited in many ways, large and small, from the contributions of a number of other people.

Firstly I would like to acknowledge my supervisor Tony Watts for providing me with the opportunity to undertake this project, and for his advice, assistance, and feedback throughout. I would also like to thank my secondary supervisor Mike Searle for his advice, for helping to ensure my models remained geologically sound, and guiding me through numerous geological outcrops and answering the questions of a lost geophysicist. Likewise I would also like to thank my final, Abu Dhabi based, supervisor Mohammed Ali, for his advice, for organising this project, and for hosting me at the Petroleum Institute (PI) in Abu Dhabi during my student exchange.

This project was funded by a grant from the PI (now Khalifa University), and I would like to thank them for supporting it, and for expanding the funding to allow for international student fees. I thank my two other colleagues on this project, Simone Pilia and Tyler Ambrose. Simone for maintaining the seismic network that provided much of the data used in this thesis, and for taking the time to go over his refraction models with me when we couldn't get them to agree. Tyler for being a great project partner, helping me with my gravity surveys, and for explaining the difference between peridotites and amphibolites again and again.

I thank Aisha Al-Suweidi for helping to secure the additional funding necessary to

cover international student fees, and for helping me to find an apartment in Abu Dhabi during my exchange to the PI. I also thank my PI office mates and colleagues at the PI during this exchange, Fateh, Eric, Elisha, Weining, Dominic, Meng, and Yi.

I thank Worcester College for providing an accommodation grant.

I thank the National Centre for Meteorology and Seismology (NCMS) of the United Arab Emirates for meeting with us, and giving us access to their passive seismic datasets.

I thank Thomas Richter, for liasing with me regarding his receiver function codes *rf*, and updating them to allow for custom deconvolution methods. Thomas Bodin and Jordi Julia for providing me with the joint receiver function and surface wave dispersion inversion codes, and Sofia Filippi from Guralp for helping me track down the correct instrument response files.

I thank Bruce Levell, Mike Daly, Dave Waters, Karen Sigloch, Conall Mac Niocaill, Chris Ballentine, Richard Walker, Hauke Marquardt, and Thomas Garth for valuable discussions and input over the course of this thesis.

I thank Tony Watts, Brook Tozer, Tyler Ambrose, Harriet Godwin, Phil Cilli, and Mike Searle for proof reading and commenting on earlier drafts of this thesis.

I thank my office mates, old and new, for their interesting discussions (work related or otherwise), and for helping out with all the little technical and administrative issues you encounter during a thesis. To Brook Tozer, Rebecca Morgan, Johnny Hunter, Lily Muller, Maria Tsekhmistrenko, Harriet Godwin, Marta Pienkowska-Cote, Eoghan Totten, and Alex Szenicer, thank you! You've been great company. Special thanks go to Brook Tozer, for encouraging me to apply for this project, and for helping me settle into life in Oxford, and to Harriet Godwin for keeping me going in the final stages.

Finally, I would like to thank my parents, Kaye and Alan, for always supporting me in everything that I do.

Contents

Declaration i

Abstract iii

Extended Abstract v

Acknowledgements xiii

Contents xx

List of Figures xxv

List of Tables xxvii

1 Introduction **1**

1.0.1 Thesis structure 1

1.1 Tectonic setting 2

1.1.1 The Semail ophiolite complex 3

1.1.2 Metamorphic sole 5

1.1.3 The Arabian margin 7

1.1.4 Foreland basin formation 8

1.1.5 Hinterland basin formation 9

1.2 Existing constraints on crustal structure 9

2 Data **11**

2.1 Introduction 11

2.2 M/V *Hawk Explorer* Cruise 11

2.2.1 Seismic 11
2.2.2 Gravity 13
2.3 Passive seismic dataset 13
2.3.1 PI/Oxford seismic network 13
2.3.2 NCMS network 15
2.4 Fieldwork 18
2.4.1 Exchange to the PI 18
2.4.2 Vibroseis refraction survey 19
2.4.3 Final project meeting 19

3 Receiver functions 21

3.1 Introduction 21
3.2 The receiver function method 21
3.2.1 The LQT reference frame 23
3.2.2 Deconvolution 24
3.2.3 Synthetic data comparison 29
3.3 H - k stacking 31
3.4 Earthquake Dataset 32
3.5 Software and codes 35
3.6 Data preparation 35
3.7 Signal to Noise Ratio 36
3.8 Quality Control 38
3.9 Previous Studies on the Arabian Continent 39
3.10 Calibrating our codes 42
3.10.1 GSN station II.RAYN 42
3.10.2 GSN station II.PFO 43
3.11 PI/Oxford Network Receiver Functions 47
3.11.1 S-01 49

3.11.2 S-02 50
3.11.3 S-03 52
3.11.4 S-05 53
3.11.5 S-06 54
3.11.6 S-07 56
3.11.7 S-08 58
3.11.8 S-09 60
3.11.9 S-10 63
3.11.10 S-11 64
3.11.11 S-12 66
3.11.12 S-13 68
3.11.13 S-14 69
3.11.14 S-15 70
3.11.15 S-17 73
3.11.16 S-18 74
3.11.17 S-19 75
3.11.18 S-20 77
3.11.19 S-21 78
3.11.20 S-22 81
3.11.21 S-23 82
3.11.22 S-24 84
3.11.23 S-25 86
3.11.24 Summary 89
3.12 Receiver function profiles 92
3.12.1 Profile D1 92
3.12.2 Profile D4 94
3.12.3 H - k stacking profiles 96

3.13 NCMS Network receiver functions 99
3.13.1 AE.UMQ 100
3.13.2 DN.NAZ 101
3.13.3 OM.MDH 101
3.14 Discussion 106
3.15 Chapter Summary 108

4 Gravity **111**
4.1 Introduction 111
4.2 The gravitational force 111
4.2.1 Gravitational potential energy 113
4.2.2 The Earth's gravity 114
4.3 Measuring gravity 118
4.4 Gravity anomalies 119
4.4.1 Tidal corrections 120
4.4.2 Eötvös correction 121
4.4.3 Cross-coupling correction 121
4.4.4 Free-air correction 121
4.4.5 Bouguer correction 122
4.4.6 Terrain corrections 123
4.4.7 Regional correction 124
4.4.8 Isostasy and the isostatic anomaly 126
4.5 Previous gravity surveys 129
4.6 Marine gravity dataset 131
4.6.1 Base tie & drift correction 132
4.6.2 Data reduction 133
4.7 Terrestrial gravity dataset 137
4.7.1 Base station tie 139

4.7.2 Drift correction . . . 140
4.7.3 Terrain correction . . . 141
4.7.4 Reduction density . . . 142
4.7.5 Gravity profiles . . . 144
4.8 Merged dataset . . . 148
4.9 Ophiolite mass . . . 150
4.10 Discussion . . . 150
4.11 Chapter summary . . . 152

5 Modelling 153

5.1 Introduction . . . 153
5.2 Modelling gravity . . . 153
5.2.1 Line integral method . . . 155
5.3 Object oriented modelling . . . 157
5.3.1 Density . . . 158
5.3.2 Reflection seismic . . . 158
5.3.3 Refraction seismic . . . 161
5.3.4 Receiver functions . . . 164
5.3.5 Surface geology . . . 164
5.3.6 Reference model . . . 166
5.3.7 GMG . . . 168
5.3.8 Simple models . . . 170
5.3.9 D1 gravity model . . . 173
5.3.10 D4 gravity model . . . 177
5.4 Discussion . . . 181
5.5 Chapter Summary . . . 185

6 Discussion, conclusions, and future work 187

6.1 Discussion 187
6.1.1 Ophiolite thickness and geometry 187
6.1.2 Offshore extent 188
6.1.3 The Arabian continental crust 189
6.1.4 Continental-oceanic transition 190
6.1.5 Flexure and isostasy 190
6.1.6 Geological model of the Arabian margin 191
6.2 Conclusions 192
6.3 Future work 193

Bibliography **196**

A Onshore gravity survey data **211**
A.1 Introduction 211
A.2 D1 gravity survey data 211
A.3 D4 gravity survey data 214

B *H* - *k* stacking results **217**
B.1 Introduction 217
B.2 PI/Oxford network 217

List of Figures

1.1 Map of broader study area 3

1.2 Ophiolite obduction process 6

2.1 Data map 12

2.2 Group shot at S-20 14

2.3 Seimometer shed 15

2.4 PI network availability 16

2.5 Seismometer installation photos 17

2.6 NCMS network map 17

2.7 Vibroseis trucks in the foreland 20

3.1 Receiver function example 23

3.2 Slepian tapers 27

3.3 Deconvolution comparison 30

3.4 Receiver function earthquake dataset. 34

3.5 Receiver function catalogue availability 34

3.6 PI network data quality 37

3.7 PI network data quality 39

3.8 Receiver functions across the Arabian continent 41

3.9 $H - k$ stacking results at II.RAYN 44

3.10 $H - k$ stacking results at II.PFO 46

3.11 NCMS Network map 48
3.12 Receiver functions results at S-01 50
3.13 $H - k$ stacking results at S-01 51
3.14 Receiver functions results at S-02 52
3.15 Receiver functions results at S-03 53
3.16 Receiver functions results at S-05 54
3.17 $H - k$ stacking results at S-05 55
3.18 Receiver functions results at S-06 56
3.19 Receiver functions results at S-07 57
3.20 Receiver functions results at S-08 59
3.21 Receiver functions results at S-09 61
3.22 $H - k$ stacking results at S-09 62
3.23 Receiver functions results at S-10 63
3.24 Receiver functions results at S-11 65
3.25 $H - k$ stacking results at S-11 66
3.26 Receiver functions results at S-12 67
3.27 Receiver functions results at S-13 68
3.28 Receiver functions results at S-14 70
3.29 Receiver functions results at S-15 71
3.30 $H - k$ stacking results at S-15 72
3.31 Receiver functions results at S-17 73
3.32 Receiver functions results at S-18 75
3.33 Receiver functions results at S-19 76
3.34 Receiver functions results at S-20 78
3.35 $H - k$ stacking results at S-20 79
3.36 Receiver functions results at S-21 80
3.37 Receiver functions results at S-22 81

3.38 Receiver functions results at S-23 83
3.39 $H - k$ stacking results at S-23 84
3.40 Receiver functions results at S-24 85
3.41 $H - k$ stacking results at S-24 87
3.42 Receiver functions results at S-25 88
3.43 D4 $H - k$ results map 90
3.44 D4 $H - k$ results map 91
3.45 Receiver functions profile along D1 93
3.46 Receiver functions profile along D4 95
3.47 D1 $H - k$ profiles 97
3.48 D4 $H - k$ profiles 98
3.49 NCMS Network map 99
3.50 $H - k$ stacking results at AE.UMQ 102
3.51 $H - k$ stacking results at DN.NAZ 103
3.52 $H - k$ stacking results at OM.MDH 105

4.1 The force of gravity 112
4.2 The *International Reference Ellipsoid* and normal gravity 115
4.3 'Normal gravity' as a function of latitude 117
4.4 EGM2008 regional correction 125
4.5 Isostatic models 127
4.6 WGM2012 isostatic gravity anomaly in the UAE and Oman 128
4.7 Existing gravity data 131
4.8 Hawk Explorer port gravity readings map 132
4.9 Hawk Explorer port gravity readings 133
4.10 Hawk Explorer sample gravity data 135
4.11 Hawk Explorer gravity cross-overs 136
4.12 M/V *Hawk Explorer* gravity grid 137

4.13 Onshore gravity data map 138
4.14 ASTER30m DEM vs. GPS elevations 139
4.15 Naswa absolute gravity station 140
4.16 Gravimeter drift 142
4.17 Density determination via Nettleton's method 143
4.18 D1 gravity survey data 146
4.19 D4 gravity survey data 147
4.20 Merged gravity grids 149

5.1 Gravity anomaly of a buried sphere 155
5.2 Illustration of the line-integral method 156
5.3 M/V *Hawk Explorer* seismic map 160
5.4 Line FUJ_RS105P1012 162
5.5 Line FUJ_DS102P1006 163
5.6 Line SHJ_RS102P1004 163
5.7 D4 refraction model 165
5.8 Sub-sedimentary velocity profile of D4 166
5.9 Simplified geology of the UAE 167
5.10 Gravity model reference section 169
5.11 Gravity anomalies of simple geometries 170
5.12 Gravity gradient profiles 172
5.13 D1 gravity profile map 174
5.14 D1 gravity model 175
5.15 D4 gravity profile map 177
5.16 D4 gravity model 179
5.17 The Nafe-Drake curve 182
5.18 D4 refraction gravity conversion 183

6.1 Geological cross section of the Arabian margin 192

6.2 Rayleigh wave dispersion curves in the UAE 194

List of Tables

3.1 Previous receiver function results at station II.RAYN 43

3.2 Previous receiver function results at station II.PFO 45

4.1 Naswa base station 140

5.1 Density data summary 159

5.2 Reference section parameters 168

A.1 D1 gravity survey data 211

A.2 D4 gravity survey data 214

B.1 $H - K$ stacking results 217

Chapter 1

Introduction

This study is centred on the Semail ophiolite in the UAE-Oman mountains of the United Arab Emirates, and its flanking sedimentary basins. It forms part of a broader investigation into the tectonics of the region by geologists and geophysicists from the University of Oxford and the Petroleum Institute (now Khalifa University) in Abu Dhabi. While this ophiolite has been studied extensively, many questions still remain around its formation, emplacement, thickness and internal structure, and its offshore extent.

This thesis aims to: constrain the thickness and subsurface geometry of the Semail ophiolite and investigate its offshore extent, and examine the nature of the underlying Arabian margin by obtaining Moho depths and investigating the transition from continental to oceanic crust offshore in the Gulf of Oman. To do this we utilize newly acquired gravity and passive seismic data, calculating receiver functions along two east-west profiles and producing two coincident 2D crustal scale gravity models.

1.0.1 Thesis structure

We begin in this Chapter by introducing the tectonic setting, and discuss the processes that led to the formation and obduction of the Semail ophiolite, and the development of its flanking sedimentary basins. We also discuss the existing constraints on subsurface structure.

In Chapter 2 we discuss the data acquired for this project, and describe the various field trips we undertook as part of it.

In Chapter 3 we introduce the receiver function method, and apply it to our passive seismic dataset to image both the Moho, and mid-crustal impedance interfaces in our study area.

In Chapter 4 we introduce the force of gravity, as it relates to geophysical exploration, and describe the reduction of our marine and terrestrial gravity datasets to free-air and Bouguer anomalies respectively, to create a unified gravity anomaly dataset across our study area.

In Chapter 5 we discuss methods of modelling gravity anomalies, summarise the available external data constraints on tectonic structure in the region, and produce two 2D gravity profiles straddling the ophiolite. The geological implications of these models are then discussed.

In Chapter 6 we finish by discussing the implications of our results on the ophiolite, crustal structure, and the broader tectonics of the region. We also lay out our conclusions, and discuss possible avenues of future work.

Key datasets acquired as part of this thesis are presented in Appendix A and B.

1.1 Tectonic setting

The UAE-Oman mountains are a $\sim 700\ km$ long mountain belt located on the north-eastern margin of the Arabian continent. These mountains extend from the Musandam peninsula in the north, down through the United Arab Emirates (UAE) and back into Oman, to terminate past Muscat along the eastern margin of Arabia (see Figure 1.1). Their relief is generally moderate ($< 1000\ m$), reaching a maximum of $3005\ m$ at Jebel Akhdar in Oman, and their width varies from $\sim 30 - 130\ km$.

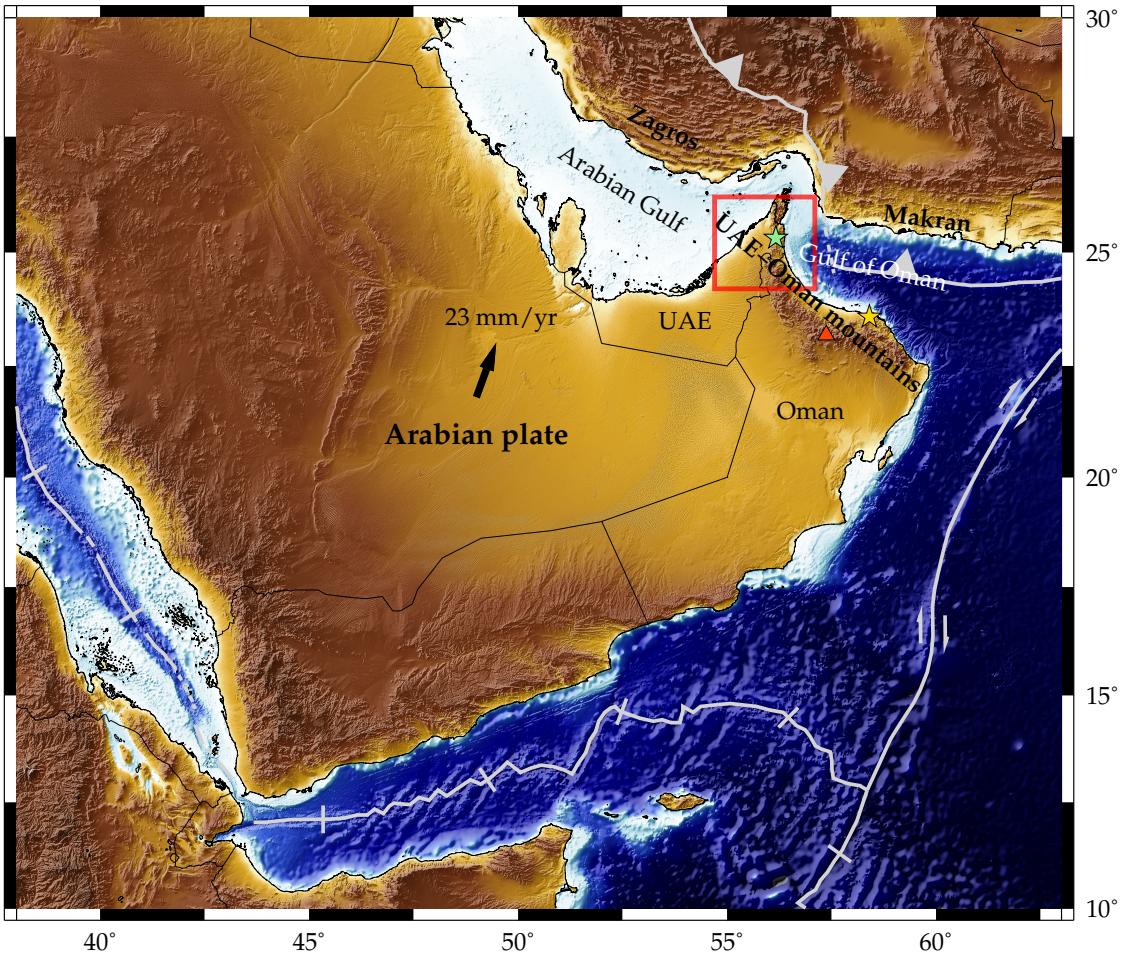


Figure 1.1: Map of the Arabian continent, with major tectonic boundaries shown in grey. The UAE-Oman mountains occupy the north-eastern margin of the continent, in the United Arab Emirates (UAE) and Oman. Muscat, Masafi, and Jebel Akhdar are marked by the the gold star, green star, and red triangle respectively. Our study area is highlighted by the red box. Plate motion is relative the Red Sea spreading centre and the Afar triple junction, and is from *Bayer et al.* (2006).

1.1.1 The Semail ophiolite complex

This mountain range hosts the Semail ophiolite complex[1], a series of allocthonous, stacked thrust sheets, that were obducted onto the Arabian continental margin in the late Cretaceous, between $\sim 95\ Ma$ and $\sim 67\ Ma$. These allocthonous units constitute a full "half ocean" sequence that includes: passive margin shelf and slope sediments of

[1]An ophiolite, by definition, is an obducted portion of oceanic crust and upper mantle. We will therefore use "the Semail ophiolite" to refer to the obducted oceanic crust and upper mantle thrust sheets, where as the "Semail ophiolite complex" term also includes the obducted passive margin and deep ocean sedimentary thrust sheets.

the Sumeini Group; distal slope and deep ocean sediments in the Hawasina complex; distal trench and seamount units in the Haybi complex; and a complete section of oceanic lithosphere (from pelagic sediments, to pillow lavas, sheeted dikes, layered and massive gabbros, and upper mantle peridotites) known as the Semail ophiolite, one of the best known and most widely studied ophiolites in the world. (*Glennie et al.*, 1973; *Coleman and Bailey*, 1974; *Lippard and Shelton*, 1986; *Rabu et al.*, 1993; *Searle and Cox*, 1999; *Nicolas et al.*, 2000; *Searle et al.*, 2014).

$U - Pb$ dating of zircons obtained from obducted gabbros and plagiogranites suggests the majority of the crustal sequence of the ophiolite crystallised between $\sim 96.5 - 95.5\ Ma$ at a mid-ocean spreading centre in the Neo-Tethys ocean (*Tilton et al.*, 1981; *Warren et al.*, 2005; *Rioux et al.*, 2012, 2013, 2016). This short ($\sim 1\ Ma$) formation time implies half spreading rates of $50 - 100\ km\, Ma^{-1}$ (*Rioux et al.*, 2012), comparable to fast spreading mid-ocean ridges such as the East Pacific Rise.

While it is clear that the ophiolite formed at a mid-ocean spreading centre, the type of spreading centre has been a topic of debate over the last few decades. Some authors have argued for a standard mid-ocean ridge origin, similar to the East Pacific Rise (e.g. *Boudier et al.* (1988, 1997); *Nicolas and Boudier* (2017)). However, geochemical analysis of upper lava units point to the presence of a significant amount of hydrous magmas (boninites) typically found in supra-subduction zone (SSZ) settings (*Pearce et al.*, 1981; *Alabaster et al.*, 1982), and a hybrid model, with an early mid-ocean ridge phase followed by a later SSZ phase has also been put forward as a likely origin (e.g. *Ernewein et al.* (1988); *Goodenough et al.* (2013)). More recent geochronological, and geochemical data has suggested that the entire ophiolite formed in an SSZ setting, and a full SSZ origin has been favoured by several recent authors (e.g. *MacLeod et al.* (2013); *Rioux et al.* (2016); *Ambrose and Searle* (2019)).

This subduction zone consumed the entire "half ocean" over the next $\sim 25\, Ma$, progressively stacking the sedimentary rocks of the Sumeini, Hawasina, and Haybi complexes, and the Semail ophiolite, in a series of thrust sheets that ultimately ended up on the Arabian continental margin (see Figure 1.2). The subduction process eventu-

ally ceased as relatively buoyant, unsubductable sedimentary rocks of the continental margin (dominantly carbonates) accumulated in the trench, resulting in significant metamorphism, up to eclogite facies (As Sifah eclogites in Oman) in the leading edge of the Arabian margin (*Searle et al.*, 2014).

The margin stabilised following ophiolite obduction, and passive margin sedimentation had resumed by $\sim 70\ Ma$ (*Glennie et al.*, 1973). This process resulted in at least 130 km of crustal shortening, resulting in a significant amount of folds and thrusts in the obducted sheets (*Searle et al.*, 2014).

1.1.2 Metamorphic sole

Accreted to the base of the ophiolite, sandwiched between mantle sequence peridotites and the dominantly sedimentary thrust sheets of the Haybi complex, is a metamorphic sole that provides additional clues to the ophiolites formation and obduction processes. In the UAE, the primary exposures of this sole can be seen in the Masafi window, north of Masafi. Other key sites for the metamorphic sole are Jebel Sumeini and Wadi Tayyin to the south in Oman (*Searle and Cox*, 1999; *Cowan et al.*, 2014; *Ambrose and Searle*, 2019). This sole is primarily made up of amphibolite and meta-sedimentary rocks, and is characterized by an inverted metamorphic gradient, with progressively lower grade rocks at deeper levels (*Searle and Malpas*, 1980, 1982; *Gnos*, 1998; *Cowan et al.*, 2014; *Ambrose and Searle*, 2019). This implies the metamorphic heat source came from the overlying mantle peridotites. $U - Pb$ dating of zircons from these amphibolites give metamorphic ages of $\sim 94.5 - 96\ Ma$, suggesting metamorphism was synchronous with the formation of the ophiolite crust (*Warren et al.*, 2005; *Rioux et al.*, 2016). The overlapping crystallisation ages of the ophiolites oceanic crust and metamorphic sole provides a key piece of evidence in support of a SSZ origin.

This metamorphism records peak pressures and temperatures of $11 - 13\ kbar$ and $770 - 900\,°C$, implying a burial depth of $30 - 40\ km$ (*Gnos*, 1998; *Cowan et al.*, 2014). This is significantly greater than the inferred original ophiolite thickness ($15 - 20\ km$), and suggests metamorphism occurred part way down the subduction channel. These

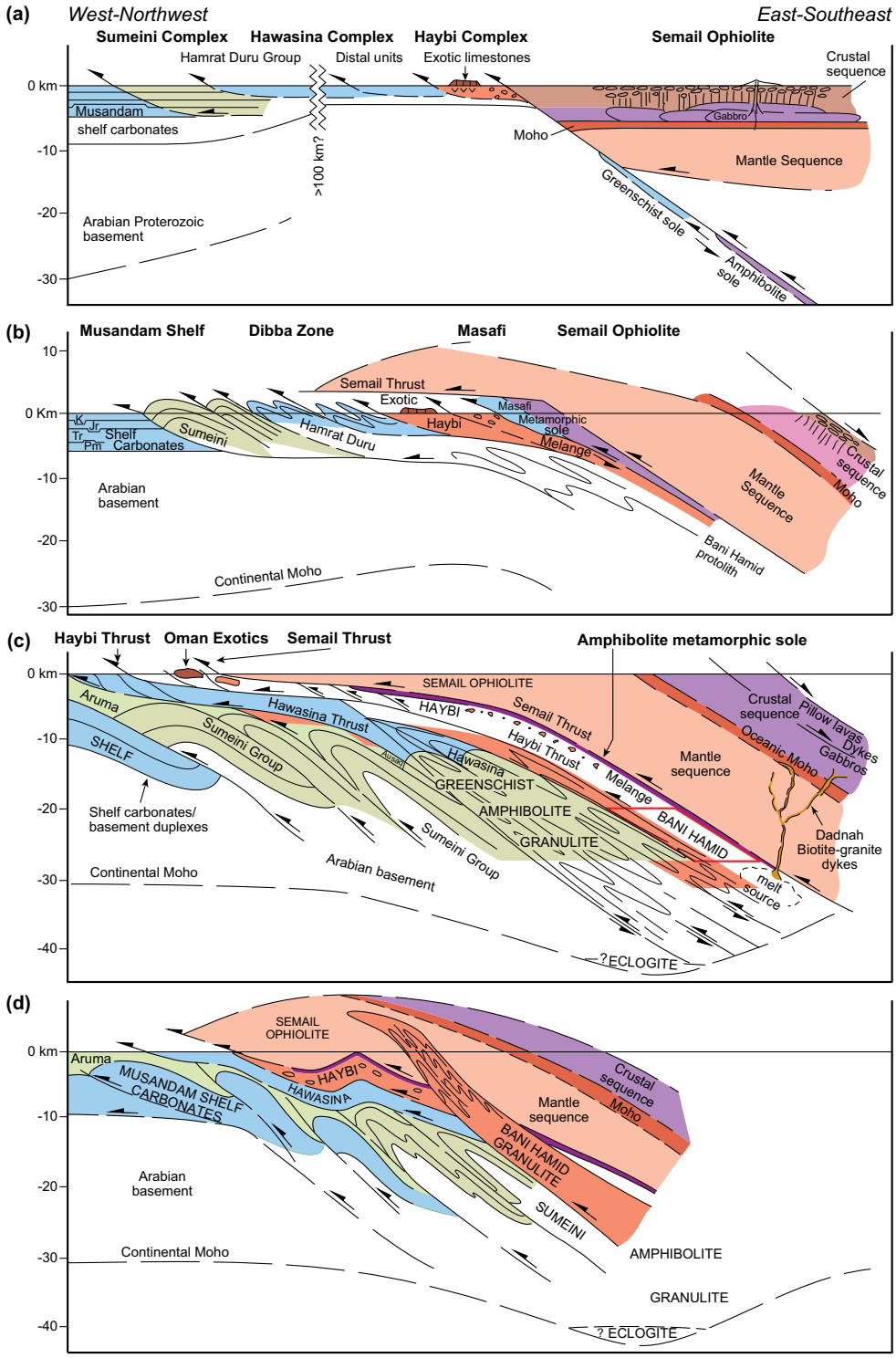


Figure 1.2: Illustration of the obduction of the Semail ophiolite complex. The initial tectonic setting when the Semail ophiolite was formed around $96.5 - 95.5\ Ma$ is shown in **(a)**. The exhumation of the metamorphic sole and the initial stages of obduction around $94 - 93\ Ma$ are shown in **(b)**. The accumulation of the accretionary wedges in the subduction channel, jamming the subduction process, and peak granulite facies metamorphism around $93 - 92\ Ma$ is shown in **(c)**. The out of sequence thrusting that exhumed the Bani Hamid granulites, and final emplacement of the former "half ocean" onto the continental margin is shown in **(d)**. Figure from *Searle et al.* (2014), see this text for further details.

metamorphic units eventually detached, and were exhumed back towards the surface with the Semail ophiolite stacked on top.

Bani Hamid granulites

An out of sequence thrust at Bani Hamid, south-east of Masafi, exposes a different series of metamorphic rocks. This window is composed almost uniformly of isoclinally folded granulites, which record the same high temperatures as the Masafi window to the north, but significantly lower pressures of $5-6$ *kbar* (*Searle et al.*, 2014, 2015). $U-Pb$ dating of zircon and titanite samples suggests metamorphism here occurred $\sim 2-3$ Ma later than the 'normal' metamorphic sole, making them somewhat enigmatic (*Searle et al.*, 2015). These granulites are dominantly meta-quartzites and meta-carbonates, and are interpreted as the stacked up lower crust of the Arabian margin that were unable to subduct due to their buoyancy.

1.1.3 The Arabian margin

The early stages of the Arabian plate formation took place in the late Neoproterozoic with the accretion of micro-continents and island arcs to the Gondwanan margin (*Al-Husseini*, 2000). It was located on the broad, stable Gondwanan rifted margin, and was the source of deposition for sandstones, shales, and carbonates from the middle Cambrian to Devonian (*Ruban et al.*, 2007; *Faqira et al.*, 2009). A period of uplift, erosion, and non-deposition followed in the Late Devonian to Early Carboniferous, caused by either far-field tectonics (e.g. *Lee* (1990); *Al-Husseini* (2004)) or thermal uplift (e.g. *Frizon De Lamotte et al.* (2013)). Thermal subsidence then followed and clastic sedimentation continued from the Late Carboniferous to the Early Permian (*Al-Husseini*, 2004; *Faqira et al.*, 2009).

The break up of the Gondwana supercontinent and the opening of the Neo-Tethys ocean in the Mid to Late Permian transformed the east of the Arabian plate into a rifted margin (*Ruban et al.*, 2007; *Muttoni et al.*, 2009), and the region was characterised by high subsidence and significant carbonate deposition until the Late Cretaceous (*Searle*

et al., 2014). *Ali et al.* (2017) suggested the margin underwent two major rifting events during this time: the first at $\sim 260\ Ma$, with a stretching factor (β) of 1.09; and the second at $\sim 180\ Ma$, with $\beta \approx 1.1$.

1.1.4 Foreland basin formation

As the Neo-Tethys "half ocean" was consumed and the Arabian margin approached the subduction zone, the stacked thrust sheets depressed the margin and formed an outer flexural bulge, and a major foreland basin (the Aruma Basin) during the process of obduction. This bulge caused uplift and erosion in the shelf and slope, resulting in terrigenous sedimentation as the shelf collapsed under the weight of the advancing load (*Robertson*, 1987; *Warburton et al.*, 1990; *Boote et al.*, 1990). The axis of this basin migrated to the south-west as the thrust sheets of the ophiolite complex were progressively loaded onto the Arabian margin throughout the Late Cretaceous.

The obduction process was complete by $\sim 70\ Ma$, and a significant load was now emplaced upon the former passive margin. The collapsed margin then subsided under this load, and the resulting flexure created the accommodation space for the formation of a foreland basin 'inland' from this load (*Patton and O'Connor*, 1988; *Ali and Watts*, 2009; *Ali et al.*, 2017). The margin was relatively stable over the next $\sim 40\ Ma$, and the subsiding basin was progressively infilled, with Late Maastrichtian shallow marine limestones uncomformably overlying autochthonous shelf carbonates and the obducted thrust sheets.

This stability was interrupted in the late Oligocene to early Miocene when the northward moving Arabian plate collided with the Eurasian continent, resulting in the closure of the Neo-Tethys ocean along the Zagros suture zone, the attempted subduction of the Arabian continent beneath the Eurasia, and the formation of the Zagros mountain range to the north (*Searle*, 1988). This transmitted transpressional forces through into the obducted nappes, reactivating former thrust faults, with the resulting uplift forming the present day UAE-Oman mountains. Subsidence continued following this, and a secondary foreland basin (the Pabdeh Basin) developed on top of the first.

1.1.5 Hinterland basin formation

The UAE-Oman mountain range, and the Semail ophiolite complex are flanked on the other side by a second 'hinterland'[2] basin offshore in the Gulf of Oman. Seismic data acquired as part of this project suggests this basin contains up to 10 km of sediments, likely consisting of shallow marine carbonates and detritus from the obducted ophiolite complex, deposited since the end of the obduction process in the Late Cretaceous (*Ali et al.*, 2019). Bathymetric data shows that this basin is widest offshore of the UAE, with a shelf width of ~ 60 km here compared to $30 - 40$ km to the south in Oman. Further offshore it quickly transitions to typical abyssal plain water depths of $2 - 4$ km, and oceanic crust is being subducted below the Eurasion continent in the Makran oceanic-continental subduction zone (e.g. *White and Klitgord* (1976); *White and Ross* (1979)). This sedimentary sequence therefore overlies and obscures the eastern termination of Semail ophiolite complex, and the transition from Arabian continental crust to the oceanic crust of the Gulf of Oman, and is therefore central to our understanding of both the obduction process and regional tectonics.

1.2 Existing constraints on crustal structure

Geophysical constraints on the current crustal structure in our study area are currently limited.

In the foreland basin to the west numerous seismic surveys have been acquired, and these provide effective constraints on the upper ~ 10 km of sedimentary structure (see Section 5.3.2). The lower crustal structure and Moho here are unconstrained by geophysical data however.

Across the UAE-Oman mountains constraints on the subsurface structure are even more limited, and much of the subsurface geometry shown in Figure 1.2d is inferred

[2]The term 'hinterland' is typically used to refer the geographic area inland from a port, or a coastal plain. We acknowledge that this term does not accurately describe the region in question, as most of this basin is offshore. However we coined it early in the project to describe the area, and it has stuck, so we will use it to describe this basin throughout this thesis.

from geological structures mapped at the surface. Vibroseis reflection profiles were acquired by the Ministry of Energy of the UAE in 2003-2004 (*Ellison and Styles* (2006), Section 5.3.2), but the data quality across the ophiolite was generally poor, and it was difficult to identify coherent structures to interpret. *Naville et al.* (2013) used this data to perform near-critical angle refraction study, and mapped what they interpreted to be the base of the ophiolite at $\sim$ 2.5 km depth west of Masafi. Numerous gravity data has been acquired across the UAE-Oman mountains over the last $\sim$ 50 years (see Section 4.5), and this data has provided some constraints on the thickness and density of the ophiolite in places. The majority of the crustal sequence here is poorly constrained however, and there are no estimates of Moho depth beneath these mountains in the UAE.

Offshore in the Gulf of Oman we have acquired new seismic and gravity data for this project that reveals a thick sedimentary sequence that we have termed the hinterland basin (*Ali et al.* (2019), Section 5.3.2 and 5.3.3). There appears to be a dearth of publications on this basin however, so our constraints here are limited to this data. Early interpretations of this data reveal a $\sim$ 10 km thick sedimentary sequence, but the nature of the underlying crust and Moho remain unconstrained.

Chapter 2

Data

2.1 Introduction

A large amount of new geophysical data was acquired for this project. This chapter will give a brief overview of the datasets used, and the fieldwork undertaken as part of this project. Further details of data processed as part of this thesis are included in Chapters 3 and 4.

2.2 M/V *Hawk Explorer* Cruise

The majority of the data acquired for part of this project comes from a cruise undertaken by Seabird Exploration on the M/V *Hawk Explorer*. This ship conducted its surveys offshore Sharjah and in the Gulf of Oman from the 25th of June 2014 to the 29th of July 2014 (see Figure 2.1).

2.2.1 Seismic

The ship was primarily tasked with collecting seismic data, and over 900 km of seismic reflection data was acquired across 22 lines, primarily in the Gulf of Oman.

Two onshore-offshore refraction lines were shot along into our network of seismometers (see Section 2.3, Figure 2.1) onshore along two profiles: The first refraction profile

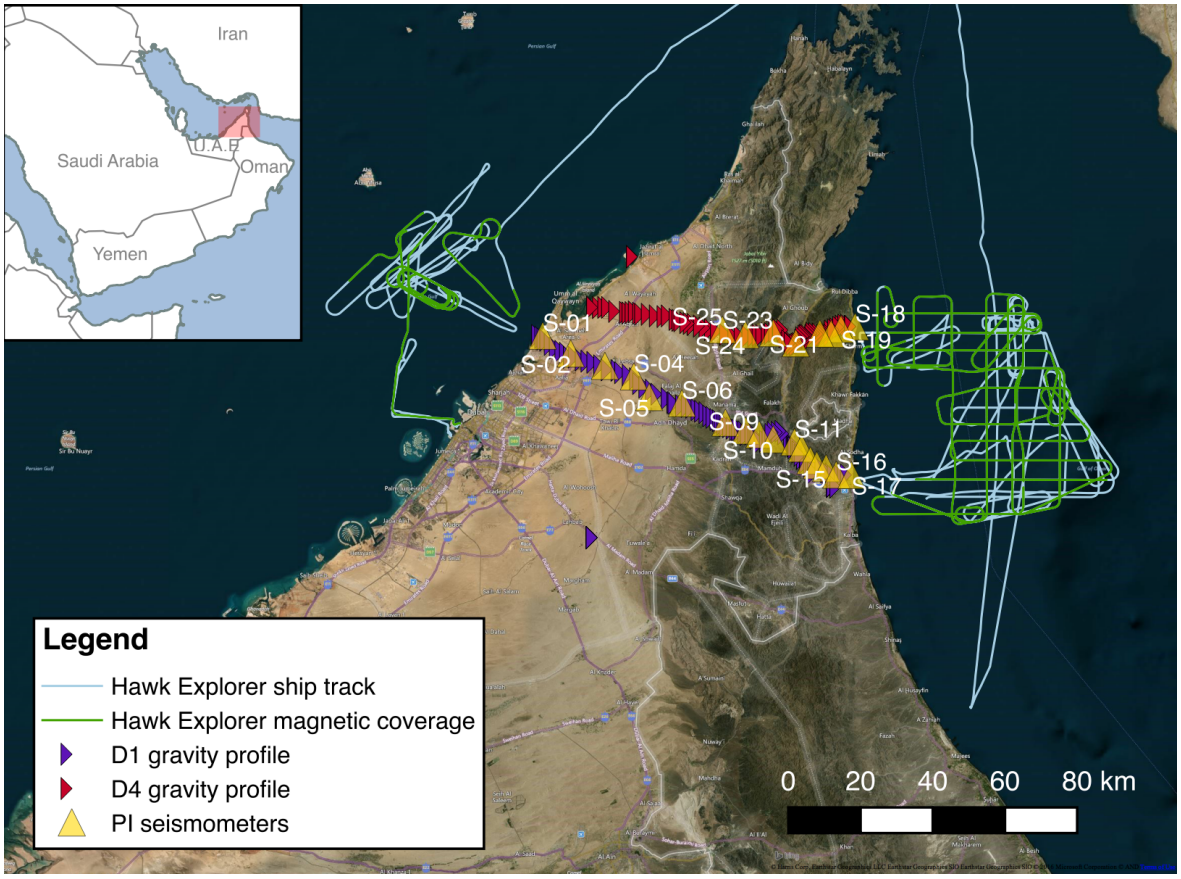


Figure 2.1: Map of our study area showing the primary datasets used in this project. Marine gravity data was acquired along the entire shiptrack, and a towed magnetometer deployed during seismic acquisition. The network of seismometers deployed for this project, and the two onshore gravity profiles highlight the locations of our two transects, D1 and D4.

stretches $\sim$ 160 km east-southeast from offshore Sharjah, across the foreland basin, UAE-Oman mountains and out into the Gulf of Oman. This profile incorporated shots from both offshore Dubai as well as the Gulf of Oman and shot into 17 three-component seismic stations (S-01 to S-17) roughly equally spaced across the foreland basin and UAE-Oman mountain range. The second refraction profile stretched $\sim 90\,km$ east-west from the western side of the UAE-Oman mountains out into the Gulf of Oman. This profile shot into 8 three-component seismic stations deployed across the UAE-Oman mountains in an east-west profile to the north, and incorporated only shots from the Gulf of Oman. We have termed these refraction profiles D1 and D4 as they are coincident with the D1 and D4 wide angle vibroseis seismic lines acquired for UAE's Ministry of Energy in 2003-2004 (see *Ellison and Styles* (2006)).

2.2.2 Gravity

Shipboard gravity data was acquired throughout the cruise by Austin Exploration Inc. The ship was equipped with a Lacoste & Romberg Ultrasys marine gravity system. The system is composed of a Lacoste & Romberg S gravity sensor (serial number S-44) modified by the ZLS Corporation to upgrade the optical beam position and negate differential pressure and moisture effects.

This dataset was processed and reduced to free-air gravity anomalies as part of this project, and is described in more detail in Section 4.6.

2.3 Passive seismic dataset

2.3.1 PI/Oxford seismic network

A network of 25 seismometers was deployed prior to the M/V *Hawk Explorer* cruise by a team from the Petroleum Institute (PI) and the University of Oxford. This network was primarily deployed to record the onshore component of the refraction profiles. 17 were deployed along profile the southern profile D1 and 8 along the northern profile D4 (see Figure 2.1). The majority of these seismometers were left in place after the cruise completed to acquire a passive seismic dataset. The network remained in place for 2 years and 3 months, and acquired approximately 500 GB of passive seismic data in that time.

The seismometers were installed on concrete base plates in holes $0.5 - 1$ m deep and buried. The associated digitiser, GPS receiver and solar panels were installed at the surface. Data was recorded continuously at 100 Hz, with waveforms saved to an SD card in the digitiser.

Seismometer sites in the Fujairah emirate were enclosed in a locked barbed wire enclosure to protect them from being tampered with or stolen (see Figure 2.2). The remaining sites, located in the desert west of the mountains, were protected by a small sheet metal shed with the GPS and solar panels installed on the roof (see Figure 2.3).



Figure 2.2: Group photo at S-20 showing the barbed wire enclosure used to protect our seismometer sites in Fujairah emirate. From left to right at the back are Simone Pilia, Tyler Ambrose, Mike Searle, and Mohammed Ali, while I am crouched in the front.

Maintenance trips were undertaken several times a year to retrieve data and ensure each station was operating smoothly.

Data availability varied significantly from station to station, as shown in Figure 2.4. There are a number of reason for this: several stations were removed early on for maintenance and memory upgrades, power outages were initially a problem at some stations due to insufficient solar capacity (this was later addressed by adding additional solar panels to these sites), and some instruments were redeployed elsewhere towards the end of the survey period.

Instruments

The Nanometrics Trillium 120 Posthole seismometer made up the bulk of our network. This is a broadband, three-component instrument designed for down-hole deployments. It has a flat velocity response between 120 s and 150 Hz and low self noise. It was deployed to all sites except at S-12, S-14, S-16 and S-17.

A set of 7 Guralp CMG-3ESPCD three-component seismometers made up of the



Figure 2.3: The seismometer site at S-05. Sheet metal sheds like these were used to protect all stations deployed in the desert foreland.

rest of the network, and were deployed from S-11 to S-17. This instrument has a flat velocity response between 60 s and 50 Hz.

2.3.2 NCMS network

The National Centre for Meteorology and Seismology (NCMS) of the UAE operates several networks of seismometers across the country, and has close links to equivalent organisations in Bahrain and Oman. They kindly granted us access to 2.5 years worth of data (from $01/06/2014 - 31/12/2016$) from across these networks to supplement our own passive seismic dataset, and these stations are shown in Figure 2.6.

The instruments deployed in their networks were a mix of Nanometrics Trillium 40's and 240's, Guralp CMG-3T's, and Streckeisen STS-2's. These instruments have varying response ranges, with the narrowest being the Trillium 40, at ~ 30 s to ~ 3 Hz.

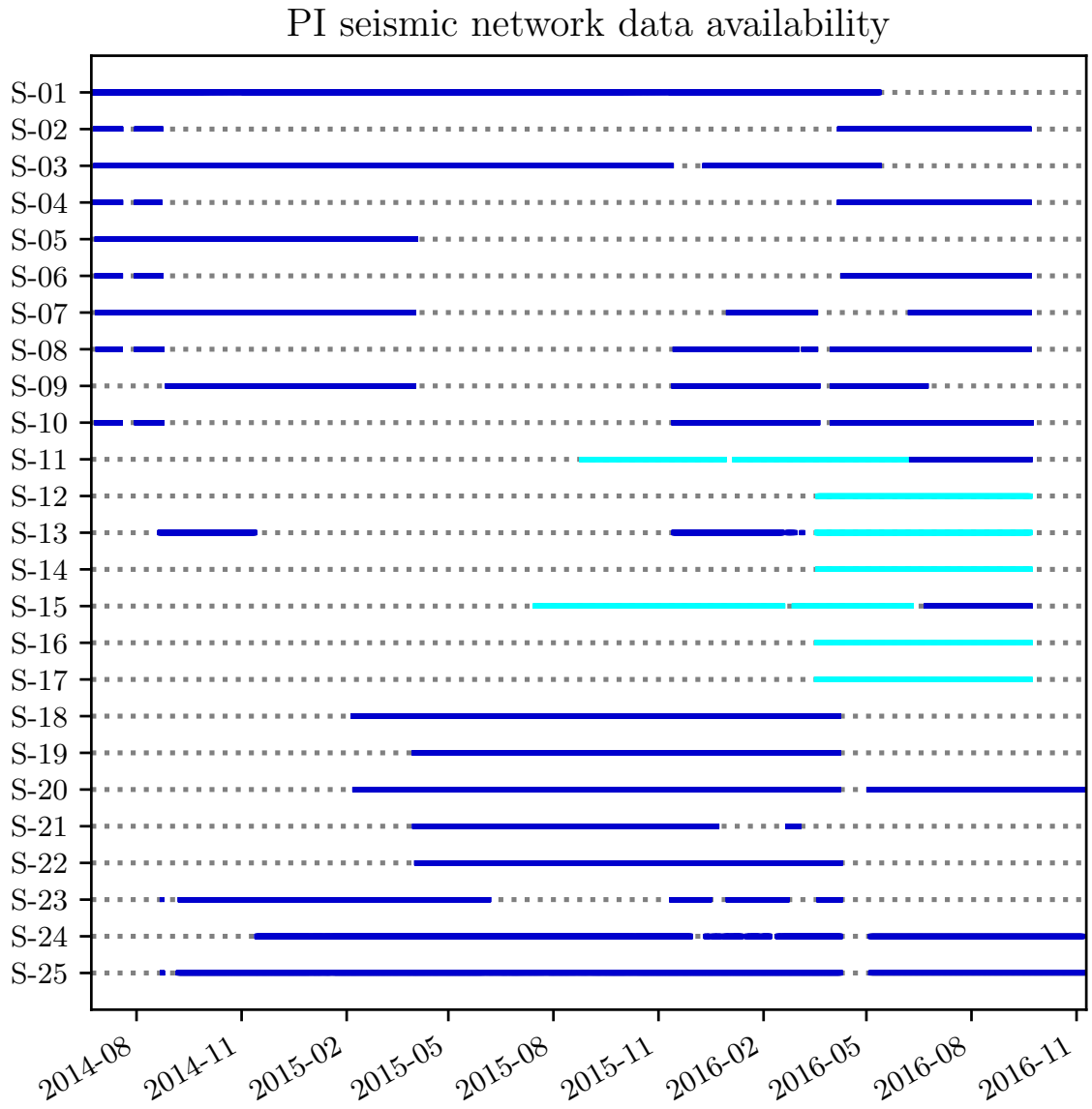


Figure 2.4: Data coverage for the PI/Oxford seismic network. Blue indicates coverage from a nanometrics instrument, cyan indicates coverage from a Guralp instrument, and the grey dotted line represents no data.



(a) Nanometrics seimometer installation. **(b)** Guralp seismometer installation.

Figure 2.5: Installation of a Nanometrics Trillium 120 Posthole seismometer in fine sands of the desert in the western foreland (left), and a Guralp 3ESPCD seismometer in loose gravels of the UAE-Oman mountains (right).

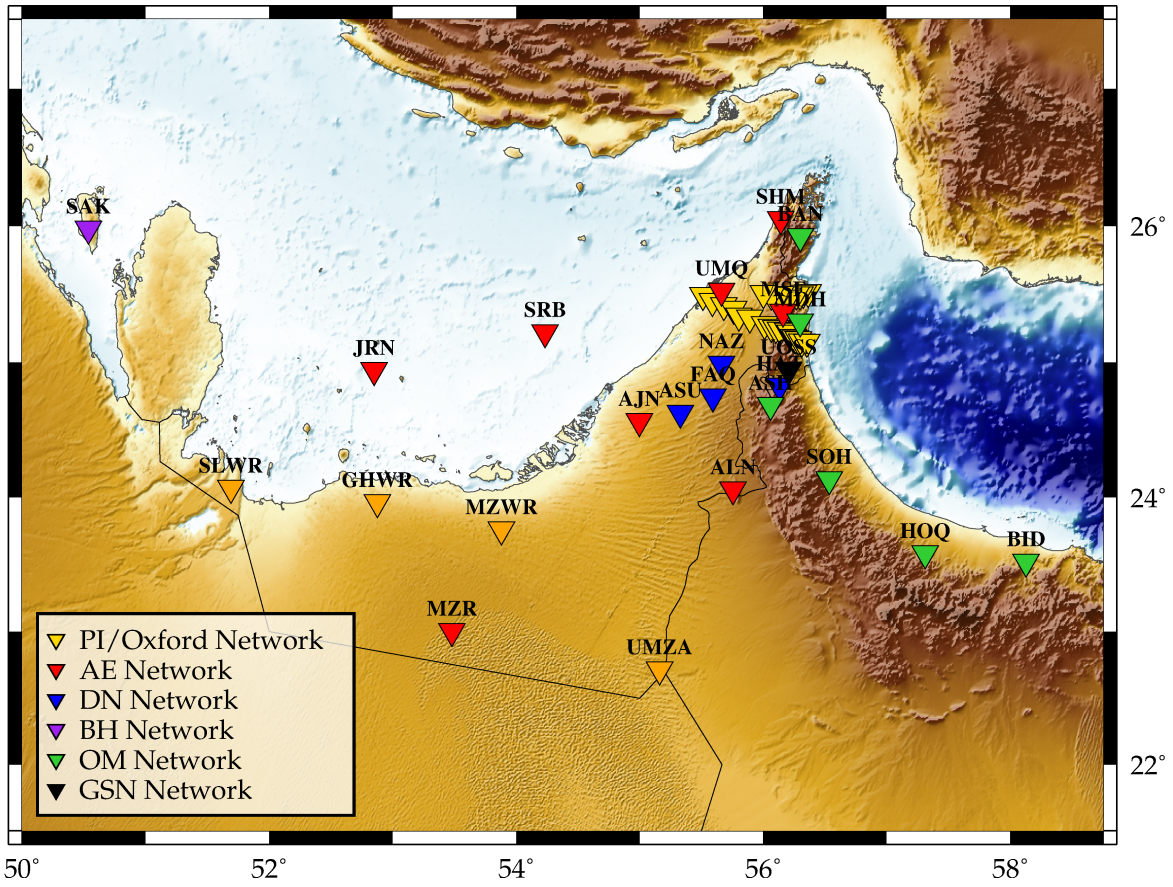


Figure 2.6: Broad map of the region showing the NCMS linked networks. The PI/Oxford network is shown for reference.

2.4 Fieldwork

This DPhil project included a number of field trips out to the UAE to collaborate with our project partners at the Petroleum Institute (PI) in Abu Dhabi, explore the key geological outcrops in the UAE-Oman mountains, and acquire new data.

The first of these was a group trip that took place between the 5^{th} to the 14^{th} of January 2015. It included the full project team from Oxford of Tony Watts, Mike Searle, Tyler Ambrose, and myself. We linked up with our Abu Dhabi based project lead Mohammed Ali, and his post-doctoral researcher Simone Pilia at the PI to discuss the project and assign responsibilities before heading out east to the UAE-Oman mountains to tour key geological outcrops and familiarise ourselves with the study area.

2.4.1 Exchange to the PI

The second trip was a 5 month student exchange to the PI, from 7^{th} of January to the 6^{th} of June 2016. The primary purpose of this trip was to acquire new onshore gravity data along the profiles D1 and D4. These surveys were undertaken across three separate fieldtrips (from the 17^{th} to the 22^{nd} of February, the 5^{th} to the 10^{th} of April, and the 17^{th} to 19^{th} of April), as they covered close to 200 km, and stretched across both the rolling sands of the desert foreland, and the steep, rocky terrain of the UAE-Oman mountains.

A 4WD vehicle was hired for these surveys, but access to many measurement sites was still difficult, as roads across the foreland tended to be oriented north-south and access roads in the UAE-Oman mountains were often just steep, gravel tracks. The most challenging section was a $\sim$ 16 km mountainous stretch between S-21 and S-22 along the northern profile D4 that had to be undertaken on foot. This section was undertaken on the 22^{nd} of February with the assistance of Tyler Ambrose, with drop-off and pick-up arranged by Simone Pilia.

We obtained a total 193 new gravity measurements, at 149 unique sites along these profiles (see Appendix A). This data was processed to Bouguer anomalies, and is de-

scribed in more detail in Section 4.7.

This exchange also allowed me the opportunity to work more closely with Mohammed Ali and Simone Pilia at the PI during this time, to assist Tyler Ambrose with his geological fieldwork, and to assist Simone Pilia in maintaining and redeploying our passive seismic network. It also involved a presentation of our work to date to some of our UAE stakeholders, an outreach presentation on geology and geophysics to the Emirates Natural History Group by Tyler Ambrose and myself, and a second group tour of key geological sites.

2.4.2 Vibroseis refraction survey

I travelled to the UAE again from the 16th to the 26th of November in 2016 to assist with a vibroseis refraction survey along the southern profile D1. This involved removing the instruments installed along the northern profile D4 (S-18 - S-25), and re-deploying them at temporary sites along D1 to increase the station density on this profile. Two vibroseis trucks moved westwards along this line from Fujairah, and deployed at 13 sites to undertake a shot sweep (e.g. Figure 2.7). As these trucks moved westwards into the foreland, we progressively removed the easternmost seismometers, and redeployed them closer to the shotpoint to increase the receiver density. Following this survey, all of the seismic instruments were removed, to be redeployed for a tomography project elsewhere in the UAE.

2.4.3 Final project meeting

A final trip to the UAE took place from the 9th to the 13th of January 2017 to discuss the results of our work to date, and discuss the publication of a summary paper. This trip also included a field trip to key geological outcrops, with a focus on the metamorphic sole.



Figure 2.7: The two vibroseis trucks in action in the desert foreland during the survey in November 2016.

Chapter 3

Receiver functions

3.1 Introduction

Receiver functions are a method of imaging impedance contrasts in the crust and upper mantle. In this chapter we introduce the method, and discuss its origins. We detail the steps involved in their calculation, and compare the various deconvolution methods. We also describe the $H - k$ stacking method for reliably converting receiver function results from the time domain to depth. We then obtain an earthquake dataset from global catalogues, and apply the method to data recorded by the passive seismic network deployed for this project, and selected NCMS stations, using existing and newly developed software codes. The results obtained are then interpreted to identify major impedance interfaces in the mid to lower crust below our seismometer profiles.

3.2 The receiver function method

A receiver function is a time series record that describes the response function of the Earth beneath a three-component seismometer (the receiver) to reveal crustal and upper mantle structures. The method was pioneered by *Phinney* (1964); *Burdick and Langston* (1977); *Langston* (1979), and aims to highlight phase conversions from upward travelling primary compressional (P) waves to secondary shear (S) waves at

significant impedance interfaces beneath the receiver. Approximately vertically incident P-waves are required for these phase conversions to be reliably observed, and large magnitude teleseismic earthquakes are therefore used as an energy source. P-wave energy from these events travels into the mantle and is refracted back towards the surface due to the velocity gradient of the mantle. A portion of this P-wave energy is converted to a vertically polarised S-wave (S_v) at significant impedance interfaces and transmitted to the surface where it can be recorded by a seismometer (Figure 3.1). The lower velocity of S-waves relative to P-waves means that there is a delay time between these phases, and this delay time can be used to obtain the depth of the converting interface. These P and S phases can also reverberate in the upper layer, and these reverberated phases can be used as an additional constraint on interface depth. They can also provide an estimate of the P-wave to S-wave velocity ratio.

Converted S-wave energy is often too weak to be visible above the noise on raw passive seismic records. To highlight these phase conversions, we rotate the seismometer components into a reference frame aligned with the maximum compressional, radial and transverse energy of the incoming earthquake phases (see Section 3.2.1). This isolates the P-wave energy onto the new 'vertical' component and the converted, vertically polarised, S-waves onto the radial component. In practice the transverse component will also contain some energy. While it is not usually interpreted, this trace can be useful for quality control purposes.

To better highlight the converted S waves near the receiver, the 'vertical' component of the signal is deconvolved from the radial and transverse components, as the common source and path effects should be present on all components. This deconvolution gives us our radial and transverse receiver function. While deconvolution is not strictly necessary, it has the disadvantage of removing the P-wave reverberations. Good results have been obtained with component rotation and stacking alone (e.g. *Kumar et al.* (2010)), but deconvolution provides a significant improvement in signal quality however, and is essential when a limited number of events are available for analysis.

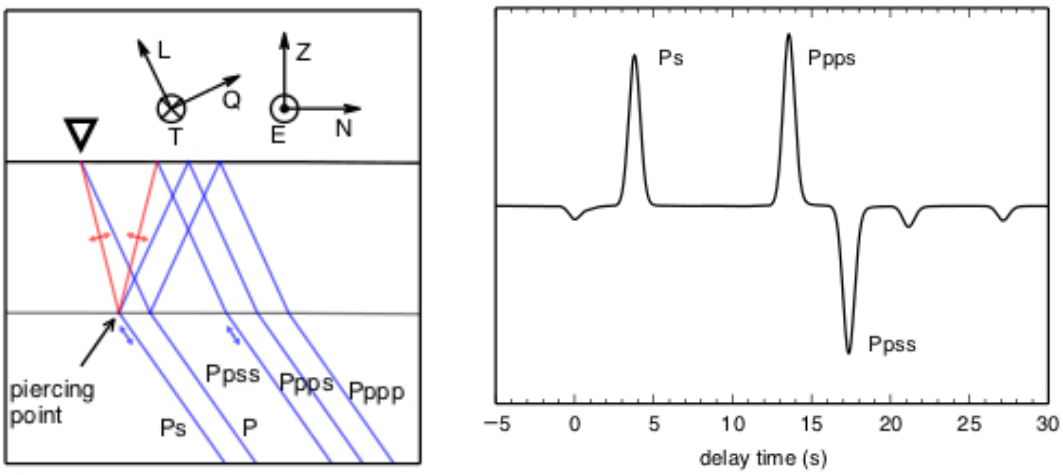


Figure 3.1: A synthetic receiver function (right) obtained from a simple 2 layer geometry (left). Primary (P), converted (Ps), and reverberated ($PpPs$, $PpSs$, $PpPp$) phase paths are shown, with P legs coloured blue and S legs red. Figures from `rf.readthedocs.io`.

The receiver function method is ideally suited to regions with a flat and laterally homogeneous velocity structure. This allows all available results to be stacked, which significantly improves the signal to noise ratio. The method can also be applied in regions with dipping layers and lateral heterogeneities, but care must be taken to avoid stacking results from different interfaces or different depths on a dipping interface. This can be achieved by inspecting results at each station for variations with back azimuth and epicentral distance and grouping them accordingly.

3.2.1 The LQT reference frame

Seismometers are typically installed in a ZNE configuration, with their components aligned to a vertical (Z), north (N) and east (E) axis. For receiver functions, we are interested in isolating primary P arrivals from P to S_v conversions, and this can be achieved by rotating the seismometer reference frame to one aligned with these phases.

We make use of the LQT reference frame, in which the vertical component is rotated to be aligned with the incidence angle of the primary P phase (L) and the north and east components are aligned to the radial (Q) and transverse (T) orientations of the converted S phases (Figure 3.1, left). In this thesis, this rotation is achieved using the

theoretical back azimuth (ϕ) and incidence angle (θ) of the primary P-wave for each event, calculated using the *iasp91* global velocity model (*Kennett and Engdahl*, 1991).

$$\begin{bmatrix} L \\ Q \\ T \end{bmatrix} = \begin{bmatrix} \cos(\theta) & -\sin(\theta)\cos(\phi) & -\sin(\theta)\sin(\phi) \\ \sin(\theta) & \cos(\theta)\cos(\phi) & \cos(\theta)\sin(\phi) \\ 0 & \sin(\phi) & -\cos(\phi) \end{bmatrix} \begin{bmatrix} Z \\ N \\ E \end{bmatrix} \tag{3.1}$$

3.2.2 Deconvolution

Receiver functions are simple to calculate in principle. We are interested in the response function of the Earth beneath a seismic station, and this can be obtained by deconvolving the radial and transverse components of the earthquake record from its vertical component. This can be accomplished by spectral division (e.g. *Langston* (1979))

$$H_R(f) = \frac{Y_R(f)}{Y_Z(f)} \tag{3.2}$$

where $Y_R(f)$ and $Y_Z(f)$ correspond to the Fourier transforms of the radial and vertical components of the seismic record and $H_R(f)$ is the spectral representation of the radial receiver function. The transverse receiver function ($H_T(f)$) is obtained by substituting the spectrum of the transverse component ($Y_T(f)$) for the radial component ($Y_R(f)$) into this equation.

In practice, applying Equation 3.2 is often problematic. It encounters stability problems when $Y_Z(f)$ approaches zero and the source spectrum is often masked by noise at higher frequencies, distorting the signal. Several deconvolution methods for receiver functions have been proposed to overcome these problems.

'Water level' spectral division

Many of the issues in calculating receiver functions by spectral division can be overcome with some simple modifications to Equation 3.2 (*Langston*, 1979; *Ammon*, 1991). The 'water level' modification proposed by *Clayton and Wiggins* (1976) introduces a lower

limit to the denominator in this equation to prevent instabilities when $Y_Z(f)$ approaches zero. A filter is also used to restrict the influence of higher frequency noise and ensure the source signal dominates the spectrum, and the deconvolution becomes

$$H_R(f) = \frac{Y_R(f)Y_Z(f)^*}{\phi(f)}G(f) \tag{3.3}$$

with $Y_Z(f)^*$ denoting the complex conjugate of $Y_Z(f)$, and

$$\phi(f) = max\{Y_Z(f)Y_Z^*(f),\ c \cdot max\{Y_Z(f)Y_Z^*(f)\}\} \tag{3.4}$$

representing the water level modification where the parameter c selects the minimum allowable energy as a proportion of the maximum energy on the vertical component ($0 \leq c \leq 1$). This parameter should be chosen to be the lowest value that allows for a stable deconvolution result, and is often selected via trial and error. The additional function $G(f)$ represents a frequency domain filter to limit the spectral content of the receiver function to lower frequencies. The Gaussian function

$$G(f) = \exp\left(\frac{-\omega^2}{4a^2}\right) \tag{3.5}$$

is typically used, with ω representing angular frequency ($\omega = 2\pi f$) and a representing the Gaussian width factor determining the cut-off frequency of the filter. A width factor of $a = 4$ for example, would restrict the frequency content of the resulting receiver function to below $\sim 2\ Hz$.

The 'water level' method remains popular, but has several drawbacks. The experimentation required to find an optimal c value makes it problematic when applying the method automatically to large numbers of events, and the higher frequency components of the signal are often obscured by either noise, or the whitening process of the water level application. This restricts analysis to the low frequency components of the signal, thus limiting the resolution of the resulting receiver function.

Time domain deconvolution

Many of the limitations of frequency domain deconvolution methods can be overcome by instead performing the deconvolution in the time domain (*Abers et al.*, 1995; *Gurrola et al.*, 1995; *Ligorría and Ammon*, 1999).

In the time domain, the receiver function problem can be expressed as:

$$\boldsymbol{V} \cdot \boldsymbol{r} = \boldsymbol{h} \tag{3.6}$$

where $\boldsymbol{h}$ is the radial (or transverse) component of the seismometer and $\boldsymbol{r}$ represents the radial (or transverse) receiver function. The matrix $\boldsymbol{V}$ is composed of m columns containing zero padded, time shifted copies of the vertical component.

$$\boldsymbol{V} = \begin{bmatrix} v_1 & 0 & \dots & 0 \\ \vdots & v_1 & \ddots & \vdots \\ v_n & \vdots & \ddots & 0 \\ 0 & v_n & \ddots & v_1 \\ \vdots & \ddots & \ddots & \vdots \\ 0 & \dots & \dots & v_n \end{bmatrix} \tag{3.7}$$

The solution to Equation 3.6 can be found via damped least squares, and takes the form

$$\boldsymbol{r} = (\boldsymbol{V}^T\boldsymbol{V} + w\boldsymbol{I})^{-1} \cdot \boldsymbol{V}^T\boldsymbol{h} \tag{3.8}$$

where $\boldsymbol{I}$ is the identity matrix, $\boldsymbol{V}^T$ is the transpose of $\boldsymbol{V}$, and w is damping scalar.

This method is more computationally demanding than frequency domain methods, but eliminates the need for water level experimentation. The lack of a 'water level' means this approach is also stable at higher frequencies, allowing higher resolution receiver functions to be obtained. It should be noted that noise will likely dominate the signal at frequencies above $\sim 2\ Hz$ so it is usually necessary to apply a low pass filter to the data before the application of this method.

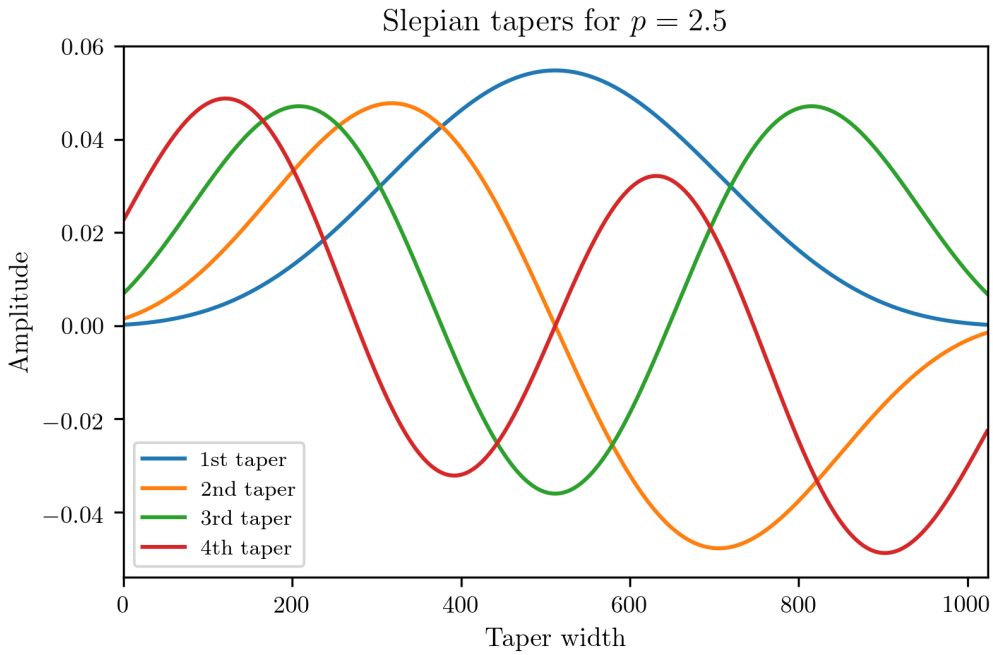


Figure 3.2: Slepian tapers of sample length 1024 for the time-bandwidth product $p = 2.5$. These tapers are orthogonal and each one provides an independent estimate of the spectral content of the signal when combined with a Fourier transform.

Multi-taper correlation (MTC)

A reformulation of the deconvolution problem in the frequency domain using multi-taper correlation (MTC) methods (*Kuo et al.*, 1990; *Vernon et al.*, 1991) has been developed by *Park and Levin* (2000). This method avoids the numerical instabilities associated with spectral division and aims to distinguish 'coherent' from 'incoherent' scattering to provide improved resistance to noise.

The MTC method utilizes Slepian tapers (Figure 3.2) to provide K independent estimates of the spectral content of the data for a given time-bandwidth product p. The spectrum of each component $Y(f)$ is taken as the sum of these K estimates

$$Y_{Z/R/T}(f) = \sum_{k=0}^{K-1} \sum_{n} u_n^{Z/R/T} w_n^k e^{i2\pi f n \tau} \tag{3.9}$$

where u_n is the time series of the respective seismometer component, w^k is the k^{th} Slepian taper, and τ is the sampling interval.

The radial or transverse receiver function $H_R(f)$ is then calculated in a similar manner to the 'water level' method

$$H_{R/T}(f) = \frac{Y_{R/T}(f)Y_Z^*(f)}{Y_Z^*(f)Y_Z(f) + S(f)}G(f) \tag{3.10}$$

where $S(f)$ is a damping factor taken from the spectral content of the pre-event signal on the vertical component and $G(f)$ is again a frequency domain filter. In this case a cosine squared function with a cut-off frequency f_c is used.

$$G(f) = \cos^2\left(\frac{\pi f}{2f_c}\right) \tag{3.11}$$

A time-bandwidth product (p) of 2.5 is suggested by *Park and Levin* (2000), allowing up to 4 ($K_{max} = 2p - 1$) Slepian tapers to be applied. In practice $K = 3$ is usually sufficient however. Application of these tapers provides the additional benefit of reduced spectral leakage and a more reliable estimate of the true spectrum of the signal (*Thomson*, 1982; *Park et al.*, 1987).

A limitation of this method is a decline in the amplitude of later phases due the application of the tapers. Phases with a delay time $t > \frac{T}{2p}$, where T is the duration of the analysis signal, cannot be reliably retrieved (*Park and Levin*, 2000). A modification to the method by *Helffrich* (2006) using overlapping data windows overcomes this deficiency. This modified method is termed Extended Time Multi-Taper Correlation (ET-MTC).

The stability of this method provided by the damping factor, and its resistance to spectral leakage mean the MTC method can be extended to higher frequencies than either of the previous methods. The improved resolution this provides make it ideal for investigating mid-crustal discontinuities that may not be evident using the 'water level' or time domain methods (e.g *Leahy et al.* (2010)). If the pre-event window used to generate this damping factor is particularly noisy, due to a local earthquake for example, the quality of the resulting receiver function will be compromised. This can be partially mitigated by employing signal to noise ratio tests prior to calculation (see

section 3.7)

3.2.3 Synthetic data comparison

In order to compare the performance of these deconvolution methods, they were applied to synthetic data using a 0.5 Hz Ricker wavelet of unit peak amplitude as a signal. Our synthetic radial component consisted of unit amplitude Ricker wavelets of alternating polarity at 2, 5 and 10 s delay time. Both components were contaminated with random noise convolved with 2 and 4 Hz Ricker wavelets (see Figure 3.3).

All methods are able to reproduce the three radial component peaks. The 'water level' method reproduces the original amplitudes of the signal most accurately, but is low resolution and features warping around the peaks. The time domain method struggles with the high frequency noise (no low pass filter was applied prior to its application) and features an artifact signal at 0 s delay, but it is still able to accurately reproduce all three peaks. The MTC methods produce the cleanest signal, with very clear peaks at for all delay times and little contamination from noise. The ET-MTC modification accurately preserves the relative amplitudes of the three peaks but is contaminated by slightly higher levels of ringing, particularly at large offsets.

On synthetic data the MTC methods clearly produce the best results, and they were favoured going forward. It should be noted that contrary to what this analysis suggests, the time domain method generally performed very well when applied to real data and was also utilised extensively.

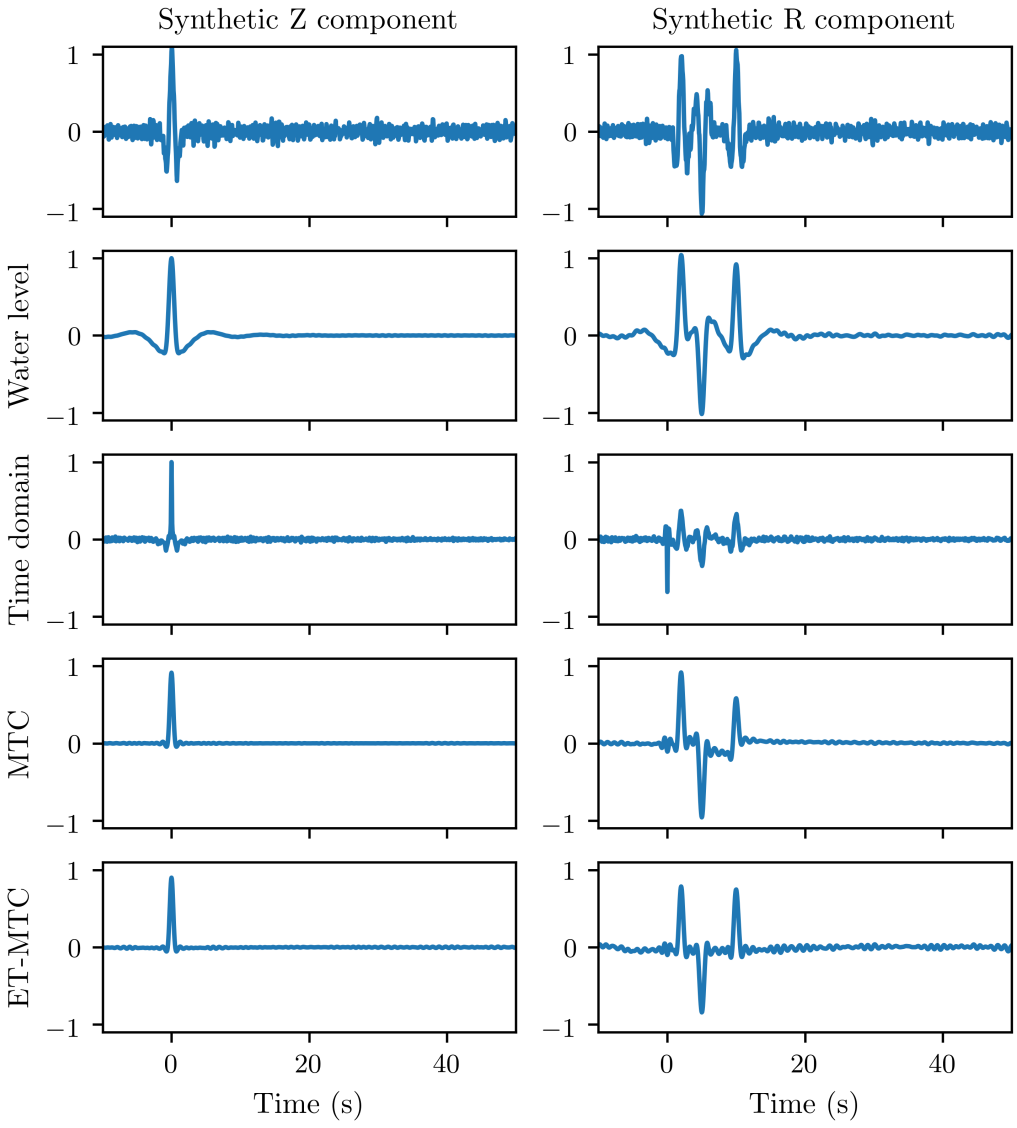


Figure 3.3: Comparison of the various deconvolution methods on synthetic data. We utilize 0.5 Hz Ricker wavelets of unit amplitude as a signal. The synthetic radial component features 0.5 Hz Ricker wavelets of alternating polarity at 2, 5 and 10 s delay time. The Z component is taken as the source and deconvolved from both components to obtain the respective receiver function. All methods are able to reproduce the three peaks but the MTC methods are clearly superior.

3.3 H - k stacking

Receiver functions provide an effective method of finding significant velocity discontinuities in the crust and upper mantle by providing a time delay between the primary P arrival and a Ps conversion. Converting these delay times to depth is not always straight forward however, as it requires accurate knowledge of both the P and S velocity profiles (or alternatively, a P velocity profile and the $\frac{v_p}{v_s}$ ratio k). $H-k$ stacking provides a solution to this problem.

Given a delay time of t_{Ps}, the depth to a discontinuity H is

$$H = \frac{t_{Ps}}{\sqrt{\frac{1}{v_s^2} - p^2} - \sqrt{\frac{1}{v_p^2} - p^2}} \tag{3.12}$$

where v_p and v_s are the P and S wave velocities respectively and p is the ray parameter of the incident wave. There is an obvious trade off between depth (H), seismic velocity, and the P to S velocity ratio k in this equation. The $H-k$ stacking algorithm was developed by *Zhu and Kanamori* (2000) as a method to explore this trade off.

The algorithm takes advantage of the fact that depth, as defined by equation 3.12, is approximately ten times more sensitive to variations in k than v_p (*Zhu and Kanamori*, 2000). An average value of v_p is therefore assumed (an appropriate value can often be found in the literature) and the problem reduced to two independent variables, H and k.

Obtaining both H and k from the Ps delay time alone is not possible, so the reverberated $PpPs$ and $PsPs/PpSs$ phases[1] often seen following the primary Ps conversion are incorporated. The delay times for these phases can be related to depth by

$$H = \frac{t_{PpPs}}{\sqrt{\frac{1}{v_s^2} - p^2} + \sqrt{\frac{1}{v_p^2} - p^2}} \tag{3.13}$$

[1]For laterally homogeneous velocity profiles the travel time and polarity of the $PsPs$ and $PpSs$ phases will be identical so they can be grouped together.

$$H = \frac{t_{PsPs/PpSs}}{2\sqrt{\frac{1}{v_s^2} - p^2}} \tag{3.14}$$

The $H - k$ stacking algorithm performs a grid search across the projected arrival times for a range of H and k values and the amplitudes of the radial receiver function at these projected arrival times summed across all three phases

$$S(H,k) = w_1 r(t_1) + w_2 r(t_2) + w_3 r(t_3) \tag{3.15}$$

where $r(t)$ is the radial receiver function, w_{1-3} are user defined weights corresponding the Ps, $PpPs$ and $PsPs/PpSs$ phase respectively (note that these weights must sum to 1), and t_{1-3} are similarly assigned projected travel times for a given value of H and k, as defined by equations 3.12-3.14.

This algorithm searches the whole $H - k$ parameter space and automatically highlights values of H and k that produce high stacked amplitudes. If the primary Ps conversion and at least one of the $PpPs$ or $PsPs/PpSs$ phases are observed then a value for both H and k can be obtained.

Zhu and Kanamori (2000) also provide equations to formally assess the uncertainty of an $H - k$ stacking result. However these equations provided unreasonably small uncertainties in most of our test cases. We have therefore followed the approach of *Al-Damegh et al.* (2005) and (*Julià*, 2007), and estimated uncertainties in H and k using bootstrapping instead (*Effron and Tibshirani*, 1991). It should be noted that the uncertainties obtained via this method are based solely on statistical re-sampling and do not take into account potential errors in the physical parameters used, such as average crustal velocity. They are therefore likely to underestimate the true uncertainty.

3.4 Earthquake Dataset

The source signal for receiver function analysis comes from large magnitude (typically $M > 5$) distal earthquakes. The primary P-wave from these earthquakes must first

travel down into the mantle before being refracted back to the surface. This ensures the energy is approximately vertically incident when it arrives at the receiver and allows clear P to S conversions to occur at velocity discontinuities beneath the seismic station. This restricts the earthquakes available as potential sources to events that occur far enough away for the energy to be refracted in the mantle, but not so far that it is refracted by the outer core. The exact values chosen vary from study to study, but is typically between $30 - 90^{\circ}$ of the analysis station.

The earthquake dataset used for this project was generated from the United States Geological Survey (USGS) global earthquake catalogue. Our network is closely spaced relative to teleseismic earthquake distances, so we generate a single earthquake dataset from a central point in our network ($25.5^{\circ}N$, $56^{\circ}E$) rather than a unique catalogue for each station. After testing a range of search parameters, all earthquakes within a range of $30 - 98^{\circ}$ from this central point, and with a moment magnitude $M_w > 5.5$ were selected, as smaller events consistently failed our signal to noise ratio tests. Our network was first deployed in July 2014 and operated until November 2016 so our catalogue is restricted to this time range.

The total dataset includes 382 events and is shown in Figure 3.4. It features limited coverage at almost all back-azimuths, with a bias towards the east due to the large number of high magnitude events occurring in the subduction zones of Java, Sumatra and the western Pacific Ocean.

Due to the limited data availability at many stations our network (Figure 2.4), not every event in this dataset was recorded at each station. The number of these events recorded at each station in the PI network is shown in Figure 3.5. Stations with greater data availability naturally recorded more events, with S-01, S-03 and S-25 standing out with over 200 events available for analysis.

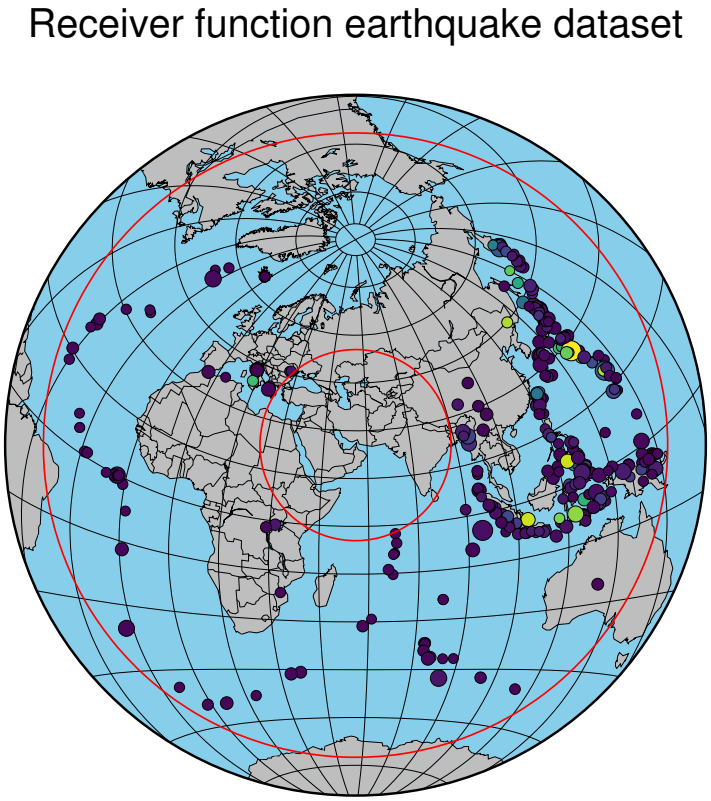


Figure 3.4: Earthquake dataset used for receiver function analysis. Individual events are plotted as circles coloured by hypocentre depth and scaled by magnitude. The lower and upper limits of the search radius ($30 - 98°$) are shown as red circles.

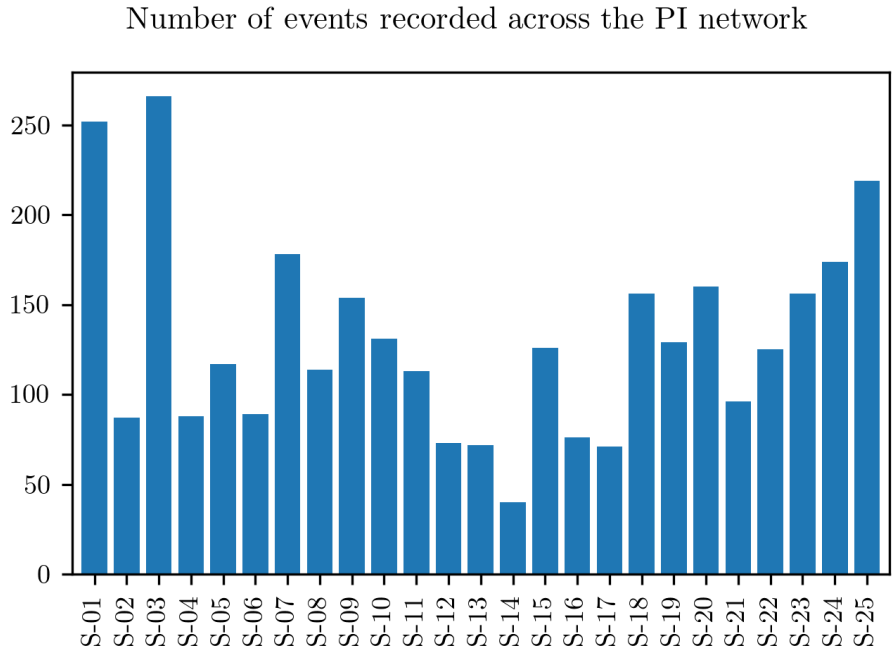


Figure 3.5: Number of events in our earthquake dataset that were recorded at each station in the PI network.

3.5 Software and codes

The majority of our data processing and analysis is done within the cross-platform programming language *python* (`https://www.python.org`). The primary packages used were *ObsPy* (*Beyreuther et al.*, 2010), and a receiver function analysis package written by Tom Richter that builds on *ObsPy* called *rf* (`https://rf.readthedocs.io`). This package includes many receiver function processing, analysis and plotting routines, but lacked several capabilities that we sought to employ in this project. We therefore developed a large amount of supplementary python routines (amounting to over 10,000 lines of code) to build upon the capability of *ObsPy* and *rf*, and to test and run our algorithms. Examples include MTC and ET-MTC deconvolution algorithms, receiver function quality control algorithms, and the $H - k$ stacking routines.

3.6 Data preparation

Data for receiver function analysis is taken from our passive seismic dataset. To prepare this data for receiver function analysis we followed the work-flow described below.

1. Calculate the projected arrival time for the primary P phase (t_P) for each event using the *TauP* (*Crotwell et al.*, 1999) module in *ObsPy* (*Beyreuther et al.*, 2010).

2. Cut the raw seismogram records to a 200 s initial analysis window centred around the projected arrival time t_P.

3. Attach the appropriate transfer function (these are instrument dependent), and correct for the instrument response.

4. De-trend, de-mean, downsample data to 25 Hz, and apply a Butterworth band-pass filter to restrict the frequency content to between 20 s and 4 Hz to limit potential artifacts.

The seismometer reference frame is then rotated to the LQT system (see Section 3.2.1), and trimmed again to create receiver function signal windows and noise

windows (for the MTC deconvolution methods). For 'water level', time domain, and ET-MTC deconvolution methods a receiver function windows of $-20 - 40$ s around t_P were selected. For the MTC method, the receiver function and noise windows were $-10 - 80$ s and $-100 - 10$ s. This gives a reliable receiver function amplitudes out to approximately 18 seconds delay time (see section 3.2.2). For the ET-MTC method a noise window of $-80 - -20$ s was used.

3.7 Signal to Noise Ratio

The receiver function method requires a clear recording of distant teleseismic event so it is important that phases from this event are clearly recorded above background noise. We therefore filter the seismograms from our earthquake dataset prior to receiver function calculation using signal to noise ratios (SNR). We define a SNR test statistic as simply the ratio of amplitudes on a 'signal window' and a 'noise window' on the rotated vertical component (L) of our seismogram

$$SNR = \frac{n_n}{n_s}\sqrt{\frac{\sum S_i^2}{\sum N_i^2}} \tag{3.16}$$

where S and N are the signal and noise windows respectively, and n_s and n_n are the number of data points in the signal and noise windows respectively. The signal window is defined to extend from 5 s prior to the projected t_P onset to 15 s afterwards, and the noise window from 30 s to 10 s prior to the t_P onset.

Analysis of sample waveforms at several stations confirmed this test statistic (equation 3.16) appropriately classifies the signal quality for our earthquake dataset, and after some experimentation a SNR threshold of 2 was selected as pre-requisite for receiver function analysis.

The mean SNR across our network is shown in Figure 3.6. All stations, with the exception of S-16, had a mean SNR above this threshold. Stations deployed in the desert to the west (S-01 - S-07) had a lower mean SNR than the rest of our network. This is likely due to poorer ground coupling and higher attenuation associated with the

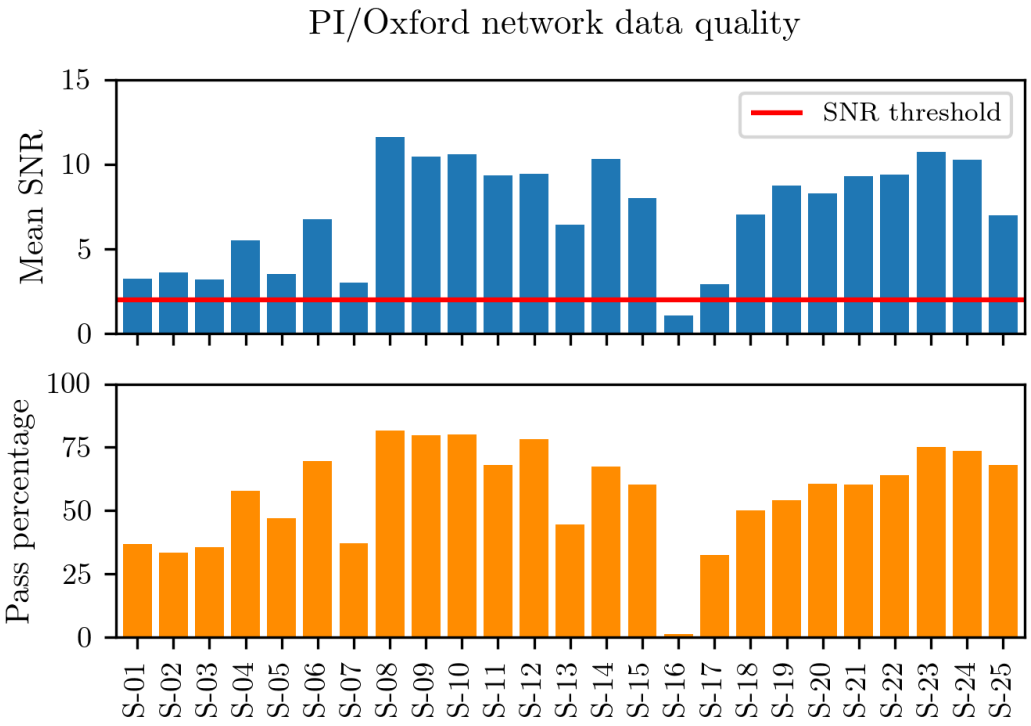


Figure 3.6: Data quality of the PI/Oxford network. The mean signal to noise ratio (SNR) at each station is plotted top, with the cut-off threshold (2) displayed in red. The percentage of events above this threshold at each station is displayed below.

desert sands in which the instruments were deployed. S-16 and S-17 are the exception to this trend. S-17 is located near the busy corniche in Fujairah city and the high noise level is therefore likely to be related to nearby traffic and construction activity. S-16 is located in a relatively quiet valley behind Fujairah city so its high noise level is more surprising. It is possible this station had poor ground coupling, but it was installed within a few hundred metres of a large compound that was then under construction and this may have also contributed to the high noise levels here.

The SNR cut-off eliminated a significant amount of potential receiver function signal sources ($30 - 80\%$, see Figure 3.6). However, restricting our dataset to clearly recorded events ensures that the resulting receiver function is actually associated with our teleseismic event and greatly improved the quality of our stacked traces at each station.

3.8 Quality Control

Assessing the quality of a receiver function result in a quantitative way is not straightforward. Proposed methods include:

- Comparing the ratio of energy on the radial and transverse receiver function. High amplitudes on the transverse result are indicative of an unsuccessful coordinate system rotation, or a high degree of scattering in the upper layer.
- Comparing the amplitudes before and after onset (0 s delay time) on the radial result. High amplitudes pre-onset are indicative of noisy spectrum and unreliable deconvolution.
- Convolving the radial and vertical results and comparing the result to the original seismogram.
- Checking for a high amplitude signal at 0 s offset associated with the primary P arrival.
- Checking the coda of the radial result for reverberations or anomalous signals.

In contrast to many other studies, a clear peak at 0 s offset was generally not present, even on otherwise high quality results, in our dataset. High amplitudes on the transverse results were also a common feature, suggesting a high degree of scattering. This is perhaps unsurprising given that the velocity structure is likely to be complex and highly inhomogeneous, especially across the ophiolite.

With this in mind, we implemented an automatic quality control (QC) regime based on the ratio of energy (in both the time and frequency domains) of the radial (Q) and transverse (T) results, and the amplitudes of the radial result before and after onset of the primary P arrival (see Figure 3.7). All results with a Q/T amplitude ratio < 1.5 and pre/post onset ratio < 2 were automatically rejected. The remaining results could then be inspected manually and accepted or rejected based on the above criteria.

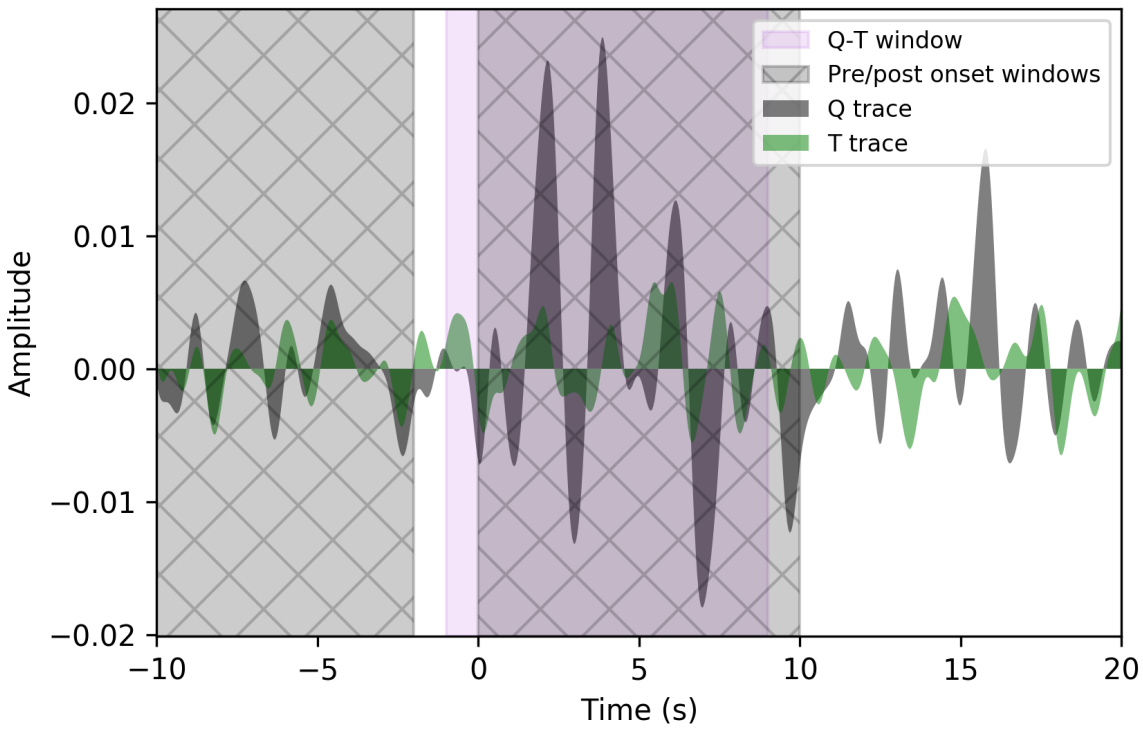


Figure 3.7: An example of receiver function quality control from an ET-MTC result at S-01, highlighting the analysis windows for Q/T and pre-post onset energy ratios. This is a good quality result, with Q/T energy ratio of 3.82 and a pre-post onset ratio of 3.75.

3.9 Previous Studies on the Arabian Continent

Several receiver function studies have been previously undertaken on the Arabian continent. The majority of work to date has been focused on the Arabian platform and the Red Sea margin however, and results in and around the UAE-Oman mountains and its associated foreland are limited. Indeed, that was part of the motivation for undertaking this study. This section will present a brief overview of the work published to date.

Sandvol et al. (1998) undertook a study with a temporary network of 9 stations in western Saudi Arabia. Ps conversions from the Moho were observed at all operational stations, along with a few mid crustal conversions on the Arabian shield and deep scattered upper mantle conversions. Moho depths were obtained using grid search modelling and were found to vary from $\sim$ 35 km near the Red Sea to $\sim$ 45 km in central Arabia, consistent with an earlier controlled source seismic refraction profile by

Mooney et al. (1985). They also noted that the crust appeared to thin back to $\sim 37\ km$ to the north of the shield.

Al-Lazki et al. (2002) calculated receiver functions along a profile of four temporary stations across the UAE-Oman mountains in Oman in a study similar to this one. The profile was oriented roughly north-south and was centred on Jebel Akhdar, west of Muscat. Their stations were deployed for only 2 months. As such, his earthquake dataset consisted of just 8 events. They were able to obtain Ps conversions from the Moho at 3 of the four stations, and converted these to depths using an average crustal velocity of between 6.4 and 6.8 $km\,s^{-1}$. Their results suggested a mantle root existed beneath Jebel Akhdar, with crustal thickness of 49 km here compared to $\sim 41\ km$ to the north and south.

Kumar et al. (2002) and *Julià et al.* (2003) used the same dataset as *Sandvol et al.* (1998) to separately calculate receiver functions on the Arabian platform. *Kumar et al.* (2002) used a variation of the $H-k$ stacking algorithm (see section 3.3) to obtain Moho depths and Poisson's ratios across the network. The Moho depths they obtained were slightly lower than *Sandvol et al.* (1998), ranging from $35-38\ km$. *Julià et al.* (2003) jointly inverted them with surface wave dispersion curves to obtain detailed velocity profiles at each station. The Moho depths they obtained were broadly comparable to the earlier results, but revealed the mid crustal structure in more detail. They also noted that the upper mantle conversions modelled by *Sandvol et al.* (1998) were more likely to be reverberated phases.

Al-Damegh et al. (2005) generated receiver functions across 23 mid and broad-band stations across Saudi Arabia and Jordan and estimated Moho depths using $H-k$ stacking. Moho depths were found to be $33-37\ km$ in the northern platform and $40-53\ km$ towards the south and east. Rapid crustal thinning was observed towards the Red Sea margin, with Moho depths decreasing from continental to oceanic levels over a lateral distance of 250 km.

Tkalcic et al. (2006) calculated and jointly inverted receiver functions and surface wave dispersion curves for velocity profiles across 10 stations on the Arabian continent.

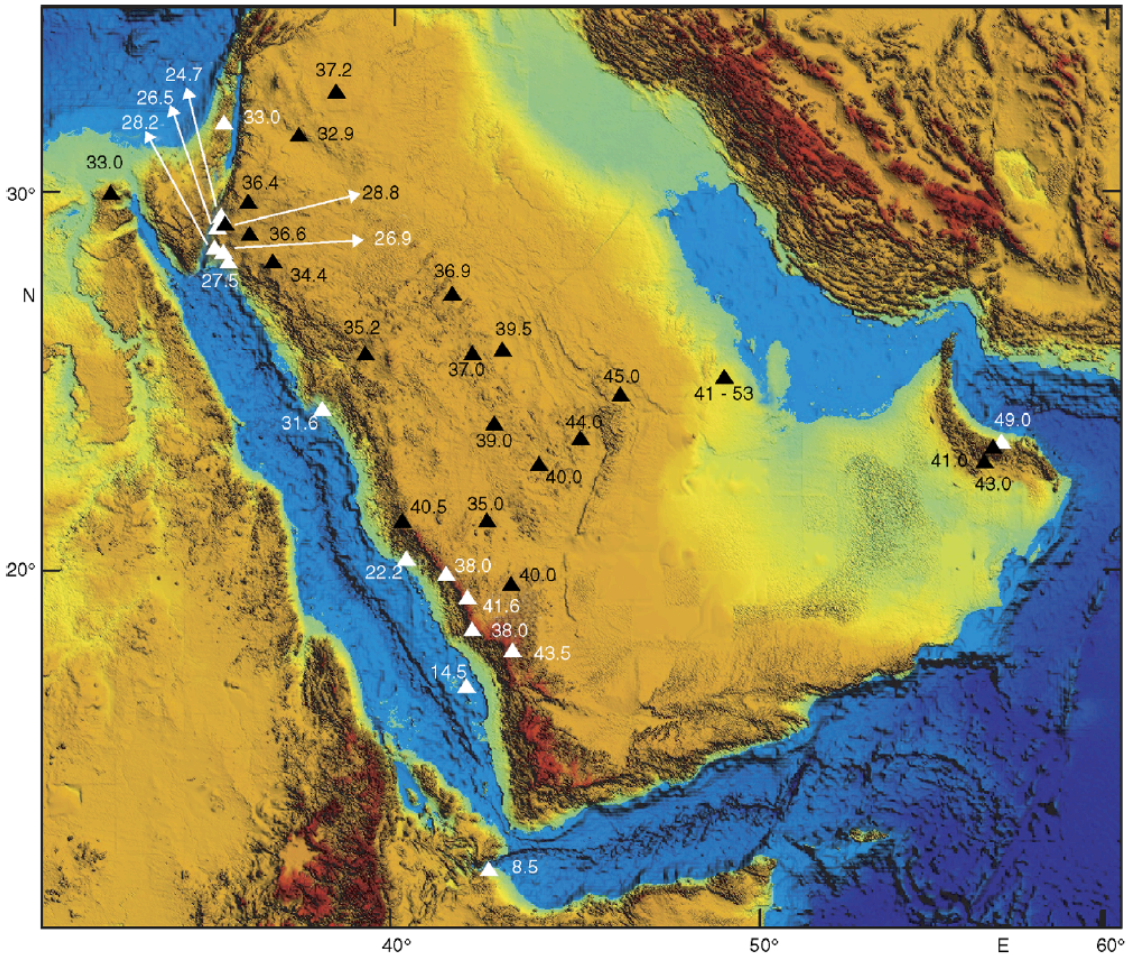


Figure 3.8: Moho depths (in *km*) from Receiver function results from previous studies across the Arabian continent (i.e. *Sandvol et al.* (1998); *Al-Lazki et al.* (2002); *Al-Damegh et al.* (2005)). Note the scarcity of the results in the east, away from the platform. Black and white colouring of the stations is a stylistic choice, and does not represent any difference in the underlying result. Figure from *Al-Damegh et al.* (2005).

The majority of results were on the Arabian platform, and the results for Moho depth were broadly similar to those of *Al-Damegh et al.* (2005). One station (MEZE) was located just south of Al-Ain, in the foreland of UAE just west of the UAE-Oman mountains. They noted the data quality was poor, but reported a crustal thickness here of 38 *km* and no seismic anisotropy.

Hansen et al. (2007) used *S-P* receiver functions (*Farra and Vinnik*, 2000) to estimate Moho depths and the depth the the Lithosphere-Asthenosphere boundary (LAB) thickness at a number of stations across the Arabia, including two in the UAE (MEZE

and HALE). Results from the Arabian platform were largely consistent with those cited above. In the UAE Moho depth was estimated to be 44.5 km at MEZE. No result was obtained at HALE to the north, suggesting data quality here was poor.

Tiberi et al. (2007) used a network of 11 temporary seismic stations in southern Oman and the $H-k$ stacking algorithm to constrain the crustal structure on the Gulf of Aden margin. They found Moho depths decreased from ~ 35 km inland to ~ 26 km near the coast. This decrease of around 10 km over 30 km horizontal distance implies a stretching factor β of $1.38 - 1.54$.

3.10 Calibrating our codes

Initial receiver function results at stations across both the PI/Oxford and NCMS networks were highly variable, and a clear Moho signal was often not visible. To ensure that our data and codes were prepared and parametrised in a way that would produce consistent and reliable results, we decided to test them at geographic locations where receiver functions had been calculated previously and a reliable Moho depth obtained.

The Global Seismograph Network (GSN) is a network of over 150 seismic stations distributed around the globe. Data from this network is publicly available and published receiver function results are available at several GSN stations. We select station II.RAYN in central Saudi Arabia, as it is also on the Arabian plate, and numerous other previous receiver function studies have been undertaken in this region (see Section 3.9), and station II.PFO in southern California, as it was one of the original stations used by *Zhu and Kanamori* (2000) to pioneer $H-k$ stacking, as test locations.

3.10.1 GSN station II.RAYN

II.RAYN is located approximately 175 km south-west of Riyadh on the Arabian platform. Several receiver function studies have been undertaken at this station, with the Moho depths ranging from $35-44$ km (see Table 3.1). Mid and upper crustal velocity discontinuities have also been noted at this site (*Sandvol et al.*, 1998) as well as vari-

Depth (km)	v_p/v_s	Method	Reference
44 ± 2.5	-	Inversion	*Sandvol et al.* (1998)
41	-	Forward modelling	*Levin and Park* (2000)
40	1.766	$H-k$ stacking	*Kumar et al.* (2002)
~ 41	-	Inversion	*Julià et al.* (2003)
35	-	Forward modelling	*Hansen et al.* (2007)

Table 3.1: Previous receiver function results at station II.RAYN. The approach taken in converting phase delay time to depth is listed in the method column. For further details see the respective reference.

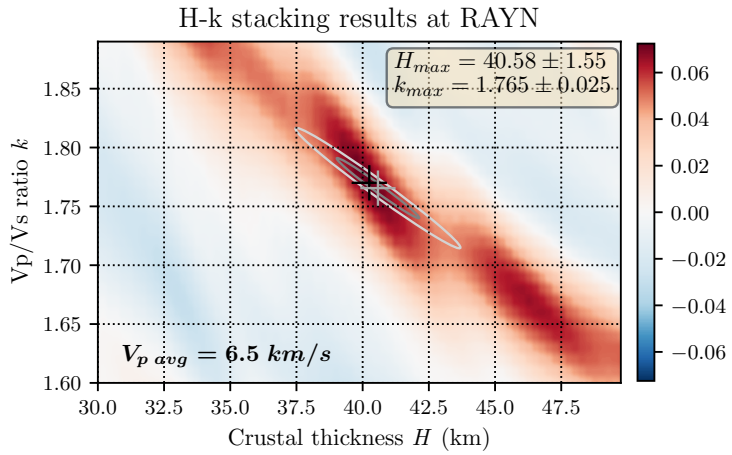
ations with back azimuth that were attributed to crustal anisotropy *Levin and Park* (2000).

We calculate receiver functions using M5.5+ earthquakes from the USGS global catalogue occurring between 2015 and 2017, and located between $30-95°$ of the station. Following the data preparation and processing methods outlined above, we obtained 106 receiver functions for analysis using both the MTC and time domain deconvolution methods. Though both methods produced broadly similar results, we favoured the time domain method with an upper frequency of 1 Hz. Only 15 results passed our quality control tests, with the majority of events failing due to large amounts of energy on the transverse component. A clear Moho conversion was evident on all remaining results at 5 s delay time, and $H-k$ stacking mapped this phase to an interface at depth of 40.47 ± 1.31 km with a k value of 1.767 ± 0.023 (see Figure 3.9). This result is in good agreement with all previous studies, with the exception of *Hansen et al.* (2007) which was based on S-P receiver functions.

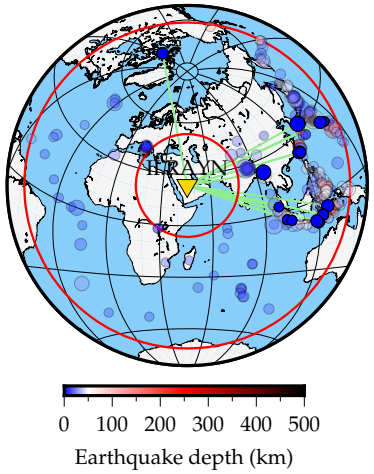
3.10.2 GSN station II.PFO

II.PFO is located in tectonically active Southern California in the mountains south of the Salton Trough. Moho depth estimates range from $25-30$ km, (see Table 3.2). A possible velocity inversion, attributed to trapped saline fluids, was been modelled at ~ 9 km depth by *Baker et al.* (1996), along with significant Moho topography.

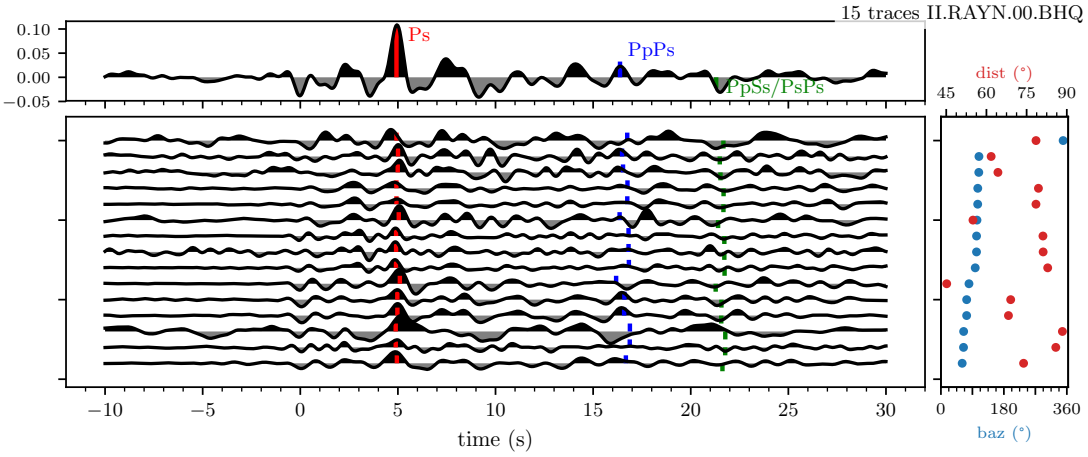
We calculate receiver functions using M5.5+ earthquakes from the USGS global catalogue occurring between 2015 and 2017, and located between $30-95°$ of the station.



(a) Bootstrapped (B=100) $H-k$ stacking plot for II.RAYN. Ellipses represent 1 and 2 bootstrap standard deviations.



(b) II.RAYN earthquake dataset. Unused events are faded.



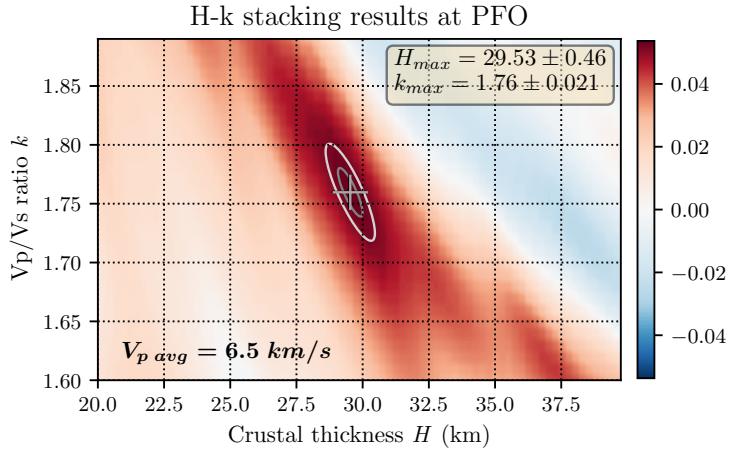
(c) Receiver functions results at II.RAYN, sorted by back azimuth. Individual results are shown bottom and the stacked trace shown top. The locations of the phases representing the highest amplitude $H-k$ stacking result are highlighted on each trace.

Figure 3.9: $H-k$ stacking results at the GSN station II.RAYN. Receiver functions are calculated using the time domain method with an upper frequency of 1 Hz. An average crustal velocity of 6.5 km/s was used for the $H-k$ stack, with weights of 0.5, 0.3 and 0.2 for w_1, w_2 and w_3 respectively. The algorithm picks out the large amplitude Moho conversion at 5 s, and its reverberations, as the most dominant set of phases, and selects an H and k value of 40.58 ± 1.55 km and 1.765 ± 0.025 respectively.

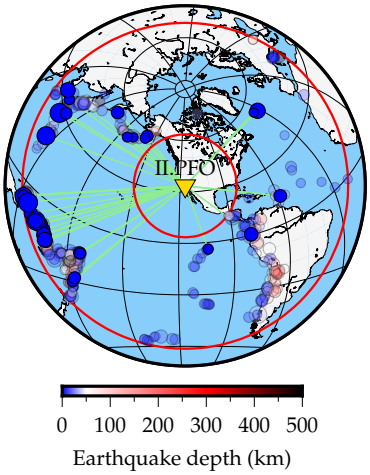
Depth (km)	v_p/v_s	**Method**	**Reference**
25 & 30	-	Forward modelling	*Baker et al.* (1996)
29.4 ± 1.4	1.75 ± 0.06	$H-k$ stacking	*Zhu and Kanamori* (2000)
29	1.75	$H-k$ stacking	*Ramesh et al.* (2002)
29 ± 2	-	Forward modelling	*Abt et al.* (2010)

Table 3.2: Previous receiver function results at station II.PFO. The approach taken in converting phase delay time to depth is listed in the method column. For further details see the respective reference.

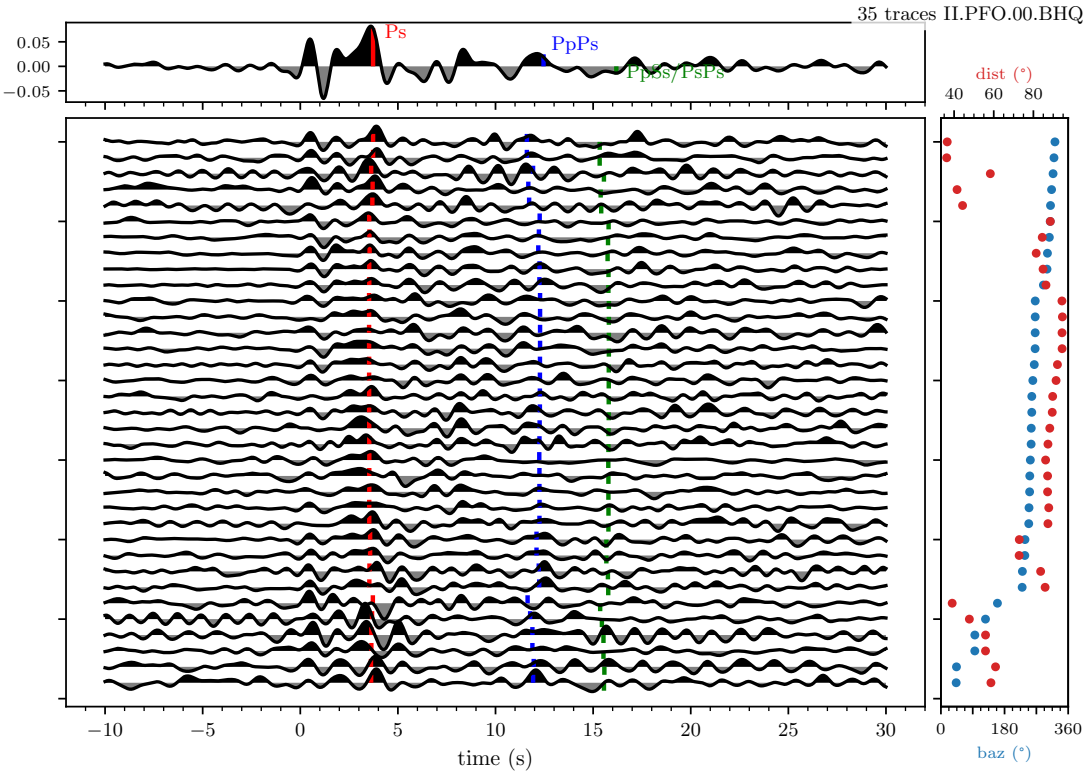
Following the data preparation and processing methods outlined above, we obtained 206 receiver functions for analysis using both the MTC and time domain deconvolution methods. Though the results from both methods were again broadly similar, we favoured the ET-MTC method with a cutoff frequency of 1.5 Hz at this site. 35 results passed our quality control tests and are shown in Figure 3.10. A Moho conversion is evident on all results at ~ 4 s delay time, along with a consistent negative polarity phase at ~ 1 s. $H-k$ stacking mapped the Moho phase to an interface at depth of 29.52 ± 0.54 km with a k value of 1.761 ± 0.025. This result is in very good agreement with all previous studies, with the negative polarity phase at ~ 1 s providing support for the velocity inversion modelled by *Baker et al.* (1996).



(a) Bootstrapped (B=100) $H - k$ stacking plot for II.PFO. Ellipses represent 1 and 2 bootstrap standard deviations.



(b) II.PFO earthquake dataset. Unused events are faded.



(c) Receiver functions results at II.PFO, sorted by back azimuth. Individual results are shown bottom and the stacked trace shown top. The locations of the phases representing the highest amplitude $H - k$ stacking result are highlighted on each trace.

Figure 3.10: $H - k$ stacking results at the GSN station II.PFO. Receiver functions are calculated using the ET-MTC method with a cutoff frequency of 1.5 Hz. An average crustal velocity of 6.5 km/s was used for the $H - k$ stack, with weights of 0.5, 0.3 and 0.2 for w_1, w_2 and w_3 respectively. The algorithm picks out the large amplitude Moho conversion at ~ 4 s, and its reverberations, as the most dominant set of phases, and selects an H and k value of 29.53 ± 0.46 km and 1.76 ± 0.021 respectively.

3.11 PI/Oxford Network Receiver Functions

We present here results from stations deployed as part of the PI/Oxford seismic network (see Figure 3.11). The quality and nature of these receiver functions varied significantly both within and between stations, and a few did not produce any interpretable results (S-04 and S-16).

All deconvolution methods were tested, with both the time domain (TD) and MTC methods producing good quality results. Results with the MTC methods tended to be cleaner and easier to interpret, but a higher proportion were filtered out by our quality control (QC) checks relative to the TD method. We therefore elected to favour the TD deconvolution method for the PI stations. The results shown below have been calculated with a 1 Hz low pass filter, and passed through an additional manual QC check after the automatic QC routine had eliminated the poorer quality results.

Results at each station were inspected for variations with back azimuth and epicentral distance and grouped accordingly for $H-k$ stacking. We use an average crustal velocity of 6.5 $km\,s^{-1}$ for the majority of results. A value consistent with global averages (*Christensen and Mooney*, 1995). This value was reduced to between $5-6$ $km\,s^{-1}$ for shallow and mid crustal results in the foreland as well data from this area suggests a value in this range is more appropriate. Weights for each phase were generally set at 0.5, 0.3 and 0.2 for the Ps, $PpPs$ and $PsPs/PpSs$ phase respectively, but were altered slightly when some phases were either weak or not observed.

The H search ranges were initially set to broad full crustal windows, and later reduced to narrower windows around the potential interface depths to allow local maxima to be highlighted. The H search range increment was set at 0.2 km as our results are very unlikely to exceed this resolution and computational efficiency is highly desirable during bootstrap error estimation. The k search range was typically set at $1.6-1.9$ with an increment of 0.01. For bootstrapping error estimation the search space was further restricted to improve computation time and avoid the $H-k$ algorithm jumping to alternative sets of phases and providing erroneously large errors.

With this methodology we apply the $H-k$ stacking algorithm to each subset of

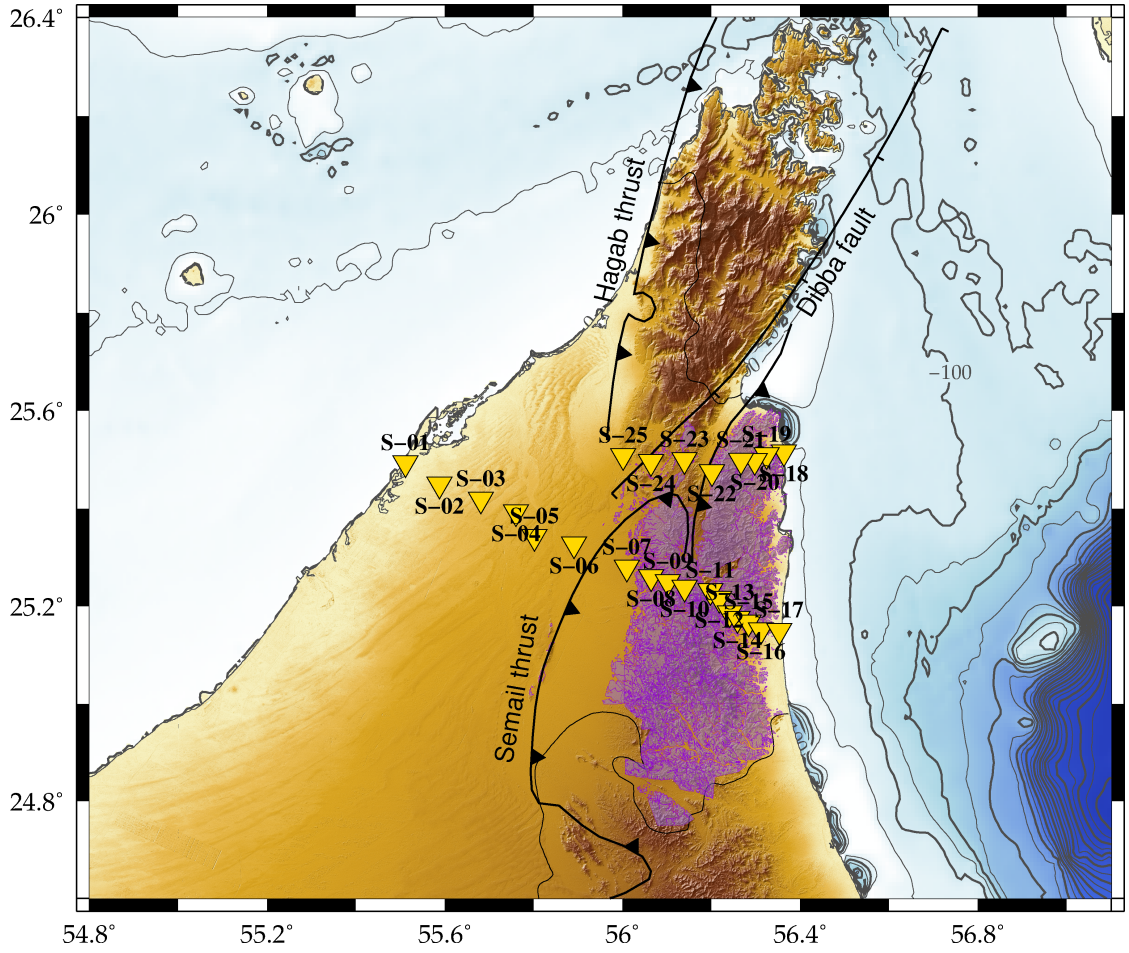


Figure 3.11: The PI/Oxford seismic network. These stations were deployed for up to 2.3 years to gather passive seismic data as part of this project. Locations of major faults are marked, and ophiolite outcrops are marked in purple.

receiver function results, and repeat the process across a range of H and k windows to extract a number of depth points at each station. For some results a strong primary phase could be matched to several potential multiples, typically one with a high k value and one with a low k value. In this case the preferred result was typically selected by favouring high k values at shallow depth (and vice versa), by comparing the results to those at nearby stations, or by comparing results to those calculated with different deconvolution methods.

3.11.1 S-01

Station 01 (S-01) is our western-most station on the southern profile D1, and is located in the desert foreland near the coast. It was active for the majority of our 2.3 year deployment, recording 252 of the events in our earthquake dataset. A poor signal to noise ratio meant over half of these events were eliminated as potential sources. Receiver functions were calculated for the remaining 109 sets of waveforms and passed to our automatic quality control routines for analysis. These routines determined 52 of these receiver functions to be of good quality, with manual QC reducing this number to 43. These results are displayed in Figure 3.12.

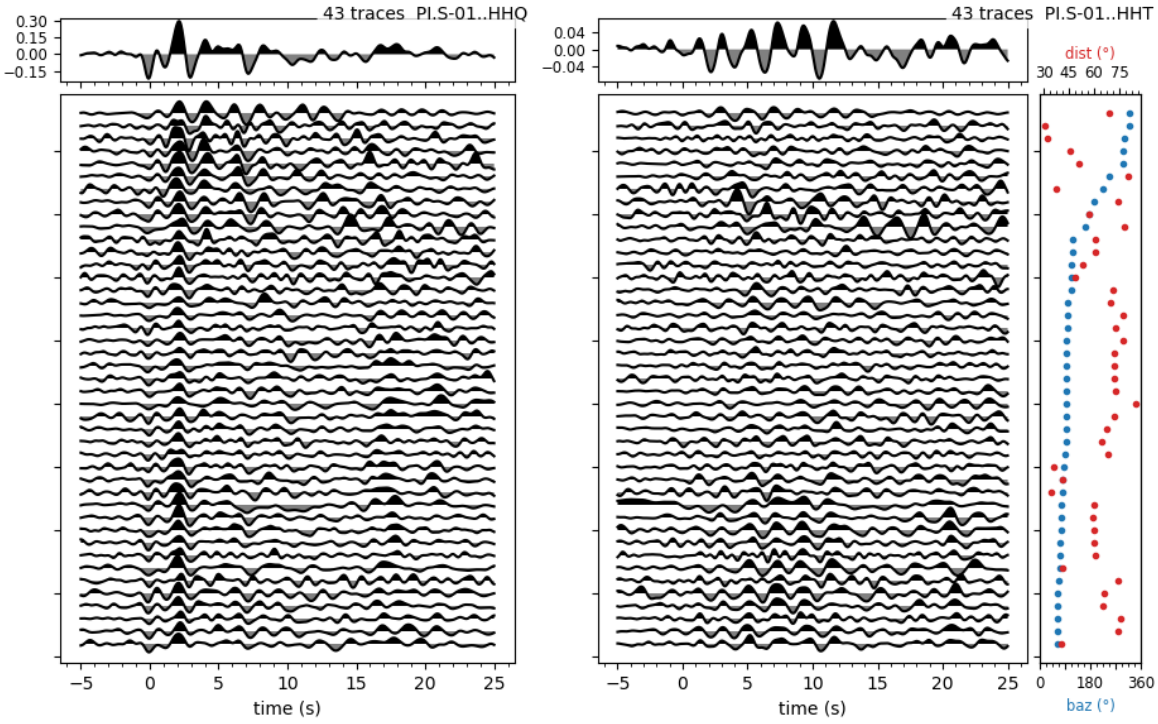
Receiver functions at S-01 exhibited a strong, consistent peak across all traces at 2 s delay time. Another clear peak is present at ~ 4 s, however this phase has a strong azimuthal dependence and was only present on western events. Later phases do not show much consistency, however this is to be expected as the reverberated phases are more sensitive to variations in incidence angle and no moveout correction has been applied.

The poor coherency and low amplitude of the stacked trace on the transverse component relative to the radial indicate a low degree of scattering and a relatively homogeneous lateral velocity structure.

H - *k* stacking

$H - k$ stacking showed that the dominant phase at 2 s could be mapped to either an interface at $\sim$ 14 km with a high k value or $\sim$ 19.5 km depth with a low k value. We believe the former is more likely as $H - k$ analysis at nearby stations also contain phases that map to interfaces around this depth. The strength of this phase suggests a strong impedance contrast. It could be a conversion from basement to the base of the foreland sedimentary sequence, though its depth is slightly greater than we would expect for such a conversion. It could also be a conversion from a deep salt layer.

The secondary phase at $\sim 4s$ from southern and western events is most probably a conversion from the Moho as it is too early to be a reverberation from the mid crustal



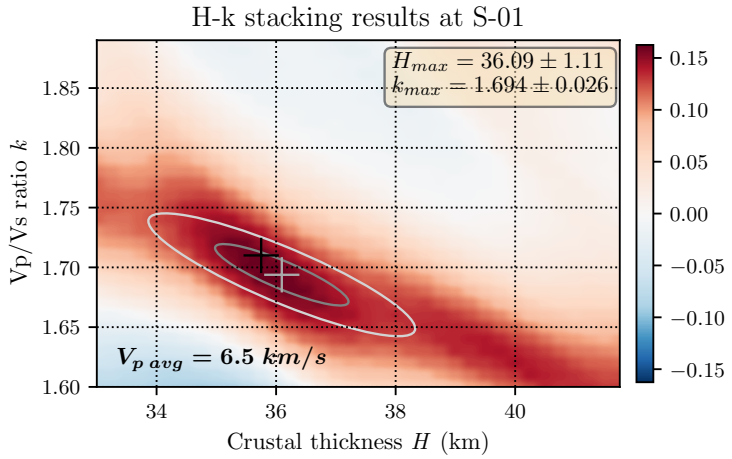
(a) Radial component **(b)** Transverse component

Figure 3.12: Receiver function results at S-01. Individual results are plotted in the main section of each component and sorted by back azimuth, with the stacked trace displayed at the top. The epicentral distance and back azimuth of each event is shown to the right.

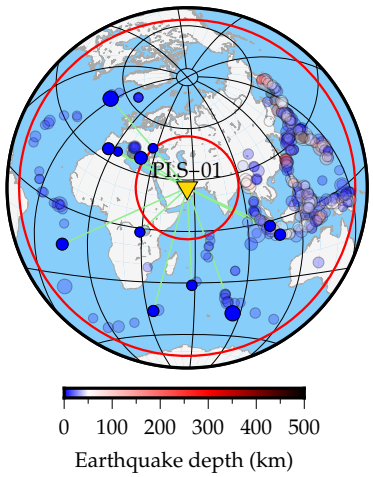
phase. $H - k$ stacking gives a depth of $\sim 36\ km$ (see Figure 3.13), suggesting crustal thickness in the foreland is slightly thicker than typical continental values of $\sim 30\ km$ (*Christensen and Mooney*, 1995). The absence of a Moho signal from events originating to the north and east of the station is puzzling. It could indicate a weaker velocity contrast across the Moho to the north-east of S-01, either due to a change in the nature of the lower crust or the upper mantle.

3.11.2 S-02

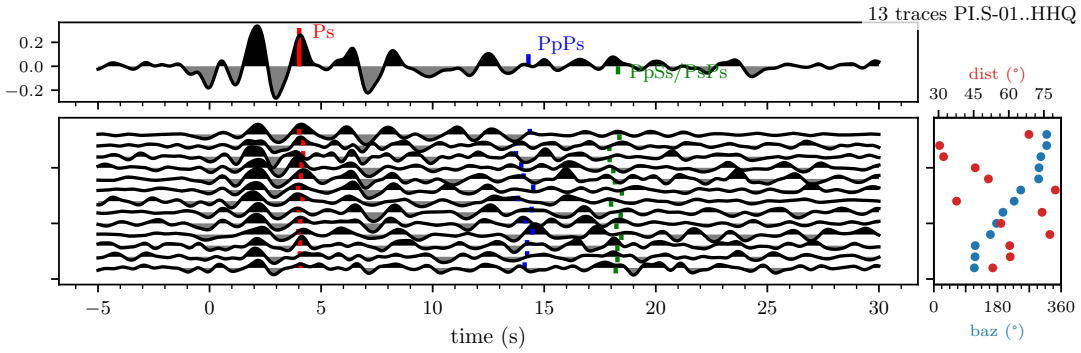
Station 02 (S-02) is located $\sim 10\ km$ inland from S-01 on the southern profile D1. It was inactive for the majority of our 2.3 year deployment, and consequently it recorded only 87 events. A poor signal to noise ratio meant over half of these events were eliminated as potential sources. Receiver functions were calculated for the remaining 36 sets of waveforms and passed to our automatic quality control routine for analysis.



(a) Bootstrapped (B=50) $H - k$ stacking results at S-01. Ellipses represent 1 and 2 bootstrap standard deviations.



(b) S-01 earthquake dataset. Unused events are faded.



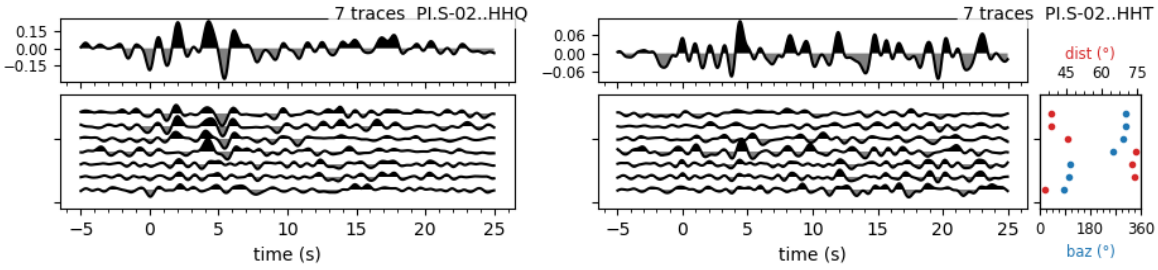
(c) Receiver functions results at S-01, sorted by back azimuth. Individual results are shown bottom and the stacked trace shown top. The locations of the phases representing the highest amplitude $H - k$ stacking result are highlighted on each trace.

Figure 3.13: $H - k$ stacking results at station S-01. $H - k$ stacking weights of 0.6, 0.3 and 0.1 were used for w_1, w_2 and w_3 respectively. The algorithm picks out the secondary peak at ~ 4 s, and its reverberations, as the most dominant set of phases, and picks out H and k values of 36.06 ± 1.11 km and 1.694 ± 0.026 as the highest amplitude result.

These routines determined the that the majority of results were of poor quality, with only 10 receiver functions passing. Manual QC reduced this number to 7. These results are displayed in Figure 3.14.

Receiver functions at S-02 are similar to those observed at S-01, with dual peaks at 2 and 4 s, with both phases more prominent on events originating in the west.

Amplitudes on the radial component were again much stronger than the transverse



(a) Radial component **(b)** Transverse component

Figure 3.14: Receiver function results at S-02. Individual results are plotted in the main section of each component and sorted by back azimuth, with the stacked trace displayed at the top. The epicentral distance and back azimuth of each event is shown to the right.

component, indicating a low degree of scattering.

H - *k* stacking

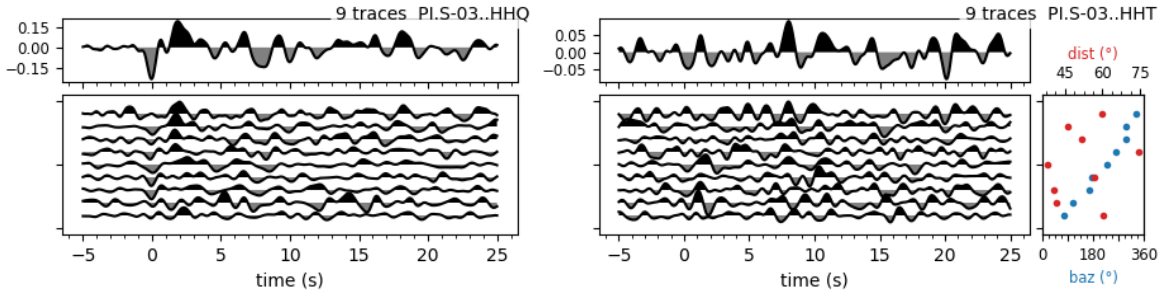
$H - k$ stacking mapped the 2 s phase to an interface at $\sim$ 15 km depth, with a high k-value of $\sim$ 1.8. Eastern events were slightly shallower than those from the west, suggesting an a dipping, or undulating surface.

The later phase at 4 s on western events is likely a Moho conversion and was mapped to an interface at $\sim$ 35 km depth, similar to S-01.

3.11.3 S-03

Station 03 (S-03) is located $\sim$ 10 km east of S-02 on the southern profile D1. It was active for the majority of the 2.3 year deployment, and recorded 266 events. A poor signal to noise ratio meant over half of these events were eliminated as potential sources. Receiver functions were calculated for the remaining 110 sets of waveforms and passed to our automatic quality control routines for analysis. These routines determined the that the vast majority of results were of poor quality, with only 9 results passing. Manual QC reduced did not eliminate any further results. These results are displayed in Figure 3.15.

Receiver functions at S-03 show a single strong phase at $\sim$ 2 s. There is some minor variation with back azimuth, with events from the south-east not showing this phase



(a) Radial component **(b)** Transverse component

Figure 3.15: Receiver function results at S-03. Individual results are plotted in the main section of each component and sorted by back azimuth, with the stacked trace displayed at the top. The epicentral distance and back azimuth of each event is shown to the right.

so strongly.

The amplitudes on the radial component are roughly three times stronger than the tranverse component, indicating a low degree of scattering.

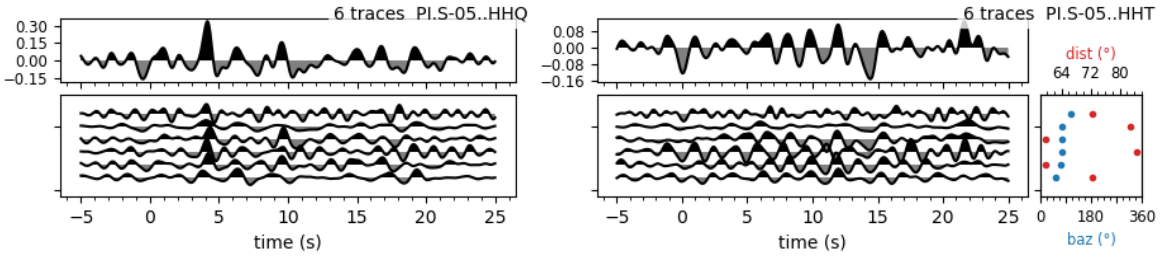
H - *k* stacking

$H-k$ stacking of the 2 s phase was mapped to an interface at $\sim$ 16 km depth, though with a low k-value of 1.62 this time. This interface is consistently observed at all stations in the foreland so far suggesting a large, laterally coherent conversion surface is present in the mid crust.

3.11.4 S-05

Station 05 (S-05) is located in the foreland roughly halfway between the mountains and the coast. It was active for roughly a year from the start of the deployment before being removed, recording 117 of the events in our catalogue. A poor signal to noise ratio meant just under half of these events were eliminated as potential sources. Receiver functions were calculated for the remaining 66 sets of waveforms and passed to our automatic quality control routine for analysis. These routines determined the that the vast majority of results were of poor quality, with only 9 results passing. Manual QC cut this down to 6. These results are displayed in Figure 3.16.

Receiver functions at S-05 showed a strong peak at $\sim$ 4 s, suggesting a dominant



(a) Radial component **(b)** Transverse component

Figure 3.16: Receiver function results at S-05. Individual results are plotted in the main section of each component and sorted by back azimuth, with the stacked trace displayed at the top. The epicentral distance and back azimuth of each event is shown to the right.

Moho conversion. There was minimal variation with back azimuth observed but all events originated in the east. The 2 s phase observed at previous stations appears to be weak, or absent entirely here.

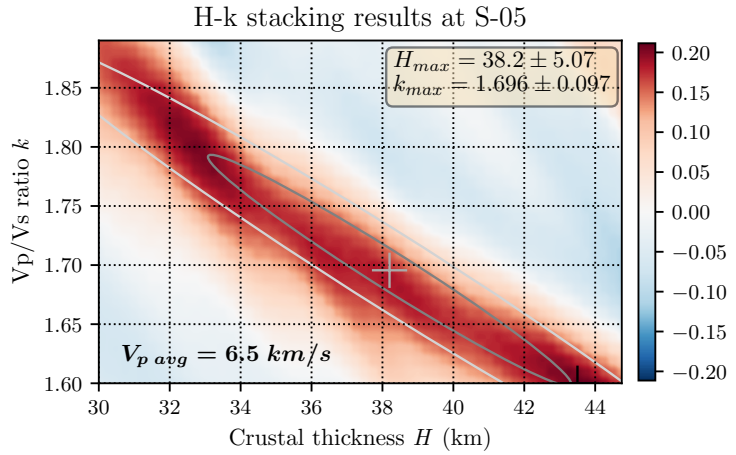
Amplitudes on the radial component were again much stronger than the transverse component, indicating a low degree of scattering.

H - k stacking

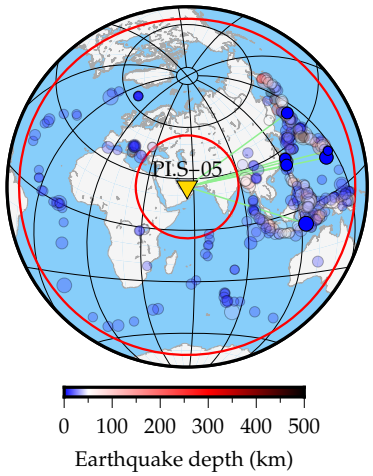
$H - k$ stacking of the probable Moho phase at 4 s had difficulty locking down a fixed H and k value due to the presence of several possible reverberated phases between $15 - 20$ s. The result was a large uncertainty in the results, with H ranging from $32 - 42$ km depending on whether a high or low k value is favoured (see Figure 3.17). Other Moho conversions in the foreland favoured a k-value of around 1.7, so an intermediate depth of around 38 km for this phase seems reasonable. A Moho thickening in this direction would be consistent with the formation of a flexural root that is typically present beneath a mountain range or flexural load.

3.11.5 S-06

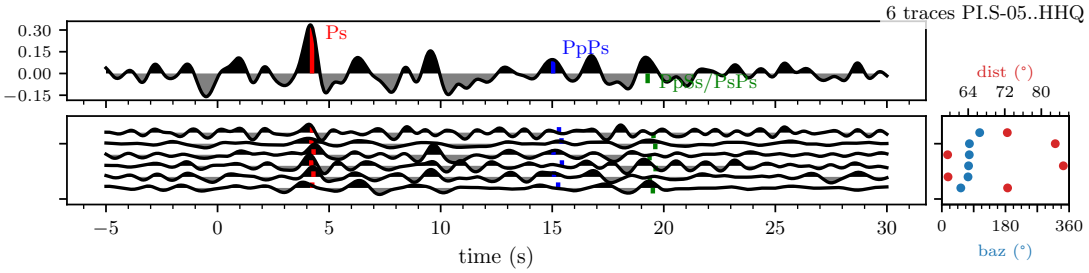
Station 06 (S-06) is located 9 km east of S-05 on the southern profile D1, just north of the town of Al-Dhaid. It was inactive for the majority of the 2.3 year deployment, and recorded only 89 of the events in our catalogue. A good signal to noise ratio meant the



(a) Bootstrapped (B=50) $H - k$ stacking plot for S-05. Ellipses represent 1 and 2 bootstrap standard deviations.



(b) S-05 earthquake dataset. Unused events are faded.

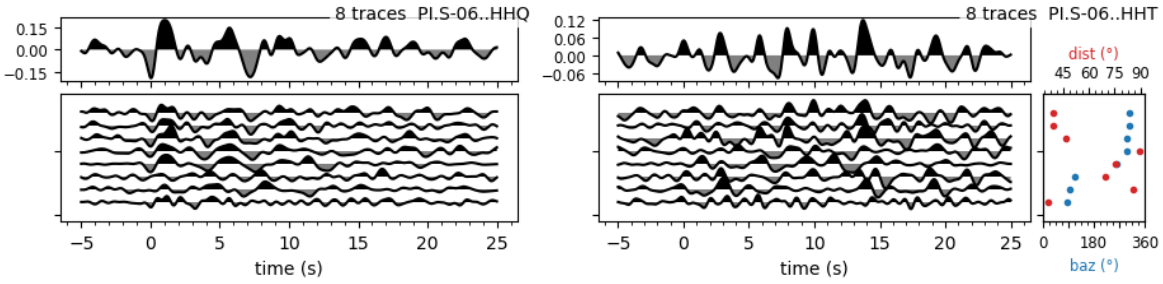


(c) Receiver functions results at S-05, sorted by back azimuth. Individual results are shown bottom and the stacked trace shown top. The locations of the phases representing the highest amplitude $H - k$ stacking result are highlighted on each trace.

Figure 3.17: $H - k$ stacking results at station S-05. $H - k$ stacking weights of 0.5, 0.3 and 0.2 were used for w_1, w_2 and w_3 respectively. The algorithm picks out the primary peak at $\sim 4\ s$, but struggles to identify the reverberated phases. It picks out H and k values of 38.2 ± 5.07 km and 1.696 ± 0.097 as the highest amplitude result.

majority of events were could be used as sources. Receiver functions were calculated for these 68 sets of waveforms and passed to our automatic quality control routine for analysis. These routines determined the that the vast majority of results were of poor quality however, with only 9 results passing. Manual QC reduced this to 8. These results are displayed in Figure 3.18.

Receiver functions at S-06 are similar to those observed at further west in the foreland, with dual peaks at ~ 1.5 and $\sim 5.5\ s$ and a trough at $7\ s$. All phases were much more prominent on eastern events.



(a) Radial component **(b)** Transverse component

Figure 3.18: Receiver function results at S-06. Individual results are plotted in the main section of each component and sorted by back azimuth, with the stacked trace displayed at the top. The epicentral distance and back azimuth of each event is shown to the right.

Amplitudes on the radial component were only slightly stronger than the transverse component, indicating a high degree of scattering.

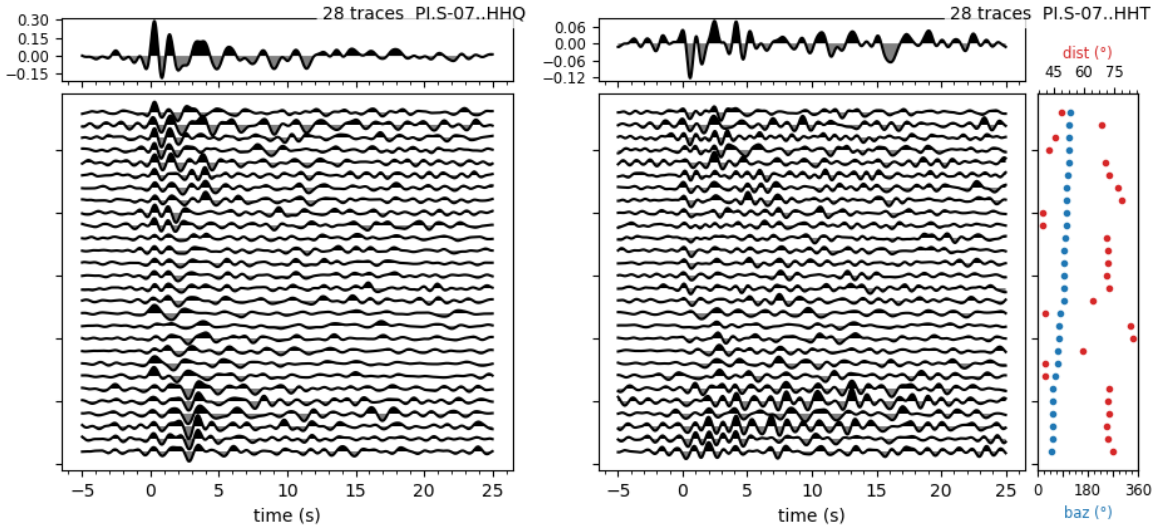
H - *k* stacking

$H - k$ stacking suggested the later peak and trough observed on western events at 5.5 and 7 s were reverberations from the first peak at 1.5 s, and mapped them to an interface at 14 km depth, suggesting the mid-crustal phase extends right across the foreland.

Eastern events had a weak peak at ~ 4.5 s that was mapped to a potential Moho interface at ~ 40 km depth, with a k-value of 1.68. This is further evidence for the presence of a flexural root.

3.11.6 S-07

Station 07 (S-07) is located at the eastern edge of the foreland, east of the Semail thrust on the southern profile D1. It was active for the majority of the 2.3 year deployment, and recorded 178 of the events in our catalogue. A poor signal to noise ratio meant over half of these events were eliminated as potential sources. Receiver functions were calculated for the remaining 79 sets of waveforms and passed to our automatic quality control routine for analysis. These routines determined the that the majority of results were of poor quality, with 29 results passing. Manual QC reduced this to 28. These



(a) Radial component **(b)** Transverse component

Figure 3.19: Receiver function results at S-07. Individual results are plotted in the main section of each component and sorted by back azimuth distance, with the stacked trace displayed at the top. The epicentral distance and back azimuth of each event is shown to the right.

results are displayed in Figure 3.19.

All of our results were confined to relatively narrow range of back azimuths, with all results originating from events in the north and east. There was also significant variation with epicentral distance, suggesting the structures beneath this station may be dipping, or offset slightly, to the west. There was a distinct set of results from the north-east, with a weak set of phases between $0-2$ s, and a strong trough-peak combo between $2-4$ s. The remaining easterly results exhibited a pair of peaks and troughs between $0-3$ s, and a strong peak at 4 s on events with an epicentral distance greater than $60°$.

Amplitudes on the radial component were significantly stronger than the transverse component, however many events failed the QC checks due to high relative energy on the transverse component. This indicates out-of-plane scattering is an issue here.

H - *k* stacking

Computing $H-k$ stacking results at this station was particularly difficult as there were several sub-groups, each with several phases to disentangle. The interfaces that could be identified with the most confidence where a reverse polarity (slow to fast) conversion at $\sim 5\ km$ depth with a k-value of ~ 1.8. The mid-crustal conversion observed further west was also present at $\sim 14\ km$ depth, though with a low k-value of ~ 1.63.

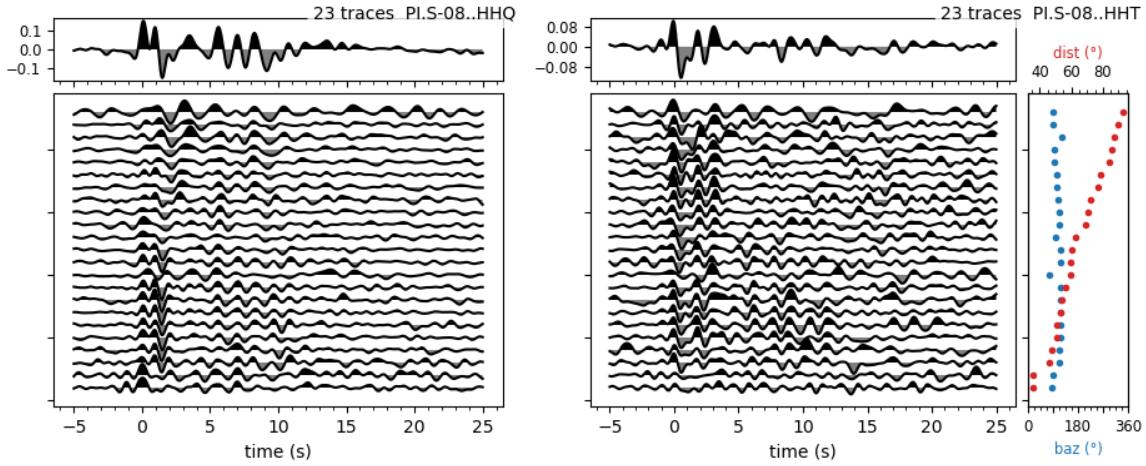
For the north-easterly sub-group, the strong trough at $2.5\ s$ could be mapped to a reverse polarity interface anywhere between $20-30\ km$ depth, as multiple reverberated phase options were available. The strong peak at $3.5\ s$ was mapped to a potential Moho interface at $\sim 35\ km$ depth, though with a very low k-value of 1.62.

For the easterly events the reverse polarity interface could again not be constrained to a single set of reverberated phases, but occupied a shallower depth range of $\sim 15-25\ km$. The strong peak observed on more distant events could be mapped to a potential Moho interface at $\sim 38\ km$ depth, with a k-value of 1.65.

3.11.7 S-08

Station 08 (S-08) is located on the southern profile D1 on the western foothills of the UAE-Oman mountains. It was active for a little under half of our 2.3 year deployment, and recorded 115 of the events in our catalogue. An excellent signal to noise ratio meant 95 of these could be used as sources. Receiver functions calculated from these events were passed to our quality control routines, with only 26 deemed to be of good quality. Manual QC cut this down to 23. These results are displayed in Figure 3.20.

Receiver functions at S-08 were similar to those at S-07. They were again confined to relatively narrow range of back azimuths, with all results originating from events in the east. There was significant variation with epicentral distance however, suggesting the structures beneath this station are again dipping, or offset, to the west. The most consistent phase was the negative polarity trough increasing from $\sim 1.5-2\ s$ with epicentral distance.



(a) Radial component **(b)** Transverse component

Figure 3.20: Receiver function results at S-08 for the radial (left) and transverse (right) components. Individual results are plotted in the main section of each component and sorted by epicentral distance, with the stacked trace displayed at the top. The epicentral distance and back azimuth of each event is shown to the right.

The comparable amplitudes of the stacked radial and transverse results, along with the high degree of coherency on the transverse component indicate a significant amount of scattering has occurred. This suggests that assumptions of simple, laterally homogeneous velocity structure are unlikely to be true in this part of the profile.

H - *k* stacking

Receiver function results were divided into proximal and distal sub-groups for $H - k$ stacking, with the former group defined as events between 40 and 65° epicentral distance, and the latter as events further than 75°.

The proximal group had two early peaks and a trough before 2 s, and these could be mapped to an interface at $\sim$ 2 km depth with a k-value of 1.61. The strength of the 2 s trough suggested it was not just a reverberation, and it could mapped as a primary phase to a reverse polarity interface at $\sim$ 11 km depth with a k-value of 1.736. A weaker peak at $\sim$ 5.5 s could mapped to a potential Moho interface at $\sim$ 47 km depth with a k-value of 1.745.

The distal group has a peak at 1 s that could paired to the peak and trough at 3

and 4 s to give an interface at ~ 7 km depth. The trough at ~ 2 s could be mapped to a reverse polarity interface at ~ 14 km depth, though with a high k-value of 1.85. The strength of the peak at 3 s suggested this may also be a primary phase, and it was mapped to a deep interface at ~ 30 km depth. There was again a weaker peak at ~ 5.5 s, and this was mapped to a potential Moho between $42 - 46$ km, depending on which reverberated phases were favoured.

3.11.8 S-09

Station 09 (S-09) is located 4 km east of S-08 on the southern profile D1, near a major quarry. It was active for around half of the 2.3 year deployment, and recorded 154 of the events in our catalogue. An excellent signal to noise ratio meant 127 of these were available as potential sources. Receiver functions were calculated for these events and passed to our automatic quality control routine for analysis. These routines determined that a large amount of these results were of poor quality, with 43 results passing. Manual QC reduced this to 40. These results are displayed in Figure 3.21.

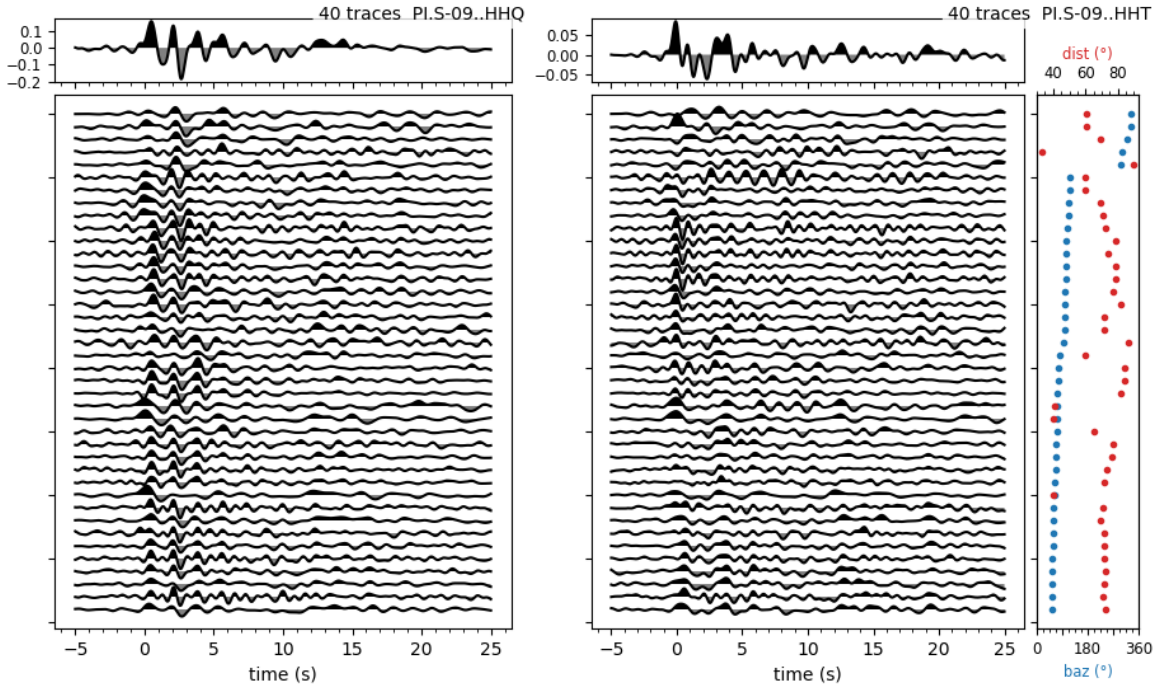
Receiver functions at S-09 were very consistent, with a distinct set of results from both the east and west. The most prominent phase was a trough at ~ 2.5 s for easterly events, and ~ 3 s for westerly events.

Amplitudes on the radial component are roughly twice as strong as the transverse component, and many events failed the QC checks due to high relative energy on the transverse component. This indicates out-of-plane scattering is an issue here.

H - *k* stacking

$H - k$ stacking at this station was also challenging despite the consistency of the results, as it was difficult to disentangle deeper primary Ps conversions from shallower reverberations.

On eastern events the shallowest 0.5 s phase could be coupled with the positive and negative phases at 2 and 2.5 s as $PpPs$ and $PsPs/PpSs$ multiples respectively for a shallow ~ 4.3 km conversion (see Figure 3.22). The strength of both the $PpPs$ and

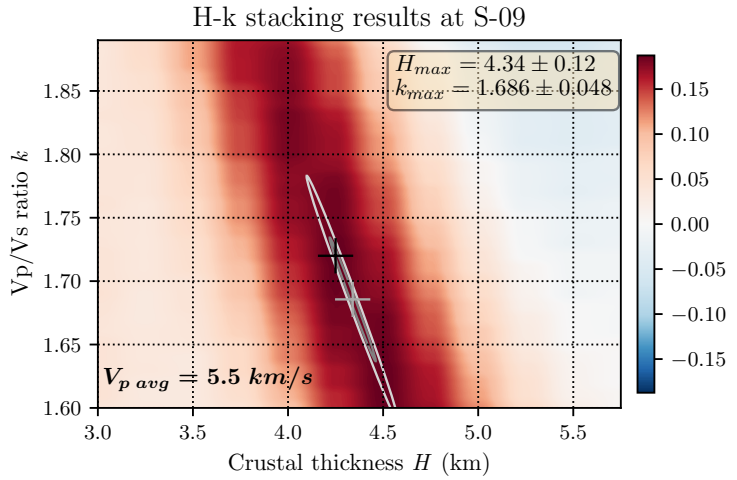


(a) Radial component **(b)** Transverse component

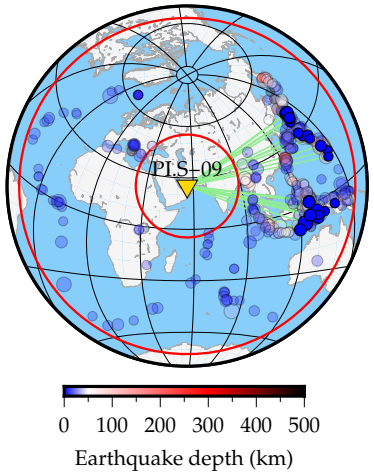
Figure 3.21: Receiver function results at S-09. Individual results are plotted in the main section of each component and sorted by back azimuth, with the stacked trace displayed at the top. The epicentral distance and back azimuth of each event is shown to the right.

the $PsPs/PpSs$ phases suggested they may also be primary phases however. In this case they mapped to an interface at $\sim 18\ km$ depth, and a reverse polarity interface at $\sim 24\ km$ depth respectively. The later 4 s phase could mapped to a potential Moho conversion at $\sim 35\ km$ depth.

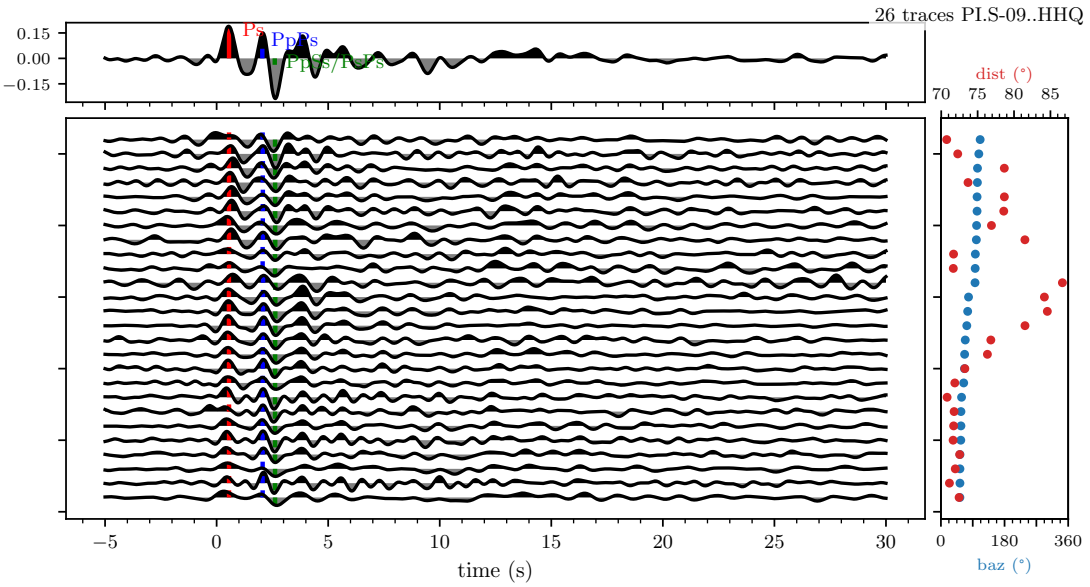
Western events were fewer in number, but could also be mapped to multiple interfaces. The primary peak for the shallow interface did not appear to be present. A peak and trough at 2 and 2.5 s could be mapped to an interface at $\sim 18\ km$ depth and a reverse polarity interface at 23 km depth, similar to the eastern results. The later peak at 5.5 s could be mapped to an interface at $\sim 40\ km$ depth with a very high k-value of 1.86 or, alternatively, a $\sim 48\ km$ interface with a more moderate k-value of 1.70.



(a) Bootstrapped (B=50) $H - k$ stacking plot for S-09. Ellipses represent 1 and 2 bootstrap standard deviations.

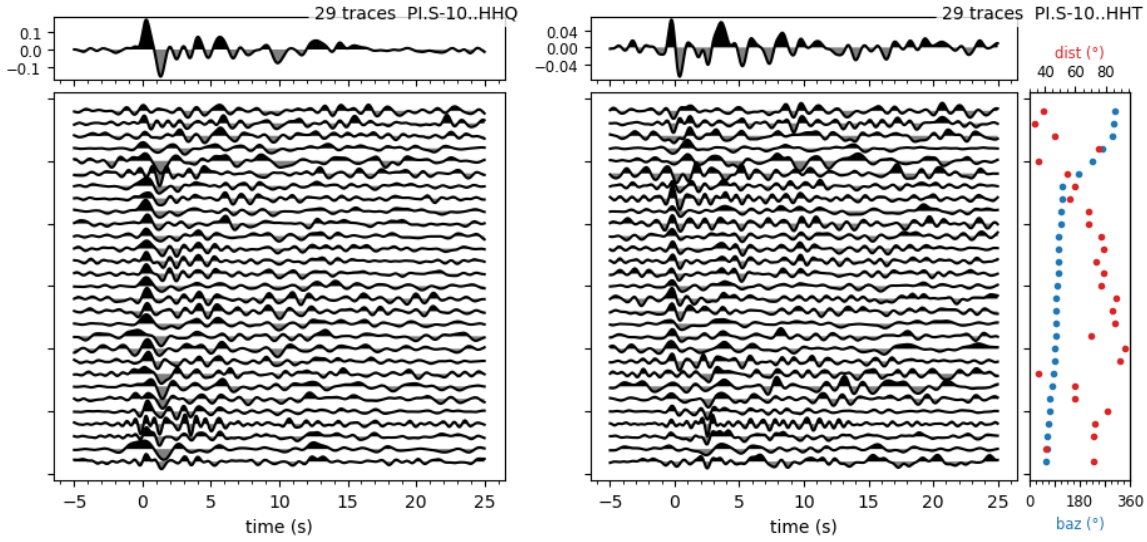


(b) S-09 earthquake dataset. Unused events are faded.



(c) Receiver functions results at S-09, sorted by back azimuth. Individual results are shown bottom and the stacked trace shown top. The locations of the phases representing the highest amplitude $H - k$ stacking result are highlighted on each trace.

Figure 3.22: $H - k$ stacking results at station S-09. $H - k$ stacking weights of 0.5, 0.3 and 0.2 were used for w_1, w_2 and w_3 respectively. The algorithm picks out the primary peak at $\sim 0.5\ s$, with strong reverberations at 2 and 2.5 s. It picks out H and k values of $4.34 \pm 0.12 km$ and 1.686 ± 0.048 for these phases.



(a) Radial component **(b)** Transverse component

Figure 3.23: Receiver function results at S-10. Individual results are plotted in the main section of each component and sorted by back azimuth, with the stacked trace displayed at the top. The epicentral distance and back azimuth of each event is shown to the right.

3.11.9 S-10

Station 10 (S-10) is located 4 *km* east of S-09 on the southern profile D1, near a major quarry. It was active for around half of the 2.3 year deployment, and recorded 132 of the events in our catalogue. An excellent signal to noise ratio meant 104 of these were available as potential sources. Receiver functions were calculated for these events and passed to our automatic quality control routine for analysis. These routines determined that a large amount of these results were of poor quality, with 30 results passing. Manual QC reduced this to 29. These results are displayed in Figure 3.23.

Receiver functions at S-10 were slightly messy, with a clear division between easterly and westerly events again evident. The most prominent phases were a strong peak at 0.5 s and a trough at $\sim$ 1.5 s for easterly events, and peak at $\sim$ 5.5 s for westerly events.

Amplitudes on the radial component are roughly twice as strong as the transverse component, and many events failed the QC checks due to high relative energy on the transverse component. This indicates out-of-plane scattering is an issue here.

H - *k* stacking

$H-k$ stacking on eastern results mapped the 0.5 s peak on eastern events to an interface at ~ 4.2 km depth, and the ~ 1.5 s trough to a reverse polarity interface at ~ 11 km depth. Weak peaks were also present at both 4 and 5.5 s, both representing possible Moho phases. The earlier phase could be mapped to anywhere from $28-40$ km depth, as multiple potential reverberated phases were available. The latter was mapped to an interface at ~ 47.5 km depth, with a k-value of 1.754.

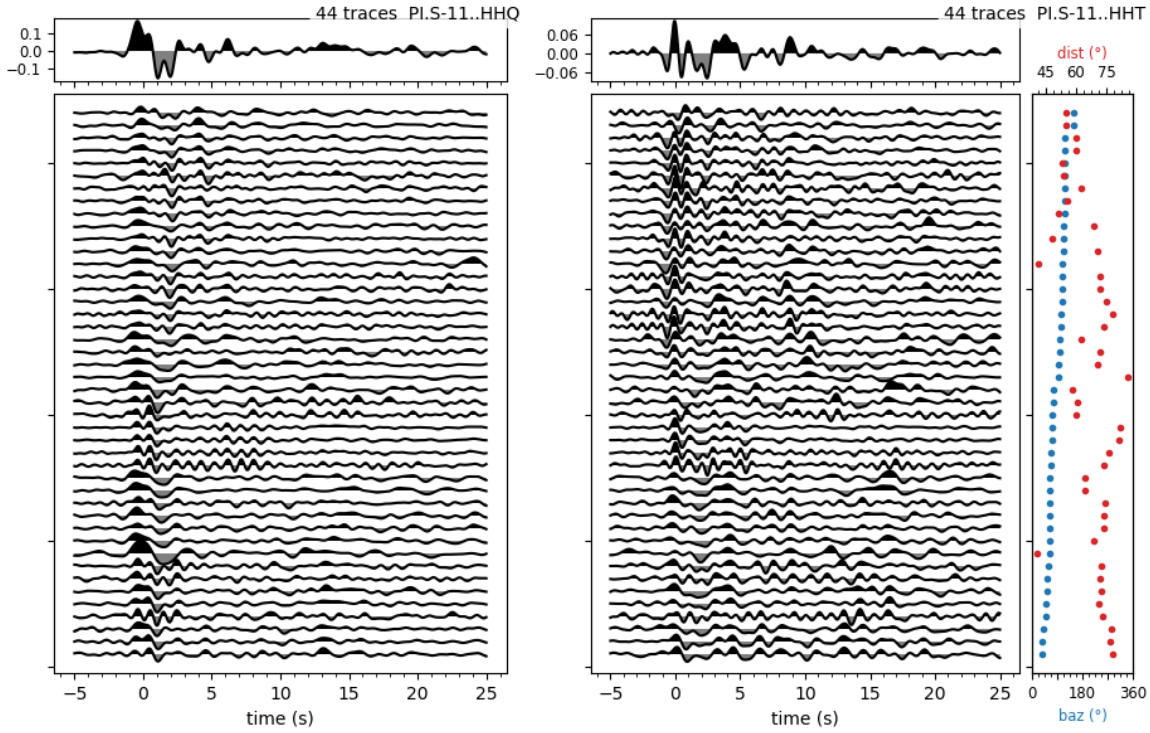
Western results were more limited in number, and not so consistent. A weak trough at ~ 1.5 s was mapped to a reverse polarity interface at ~ 24 km depth. A stronger peak at ~ 5.5 s was could be mapped to an interface between $38-53$ km depth due to numerous potential reverberated pairings.

3.11.10 S-11

Station 11 (S-11) is located 6 km east of S-10, just off the highway between Masafi and Fujairah on the southern profile D1. It was active for under half of the 2.3 year deployment, and recorded 156 of the events in our catalogue. An excellent signal to noise ratio meant that 120 of these were available as potential sources. Receiver functions were calculated for these events and passed to our automatic quality control routine for analysis. These routines determined that around half of these results were of good quality, with 63 results passing. Manual QC reduced this to 44. These results are displayed in Figure 3.24.

Receiver functions at S-11 were quite consistent, though with significant variation with back azimuth. The most prominent phase was a trough at ~ 1 s for north-easterly events, and ~ 2 s for south-easterly events.

Amplitudes on the radial component were roughly twice as strong as the transverse component, indicating out-of-plane scattering is a minor issue.



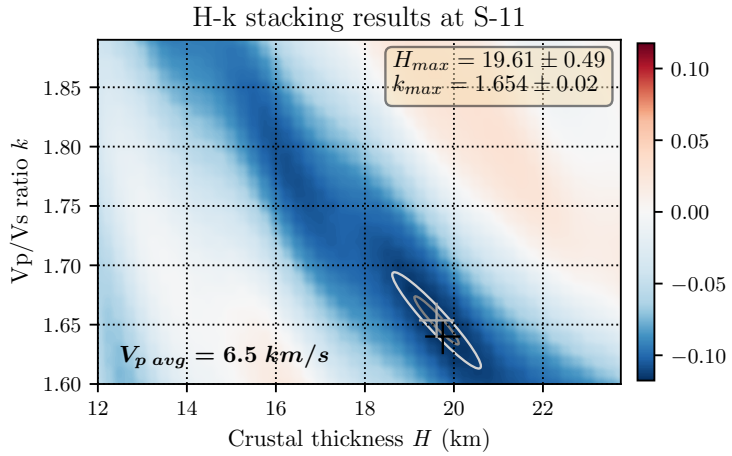
(a) Radial component **(b)** Transverse component

Figure 3.24: Receiver function results at S-11. Individual results are plotted in the main section of each component and sorted by back azimuth, with the stacked trace displayed at the top. The epicentral distance and back azimuth of each event is shown to the right.

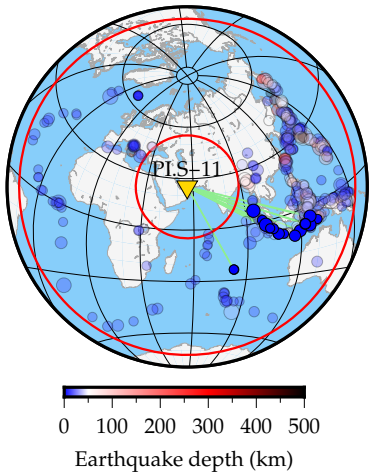
H - *k* stacking

$H-k$ stacking of the north-easterly sub-group was restricted to distal events ($>71°$), and mapped several shallow interfaces. A consistent peak at 0.5 s was mapped to a an interface at $\sim$ 3 km depth, with a k-value of 1.762. The trough at 1 s could be mapped to a reverse polarity interface at 7 km depth, though with a high k-value of 1.851. A later peak at $\sim$ 2.5 s did not correspond with any shallower multiples, and was mapped as a primary phase to an interface at $\sim$ 22 km depth, with a k-value of 1.721.

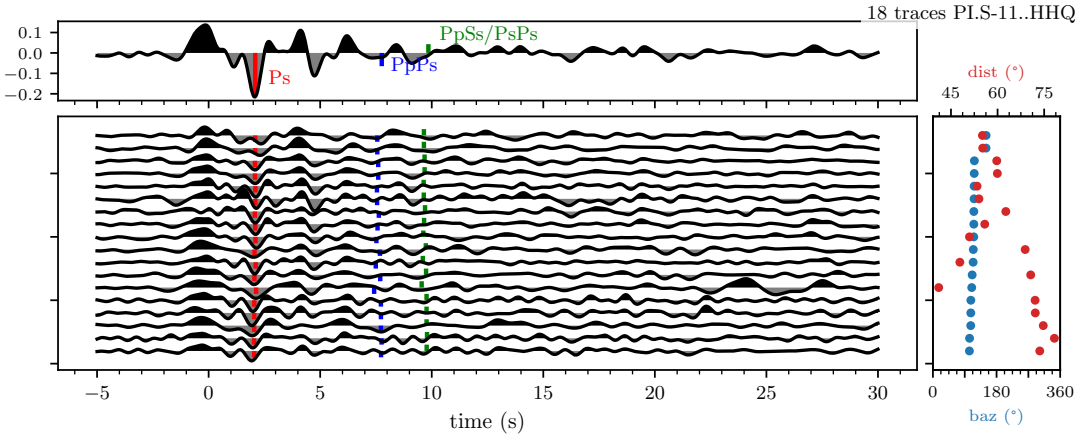
The south-easterly subgroups phases were consistently later, and were mapped to several mid to lower crustal interfaces. The dominant trough at 2 s was mapped to a reverse polarity interface at $\sim$ 19 km depth, with a k-value of 1.65 (see Figure 3.25). A peak at 4 s represented a potential Moho conversion, and was mapped to an interface



(a) Bootstrapped (B=50) $H - k$ stacking plot for S-11. Ellipses represent 1 and 2 bootstrap standard deviations.



(b) S-11 earthquake dataset. Unused events are faded.



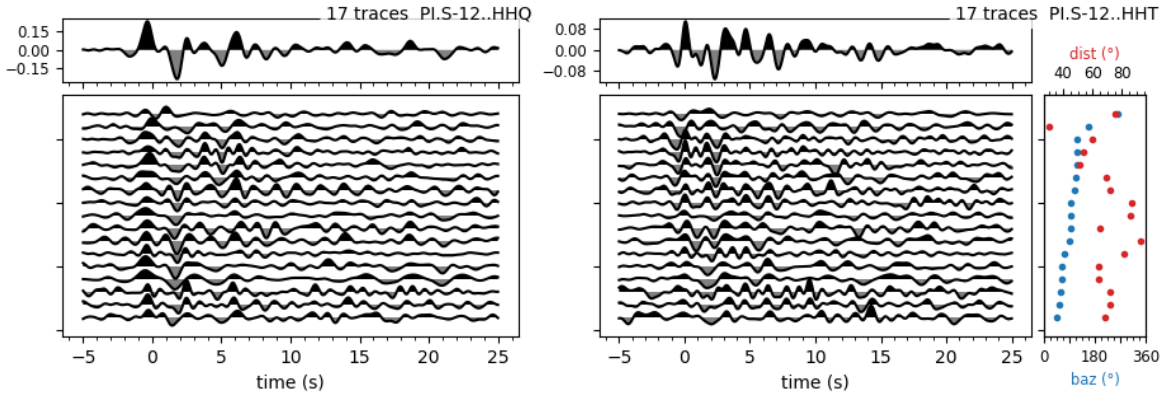
(c) Receiver functions results at S-11, sorted by back azimuth. Individual results are shown bottom and the stacked trace shown top. The locations of the phases representing the highest amplitude $H - k$ stacking result are highlighted on each trace.

Figure 3.25: $H - k$ stacking results at station S-11. $H - k$ stacking weights of 0.5, 0.3 and 0.2 were used for w_1, w_2 and w_3 respectively. The algorithm picks out the trough at ~ 2 s, and identifies the weak trough and peak at 8 and 10 s as reverberations. It picks out H and k values of 19.61 ± 0.49 km and 1.654 ± 0.002 as the highest amplitude result.

at ~ 35 km depth with a k-value of 1.73.

3.11.11 S-12

Station 12 (S-12) is located 3 km south-east of S-11 just off the highway between Masafi and Fujairah on the southern profile D1. It was inactive for the majority of the 2.3



(a) Radial component **(b)** Transverse component

Figure 3.26: Receiver function results at S-12. Individual results are plotted in the main section of each component and sorted by back azimuth, with the stacked trace displayed at the top. The epicentral distance and back azimuth of each event is shown to the right.

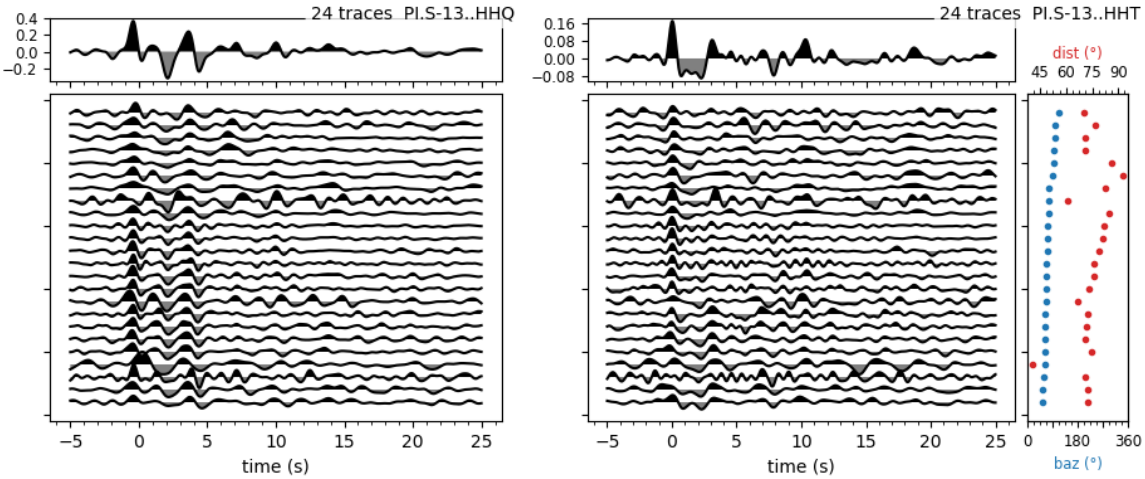
year deployment, and recorded only 73 of the events in our catalogue. An excellent signal to noise ratio meant 58 of these were available as potential sources. Receiver functions were calculated for these events and passed to our automatic quality control routine for analysis. These routines determined that a large number of these results were of poor quality, with 22 results passing. Manual QC reduced this to 17. These results are displayed in Figure 3.26.

Receiver functions at S-12 were relatively consistent, with the majority coming from eastern events. The most prominent phase was a trough at $\sim 1.5\ s$, and a peak at ~ 2.5 and $\sim 6\ s$.

Amplitudes on the radial component are roughly twice as strong as the transverse component, and many events failed the QC checks due to high relative energy on the transverse component. This indicates out-of-plane scattering is an issue here.

H - *k* stacking

$H-k$ stacking revealed the prominent trough at $\sim 1.5\ s$ could be mapped to a reverse polarity interface at either $\sim 12\ km$ with a high k-value, or $\sim 18\ km$ depth with a low k-value. The peak at $\sim 2.5\ s$ was mapped to an interface at $\sim 22\ km$ depth, with a k-value of 1.705. The strength of the phase at $\sim 6\ s$ suggested it was unlikely to



(a) Radial component **(b)** Transverse component

Figure 3.27: Receiver function results at S-13. Individual results are plotted in the main section of each component and sorted by back azimuth, with the stacked trace displayed at the top. The epicentral distance and back azimuth of each event is shown to the right.

be a reverberation, and this was mapped to a potential Moho interface at $42 - 50\ km$ depth, with a high to medium k-value.

3.11.12 S-13

Station 13 (S-13) is located 4 km south-east of S-12 near the town of Al Bithnah on the southern profile D1. It was active for under half of the 2.3 year deployment, and recorded 144 of the events in our catalogue. A good signal to noise ratio meant 86 were available as potential sources. Receiver functions were calculated for these events and passed to our automatic quality control routine for analysis. These routines determined that a large amount of these results were of poor quality, with 32 results passing. Manual QC reduced this to 24. These results are displayed in Figure 3.27.

Receiver functions at S-13 were very consistent, and all from easterly events. The most prominent phases were a trough at $\sim 2\ s$, and a peak at $\sim 3.5\ s$.

Amplitudes on the radial component were over two times stronger than the transverse component, indicating out-of-plane scattering is not such an issue here.

H - *k* stacking

$H-k$ stacking at S-13 was restricted to a sub-group of distal events ($> 70°$), as there appeared to be a small variation with epicentral distance. A minor peak at $\sim 1\ s$ could be paired with the peak and trough at $3-5\ s$ as reverberations to give an interface at $\sim 8\ km$ depth, with a k-value of 1.789. The dominant trough at $\sim 2\ s$ was mapped to a reverse polarity interface at $\sim 18\ km$ depth, with a k-value of 1.66. The strength of the peak at $\sim 3.5\ s$ suggested it may also be a primary phase, and it was mapped to a potential Moho interface at $\sim 35\ km$ depth with a k-value of 1.654.

3.11.13 S-14

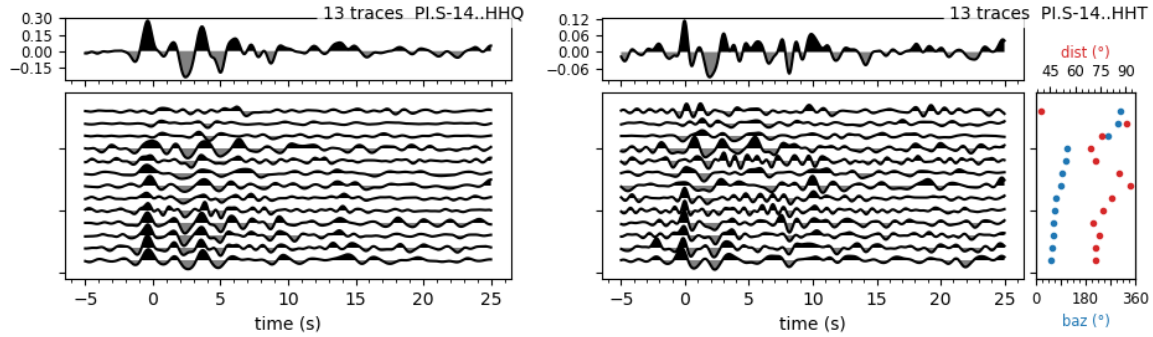
Station 14 (S-14) is located 2 km south-east of S-13, north of Masafi to Fujairah highway on the southern profile D1. It was inactive for the majority of the 2.3 year deployment, and recorded only 40 of the events in our catalogue. An excellent signal to noise ratio meant 30 of these were available as potential sources. Receiver functions were calculated for these events and passed to our automatic quality control routine for analysis. These routines determined that half of these results were of good quality, with 15 results passing. Manual QC reduced this to 13. These results are displayed in Figure 3.28.

Receiver functions at S-14 were very consistent, with a clear division between easterly and westerly events. The most prominent phases on easterly events were a trough at $\sim 2.5\ s$, and a peak at $\sim 3.5\ s$. Westerly events did not exhibit any clear signal.

Amplitudes on the radial component were over two times stronger than the transverse component, indicating out-of-plane scattering is not such an issue here.

H - *k* stacking

$H-k$ stacking on the eastern events revealed two clear interfaces: The strong trough at $\sim 2\ s$ was mapped to a reverse polarity interface at $\sim 19\ km$ depth, with a k-value of 1.715; The strong peak at $\sim 3.5\ s$ meanwhile was mapped to a potential Moho



(a) Radial component **(b)** Transverse component

Figure 3.28: Receiver function results at S-14. Individual results are plotted in the main section of each component and sorted by back azimuth, with the stacked trace displayed at the top. The epicentral distance and back azimuth of each event is shown to the right.

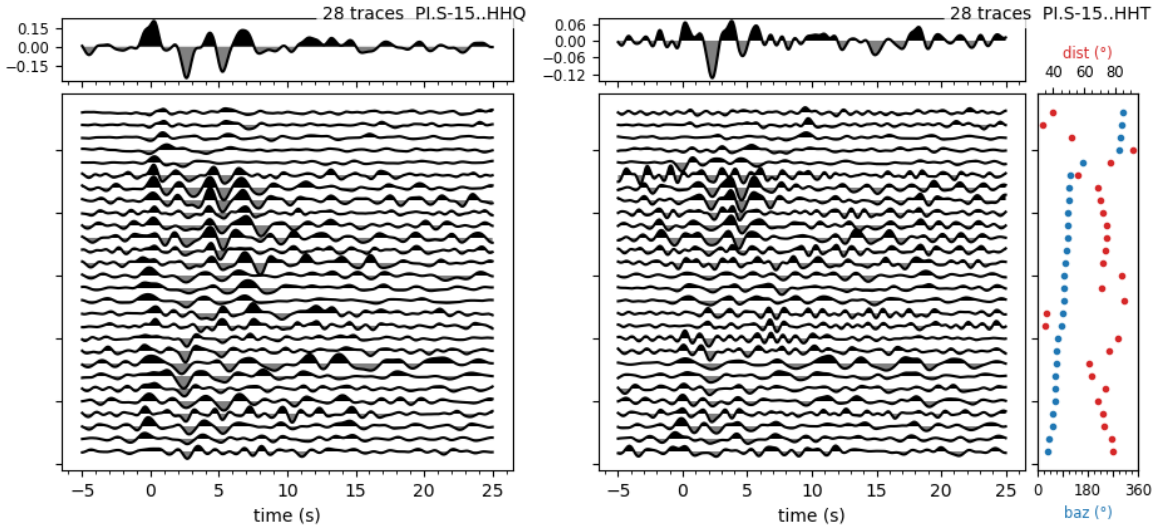
interface at $\sim 34\ km$ depth, with a k-value of 1.693.

3.11.14 S-15

Station 15 (S-15) is located under 3 km east of S-14, north of Masafi to Fujairah highway on the southern profile D1. It was active for under half of the 2.3 year deployment, and recorded 163 of the events in our catalogue. An excellent signal to noise ratio meant 105 of these were available as potential sources. Receiver functions were calculated for these events and passed to our automatic quality control routine for analysis. These routines determined that under half of these results were of good quality, with 41 results passing. Manual QC reduced this to 28. These results are displayed in Figure 3.29.

Receiver functions at S-15 were varied, but had a clear division between easterly and westerly events. The most prominent phases on easterly events were a trough at $\sim 2.5\ s$. A peak-trough-peak combo from $4 - 7\ s$ was also evident for south-easterly results. Westerly events exhibited a weak peak at ~ 1 and $\sim 6\ s$.

Amplitudes on the radial component were over two times stronger than the transverse component, indicating out-of-plane scattering is not such an issue here.



(a) Radial component **(b)** Transverse component

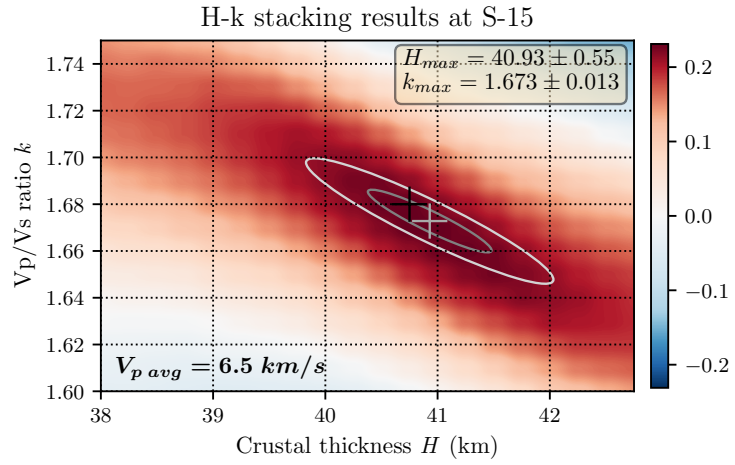
Figure 3.29: Receiver function results at S-15. Individual results are plotted in the main section of each component and sorted by back azimuth, with the stacked trace displayed at the top. The epicentral distance and back azimuth of each event is shown to the right.

H - *k* stacking

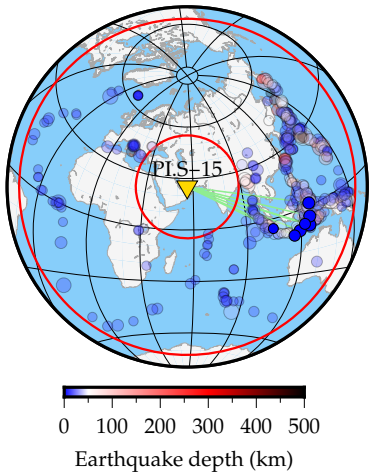
$H - k$ stacking results at S-15 were divided into three sub-groups: A north-easterly sub-group, a south-easterly sub-group, and a westerly sub-group.

The north-easterly group had a prominent trough at $\sim 2.5\ s$ that was mapped to a reverse polarity interface at $\sim 22\ km$ depth, with a k-value of 1.73. A weak peak at $\sim 3.5\ s$ could be mapped to a potential Moho interface at either $\sim 30\ km$ depth with a intermediate k-value, or $\sim 36\ km$ depth with a low k-value.

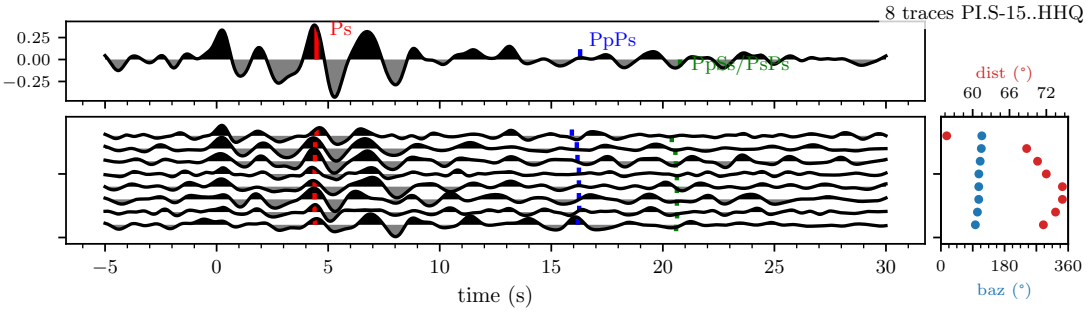
The south-easterly group was difficult to interpret, with a number of shallow phases to disentangle. A weak trough at $1\ s$ could be paired with either the trough and peak at $3 - 5\ s$ or $5 - 7\ s$ for a reverse polarity interface at either $\sim 7\ km$ depth with a relatively high k-value, or $\sim 13\ km$ depth with a relatively low k-value. A weak peak at $\sim 2\ s$ could also be mapped to an interface at $\sim 16\ km$ depth with the peak and trough between $6 - 9\ s$. These later phases were of significantly greater in amplitude though, suggesting they may also be primary phases. The broad trough at $\sim 3\ s$ could be mapped to a reverse polarity interface at either $\sim 19\ km$ depth with a high k-value, or $\sim 26\ km$ depth with a low k-value. The peak at $\sim 4.5\ s$ could be mapped to a



(a) Bootstrapped (B=50) $H - k$ stacking plot for S-15. Ellipses represent 1 and 2 bootstrap standard deviations.



(b) S-15 earthquake dataset. Unused events are faded.

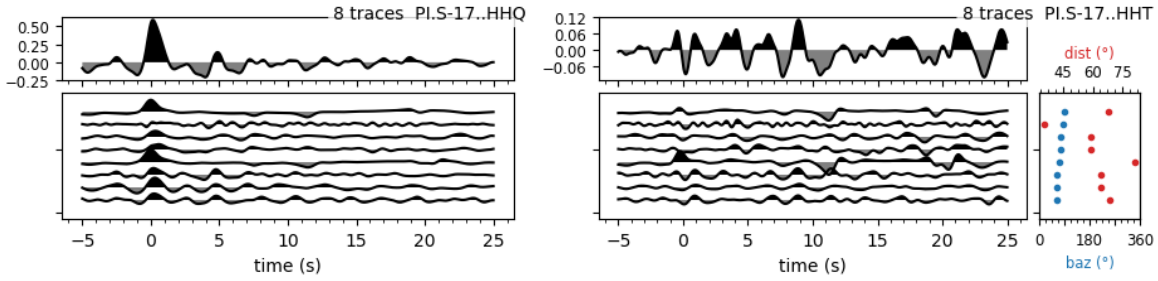


(c) Receiver functions results at S-15, sorted by back azimuth. Individual results are shown bottom and the stacked trace shown top. The locations of the phases representing the highest amplitude $H - k$ stacking result are highlighted on each trace.

Figure 3.30: $H - k$ stacking results at station S-15. $H - k$ stacking weights of 0.5, 0.3 and 0.2 were used for w_1, w_2 and w_3 respectively. The algorithm picks out the peak at $\sim 4.5\ s$, and identifies a weak peak and trough at 16 and 20.5 s as reverberations. It picks out H and k values of 40.93 ± 0.55 km and 1.673 ± 0.013 as the highest amplitude result. Note that this phase could also be mapped to a shallower interface with a high k-value.

potential Moho interface at $\sim 32\ km$ depth with a very high k-value, or $\sim 41\ km$ depth with a low k-value.

The westerly group was relatively easy to interpret in comparison, with the strong peaks at ~ 1 and $\sim 6\ s$ mapping to interfaces at $\sim 7\ km$ depth and $\sim 42\ km$ depth respectively. The latter result had a large uncertainty and high k-value however.



(a) Radial component **(b)** Transverse component

Figure 3.31: Receiver function results at S-17. Individual results are plotted in the main section of each component and sorted by back azimuth, with the stacked trace displayed at the top. The epicentral distance and back azimuth of each event is shown to the right.

3.11.15 S-17

Station 17 (S-17) is located in Fujairah city near the beach, at the easterly end of the southern profile D1. It was inactive for the majority of the 2.3 year deployment, and recorded only 71 of the events in our catalogue. A poor signal to noise ratio meant only 26 of these were available as potential sources. Receiver functions were calculated for these events and passed to our automatic quality control routine for analysis. These routines determined that the majority of these results were of poor quality, with only 10 results passing. Manual QC reduced this to 8. These results are displayed in Figure 3.31.

Receiver functions at S-17 were consistent, but did not show any strong phases beyond a strong peak at $\sim 0.5\ s$. A weak trough and peak was evident between $3-5\ s$ on some traces, but it did not stand out strongly from the background noise making it difficult to know whether it should be interpreted.

Amplitudes on the radial component were much stronger than the transverse component, indicating out-of-plane scattering is not an issue here.

H - *k* stacking

The shallow peak that dominated at this station could not be mapped to any interface with $H-k$ stacking. The weak trough at $\sim 3.5\ s$ could be mapped to a reverse polarity interface at either $\sim 27\ km$ depth with a high k-value, or $\sim 34\ km$ depth with a low

k-value. The weak peak at ~ 5 s could be mapped to a potential Moho interface at ~ 42 km depth.

The low amplitudes of these phases meant we did not have a lot of confidence in these results, and they were not used to constrain our models.

3.11.16 S-18

Station 18 (S-18) is located near the beach in Dadna, at the easterly end of the northern profile D4. It was active for around half of the 2.3 year deployment, and recorded 156 of the events in our catalogue. A good signal to noise ratio meant 83 of these were available as potential sources. Receiver functions were calculated for these events and passed to our automatic quality control routine for analysis. These routines determined that the majority of these results were of poor quality, with 33 results passing. Manual QC reduced this to 25. These results are displayed in Figure 3.32.

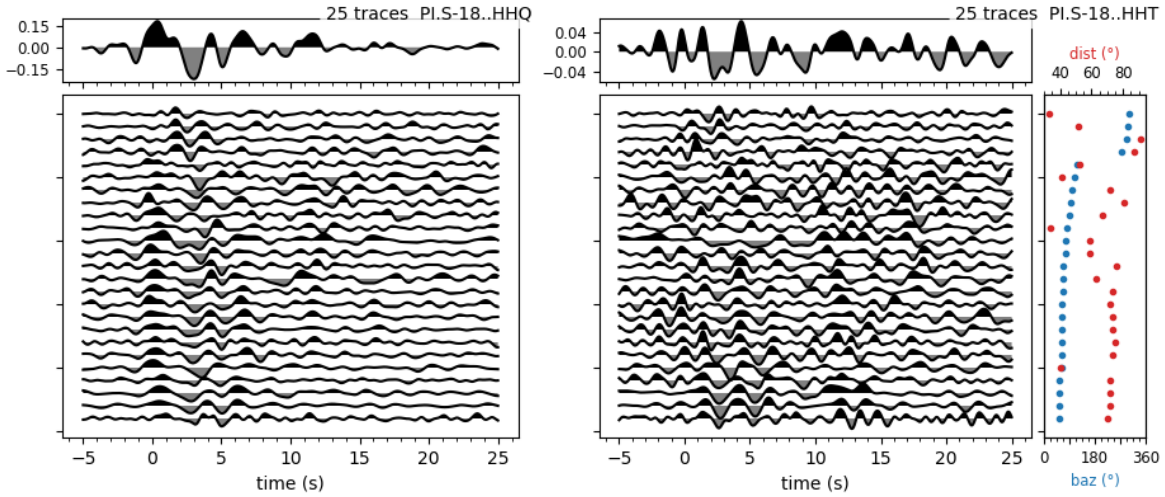
Receiver functions at S-18 were quite consistent, with a small difference between easterly and westerly events. The most prominent phases on easterly results was a strong peak at ~ 0.5 s, and a negative-positive-negative triplet between $2.5 - 5$ s. On westerly events this was replaced with a positive-negative-positive triplet was between $1.5 - 4$ s.

Amplitudes on the radial component were much stronger than the transverse component, indicating out-of-plane scattering is not an issue here.

H - *k* stacking

Receiver functions at S-18 were divided into two sub-groups for $H - k$ stacking. An eastern group of distal events ($> 70°$), and a western group.

The strong ~ 0.5 s peak on easterly results could be paired with a weak secondary peak and strong trough at 1.8 and 2.2 s to map an interface at ~ 4 km depth. The strong, broad trough at ~ 2.5 s was also likely to be a primary phase, and this was mapped to a reverse polarity interface at ~ 23 km depth, with a k-value of 1.79. A later peak at ~ 4 s did not correspond to any shallow multiples, and could be mapped



(a) Radial component **(b)** Transverse component

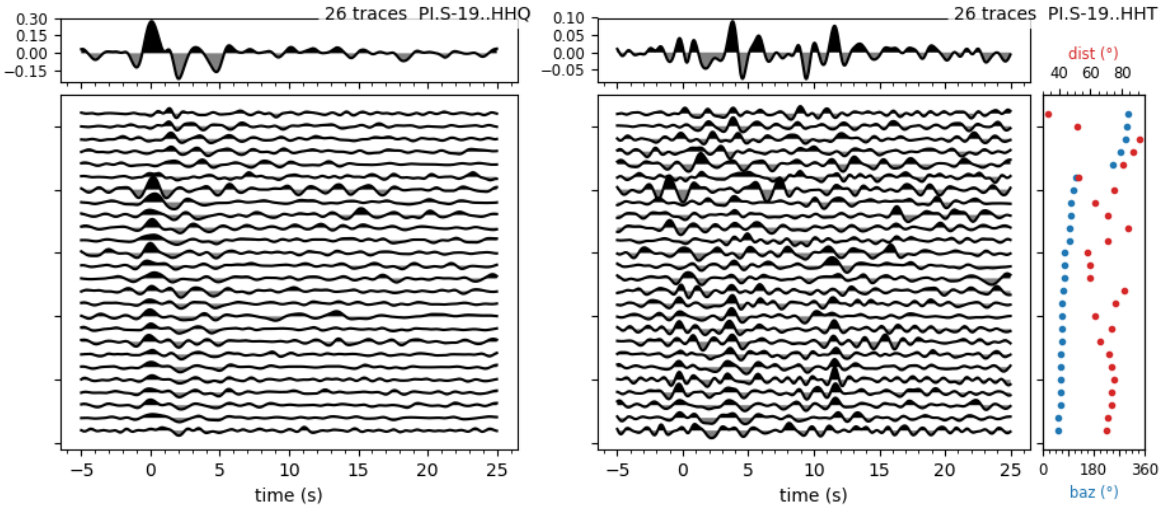
Figure 3.32: Receiver function results at S-18. Individual results are plotted in the main section of each component and sorted by back azimuth, with the stacked trace displayed at the top. The epicentral distance and back azimuth of each event is shown to the right.

to a potential Moho interface at $\sim 32\ km$ depth.

Analysis of westerly results showed three distinct primary phases. The peak at $\sim 2\ s$ was mapped to an interface at $\sim 13\ km$ depth, with a k-value of 1.74. The trough at $\sim 2.5\ s$ could be mapped to a reverse polarity interface at either $\sim 21\ km$ depth with a high k-value, or a $\sim 27\ km$ depth with a low k-value. Finally, the peak at $\sim 4\ s$ could again be mapped to a potential Moho interface at $\sim 32\ km$ depth, with a k-value of 1.71.

3.11.17 S-19

Station 19 (S-19) is located 4 km west of S-18, at the western edge of the town of Dadna on the northern profile D4. It was active for under half of the 2.3 year deployment, and recorded 129 of the events in our catalogue. A very good signal to noise ratio meant 77 of these were available as potential sources. Receiver functions were calculated for these events and passed to our automatic quality control routine for analysis. These routines determined that over half of these results were of poor quality, with 32 results passing. Manual QC reduced this to 26. These results are displayed in Figure 3.33.



(a) Radial component **(b)** Transverse component

Figure 3.33: Receiver function results at S-19. Individual results are plotted in the main section of each component and sorted by back azimuth, with the stacked trace displayed at the top. The epicentral distance and back azimuth of each event is shown to the right.

Receiver functions at S-19 were very consistent, with a clear difference between easterly and westerly events. The most prominent phase on easterly events was a negative polarity trough at 2 s. On westerly events the most dominant phase was a positive polarity peak at ~ 1.5 s.

Amplitudes on the radial component were much stronger than the transverse component, indicating out-of-plane scattering is not an issue here.

H - *k* stacking

Results at S-19 were divided into a north-eastern and a western sub-group, with both groups restricted to distal events ($> 72°$ and $> 60°$ respectively).

For north-eastern events, the strong trough at 2 s was mapped to a reverse polarity interface at ~ 19 km depth, with a k-value of 1.71. A weak peak at ~ 3.5 s could be mapped to a potential Moho interface at ~ 32 km depth, with a k-value of 1.65.

For western events, a strong peak at ~ 1.5 s could be paired with a peak and trough between $5.5 - 7$ s to map to an interface at ~ 13 km depth, with a k-value of 1.67. A secondary peak at ~ 3.5 s could be mapped to a potential Moho interface at ~ 31 km

depth, with a k-value of 1.73.

3.11.18 S-20

Station 20 (S-20) is located on obducted peridotites, in a wadi 3 km south-west of S-19 on the northern profile D4. It was active for the majority of the 2.3 year deployment, and recorded 160 of the events in our catalogue. An excellent signal to noise ratio meant 102 of these were available as potential sources. Receiver functions were calculated for these events and passed to our automatic quality control routine for analysis. These routines determined that just under half of these results were of good quality, with 49 results passing. Manual QC reduced this to 33. These results are displayed in Figure 3.34.

Receiver functions at S-20 were very consistent, with a clear difference between easterly and westerly events, and a slight difference between north-easterly and south-easterly events. The most prominent phase on north-easterly events was a strong trough at ~ 2 s, falling back to ~ 1.5 s on south-easterly results. This suggest the structure is dipping, or offset slightly to the north. On westerly events the most dominant phase was a peak at ~ 1 s.

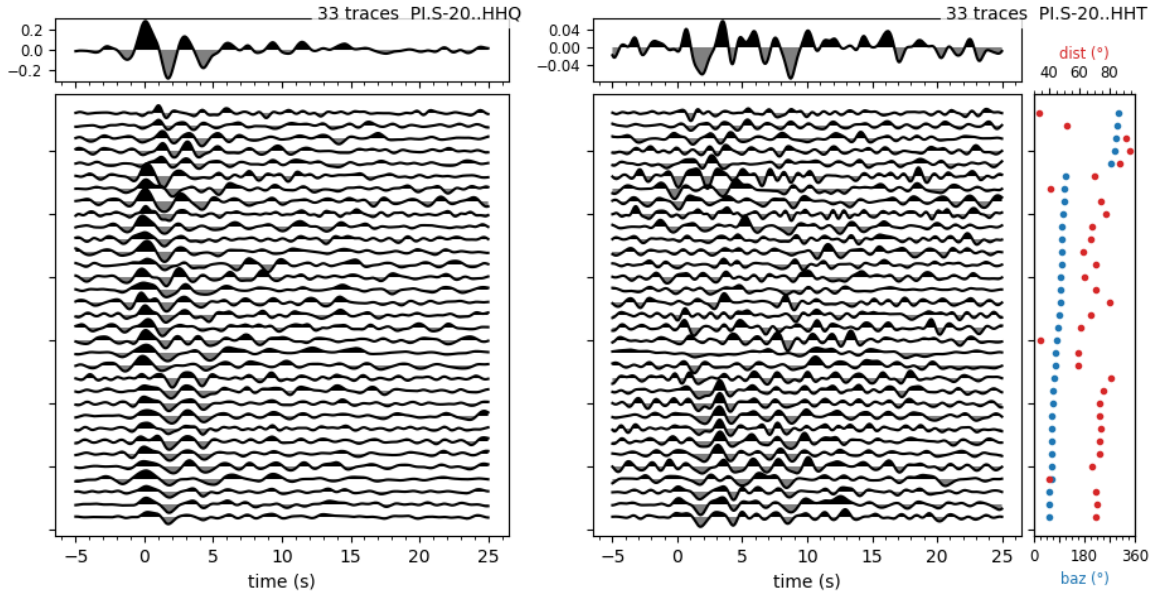
Amplitudes on the radial component were much stronger than the transverse component, indicating out-of-plane scattering is not an issue here.

H - *k* stacking

Results at S-20 were divided into a north-eastern, south-eastern, and western subgroups, with all groups restricted to distal events ($> 60°$).

For north-eastern events, a weak peak at 1 s could be paired with the peak and trough from to $3 - 5$ s to map an interface at ~ 8 km depth, with a low k-value of 1.63. The dominant trough at ~ 2 s could be mapped to a reverse polarity interface at ~ 18 km depth, with a k-value of 1.67 (see Figure 3.35).

For south-eastern events, a strong trough at ~ 1.5 s could be paired with the weaker trough and peak from to $4 - 6$ s to map a reverse polarity interface at ~ 10 km



(a) Radial component **(b)** Transverse component

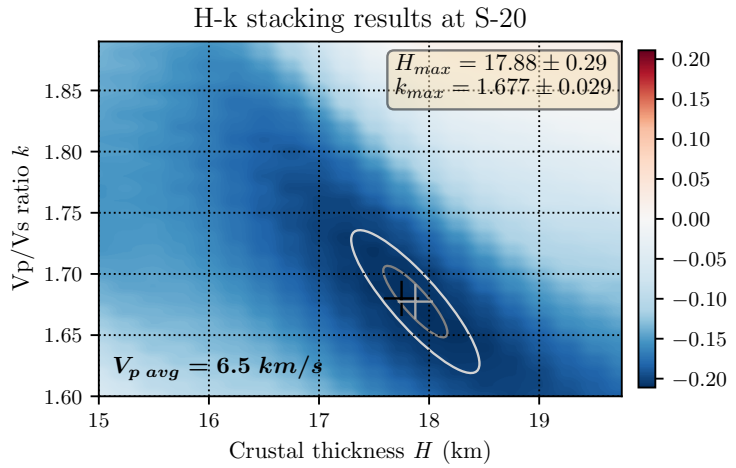
Figure 3.34: Receiver function results at S-20 for the radial (left) and transverse (right) components. Individual results are plotted in the main section of each component and sorted by back azimuth, with the stacked trace displayed at the top. The epicentral distance and back azimuth of each event is shown to the right.

depth, though with a high k-value of 1.86. This discrepancy in k-values exaggerates the difference in mapped depths on results from the north-east and south-east. The weaker peak at $\sim 3\ s$ was possibly a shallow reverberation, but it was mapped to an interface at $\sim 26\ km$ depth, though with a large uncertainty and a k-value of ~ 1.67.

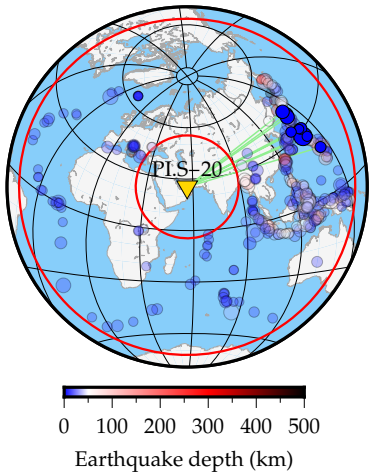
For western events, a strong peak at $\sim 1\ s$ could be paired with a peak and trough between $2.5 - 5\ s$ to map to an interface at $\sim 7\ km$ depth with a k-value of 1.80, or $\sim 12\ km$ depth with a k-value of 1.61. A weaker trough at $\sim 2\ s$ meant we had difficulty finding a suitable peak for a $PsPs/PpSs$ phase, but it could be mapped to a reverse polarity interface at $\sim 21\ km$ depth with a low k-value of 1.63.

3.11.19 S-21

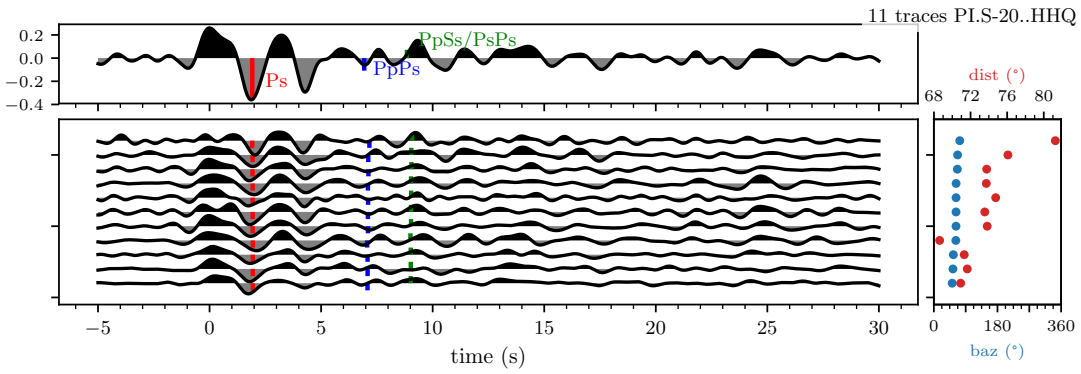
Station 21 (S-21) is located on obducted peridotites, in a wadi 3 km west of S-20 on the northern profile D4. It was inactive for the majority of the 2.3 year deployment, and recorded only 96 of the events in our catalogue. An excellent signal to noise ratio meant



(a) Bootstrapped (B=50) $H - k$ stacking plot for S-20. Ellipses represent 1 and 2 bootstrap standard deviations.



(b) S-20 earthquake dataset. Unused events are faded.

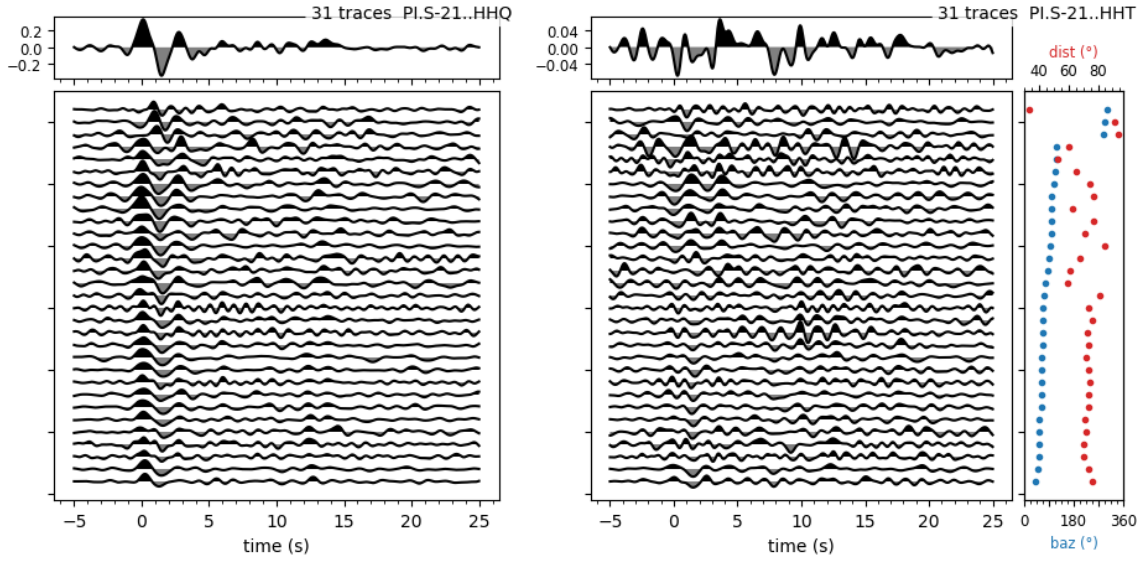


(c) Receiver functions results at S-20, sorted by back azimuth. Individual results are shown bottom and the stacked trace shown top. The locations of the phases representing the highest amplitude $H - k$ stacking result are highlighted on each trace.

Figure 3.35: $H - k$ stacking results at station S-20. $H - k$ stacking weights of 0.5, 0.3 and 0.2 were used for w_1, w_2 and w_3 respectively. The algorithm picks out the primary trough at ~ 2 s, and identifies a weak trough and peak at 7 and 9 s as reverberations. It picks out H and k values of 17.88 ± 0.29 km and 1.677 ± 0.029 as the highest amplitude result.

62 of these were available as potential sources. Receiver functions were calculated for these events and passed to our automatic quality control routine for analysis. These routines determined that over half of these results were of good quality, with 37 results passing. Manual QC reduced this to 31. These results are displayed in Figure 3.36.

Receiver functions at S-21 were very consistent, with a clear difference between easterly and westerly events. The most prominent phase on easterly events was a



(a) Radial component **(b)** Transverse component

Figure 3.36: Receiver function results at S-21 for the radial (left) and transverse (right) components. Individual results are plotted in the main section of each component and sorted by back azimuth, with the stacked trace displayed at the top. The epicentral distance and back azimuth of each event is shown to the right.

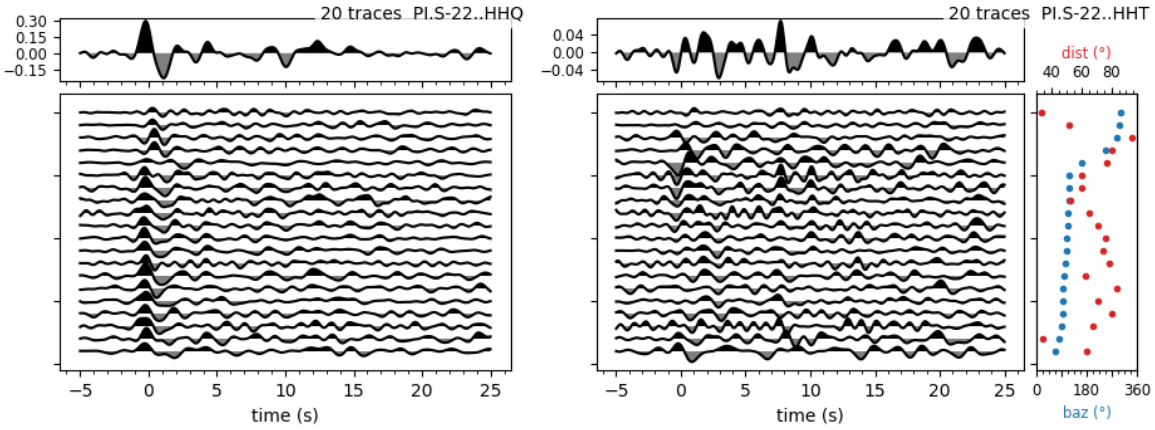
strong trough at $\sim 1.5\ s$. On westerly events the most dominant phase was a peak at $\sim 1\ s$.

Amplitudes on the radial component were much stronger than the transverse component, indicating out-of-plane scattering is not an issue here.

H - *k* stacking

For eastern events, the strong trough at $1.5\ s$ was mapped to a reverse polarity interface at $\sim 11\ km$ depth, with a high k-value of 1.82. A weak peak at $\sim 2.5\ s$ was possibly a shallow reverberation, but could be mapped to a an interface at $\sim 27\ km$ depth, with a k-value of 1.65.

For western events, the strong peak at $1\ s$ could be paired with a peak and trough between $2 - 4\ s$ to map to an interface at $\sim 6\ km$ depth, though with a very high k-value of 1.88. A trough at $\sim 2\ s$ could be mapped to a reverse polarity interface at $\sim 12\ km$ depth, again with a high k-value of 1.85.



(a) Radial component **(b)** Transverse component

Figure 3.37: Receiver function results at S-22. Individual results are plotted in the main section of each component and sorted by back azimuth, with the stacked trace displayed at the top. The epicentral distance and back azimuth of each event is shown to the right.

3.11.20 S-22

Station 22 (S-22) is located on obducted peridotites, in a wadi 7 km south-west of S-21 on the northern profile D4. It was active for just under half of the 2.3 year deployment, and recorded 125 of the events in our catalogue. An excellent signal to noise ratio meant 86 of these were available as potential sources. Receiver functions were calculated for these events and passed to our automatic quality control routine for analysis. These routines determined that the majority of these results were of poor quality, with 25 results passing. Manual QC reduced this to 20. These results are displayed in Figure 3.37.

Receiver functions at S-22 were reasonably consistent, with a clear difference between easterly and westerly events. The most prominent phase on easterly events was a strong trough at $\sim 1\ s$. On westerly events the most dominant phase was a peak at $\sim 0.5\ s$.

Amplitudes on the radial component were much stronger than the transverse component, indicating out-of-plane scattering is not an issue here.

***H* - *k* stacking**

For eastern events, the strong trough at ~ 1 s was mapped to a reverse polarity interface at ~ 8 km depth, with a k-value of 1.75.

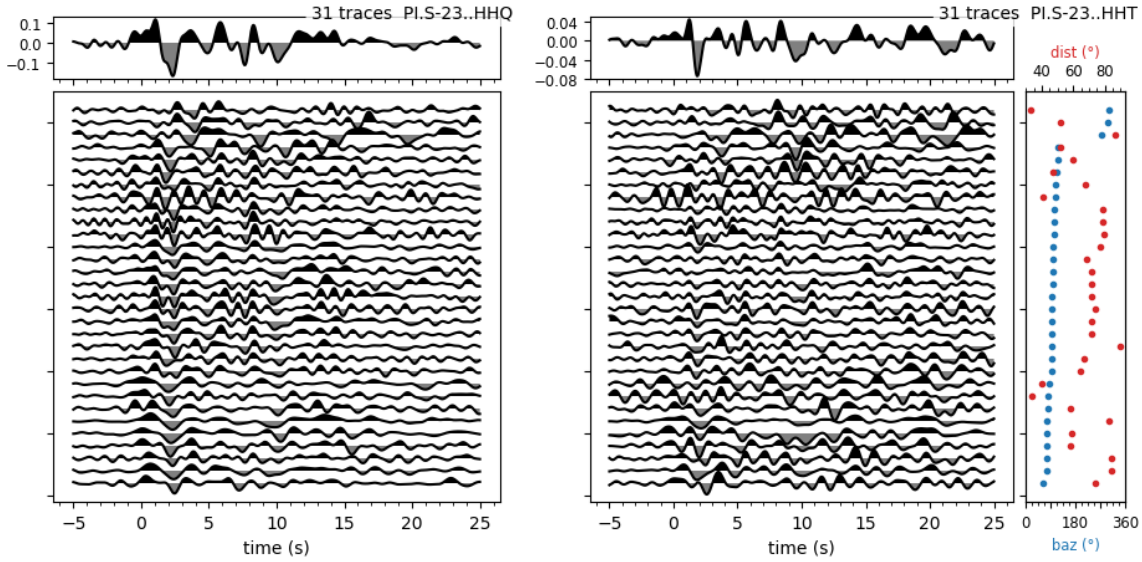
For western events, a strong peak at 0.3 s could be paired with a weak peak and trough between $1.5-3$ s to map an interface at ~ 3 km depth, with a very low k-value of 1.62. A trough at ~ 1 s could again be mapped to a reverse polarity interface at ~ 8 km depth with a k-value of 1.75. A weak peak at ~ 4.5 s represented a potential Moho conversion, and could be mapped to ~ 36 km depth, though with a large uncertainty.

3.11.21 S-23

Station 23 (S-23) is located on cherts of the obducted Hawasina group, 7 km north-west of S-22 on the northern profile D4. It was active for around half of the 2.3 year deployment, and recorded 156 of the events in our catalogue. An excellent signal to noise ratio meant 123 of these were available as potential sources. Receiver functions were calculated for these events and passed to our automatic quality control routine for analysis. These routines determined that the majority of these results were of poor quality, with 45 results passing. Manual QC reduced this to 31. These results are displayed in Figure 3.38.

Receiver functions at S-23 were not as clean as previous results on this profile, but contained some consistent phases, and exhibited a clear difference between easterly and westerly events. The most prominent set of phases on easterly results were a strong peaks at 1, 3.5, and 6 s, and a trough at 2 s. On westerly events the same key phases were observed, but the shallow phases were pushed back by about 1 s.

Amplitudes on the radial component were roughly twice as strong than the transverse component, indicating out-of-plane scattering is a minor issue here.



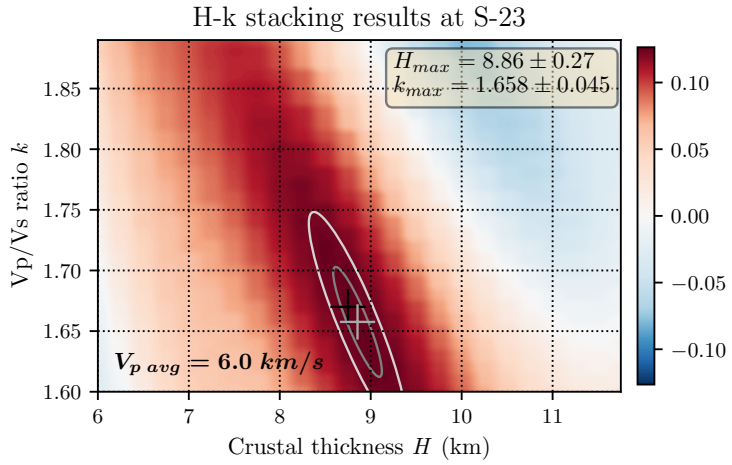
(a) Radial component **(b)** Transverse component

Figure 3.38: Receiver function results at S-23. Individual results are plotted in the main section of each component and sorted by back azimuth, with the stacked trace displayed at the top. The epicentral distance and back azimuth of each event is shown to the right.

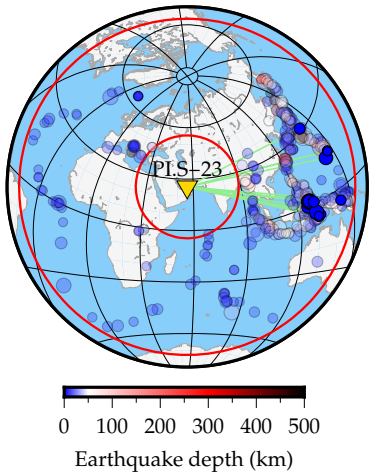
H - *k* stacking

Easterly results were restricted to distal events ($> 68°$) for $H-k$ stacking. The strong peak at ~ 1 s could be paired with the peak and trough at ~ 4 and ~ 5 s to map to an interface at ~ 9 km depth, with a k-value of 1.68 (see Figure 3.39). The trough at 2 s could be mapped to a reverse polarity interface at ~ 25 km depth, though with a very low k-value of 1.61.

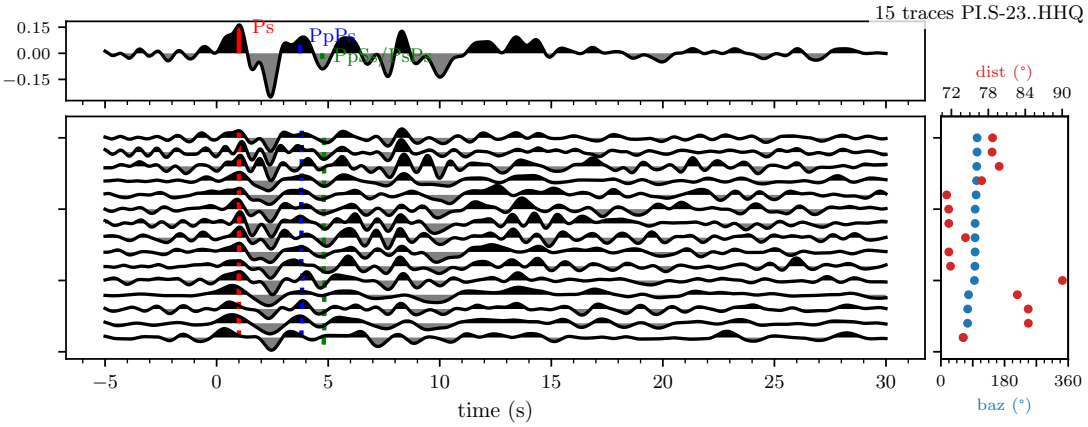
Westerly events were few in number, but had some consistent phases to work with. A strong peak at ~ 2.5 s could be mapped to an interface at ~ 26 km depth, though with a very low k-value of 1.61. A trough at ~ 3.5 s could be mapped to a deep reverse polarity interface at ~ 36 km depth with a k-value of 1.66. A peak at ~ 4 s represented a potential Moho conversion, and could be mapped to ~ 43 km depth, with a k-value of ~ 1.65.



(a) Bootstrapped (B=50) $H-k$ stacking plot for S-23. Ellipses represent 1 and 2 bootstrap standard deviations.



(b) S-23 earthquake dataset. Unused events are faded.

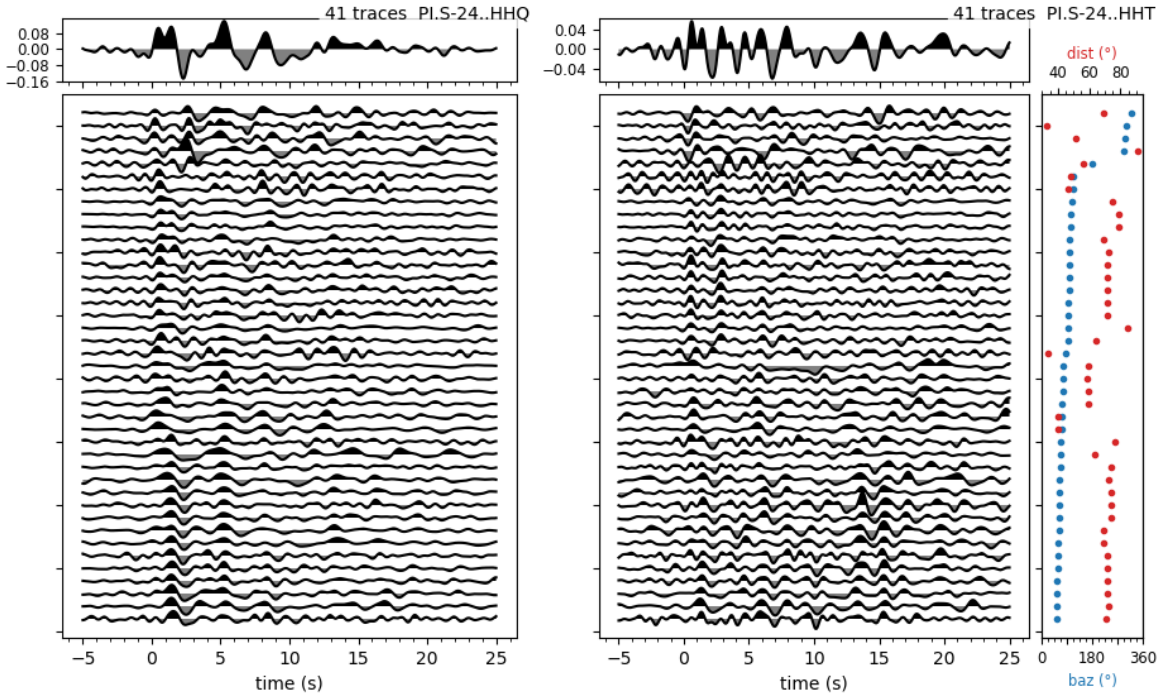


(c) Receiver functions results at S-23, sorted by back azimuth. Individual results are shown bottom and the stacked trace shown top. The locations of the phases representing the highest amplitude $H-k$ stacking result are highlighted on each trace.

Figure 3.39: $H-k$ stacking results at station S-23. $H-k$ stacking weights of 0.5, 0.3 and 0.2 were used for w_1, w_2 and w_3 respectively. The algorithm picks out the peak at ~ 1 s, and identifies a peak and trough at ~ 4 and ~ 5 s as reverberations. It picks out H and k values of 8.86 ± 0.27 km and 1.658 ± 0.045 as the highest amplitude result.

3.11.22 S-24

Station 24 (S-24) is located on cherts of the obducted Hawasina group, 8 km west of S-23 on the northern profile D4. It was active for the majority of the 2.3 year deployment, and recorded 174 of the events in our catalogue. An excellent signal to noise ratio meant 131 of these were available as potential sources. Receiver functions



(a) Radial component **(b)** Transverse component

Figure 3.40: Receiver function results at S-24. Individual results are plotted in the main section of each component and sorted by back azimuth, with the stacked trace displayed at the top. The epicentral distance and back azimuth of each event is shown to the right.

were calculated for these events and passed to our automatic quality control routine for analysis. These routines determined that the majority of these results were of poor quality, with 48 results passing. Manual QC reduced this to 41. These results are displayed in Figure 3.40.

Receiver functions at S-24 were varied, with a clear difference between easterly and westerly events. The most dominant phases on easterly events were a strong peak and trough between $1-3\ s$, and a peak at $\sim 5\ s$. On westerly events the most dominant set of phases were a peak and trough between $2-4\ s$, and a broad peak at $\sim 5\ s$.

Amplitudes on the radial component were twice as strong as the transverse component, indicating out-of-plane scattering is an issue here.

H - *k* stacking

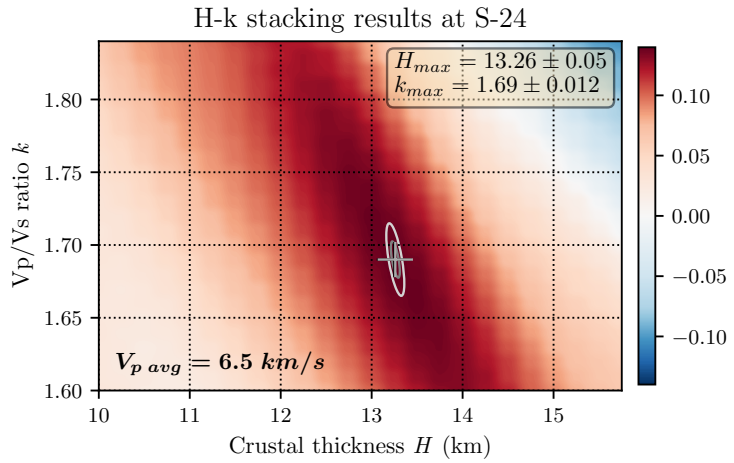
Easterly results were again restricted to distal events ($> 70°$) for $H - k$ stacking. The strong peak at ~ 1.5 s could be paired with the peak and trough at 5 and 6.5 s to map to an interface at ~ 13 km depth, with a k-value of 1.69 (see Figure 3.41). The trough at 2 s could be mapped to a reverse polarity interface at either ~ 17 km depth with a high k-value, or ~ 24 km depth with a low k-value. The peak at ~ 5 s could be mapped to a potential Moho interface at ~ 43 km depth, but it was unclear if this was a primary phase or just a shallow reverberation.

Westerly events were few in number, and very similar to those at S-23. A strong peak at ~ 2.5 s could be mapped to an interface at ~ 19 km depth, though with a high k-value of 1.86. A trough at ~ 3.5 s could be mapped to a reverse polarity interface anywhere between $24 - 36$ km depth, as no clear reverberated phase stood out. A broad peak at ~ 5 s could be mapped to a potential Moho interface at ~ 40 km depth, with a k-value of ~ 1.76, suggesting the 5 s easterly phase was not just a reverberation.

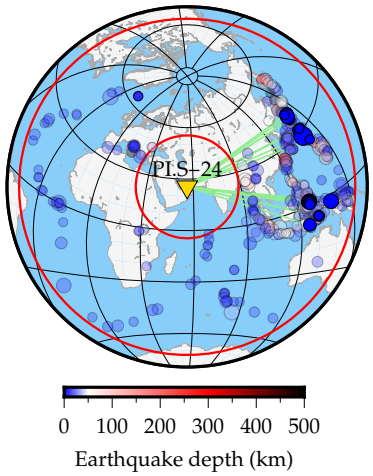
3.11.23 S-25

Station 25 (S-25) is located at the western edge of the UAE-Oman mountains, and is the western-most station on the northern profile D4. It was active for the majority of the 2.3 year deployment, and recorded 219 of the events in our catalogue. A good signal to noise ratio meant 161 of these were available as potential sources. Receiver functions were calculated for these events and passed to our automatic quality control routine for analysis. These routines determined that the majority of these results were of poor quality, with 59 results passing. Manual QC reduced this to 43. These results are displayed in Figure 3.42.

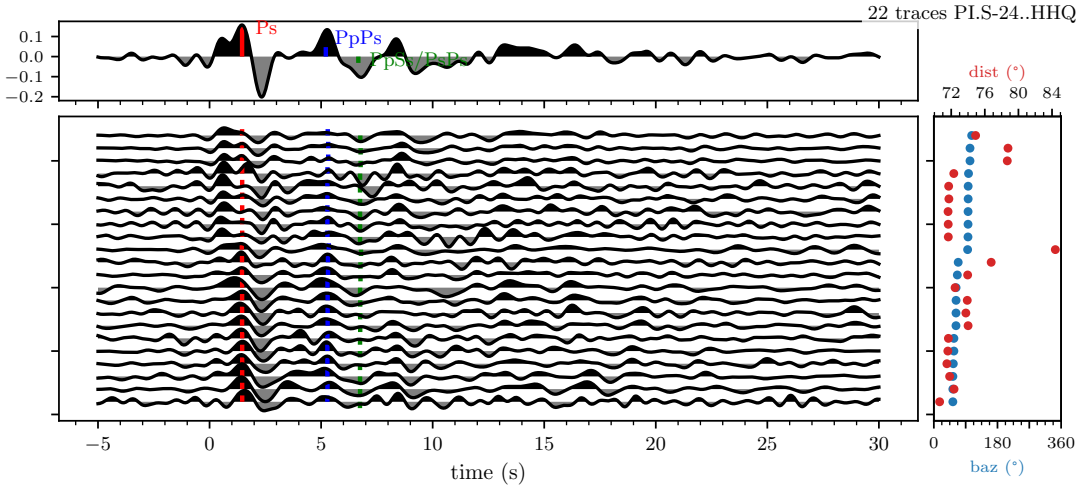
Receiver functions at S-25 were relatively consistent, with a slight difference between north-eastern and south-eastern results. The most prominent set of phases was a strong postive-negative-postive triplet between $1 - 3.5$ s. There was only a single western result, and this was not analysed.



(a) Bootstrapped (B=50) $H - k$ stacking plot for S-24. Ellipses represent 1 and 2 bootstrap standard deviations.



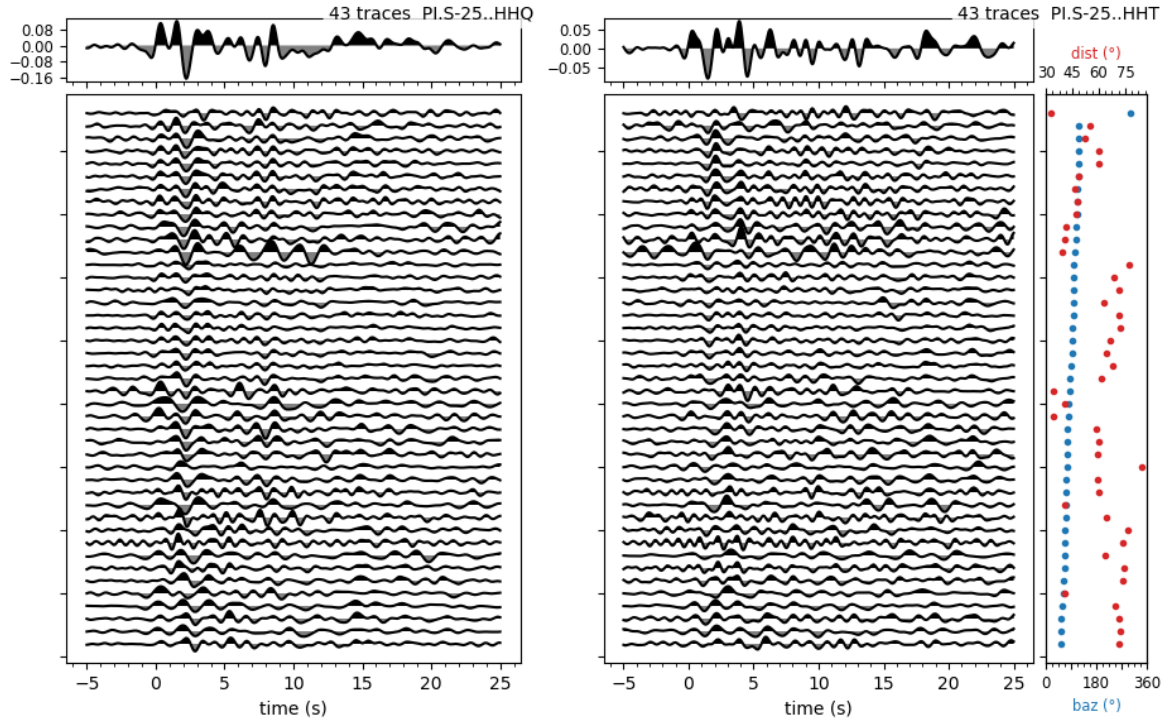
(b) S-24 earthquake dataset. Unused events are faded.



(c) Receiver functions results at S-24, sorted by back azimuth. Individual results are shown bottom and the stacked trace shown top. The locations of the phases representing the highest amplitude $H - k$ stacking result are highlighted on each trace.

Figure 3.41: $H - k$ stacking results at station S-24. $H - k$ stacking weights of 0.5, 0.3 and 0.2 were used for w_1, w_2 and w_3 respectively. The algorithm picks out the primary peak at $\sim 1\ s$, and identifies the strong peak and trough at 5 and 6.5 s as reverberations. It picks out H and k values of 13.26 ± 0.05 km and 1.69 ± 0.012 as the highest amplitude result.

Amplitudes on the radial component were less than double those of the transverse component, indicating out-of-plane scattering is an issue here.



(a) Radial component **(b)** Transverse component

Figure 3.42: Receiver function results at S-25. Individual results are plotted in the main section of each component and sorted by back azimuth, with the stacked trace displayed at the top. The epicentral distance and back azimuth of each event is shown to the right.

H - *k* stacking

$H - k$ stacking was restricted to south-easterly results, as these were very consistent compared to those from the north-east. Two peaks at ~ 0.5 and ~ 1.5 s could be paired with the trough at 2 s to map to a shallow interface at ~ 3.5 km depth, with a k-value of 1.73. The strength of trough at 2 s suggested it was also a primary phase, and it could be mapped to a reverse polarity interface at either ~ 16 km depth with a high k-value, or ~ 21 km depth with a low k-value. A strong peak at ~ 3 s could be mapped to an interface at ~ 28 km depth, with a k-value of 1.63. A weaker peak at ~ 4 s could also be mapped to a potential Moho interface from $30 - 38$ km depth with an intermediate to low k-value.

3.11.24 Summary

In total 91 depth points were extracted across the PI/Oxford network with $H - k$ stacking (see Appendix B for a summary table). Combined they provide insight into the subsurface structure in the region.

Each $H - k$ stacking result was back-projected to its spatially averaged piercing point at its mapped depth and plotted in place. Uncertainties in depth are provided by bootstrap testing. These depth points are plotted along profiles D1 and D4, coincident with our seismometer network and previous seismic surveys, and are shown in Figures 3.43 and 3.44. These profiles show accurately mapped depth points in the subsurface from our receiver functions analysis outlined above. The results are scattered though and do not reveal as much in the way of coherent lateral structures as we hoped, particularly beneath the obducted ophiolite.

On the southern profile D1 (Figure 3.43) a clear mid crustal interface is evident at $\sim 15\ km$ depth in the foreland, along with a few Moho depth points at $\sim 36\ km$ depth. Beneath the ophiolite the picture is far less coherent however. A number of possible Moho depth points are present below 30 km depth, making it difficult to know which ones to interpret. The reverse polarity points that we interpret to be from the base of the ophiolite are also scattered, with a group at $\sim 23\ km$ depth between $70 - 90\ km$ along profile disrupting the general trend of increasing depths to the east in the other results.

On the northern profile D4 (Figure 3.44) Moho depth points are generally sparser and more coherent, and suggest the presence of a root 'peaking' beneath the Masafi window. Reverse polarity results again hint at an eastward dipping base ophiolite interface from $30 - 50\ km$ along profile, but scattered reverse polarity results are also present across the rest of the profile, and these are more difficult to interpret.

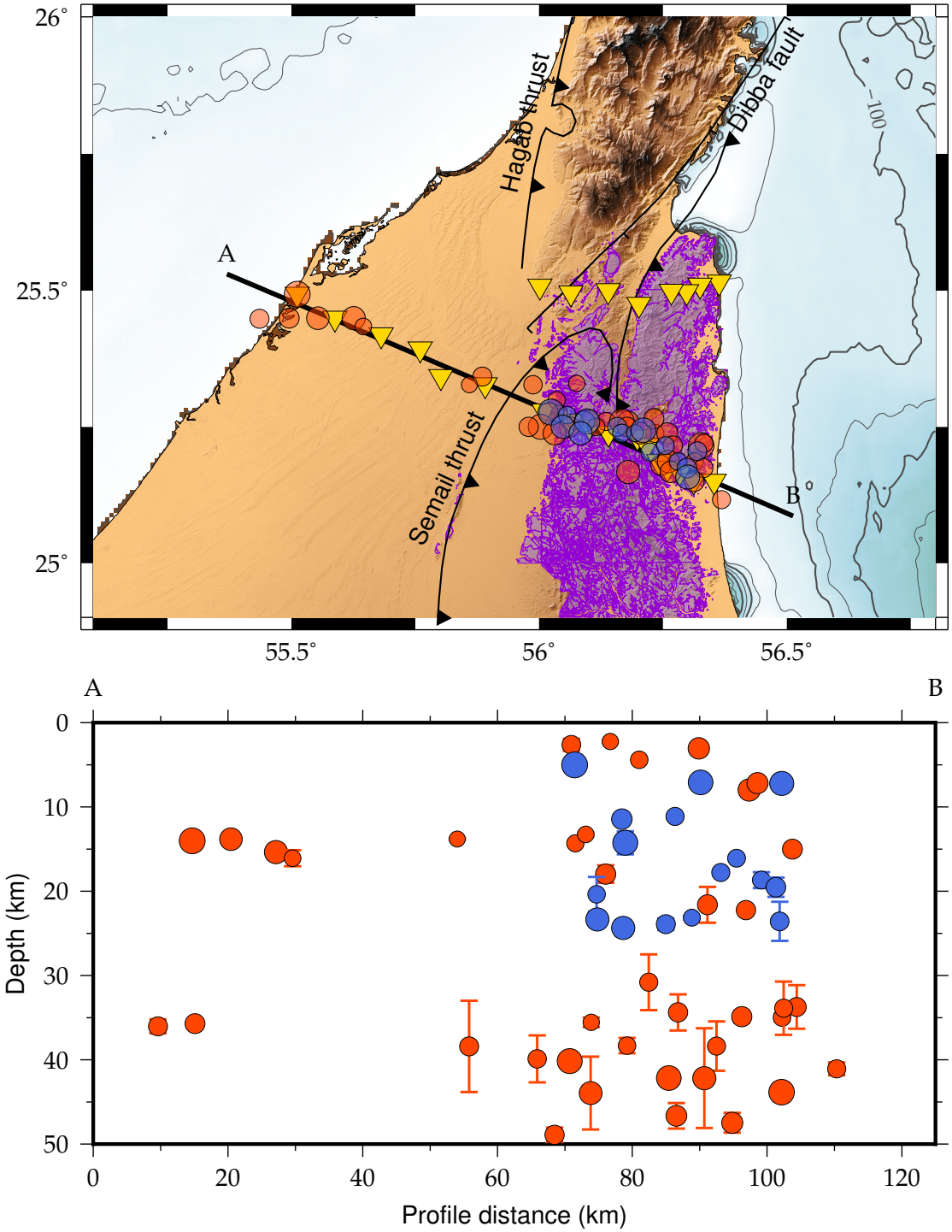


Figure 3.43: Depth points obtained with $H-k$ stacking along profile D1. Red and blue circles indicate a positive and negative polarity result respectively, with circle size proportional to k. Depth error bars are standard deviations obtained from bootstrapping.

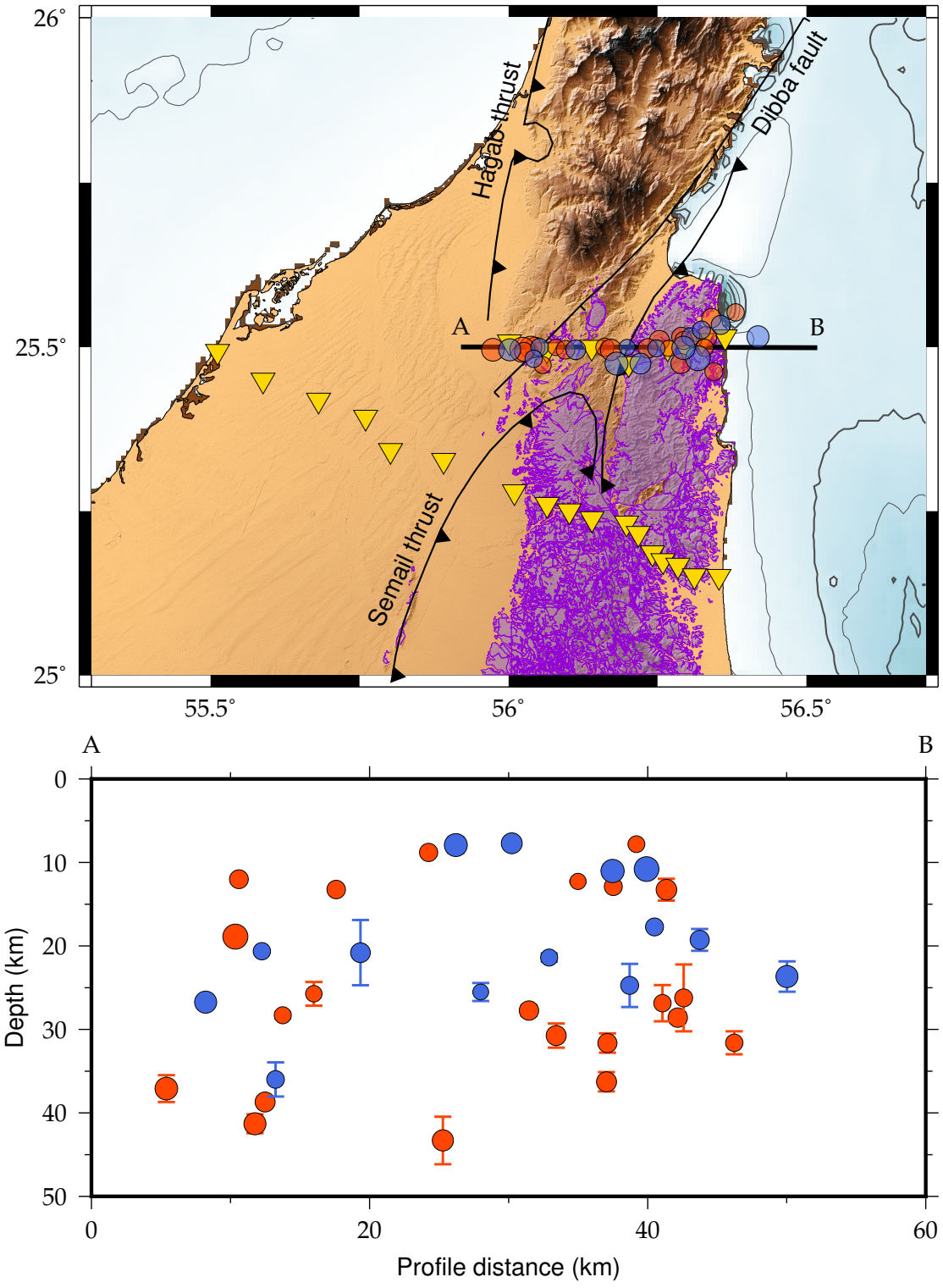


Figure 3.44: Depth points obtained with $H-k$ stacking along profile D1. Red and blue circles indicate a positive and negative polarity result respectively, with circle size proportional to k. Depth error bars are standard deviations obtained from bootstrapping.

3.12 Receiver function profiles

To better visualize the spatial variation of our receiver function results we regroup results across our network into bins related to their projected piercing point at 30 km depth below their respective station. This method is similar to the common midpoint stacking approach described by *Dueker and Sheehan* (1997).

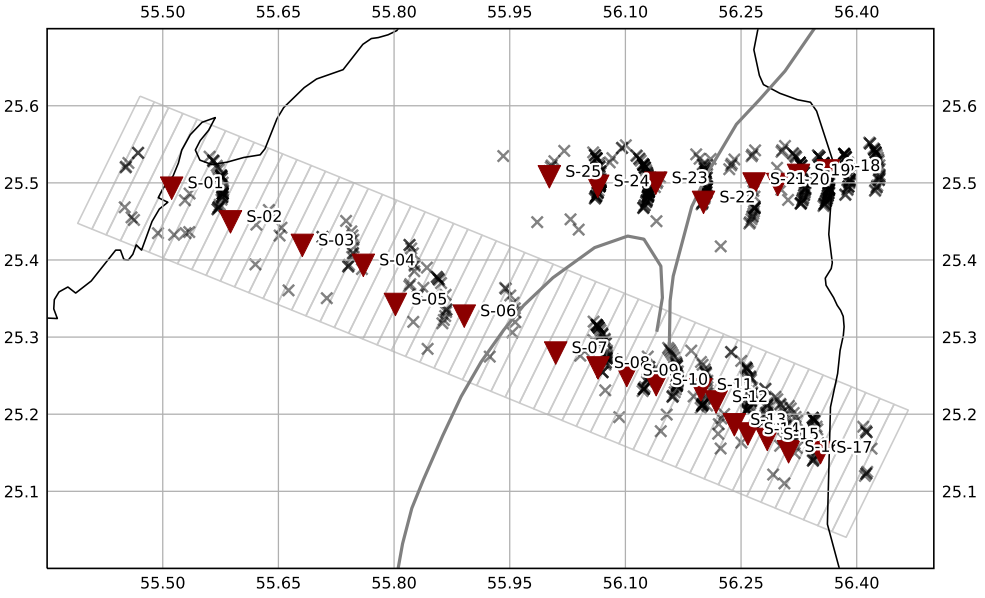
Profiles are defined along both the northern (D4) and southern (D1) lines of seismometers. The profile is then divided up into wide bins extending either side of the profile. Each receiver function result is projected back along its back azimuth to a theoretical piercing point using the *iasp91* velocity model. The back projected results in each bin are grouped together and stacked. The result is akin to a common depth point (CDP) stack in seismic reflection processing. It can improve signal to noise ratio in poorly sampled areas when results from nearby stations fall in the same bin. Structure can be more readily revealed as laterally continuous converters can be traced across results from multiple stations. However, if there is significant out-of-plane variation in receiver function results the stacked trace in that bin will be of poor quality, and these out-of-plane variations will not be represented.

Receiver functions contributing to these profiles were calculated using the MTC method with a 1 Hz cutoff frequency. This more restrictive frequency filter better highlights strong, deep signals and improves lateral continuity of the results.

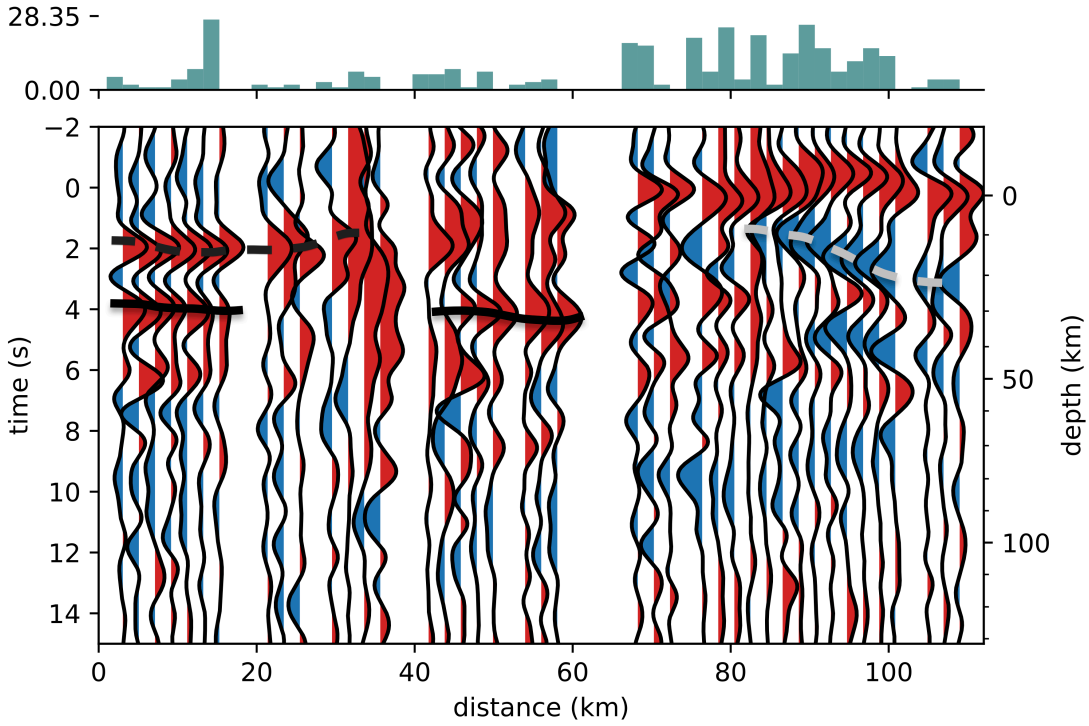
3.12.1 Profile D1

We define a profile coincident with the seismometers deployed along the southern profile D1. This profile begins on the western edge of the desert and extends 110 km east-southeast to end just offshore in the Gulf of Oman. The profile is divided into 2 km wide bins extending 10 km either side of the profile.

This profile is displayed in Figure 3.45, and features strong laterally continuous conversions in both the western and eastern ends. Coherent structures are not so clear in the middle of the profile compared to the central foreland and western mountain



(a) Profile map



(b) Receiver function profile

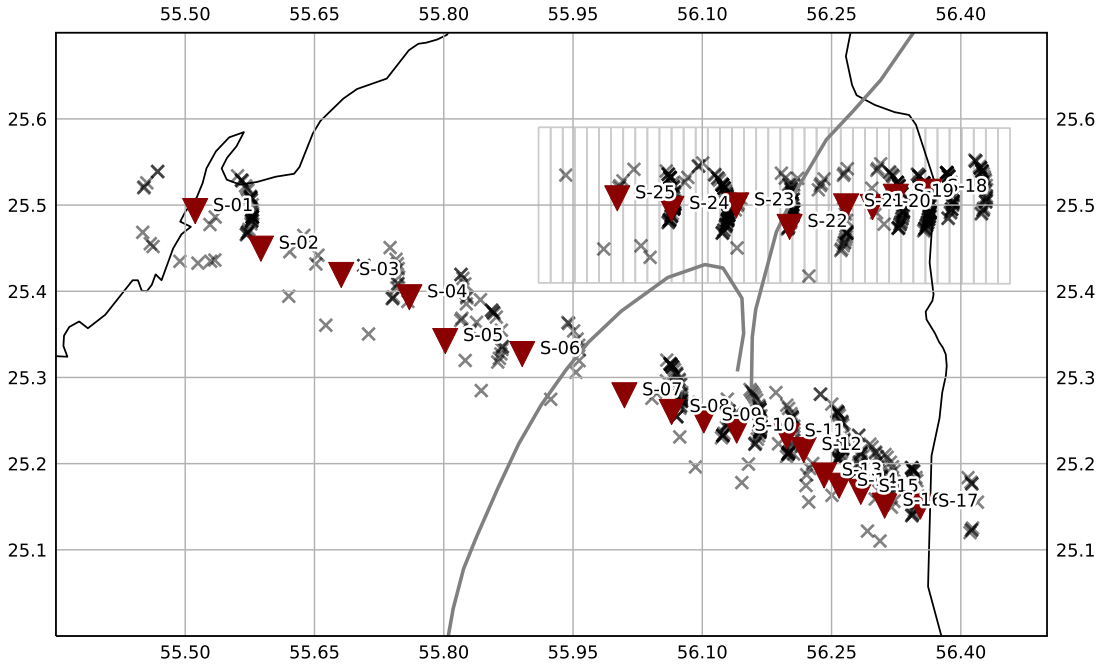
Figure 3.45: Receiver function profile along the southern seismometer line D1. The map (top) shows a rough coastline, station locations, with grey lines marking the surface expression of the Semail Thrust. The 2x20 *km* bins that are used to group the data are displayed along the southern profile D1, and projected piercing point locations at 30 *km* depth are marked by a black 'x'. The receiver function profile (bottom) shows the stacked trace from each bin with red indicating positive polarity and blue negative. Interpreted Moho conversions are marked by the solid black line, the base of the foreland basin by the dotted black line, and the base of the ophiolite by the dotted grey line. The histogram above denotes the number of traces contributing each stack. Depth conversions displayed on the right have been completed using the *iasp91* velocity model.

sections, partially due to a low number of results here. The western foreland shows a clear positive polarity signal at both 2 and 4 s delay time. This signal is very flat and laterally continuous for some 16 km east-west. We interpret the 2 s signal to be a mid crustal Ps conversion from either the top of a salt layer or from basement to the foreland sedimentary secession. The 4 s signal does not match with projected reverberation times from the 2 s arrival so we interpret this to be a second Ps conversion from the Moho. The most prominent signal from the eastern side of the line is the negative polarity troughs visible from $85 - 105$ km. The delay time of this phase increases eastwards from $\sim 1.5 - 3$ s. The polarity of this phase is consistent with a slow to fast velocity interface, such as what we might expect in a transition from 'slow' continental basement, to the 'fast' obducted oceanic crust and upper mantle of the Semail ophiolite. The eastward dip of this phase implies the ophiolite thickens from ~ 10 km to near Masafi to ~ 20 km at the Gulf of Oman coastline.

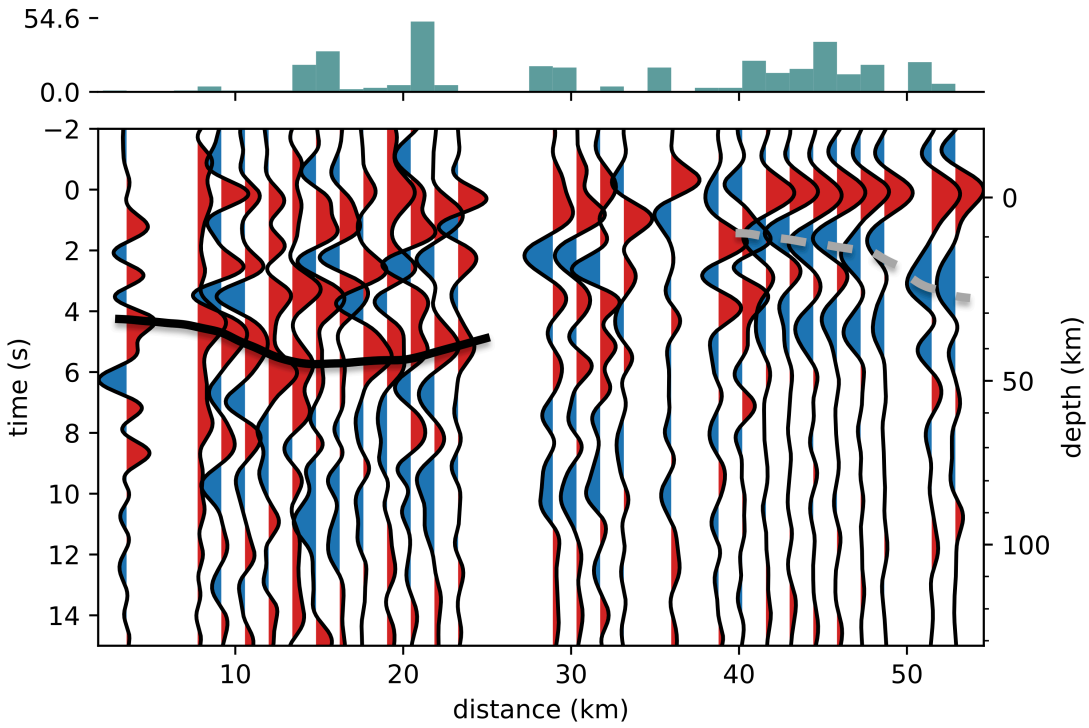
3.12.2 Profile D4

We define a second profile coincident with the seismometers deployed along the northern profile D4. This profile is again deployed east-west, but is shorter than profile D1 at 55 km. It extends from Dadna on the Gulf of Oman coastline to the western edge of the mountains. The profile is divided into 1.375 km wide bins extending 10 km either side, and is displayed in Figure 3.46.

A coherent negative polarity signal at $\sim 2s$ is evident from ~ 40 km onwards suggesting the base of the ophiolite may again be imaged here. There may be a step in thickness near the coast as suggested by the increased delay times on the last two traces. A potential Moho can be seen between $4 - 6$ s on the left side of the profile. The lateral shape of this phase suggests flexure due to ophiolite loading and mountain building has occurred. It also appears that the Moho rapidly shallows eastwards towards the coast to more typical oceanic values offshore in the Gulf of Oman.



(a) Profile map



(b) Receiver function profile

Figure 3.46: Receiver function profile along the southern seismometer line D4. The map (top) shows a rough coastline, station locations, with grey lines marking the surface expression of the Semail Thrust. The 1.375x20 *km* bins that are used to group the data are displayed along the southern profile D1, and projected piercing point locations at 30 *km* depth are marked by a black 'x'. The receiver function profile (bottom) shows the stacked trace from each bin with red indicating positive polarity and blue negative. Interpreted Moho conversions are marked by the black line, and the base of the ophiolite by the dotted grey line. The histogram above denotes the number of traces contributing each stack. Depth conversions displayed on the right have been completed using the *iasp91* velocity model.

3.12.3 *H* - *k* stacking profiles

While the individual $H-k$ stacking results provides us with more reliable depth points to use in later modelling, the scatter and erratic nature of some results make it more difficult to see the broader structure.

In an attempt to obtain the best of both worlds (the receiver function profile and $H-k$ stacking) we built $H-k$ stacking profiles using the stacked traces from the receiver function profiles shown above. This has the advantage of grouping traces together from multiple stations if their projected piercing points overlap, and maintains the lateral coherency necessary to identify consistent interfaces. $H-k$ stacking showed that high amplitude results were available for a wide range of k-values. Selecting a k-value at which to display a profile is therefore challenging, and we instead display each profile at 0.3 increments to show the effect of varying k on structure.

The $H-k$ stacking profile of D1 is displayed in Figure 3.47. The mid-crustal conversion in the western foreland shows a strong lateral coherency, particularly at high k-values, and appears to delineate an eastward shallowing basin structure. The likely Moho conversion observed at the western margin of the basin dies out rapidly eastwards, and appears to be most coherent at mid k-values. A weaker potential Moho signal reappears at the western margin of the mountains from $50-80\ km$, appearing to show a small flexural root, before rapidly shallowing and dying out. The negative polarity phase observed beneath the ophiolite shows a linearly dipping interface from $\sim 80\ km$ onwards. It could be mapped with either a high, mid, or low k-value, so it is difficult to know which depth range to favour. This structure appears to be echoed with a positive, and a negative polarity interface below it. It is unclear whether or not these represent real structures.

The $H-k$ stacking profile of D4 is displayed in Figure 3.48. The negative polarity conversion on the eastern end of the conversion dominates the $H-k$ results, and appears more coherent with a high k-value. In contrast to D1, this interface appears to be relatively flat at from $38-48\ km$, before rapidly increasing in depth eastwards. The likely Moho conversion is strongest at the western end of the profile, and appears

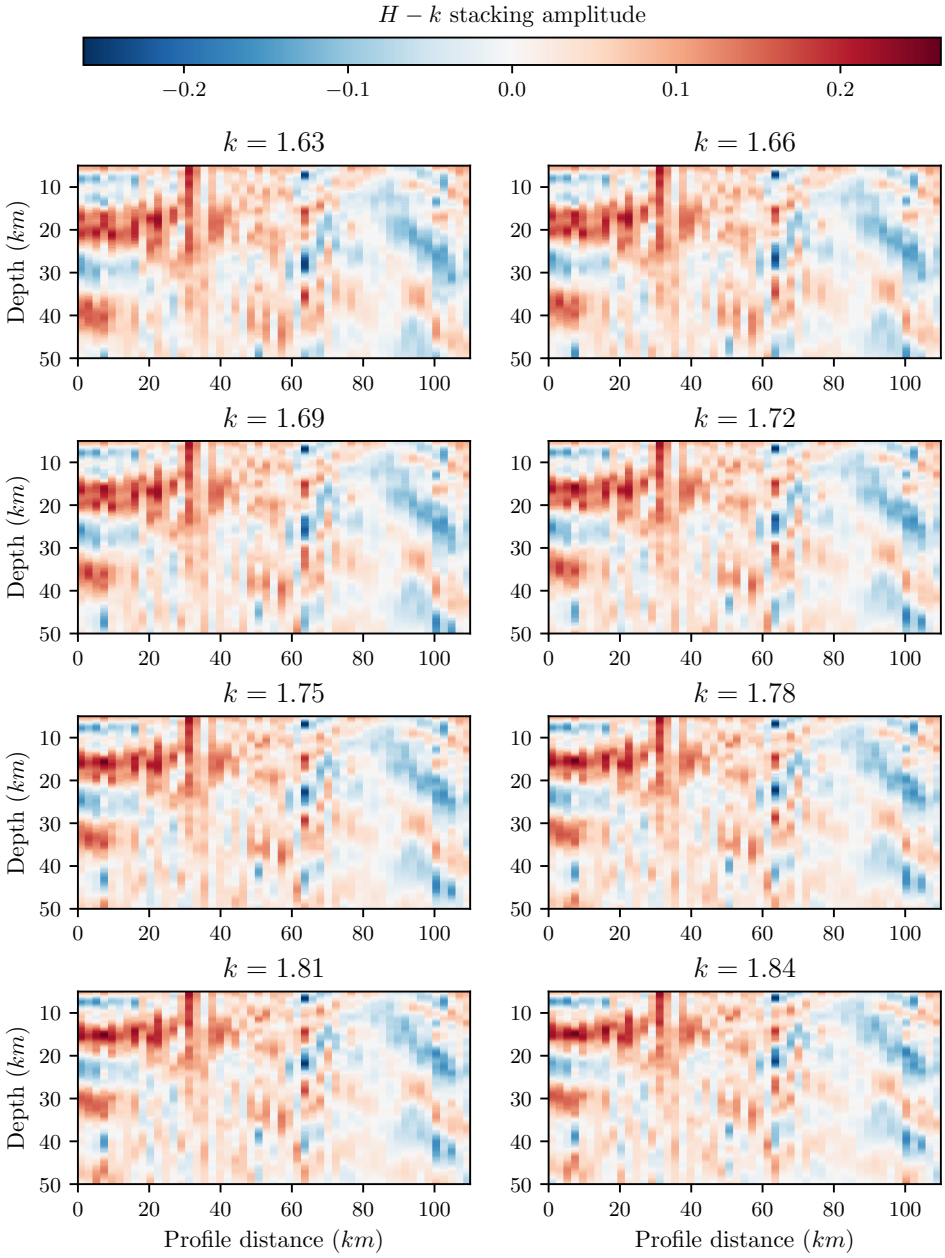


Figure 3.47: $H-k$ stacked traces along profile D1 for a range of k values. Generated from $H-k$ stacking the stacked traces of 1.5 Hz MTC receiver function profiles generated in Section 3.12.

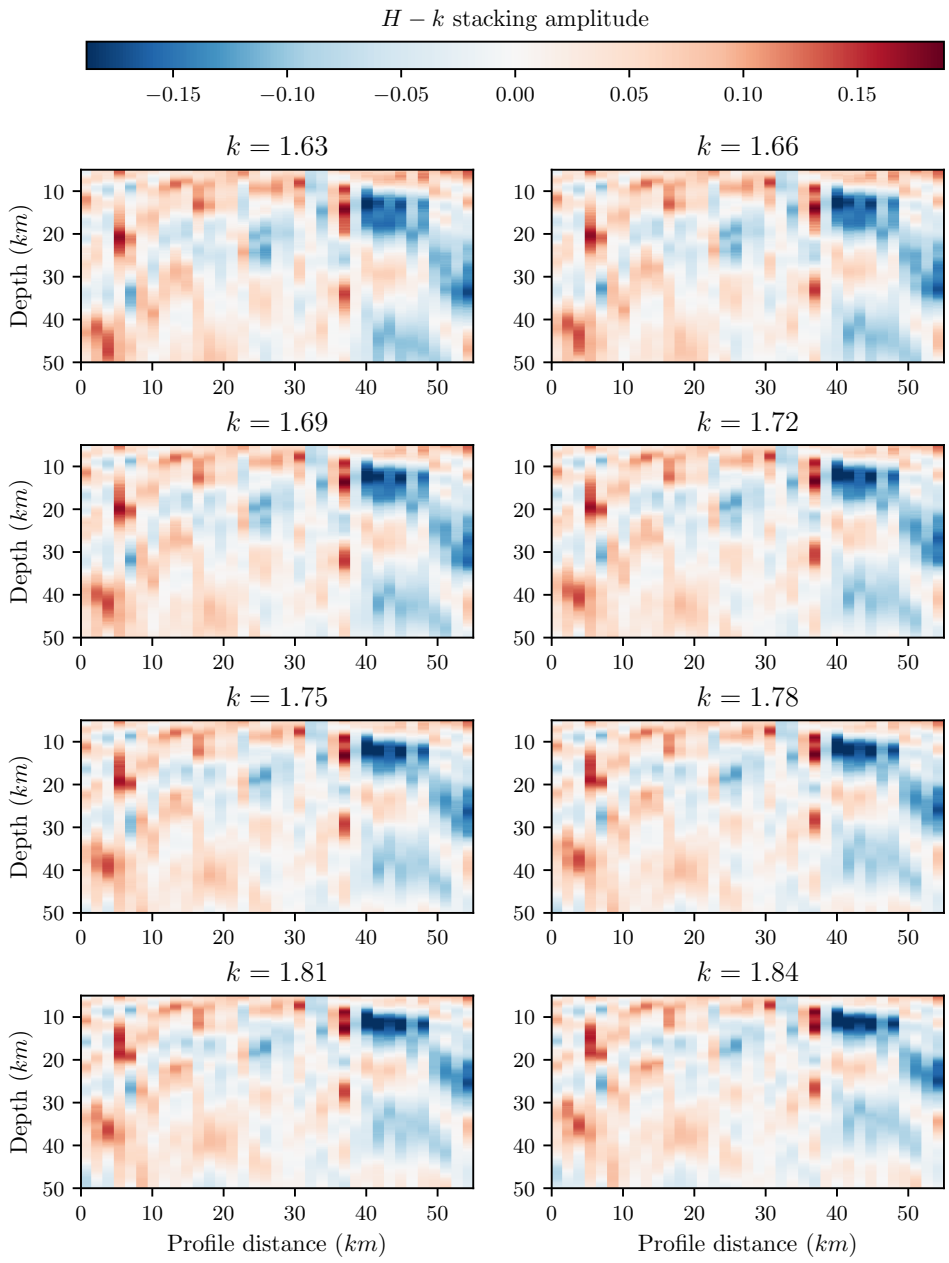


Figure 3.48: $H-k$ stacked traces along profile D4 for a range of k values. Generated from $H-k$ stacking the stacked traces of 1 Hz MTC receiver function profiles generated in Section 3.12.

again appears to delineate a small flexural root between $0-25$ km, before dying out.

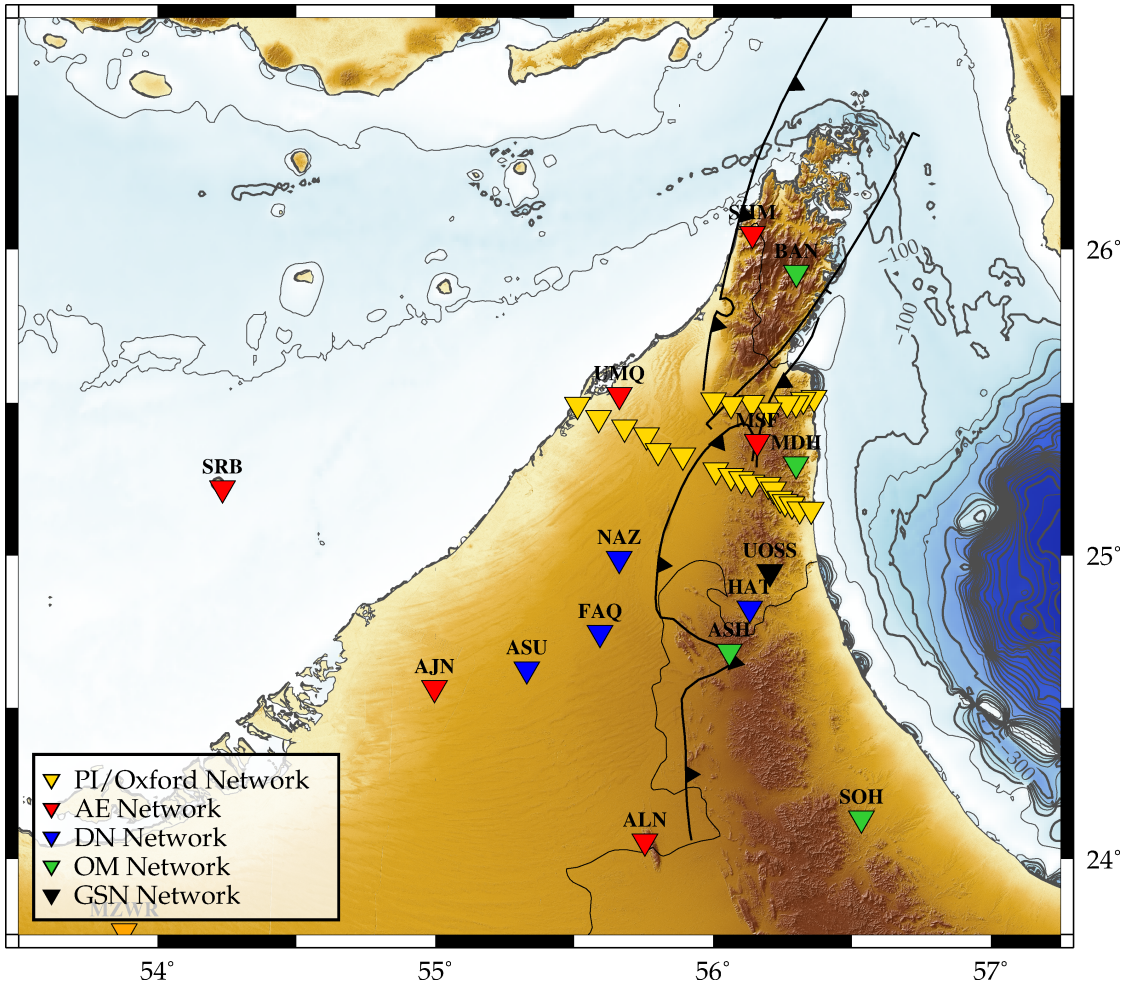


Figure 3.49: The seismic networks of the National Centre for Meteorology and Seismology (NCMS) in the UAE. The location of the PI/Oxford seismometer deployment is also marked for reference.

3.13 NCMS Network receiver functions

In addition to the seismic data collected across our own networks, we negotiated access to 2.5 years worth of data (01/06/2014 – 31/12/2016) from the networks managed by the National Centre for Meteorology and Seismology (NCMS) of the UAE. Their seismic database includes data from a number of networks across the region, with stations from the AE (Abu Dhabi), DN (Dubai), OM (Oman) Networks in the vicinity of our study area. There is also a single GSN site (UOSS) that is maintained and operated by the University of Sharjah. The stations in these networks are shown in Figure 3.49.

Receiver functions were calculated at all NCMS stations in our study area with results varying dramatically, both within and between stations. Some sites showed significant variation with back-azimuth or epicentral distance, with receiver functions from the east and west differing significantly in some cases (e.g. AE.ALN, DN.FAQ, DN.HAT, OM.ASH). At some sites very few results passed our QC tests, and the results that did typically were inconsistent and of poor quality across all deconvolution methods (e.g. AE.MSF, DN.ASU, OM.BAN). At others, large numbers of high quality, consistent results were obtained with clear mid-crustal and Moho phases present.

In general, three key phases were observed: A positive polarity mid-crustal phase was observed in the foreland, with $H-k$ stacking mapping its depth to between 9 and 17 km (AE.AJN, AE.ALN, AE.SHM, AE.UMQ, DN.FAQ, DN.NAZ, OM.ASH); A negative polarity mid-crustal phase observed across the ophiolite mapped to between 10 and 22 km (DN.HAT, OM.MDH, OM.SOH); And a Moho phase observed that was sporadically observed across the region. This phase was mapped to a depth of $33-38$ km in the foreland (AE.AJN, AE.ALN, AE.SHM, DN.NAZ), and 47.5 km at DN.HAT.

Encouragingly, these phases echo the most prominent results obtained across the PI/Oxford network. Representative examples of these phases are presented below.

3.13.1 AE.UMQ

Station UMQ is located just north of our D1 seismometer profile, and as such provides a useful comparison point to the data acquired here from the PI/Oxford network. 273 events were recorded in our search range, and just under half of these (49.08%) passed SNR thresholds for analysis. Results were calculated on all deconvolution methods, with only the TD method producing consistent, good quality receiver functions. These results were passed through our automatic quality control algorithms, and 31 (23.13%) were deemed to be of high enough quality for further analysis.

The results observed at UMQ are complex, with a number of strong phases observed, and there did not appear to be any strong variation with back azimuth or epicentral

distance. $H - k$ stacking revealed that the peak at ~ 2 s was the most dominant phase, with the later strong phase at ~ 6 s mapped as a $PpPs$ multiple. This phase was mapped to a depth of 16.34±0.18 km, with a k-value of 1.69±0.02 (see Figure 3.50).

3.13.2 DN.NAZ

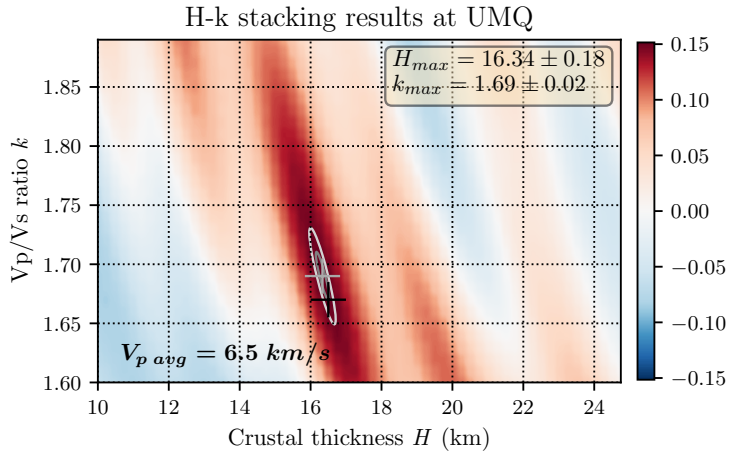
Station NAZ is located in the emirate of Dubai near the town of Naswa (where our absolute gravity station is located). It is located ~ 45 km south of our southern profile D1, but adds useful constraints for the structure of the foreland. 337 events were recorded here, and 70% of these passed the initial SNR threshold. Good quality, consistent results were obtained with all deconvolution methods, with the MTC method judged to be the best. These results were passed to our automatic quality control algorithms (with a slightly more restrictive Q/T energy ratio test of 2), and 76 (32.2%) were deemed to be high enough quality for further interpretation.

The most dominant observed phase at NAZ was a high amplitude phase at ~ 4.5 s, a clear candidate for a Moho conversion. $H - k$ stacking was applied to these QC'd traces, and bootstrapping was applied to estimate uncertainties. The result was an estimated depth of 36.73 ± 0.28 km, with a k-value of 1.756 ± 0.007 (see Figure 3.51).

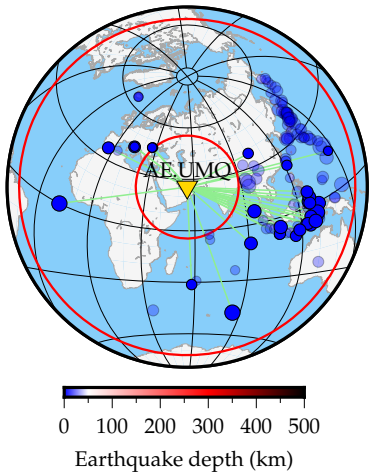
3.13.3 OM.MDH

Station MDH is located in the town of Madha in the Omani enclave, near the metamorphic sole exposures of Bani Hamid. 229 events were recorded here, and the majority of these (68.12%) passed the initial SNR thresholds. Results calculated with the MTC deconvolution method were deemed to provide the best quality results. These results were passed through our automatic quality control algorithms, and 55 (35.26%) were deemed to be of high enough quality for further interpretation.

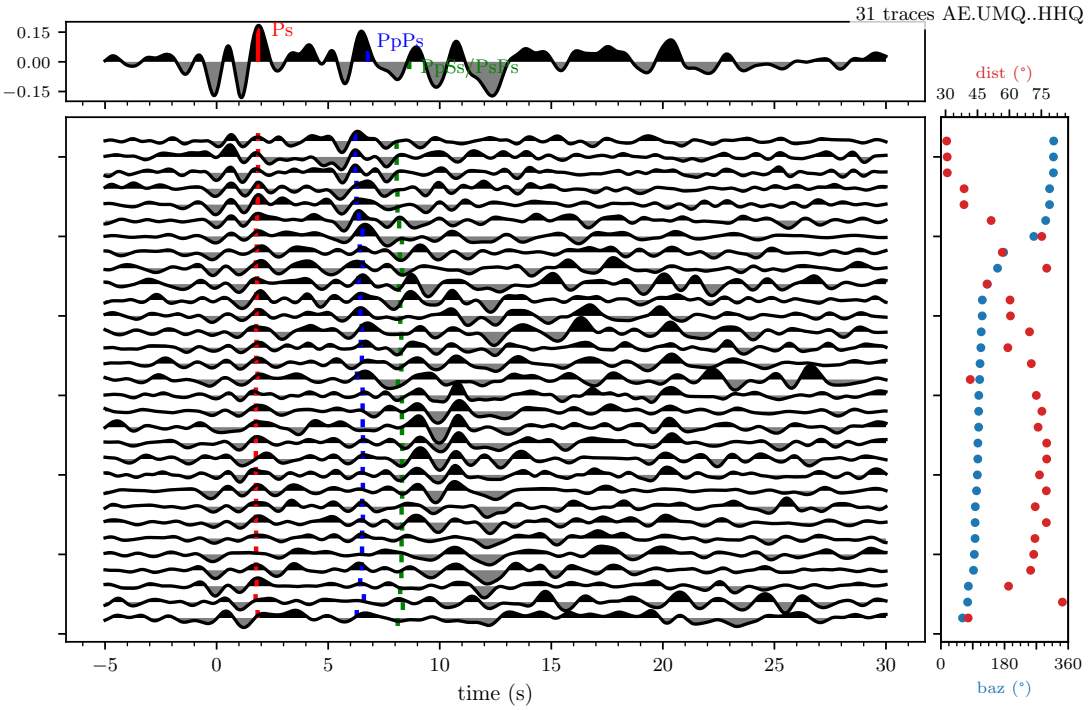
Receiver functions at MDH exhibited a broad, strong negative polarity phase at ~ 2 s, though this phase was only observed on events originating in the east. $H - k$ stacking mapped this phase to a depth of 21.33 ± 1.04 km, with a k-value of $1.685 \pm$



(a) Bootstrapped (B=50) $H-k$ stacking plot for AE.UMQ. Ellipses represent 1 and 2 bootstrap standard deviations.

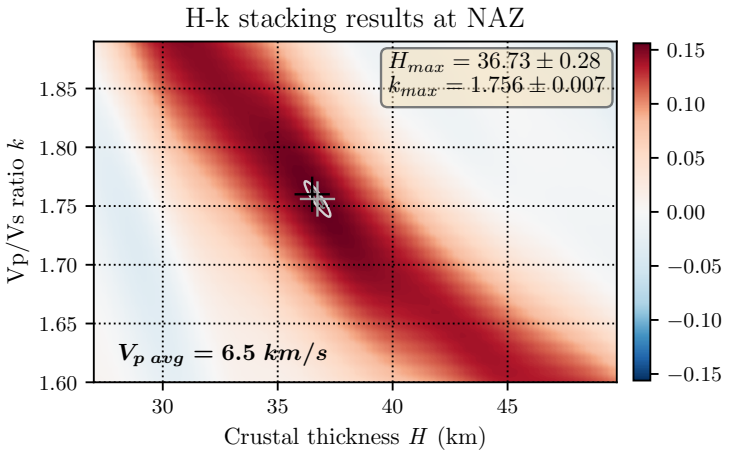


(b) AE.UMQ earthquake dataset. Unused events are faded.

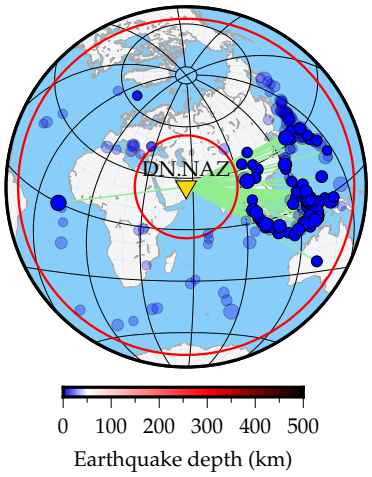


(c) Receiver functions results at AE.UMQ, sorted by back azimuth. Individual results are shown bottom and the stacked trace shown top. The locations of the phases representing the highest amplitude $H-k$ stacking result are highlighted on each trace.

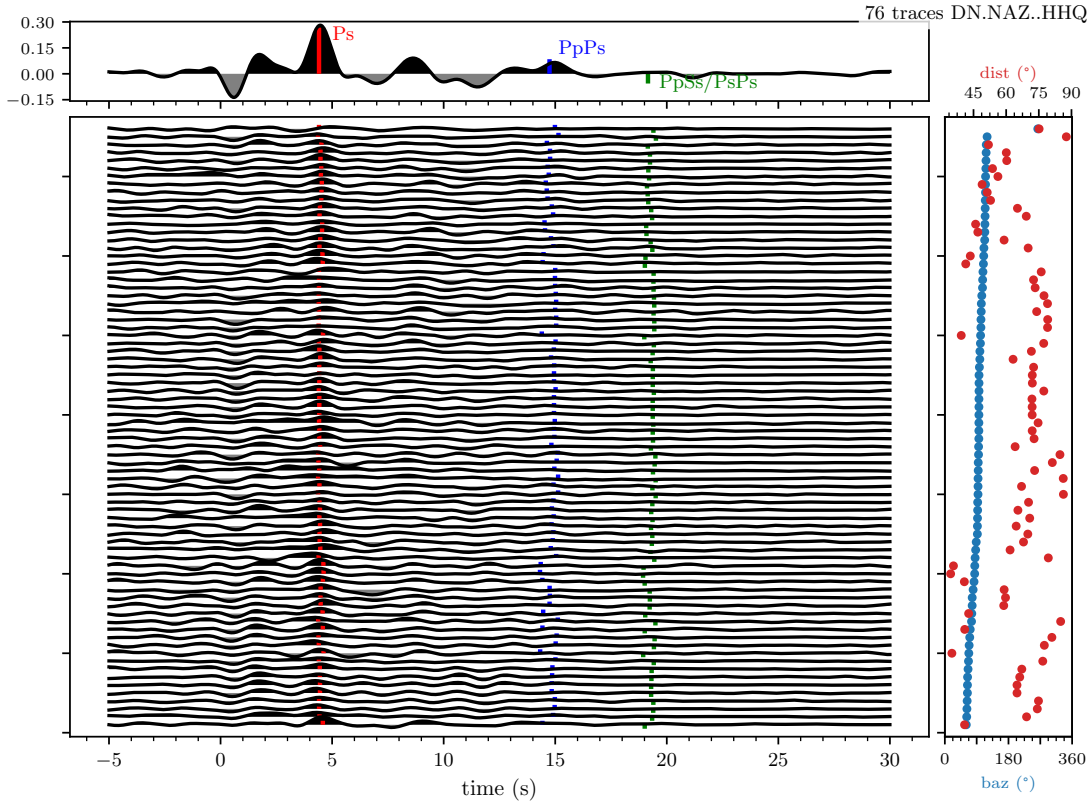
Figure 3.50: $H-k$ stacking results at the NCMS station AE.UMQ. Receiver functions are calculated using the time domain method with an upper frequency of 1 Hz. Weights of 0.5, 0.3 and 0.2 were used for w_1, w_2 and w_3 respectively. The algorithm picks out the large amplitude mid-crustal phase at $\sim 2\ s$, and its reverberations, as the most dominant set of phases, and selects an H and k value of 16.34 ± 0.18 km and 1.69 ± 0.02 respectively.



(a) Bootstrapped (B=50) $H - k$ stacking plot for DN.NAZ. Ellipses represent 1 and 2 bootstrap standard deviations.



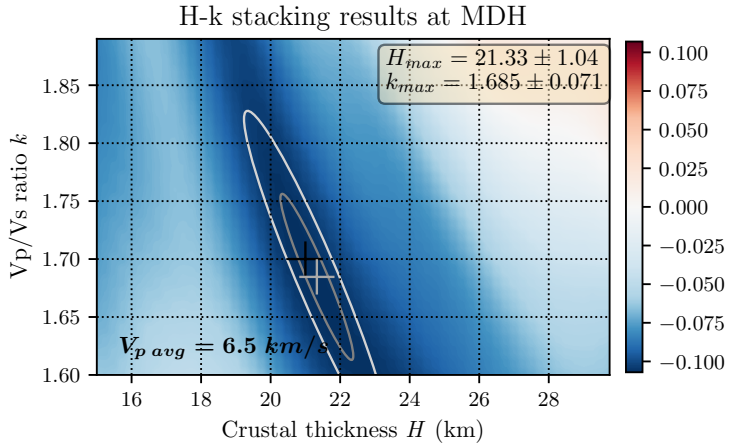
(b) DN.NAZ earthquake dataset. Unused events are faded.



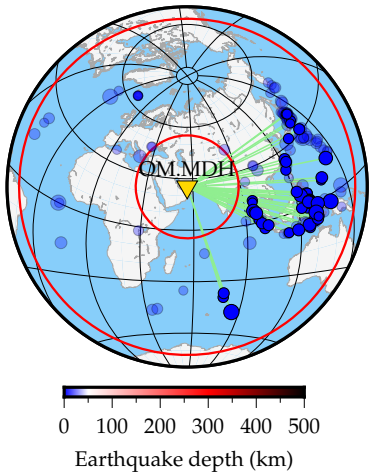
(c) Receiver functions results at DN.NAZ, sorted by back azimuth. Individual results are shown bottom and the stacked trace shown top. The locations of the phases representing the highest amplitude $H - k$ stacking result are highlighted on each trace.

Figure 3.51: $H - k$ stacking results at the NCMS station DN.NAZ. Receiver functions are calculated using the multi-taper method with an upper frequency of 1 Hz. Weights of 0.5, 0.3 and 0.2 were used for w_1, w_2 and w_3 respectively. The algorithm picks out the large amplitude Moho phase at ~ 4.5 s, and its reverberations, as the most dominant set of phases, and selects an H and k value of 36.73 ± 0.28 km and 1.756 ± 0.007 respectively.

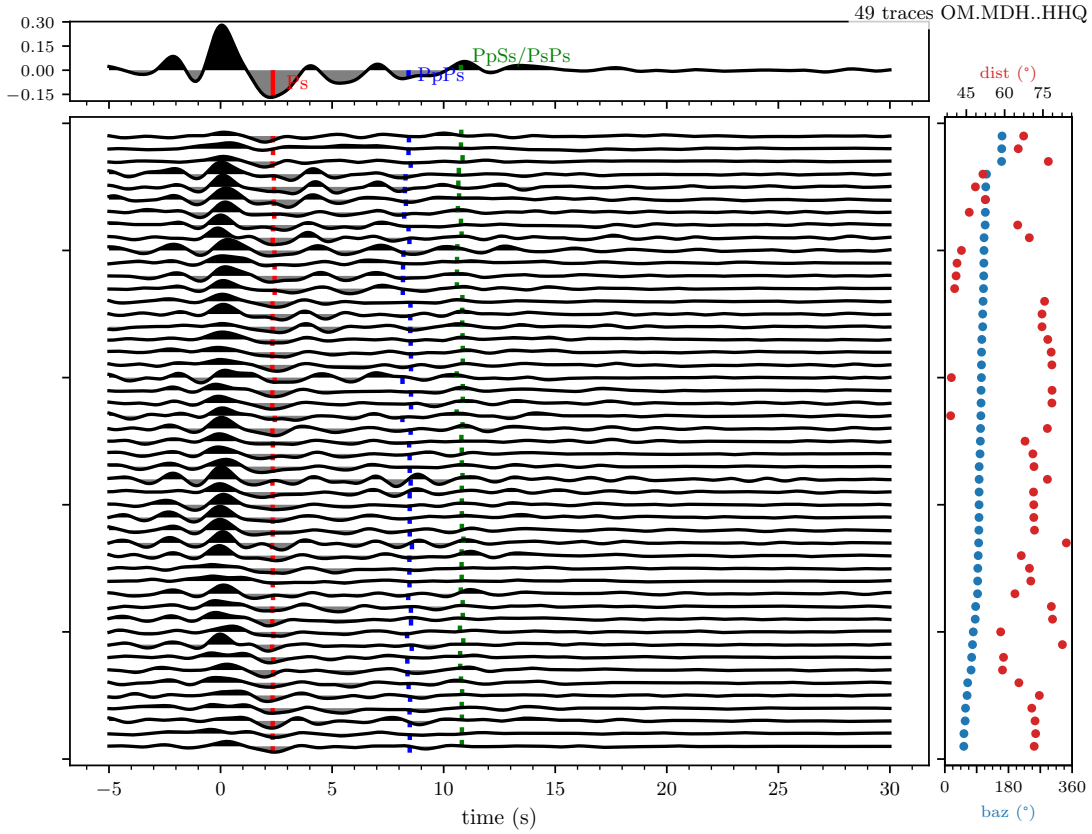
0.071. This is most likely that a conversion from the base of the ophiolite, and if this is the case the ophiolite must plunge very rapidly east of Bani Hamid.



(a) Bootstrapped (B=50) $H-k$ stacking plot for OM.MDH. Ellipses represent 1 and 2 bootstrap standard deviations.



(b) OM.MDH earthquake dataset. Unused events are faded.



(c) Receiver functions results at OM.MDH, sorted by back azimuth. Individual results are shown bottom and the stacked trace shown top. The locations of the phases representing the highest amplitude $H-k$ stacking result are highlighted on each trace.

Figure 3.52: $H-k$ stacking results at the NCMS station OM.MDH. Receiver functions are calculated using the multi-taper method with an upper frequency of 1 Hz. Weights of 0.5, 0.3 and 0.2 were used for w_1, w_2 and w_3 respectively. The algorithm picks out the large amplitude negative polarity phase at ~ 2 s, and its reverberations, as the most dominant set of phases, and selects an H and k value of 21.33 ± 1.04 km and 1.685 ± 0.071 respectively.

3.14 Discussion

Calculating receiver functions for this project proved to be a challenging process, with many difficulties needing to be overcome in order to obtain good quality, reliable results. From preparing and collating the raw seismic data, to setting up, testing, and calibrating existing codes, to building on those codes with our own modifications, and interpreting the final results.

Our study area was particularly challenging for a few reasons: Receiver function studies ideally require a simple, laterally homogenous velocity structure, and a dominant converting interface (usually the Moho) to clearly image structures beneath a station. Large numbers of high quality results are also typically stacked to improve the signal to noise ratio and reduce the risk of interpreting spurious phases. The results presented for station DN.NAZ provide a good example of a station where these conditions appear to be met (see Figure 3.51), but in general our results were complicated by strong mid-crustal conversions, multiple converted phases, strong variations with back azimuth and epicentral distance, and low numbers of 'good quality' results at many stations.

We have converted our receiver function results from time to depth using the $H-k$ stacking method. This is a well established method that automates much of the process and reduces the potential for bias in the interpretation. The presence of multiple shallow phases often complicated this process however, and identifying clear reverberated $PpPs$ and $PsPs/PpSs$ phases was often not possible as multiple options were available. This led to a large uncertainties in some cases, or to a primary Ps phase being mapped to multiple possible depth points. This trade off between k and H probably represents the largest source of uncertainty in our results.

Identifying lithologies from k-values is difficult, as there can be a significant amount of overlap between groups. However some general observations from published k-values provide useful guides. Unconsolidated, saturated, and calcareous sediments, such as those present in the western foreland, often have an elevated k-value compared to a typical crustal value of ~ 1.75 (*Hamilton*, 1979; *Christensen*, 1996). This provides some

support for high k-values for the mid-crustal interface. Water and sediment saturated basalts, along with many gabbroic rocks likely to be present in the obducted ophiolite have also been reported to have elevated k-values (*Christensen and Salisbury*, 1975; *Musacchio et al.*, 1997), again providing support to the high k-values favoured for the reverse polarity conversion observed below the ophiolite (particularly on D4).

Our results could be broadly divided into two categories based on their underlying tectonic regime: The foreland basin; and the UAE-Oman mountains, which are dominated by the obducted Semail ophiolite complex.

Receiver functions in the foreland (S-01 - S-06) were dominated by a strong, undulating, laterally continuous, mid-crustal conversion that was mapped to between 14 and 19 km depth with $H - k$ stacking. This phase could be mapped with a wide range of k-values, leading to a significant uncertainty in its actual depth, but a higher k-value (and lower depth) was favoured by the expected lithologies, and yielded a more coherent interface. This interface may represent a transition from the base of the 'slow' foreland sedimentary sequence, to faster basement below. Even at the lower end of its possible depth ranges, this is deeper than previously published values of $7 - 11$ km for this basin (*Stern and Johnson*, 2010; *Naville et al.*, 2013; *Tarapoanca et al.*, 2013; *Ali et al.*, 2014, 2017), suggesting it may be deeper than previously thought.

A possible Moho conversion was also sporadically imaged at these stations, with its depth mapped to ~ 36 km in the western foreland, and increasing slightly to ~ 40 km towards the mountains in the east.

S-07 was the first station east of the Semail thrust, and marked the start of a notable change in character in our receiver function results. The signal to noise ratio generally improved (see Figure 3.6), but there was a poorer Q/T energy ratio indicating a higher degree of scattering. Receiver functions were also notably more complex, with more shallow conversions and the rise of a dominant negative polarity phase at the many stations indicating a 'slow to fast' conversion. We have interpreted this phase to be a conversion from the 'slow' underlying continental crust to the 'fast' obducted oceanic crust and upper mantle of the Semail ophiolite, and it therefore marks the base of this

unit. On the southern profile D1, this interface dipped linearly eastwards at $\sim 30°$, to increase from $\sim 10\ km$ depth near Masafi to $\sim 25\ km$ depth below Fujairah at the coast. On the northern profile D4 this appeared to be relatively flat at $\sim 10\ km$ depth west of S-20, before rapidly dropping down to $\sim 20\ km$ further east.

Results east of the Semail thrust and beneath the UAE-Oman mountains also lacked a clear Moho phase, with some stations offering multiple potential candidates and some offering none. In general, these potential Moho results described either a shallow, flat Moho interface between $25 - 35\ km$ depth, or a deep flexed Moho in excess of $40\ km$ depth that shallows rapidly east of Masafi. We believe the flexed result is more likely given the Moho trend observed in the foreland.

These results reveal previously unknown aspects of the mid to lower crustal structure in both the western foreland, and the UAE-Oman mountains with the obducted Semail ophiolite. The results contain a lot of uncertainty however, with the depths provided by $H - k$ stacking influenced by estimated stacking velocities and the inherent trade-off between H and k.

3.15 Chapter Summary

In this chapter we have have introduced the receiver function method, described and compared the various deconvolution options, and introduced the $H-k$ stacking method, a technique to convert receiver function results from time to depth. These methods have been applied to temporary and permanent seismic station across the north and east of the UAE to yield information on the crustal structure in the foreland basin and UAE-Oman mountains. The results were often complex, and varied in quality, but three key interfaces were revealed:

1. A strong, laterally consistent, undulating mid-crustal interface in the western foreland basin at $\sim 15\ km$ depth. This was interpreted as a conversion from basement the base of the foreland sedimentary sequence.

2. A strong, reverse polarity, eastward dipping interface beneath the ophiolite in the

UAE-Oman mountains to the east, interpreted as a conversion from the 'slow' continental margin to the 'fast' obducted oceanic crust and upper mantle of the Semail ophiolite. On D1 this interface dips linearly at $\sim 30°$ increasing from $\sim 10\ km$ east of Masafi, to $\sim 25\ km$ depth near the Gulf of Oman coastline. To the north on D4 it appeared to be relatively flat at $\sim 10\ km$ depth west of S-20, before rapidly stepping down to $\sim 25\ km$ depth towards the coast.

3. Strong Moho candidates were also sporadically imaged in the foreland, suggesting a likely depth of $\sim 36\ km$ here. Weaker Moho candidates east of the Semail thrust suggested the presence of a small flexural root beneath the western UAE-Oman mountains, that then rapidly thinned eastwards.

Chapter 4

Gravity

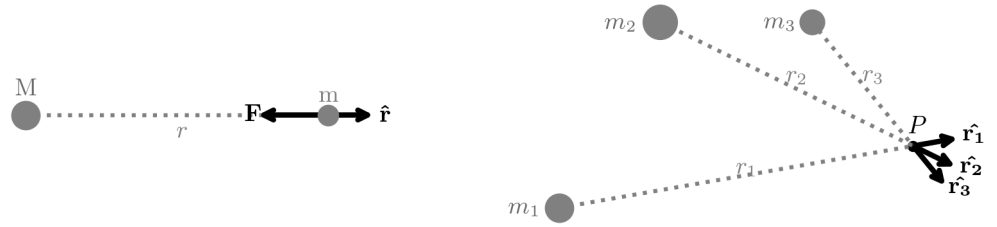
4.1 Introduction

In this chapter we will introduce the force of gravity, as it relates to geophysical exploration. We describe the process of reducing gravity observations to gravity anomalies, and explain the various corrections required. We will then discuss the gravity data acquired during this project, both marine and terrestial, and explain the steps taken to reduce these datasets to free-air and Bouguer anomalies respectively. The datasets will then be combined, and their general features and their implications discussed.

4.2 The gravitational force

Gravity, as it is applied to geophysics and geophysical exploration, is derived from classical *Newtonian* mechanics. Newton's universal law of gravitation states that every body generates a force of attraction to every other body, and that the magnitude of this force is proportionate to the product of their masses, and inversely proportional to the square of the distance between their respective centres of mass (Figure 4.1a). Mathematically this can be expressed as:

$$\mathbf{F} = -\frac{GMm}{r^2}\hat{\mathbf{r}} \tag{4.1}$$



(a) Point masses. **(b)** Multiple sources.

Figure 4.1: (a) The gravitational attraction associated with two points masses. **(b)** The cumulative gravitational attraction of multiple point masses at P. After *Lowrie* (2007).

where M and m are the masses of the respective particles, r is the distance between their centre of masses, G is a scalar known as the universal gravitational constant, and $\hat{\mathbf{r}}$ is a unit vector pointing in the direction of increasing r. The minus sign indicates that the force is an attractive force and operates in the opposite direction to $\hat{\mathbf{r}}$.

The gravitational constant G cannot be obtained theoretically and is determined via empirical observations. The *Committee on Data of the International Council for Science* (CODATA) 2016 publication lists 14 independent, experimentally derived values of G. It has a value of approximately $6.674 \times 10^{-11}\ m^3\, kg^{-1}\, s^{-2}$ (*Mohr et al.*, 2016).

In geophysics we are interested in the acceleration an object experiences due to gravity rather than the force. Newton's second law of motion states that the force experienced by an object is equal to its mass (m) times its acceleration ($\mathbf{a}$).

$$\mathbf{F} = m\mathbf{a} \tag{4.2}$$

Equating this to Equation 4.1 shows that the acceleration $\mathbf{a}$, experienced by an object of mass m due to the gravitational force of another body of mass M is

$$\mathbf{a} = -\frac{GM}{r^2}\hat{\mathbf{r}} \tag{4.3}$$

The acceleration experienced by a body due to a gravitational force is therefore independent of its mass, a phenomenon famously demonstrated by Galileo at the Leaning Tower of Pisa in 1590 (*Segre*, 1989).

4.2.1 Gravitational potential energy

An object in a gravitational field has gravitational potential energy. This potential energy is converted to work when the object is moved as a result of this field. For example when an apple falls from a tree its gravitational potential energy is converted to kinetic energy as it accelerates towards the ground. The amount of gravitational potential energy lost (dE_p) is equal to the force required to restore the apple to its original position by a moving it a distance dr against the gravitational field. This can be expressed mathematically as:

$$-dE_p = \mathbf{F} \cdot d\mathbf{r} \tag{4.4}$$

If the gravitational potential energy of a unit mass is U_G, then the change in potential energy of an object of mass m in a gravitational field is

$$dE_p = mdU_G = -m\mathbf{a} \cdot d\mathbf{r} \tag{4.5}$$

Rearranging this equation for a and equating it to Equation 4.3, we see that gravitational acceleration can be expressed as the gradient of the gravitational potential energy U_G.

$$\mathbf{a} = -\frac{dU_G}{d\mathbf{r}} = -\frac{GM}{r^2}\hat{\mathbf{r}} \tag{4.6}$$

Integrating equation 4.6 shows that gravitational potential energy takes the form

$$U_G = -\frac{GM}{r} \tag{4.7}$$

Reformulating gravity in the form of potential energy greatly simplifies the math-

ematics when dealing with the gravity field associated with heterogeneous bodies or multiple sources. For example, calculating the gravitational acceleration resulting from multiple point masses (Figure 4.1b) at location P requires a potentially complex vector sum.

$$\mathbf{a} = -\frac{Gm_1}{r_1^2}\hat{\mathbf{r_1}} - \frac{Gm_2}{r_2^2}\hat{\mathbf{r_2}} - \frac{Gm_3}{r_3^2}\hat{\mathbf{r_3}} - ... \tag{4.8}$$

A simpler approach is to first calculate the combined gravitational potential of these masses, which is simple scalar sum, and compute its gradient to find the resulting gravitational acceleration at P.

$$U_G = -\frac{Gm_1}{r_1} - \frac{Gm_2}{r_2} - \frac{Gm_3}{r_3} - ... \tag{4.9}$$

$$\mathbf{a} = \nabla U_G \tag{4.10}$$

This approach can be generalised to arbitrarily shaped bodies, provided their density distributions are known. If $\rho(x, y, z)$ represents the bodies mass distribution, and $r(x, y, z)$ describes the respective distance from P, the gravitational potential of the body at P is

$$U_G = -G \int_x \int_y \int_z \frac{\rho(x, y, z)}{r(x, y, z)} dxdydz \tag{4.11}$$

4.2.2 The Earth's gravity

In the case of a homogeneous solid sphere the integral in Equation 4.11 reduces to Equation 4.7 for reference points outside of the sphere. That is, the gravitational potential for a homogeneous sphere is the same as the gravitational potential of an equivalent point mass located at its centre.

The acceleration produced as a result of the Earth's gravitational field ($\mathbf{g}$) is there-

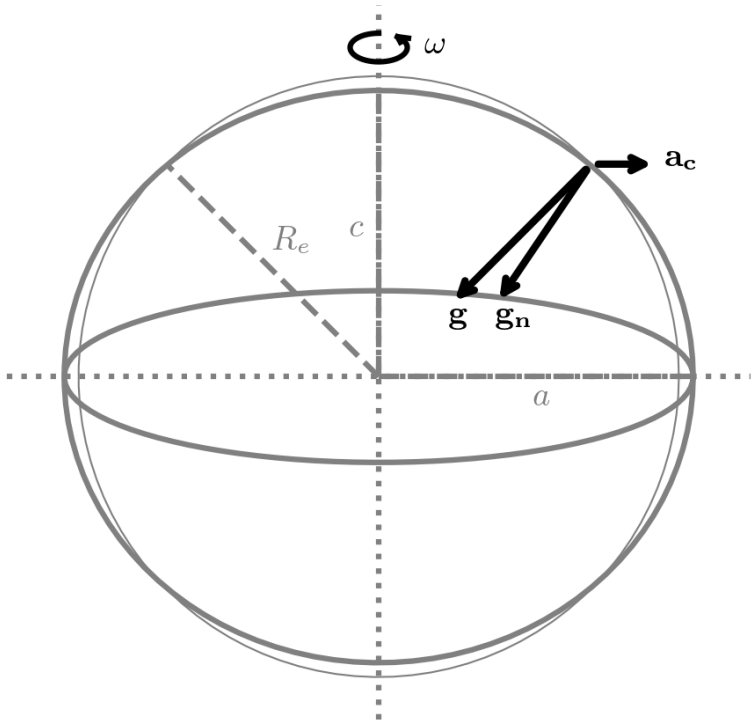


Figure 4.2: An exaggerated plot of the *International Reference Ellipsoid*, plotted with a sphere for comparison. The equatorial, polar and mean radius of this ellipsoid are represented by a, c, and R_e respectively. Black vectors show the gravitational ($\mathbf{g}$) and centrifugal ($\mathbf{a_c}$) contribution to normal gravity ($\mathbf{g_n}$) at 45° latitude.

fore

$$\mathbf{g} = -\frac{GM_e}{R_e^2}\hat{\mathbf{r}} \tag{4.12}$$

where M_e and R_e denote the Earth's mass and mean radius respectively. The Earth has a mass of $5.974 \times 10^{24}\ kg$ and a mean radius of 6371 km. Substituting these numbers into Equation 4.13 gives an acceleration of 9.82 $m\,s^{-2}$, a value very close to Earth's mean gravity ($g_m = 9.81\ m\,s^{-2}$).

The Earth is neither homogeneous, nor a perfect sphere however. The shape of the Earth is better approximated by a rotating oblate ellipsoid known as the *International Reference Ellipsoid* (Figure 4.2). The ellipsoid can be characterised by its equatorial and polar radii a and c, or alternatively by its flattening parameter f, defined as:

$$f = \frac{a - c}{a} \tag{4.13}$$

The parameters a and c can be determined by geodetic observations. The *Geodetic Reference System* of 1980 (*GRS80*) defined them as $a = 6378.137\ km$ and $c = 6356.752\ km$, giving a flattening parameter of $f = 1/298.252$. The radius of the Earth is therefore some 21 km greater at the equator than at the poles, with the centrifugal force associated with the Earth's rotation being the primary cause for this equatorial bulge.

The gravitational acceleration experienced on the surface of a rotating ellipsoid was first derived by *Clairaut* (1743) in what is known as *Clairaut's theorem*. His formula allows us to compute 'normal gravity' (g_n), the theoretical gravitational field produced by a rotating reference ellipsoid, as a function of latitude (λ).

$$g_n(\lambda) = g_e(1 + \left(\frac{5}{2}m - f\right)\sin^2\lambda) \tag{4.14}$$

Where g_e is mean equatorial gravity and m is the ratio of centrifugal to gravitational acceleration at the equator. Today this formula has largely been supplanted by *Somigliana's formula* (*Somigliana*, 1929)

$$g_n(\lambda) = g_e\left(\frac{1 + k\sin^2\lambda}{\sqrt{1 - f^2\sin^2\lambda}}\right) \tag{4.15}$$

where k is $\frac{g_p b - g_e a}{g_e a}$ and g_p is polar gravity. A truncated expansion of this formula is commonly used in its place to compute normal gravity. To a second order this expansion is

$$g_n(\lambda) = g_e(1 + \beta_1\sin^2\lambda + \beta_2\sin^2 2\lambda) \tag{4.16}$$

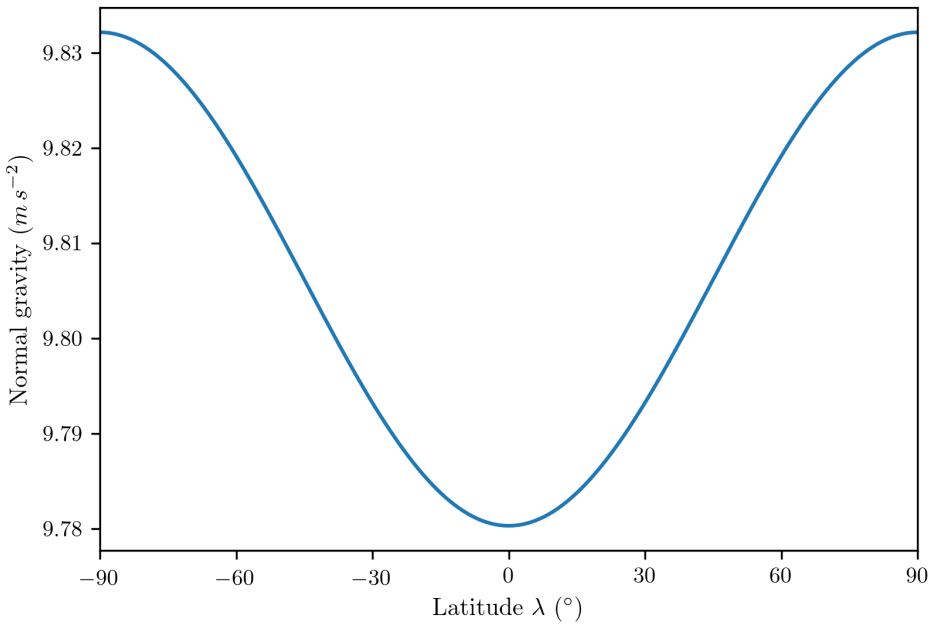


Figure 4.3: 'Normal gravity' (Equation 4.16) as a function of latitude.

where β_1 and β_2 are constants associated with f and m. This expression was adopted by *GRS80* as the formula for normal gravity, with the values adopted for the constants listed as $g_e = 9.780327\ m\,s^{-2}$, $\beta_1 = 5.30244 \times 10^{-3}$, and $\beta_2 = -5.8 \times 10^{-6}$. We use Equation 4.16, and adopt these same values to compute normal gravity for this project.

Normal gravity, as defined by Equation 4.16, is shown in Figure 4.3. It shows that Earth's gravity is some $\sim 0.05\ m\,s^{-2}$ stronger at the poles than the equator. This equatorial decrease is due to both the greater influence of the centrifugal force at lower latitudes, and the increased separation from the Earth's centre of mass due to the greater equatorial radius. However, the decrease in gravity associated with these factors is tempered by the additional gravitational pull associated with added mass of the equatorial bulge.

The reference ellipsoid is an example of a theoretical equipotential surface, in which gravity is always normal to its surface. The true equipotential surface of the Earth is known as the *geoid*, and it differs from the theoretical surface due to heterogeneous

mass distributions within the Earth. The geoid represents a reference datum, to which gravity observations are reduced. In the open ocean, the geoid is delineated by the unperturbed free ocean surface, or sea level in the absence of any atmospheric or oceanographic effects. For most purposes this can be safely approximated as mean sea level. On land it is more difficult to map, as it requires a large number of accurate, consistent gravity measurements across the continents. With the addition of satellite gravity data accurate global maps of the geoid are now available, such as the *Earth Gravity Model* 2008 (*EGM2008*, *Pavlis et al.* (2012)).

4.3 Measuring gravity

Gravity measurements can be divided into two broad categories: Absolute gravity measurements, in which the precise acceleration due to gravity is measured directly; and relative gravity measurements, in which measurements of the variation in gravity from place to place are obtained.

Absolute gravity measurements were originally obtained by precisely measuring the period of a pendulum, as the period of oscillation (T) for a pendulum of length L is related to gravity (g) by

$$T = 2\pi\sqrt{\frac{L}{g}} \tag{4.17}$$

The limitations of this method were the consistency required of the equipment, and its requirement for highly accurate determination of period ($\delta T \approx 0.5\ \mu s$ for a sensitivity of 1 $mGal$). The pendulum method remained a common method of determining gravity until the 1950's, after which more accurate methods became available. (*Lowrie*, 2007).

Modern absolute gravimeters operate by directly measuring the free-fall time of a mass in an evacuated chamber using laser interferometry to precisely measure its location with time.

Application of absolute gravimeters to geophysical surveys are limited by their

portability, with the equipment typically being too bulky for rapid transportation and operation around a field area. Geophysical gravity data is therefore generally acquired using relative gravimeters.

Relative gravimeters are based on the concept of a zero-length spring. A mass m suspended from a spring will cause the spring to extend under the force of gravity

$$F = mg = -k(s - s_0) \tag{4.18}$$

where s_0 and s is the original and extended spring length respectively, and k is the elastic constant of the spring. A zero-length spring is designed so that its un-extended length is theoretically zero ($s_0 = 0$). The restoring force on the spring is then directly proportional to the gravitational force. Gravimeters based on this principle attach a mass to a horizontal beam that is suspended against gravity with a zero-length spring. A calibration wheel is attached with the ability to adjust the tension on the spring. When the device is placed on level ground the beam can be adjusted to a neutral position by adjusting the tension on the spring. The difference in the number of calibration units required to neutralize the position of the spring between two measurement locations is then directly proportional to the difference in gravity between those localities.

Relative gravimeters are more compact, and simpler to operate than absolute gravimeters, but they are limited in that they do not measure gravity directly. They must therefore be tied to a site where absolute gravity is known before a survey can take place.

4.4 Gravity anomalies

The gravitational acceleration we experience and measure on the Earth's surface is influenced by a number of additional factors unrelated to the Earth's ellipsoidal shape. The most important of these are elevation, topography, tidal effects, and variations in density within the Earth's subsurface. With the exception of internal variations in

density, these factors are known quantities, and their effects can be calculated and accounted for. This allows us to reduce a gravity observation to a theoretically equivalent observation on the geoid. A gravity anomaly is the difference between this reduced observation and 'normal gravity', and can be interpreted in terms of variations in density in the subsurface.

There are several types of gravity anomaly, and they are defined in terms of what factors have been corrected for, in addition to core corrections: The free-air anomaly corrects for an observation's elevation relative to the geoid; the Bouguer anomaly corrects a free-air anomaly for the effects of topography above and below the geoid, and an isostatic anomaly corrects a Bouguer anomaly for the isostatic compensation of topography.

These gravity anomalies are typically on the order of $10 - 100 \times 10^{-5}\ m\,s^{-2}$. As such, gravity anomalies are typically measured in units of milliGals ($mGal$), where 1 Gal (after Galileo Galilei) is equal to 1 $cm\,s^{-2}$.

These gravity anomalies, and the corrections required to obtain them are described in the following sections.

4.4.1 Tidal corrections

The gravitational pull of both the Sun and the Moon have a small but important effect on the Earth's gravitational field. The lunar tide can be readily seen in the oceans, as it causes mean sea level to rise and fall. It has a similar effect on the solid Earth, causing small but measurable deformation in the Earth's shape. Solar tides operate in much the same way as the lunar tides, though their period is significantly longer (1 year).

These tidal effects taken together amount to only 0.3 $mGal$ (*Lowrie*, 2007). Since their mechanism is well understood and predictable, removing tidal effects from gravity measurements is relatively straightforward. The Scintrex CG-5 used for our onshore gravity survey performed tidal corrections automatically using Longman's formulas (*Longman*, 1959).

4.4.2 Eötvös correction

Objects on the surface of the Earth experience a centrifugal acceleration due to the Earth's rotation that acts to counteract the force of gravity. For stationary objects this is accounted for in the expression for 'normal gravity' (Equation 4.16). Moving objects will typically have an eastward (or westward) component to their velocity that will act to either increase (or decrease) their angular velocity (ω). This serves to increase (or decrease) the centrifugal acceleration associated with the Earth's rotation by

$$\Delta \mathbf{a_c} = 2\omega(R_e \cos\lambda)\Delta\omega \tag{4.19}$$

This correction is essential for any gravity survey from a moving platform, such as a ship or aircraft. For shipborne gravity surveys the magnitude of this correction is on the order of $0 - 100$ $mGal$, while the higher speed of an aircraft will result in a correction $1 - 2$ orders of magnitude higher.

4.4.3 Cross-coupling correction

An additional source of error in marine gravity surveys with beam type gravimeters can occur when the horizontal and vertical accelerations acting on a gravimeter have the same period. This can occur due to the rolling motion of a ship associated with ocean swell, and is known as the the cross coupling error. It is typically small in calm sea states, but can approach 50 $mGal$ in large swell (*Lacoste*, 1967).

4.4.4 Free-air correction

In order for gravity measurements to be comparable they need to be reduced to a common datum. It is therefore important to account for the elevation differences of gravity observations (g_{obs}) relative to the geoid. As gravity decreases with the inverse square of distance (Equation 4.3), measurements made above the geoid (generally approximated by mean sea level) will decrease accordingly. The magnitude of this reduction can be

obtained by differentiating gravitational acceleration (g) with respect to r.

$$\frac{dg}{dr} = \frac{d}{dr}\left(\frac{-GM_e}{r^2}\right) = \frac{2GM_e}{r^3} = -\frac{2}{r}g \tag{4.20}$$

As measurement elevations (h) are significantly smaller than the Earth's radius, the free-air correction (Δg_{FAC}) can be approximated as

$$\Delta g_{FAC} = -\frac{2}{R_e}g_m = -0.3086\ mGal\, m^{-1} \tag{4.21}$$

where R_e is Earth's mean radius ($R_e = 6371\ km$) and g_m is the Earth's mean gravity ($g_m = 9.81\ ms^{-2}$). A free-air gravity anomaly corrects for this reduction in gravity with elevation, and is defined as:

$$g_{FA} = g_{obs} - g_n + \Delta g_{FAC} \tag{4.22}$$

For gravity measurements made below mean sea level the gravitational acceleration conversely increases, and the sign of this correction is reversed. The free-air anomaly is the most commonly used gravity anomaly, and is the standard reduction for marine gravity surveys.

4.4.5 Bouguer correction

The free-air anomaly reduces a measurement to an equivalent observation on the geoid. However it makes no allowance for topography, and the additional gravitational attraction associated with a layer of earth or rock between the measurement point and the geoid. The attraction of this rock layer can be approximated by an infinite cylinder with thickness (h) equal to the measurement elevation. This cylinder is termed a Bouguer 'slab', named after Pierre Bouguer, who first theorized the contribution of topography to the gravity signal in 1749 (*Bouguer*, 1749). The gravitational attraction of such a cylinder, with an inner radius of zero and an our radius approaching infinity simplifies

to

$$\Delta g_{BC} = 2\pi G\rho h \tag{4.23}$$

where ρ is the density of the Bouguer 'slab'. Substituting expected mean rock densities from the measurement location gives the Bouguer correction. For typical crustal densities of 2700 $kg\,m^3$, the Bouguer correction would be $\Delta g_{BC} = 0.1132\ mGal\,m^{-1}$.

The Bouguer correction represents the contribution of additional mass above the geoid, the effect of which we want to remove in reducing our observation to its reference datum. The Bouguer anomaly is the free-air anomaly corrected for the effects of topography, and is defined as

$$g_{BA} = g_{obs} - g_n + \Delta g_{FAC} - \Delta g_{BC} \tag{4.24}$$

4.4.6 Terrain corrections

Note that the Bouguer correction, as defined above, makes no allowance for topographic variations. In this form it is referred to as a 'simple' Bouguer anomaly. Approximating the excess mass above the geoid with an infinite, flat 'slab' overestimates the contribution of topography to the gravity signal in two ways: The curvature of the Earth, and undulations in topography. A 'complete' Bouguer anomaly must also account for these factors.

The curvature of the Earth was first accounted for by *Bullard* (1936) during his survey of Africa, and is often termed the *Bullard B* correction (with the *Bullard A* correction being the flat Bouguer 'slab'). Precise formulations of this correction are presented by *LaFehr* (1991) and *Whitman* (1991). This correction is typically not more than 1.5 *mGal* (*Whitman*, 1991).

Topographic variations always act to reduce the magnitude of the Bouguer correction. Topographic lows (relative to the measurement) will create voids where rock mass is replaced by air, while topographic highs (relative to the measurement) will

produce a gravitational pull in the opposite direction to a classical Bouguer 'slab'. Terrain corrections, also termed the *Bullard C* correction, are therefore added back to the Bouguer anomaly to reduce the contribution of the simple Bouguer 'slab'. They typically have a magnitude in the range of $0 - 10\ mGal$.

Correcting for topography was traditionally done by dividing the region surrounding a measurement into a series of zones and sectors, such that the gravitational contribution of each sector was roughly equivalent. The mean elevation difference, relative to the measurement location, was then estimated for each sector. The gravitational contribution of each sector could then obtained by referring to an associated table (e.g. *Hayford and Bowie* (1912); *Hammer* (1939)). Such a system is often built into modern gravimeters (including the Scintrex CG-5 used in our onshore gravity survey), allowing terrain corrections to be easily incorporated into a gravity measurement. Estimating elevations is an inexact process however, and with the emergence of high resolution digital elevation models (DEM's) it is now possible to incorporate precise elevation data into terrain corrections for all but the innermost sectors.

The idea of using DEM's to calculate terrain corrections is not new, and digital gridded elevation data was first used by *Bott* (1959); *Kane* (1962) to calculate the terrain contribution to distant zones. As the resolution of DEM's have improved and the algorithms have been developed, their use has expanded to encompass zones closer and closer to the measurement location.

4.4.7 Regional correction

The corrections to gravity observations outlined in the previous sections are designed to eliminate all variations in gravity not associated with the internal mass distribution of the Earth. In geophysical studies of gravity we are typically interested in anomalies produced by shallow, crustal heterogeneities. It is therefore desirable to eliminate the longer wavelength elements of the gravity field associated with density variations in the mantle associated with convective processes. This was traditionally achieved by drawing a linear trend, or low order polynomial, through the data to approximate the

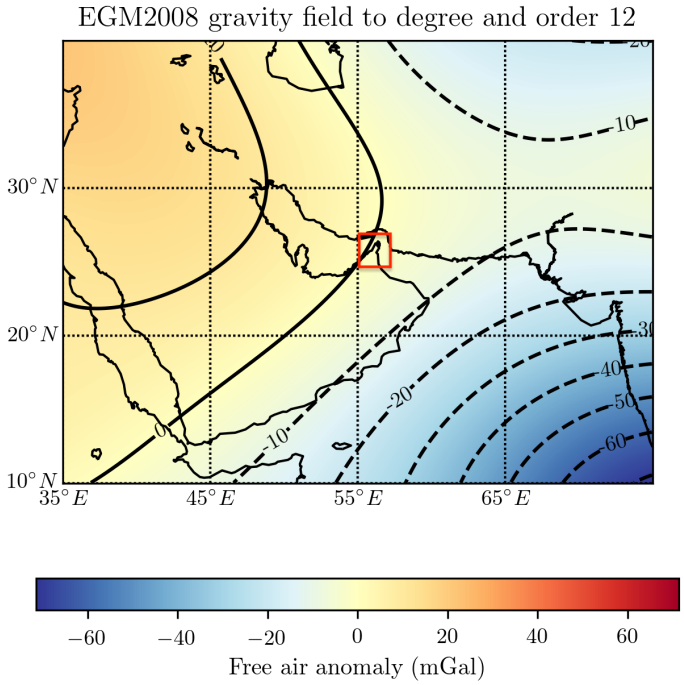


Figure 4.4: The EGM2008 global gravity field up to degree and order 12 (wavelength $\approx$ 3330 km) in the Middle East. This represents the sub-crustal contribution to gravity in the region, and will be used as our regional correction. The red box highlights our study area.

long wavelength component of gravity, removing this trend from the total anomaly, and interpreting the residual anomaly.

Analysis of global gravity (*EGM2008*, *Pavlis et al.* (2012)) and topography models (Earth2014, *Hirt and Rexer* (2015)) by *Watts and Moore* (2017) suggests that the gravity signal associated with non-isostatic processes, such as mantle convection, was restricted to *EGM2008* spherical harmonic components greater than degree and order 12. Removing the first 12 spherical harmonic components of the *EGM2008* global gravity field should therefore prove to be an effective method of eliminating sub-crustal contributions to an observed gravity anomaly.

The *EGM2008* gravity field, up to degree and order 12 (wavelength $\approx$ 3330 km), in our study region is shown in Figure 4.4. In the UAE the regional anomaly is close to zero as the broader long wavelength anomaly is transitioning from a large negative in the Indian Ocean to a small positive anomaly to the north and west. The regional

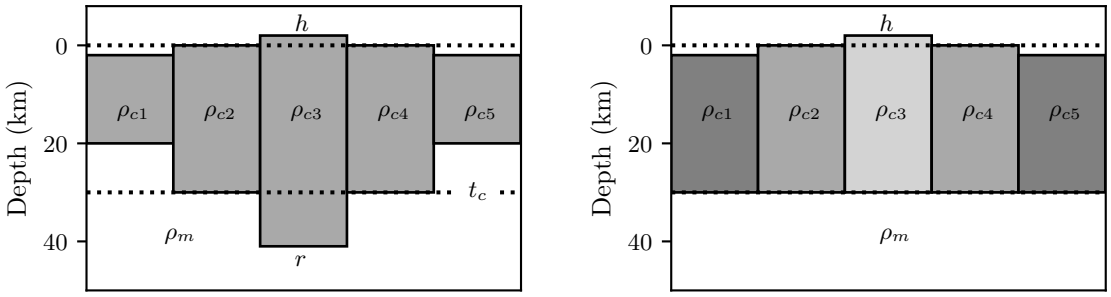
correction will therefore be small for our data. It will nevertheless be removed from our observations.

4.4.8 Isostasy and the isostatic anomaly

The Bouguer and Terrain corrections adjust the observed gravity anomaly for topographic expressions above (or below) the geoid. However no allowance is made for the gravitational effect of any isostatic compensation that may be associated with this topography. The reduction in gravity due to isostatic effects was first noted in smaller than expected plumb-line deviations near large mountain ranges by *Bouguer* (1749) in Peru, and again by *Everest* (1859) on the Ganges plain in India, though they did not understand the cause.

The solution was provided by *Airy* (1855) who proposed that the crust lies on a layer of viscous fluid, and that topographic highs must be balanced by associated crustal roots similar to timber or icebergs floating on water (see Figure 4.5a). The gravitational attraction of topography is then counteracted by the mountain roots displacing denser mantle material at depth. This type of isostatic compensation is now known as the Airy-Heiskanen model. An alternative model of isostasy was put forward by *Pratt* (1855, 1859) in which topographic highs are instead balanced at a compensation depth by lower average densities in the underlying column rather than a crustal root (see Figure 4.5b). This is now known as the Pratt-Hayford model of isostasy. A third flexural model of isostasy, pioneered by Vening Meinesz, argues that topographic highs are broadly supported by the elastic strength of the crust, and their associated isostatic compensation is distributed across a broad area rather than directly displacing the underlying column.

An isostatic correction (Δg_{IC}) can be calculated by assuming a model of isostasy and calculating the gravitational effect of the isostatic compensation predicted by that model. The isostatic anomaly is then obtained by subtracting the isostatic correction



(a) The Airy-Heiskanen model.

(b) The Pratt-Hayford model.

Figure 4.5: The two primary models of isostasy. The Airy-Heiskanen model (**a**) consists of a uniform density crust (i.e. $\rho_{c1} = \rho_{c2} = \rho_{c3} = \rho_{c4} = \rho_{c5} < \rho_m$), and topographic highs/lows counter balanced by mantle roots/anti-roots in the underlying crustal column. In the Pratt-Hayford model (**b**), topographic highs/lows are balanced by laterally varying the density in the crustal column to produce identical pressures at a given compensation depth (i.e. $\rho_m > \rho_{c1} > \rho_{c2} > \rho_{c3} < \rho_{c4} < \rho_{c5}$).

from a calculated Bouguer anomaly.

$$g_{IA} = g_{obs} - g_n + \Delta g_{FAC} - \Delta g_{BC} - \Delta g_{IC} \tag{4.25}$$

In the Airy-Heiskanen model of isostasy, topographic expressions on the surface are fully compensated by a mantle root or anti-root (see Figure 4.5a). The thickness of this root (r) can be computed by balancing pressures of a 'normal' crustal column against a compensated column with topographic height h.

$$r = h\frac{\rho_c}{\rho_m - \rho_c} \tag{4.26}$$

Where ρ_c and ρ_m are the mean density of the crust and mantle respectively.

Flexural models of isostasy are defined by the flexural rigidity (D), or elastic thickness (T_e) of the crust.

$$D = \frac{ET_e^3}{12(1-\nu^2)} \tag{4.27}$$

Where E is Young's modulus and ν is Poisson's ratio. Flexural models of isostasy have a more modest contribution to gravity relative to Airy type models, as compen-

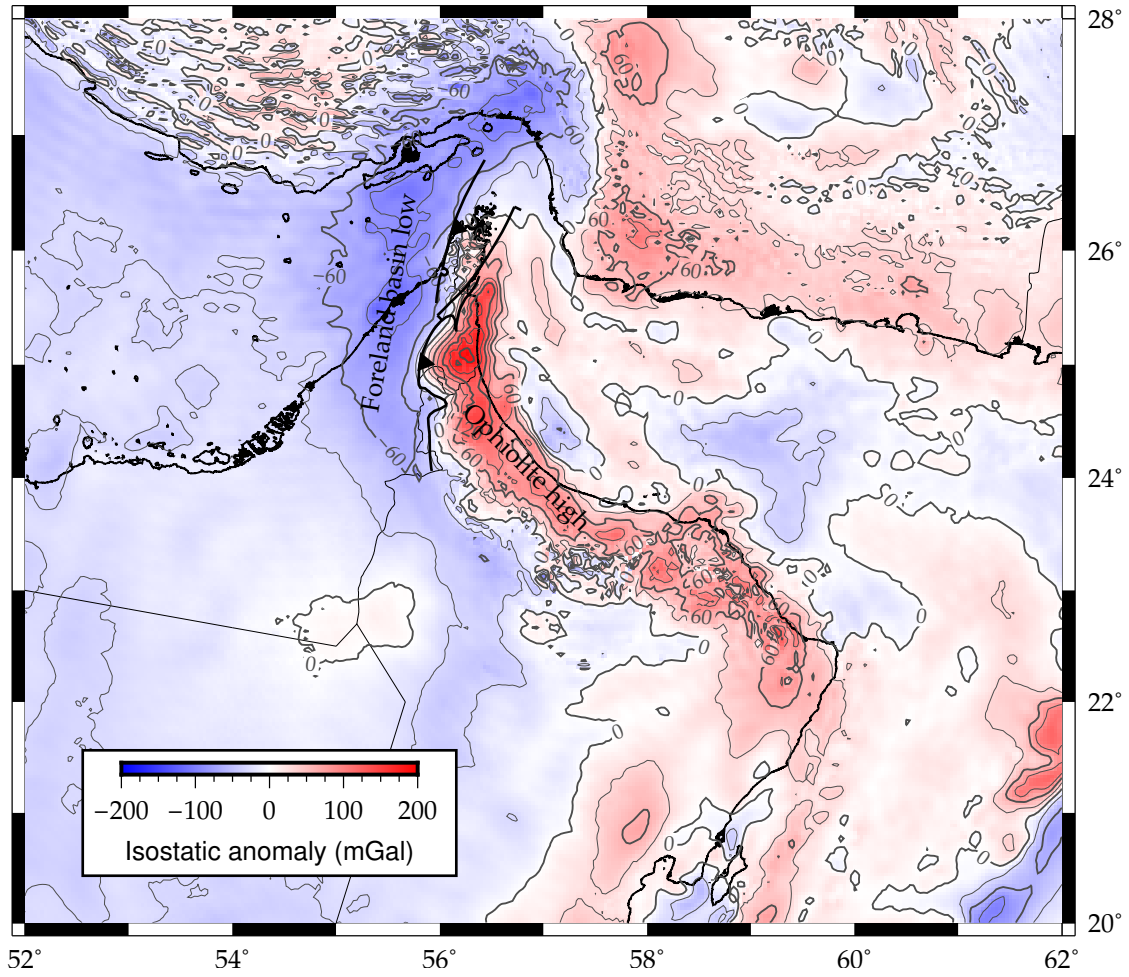


Figure 4.6: The WGM2012 isostatic gravity anomaly in the UAE and Oman. It is computed using global gravity (EGM2008) and topography (ETOPO1) models, and assumes Airy isostasy with a compensation depth of 30 *km*. High isostatic gravity anomalies associated with the Semail ophiolite are evident along the length of the UAE-Oman mountains. This is coupled with a low isostatic anomaly in the foreland to the west of these mountains.

sation for topographic loads is distributed over a broader area. The isostatic response in flexural models is also time dependent, with the response function approaching Airy isostasy as $t \rightarrow \infty$ (*Watts*, 2001). Airy isostasy can therefore be considered an end state, in which full isostatic compensation has been achieved.

The isostatic anomaly of the WGM2012 gravity model (*Balmino et al.*, 2011) for the UAE and Oman is shown in Figure 4.6. It was computed using global gravity (*EGM2008*) and topography (*ETOPO1*, *Amante and Eakins* (2009)) models, and assumes the Airy model of isostasy with a compensation depth of 30 *km*. Large positive isostatic gravity anomalies are evident across the Semail ophiolite down the length

of the UAE-Oman mountains, but are especially notable in the UAE. This suggests that the topography of the UAE-Oman mountains is significantly undercompensated at present, and that Airy isostasy has not yet been achieved. It may also indicate the presence of significant subsurface loads. The isostatic gravity high across the mountains is flanked by an associated low in the foreland to the west, particularly in the northern part. Note also that in the UAE the isostatic anomaly extends some way offshore, suggesting that the ophiolite is not truncated at the coastline here.

4.5 Previous gravity surveys

The first published onshore gravity data collected across the Semail ophiolite was the survey of *Manghnani and Coleman* (1981). They collected gravity observations across 460 sites in the UAE and Oman, traversing the UAE-Oman mountains and ophiolite several times. They observe large Bouguer anomalies of up to 140 $mGal$ associated with ophiolite outcrops, and compute gravity models across four profiles straddling the mountain range in Oman. The primary profile extends 320 km north-south from Ibra, through Muscat, and offshore into the Gulf of Oman where they utilise the data of *White and Ross* (1979). The model incorporates up to 10 km of peridotites to model the observed Bouguer anomalies, and includes a transition from 42 km thick continental crust inland to 18 km thick oceanic crust offshore north of Muscat. They found no evidence to suggest the ophiolite nappes are rooted in the mantle.

Shelton (1990) presents modelling results based on 900 gravity sites collected primarily across the Batinah coastal plain of Oman during fieldwork in 1978 and 1979. His modelling suggests the ophiolite here is made up of discrete nappes, $2 - 18$ km thick depending on their modelled density, that are not connected to the present day Gulf of Oman oceanic crust or their parent lithosphere.

Khattab (1993) presents shallow crustal models based on 68 gravity measurements along the Gulf of Oman coastline in the UAE, and along an inland profile connecting Masafi and Fujairah cities. He observes Bouguer anomalies peaking at 145 $mGal$ near

the coast, suggesting an offshore continuation of the ophiolite, and a strong regional trend interpreted as a transition from continental to oceanic crust. The north-south profile along the coast reveals two distinct peaks which are interpreted as being associated with two distinct obducted blocks.

Ravaut et al. (1997) collected 1012 new gravity measurements, primarily around Jebel Akhdar, and collated them with the data of *Manghnani and Coleman* (1981), *Shelton* (1990), offshore gravity data from *White and Ross* (1979) and *Dehghani and Makris* (1984), and around 45,000 gravity observations collected by Petroleum Development Oman (PDO) between 1955 and 1969. They supplemented this with data from the 5 *minute* free-air gravity grid of *Sandwell* (1992) and computed a Bouguer anomaly grid at 2.5 km resolution. They remove a regional trend with a low order polynomial to isolate the Bouguer anomaly associated with the ophiolite, and observe a positive-negative couple associated with the ophiolite obduction and foreland basin. They modelled the ophiolite as a seaward sloping wedge $6 - 10$ km thick, and confirm the rootless interpretation of previous authors. They also model the flexure of the Arabian plate and explain the deflection in the foreland as due to ophiolite loading, and suggest extended continental crust may extend out to within 50 km of the Makran coastline.

Ali et al. (2014) provides the most complete compilation yet of gravity data in the UAE and Oman, incorporating over $250,000$ observations. It includes the previous compilation of *Ravaut et al.* (1997) and adds numerous additional sources, including: ADNOC land and marine gravity surveys, surveys by previous Oxford students (*Jordan*, 2007; *Savage et al.*, 2007; *Lee*, 2008), data acquired during Petroleum Institute fieldtrips, and other industry surveys.

This data set is gridded at 1 *minute* resolution using *GMT*'s *nearneighbor* algorithm and displayed in Figure 4.7. The positive-negative gravity couple associated with the obducted ophiolite and foreland basin is evident. However there is also a clear lack of data across the ophiolite in the UAE where our D1 and D4 profiles are located, necessitating the acquisition of additional data.

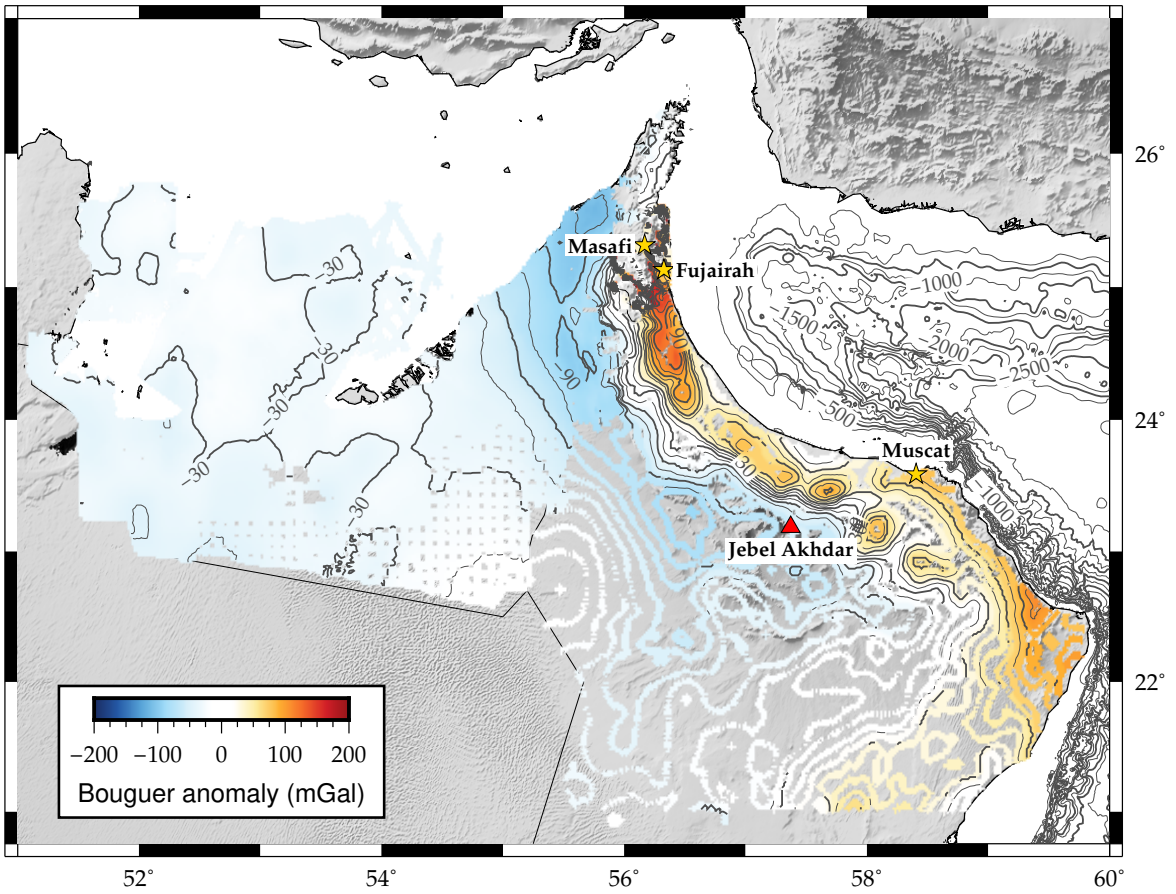


Figure 4.7: Compilation of existing gravity data across the UAE and Oman from *Ali et al.* (2014). Data is gridded at 1 *minute* resolution grid using *GMT*'s *nearneighbor* algorithm, and contoured at 15 *mGal* intervals.

4.6 Marine gravity dataset

Gravity data offshore was acquired during a cruise by the M/V *Hawk Explorer* during a cruise in mid 2014. The data was acquired with a Lacoste & Romberg Ultrasys marine gravity system, modified by the ZLS corporation to upgrade the beam position and negate pressure and moisture effects. The gravity system was mounted on a dual axis, gyro stabilised platform mounted aft of the vessel centrepoint, 2.13 m port of the centreline and 1 m above the mean waterline. The measurements were stabilised with a 4 minute convolution filter to stabilise it against short period noise and the effects of swell. The raw gravity data was filtered with a 60 point convolution filter with a 5 minute time lag.



Figure 4.8: Map showing the location of the gravimeter port readings in Pearl Jumeirah docks (reading 1) and Port Rashid (reading 2), Dubai. The location of the DDW 2 absolute gravity base station is also shown.

4.6.1 Base tie & drift correction

Gravity meter data was recorded in counter units (cu) at 1 s intervals for the duration of the cruise and logged in hourly *ascii* files with associated data regarding the ships state. Two still port readings were performed over the course of an hour on the 27^{th} and 28^{th} of July to estimate instrument drift and to perform a base station tie. The first at Pearl Jumeirah Docks, and the second a few kilometers to the north in Port Rashid, Dubai (Figures 4.8, 4.13). The first port reading was located within 500 m of the DDW-2 absolute gravity base station, with a stated gravity value of 978888.07 $mGal$ (Mohammed Ali, personal communication, 2015). Meter readings were tied to this value with a meter conversion factor of 0.9816 $mGal\,cu^{-1}$ to convert them to absolute gravity.

These reading showed a drift of -0.34 cu a day in the meter readings (Figure 4.9),

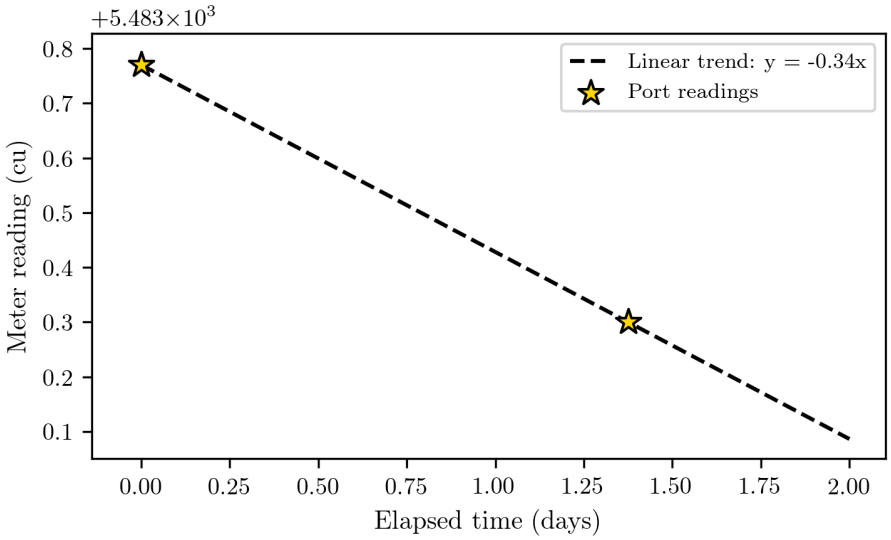


Figure 4.9: Port readings from the gravimeter aboard the Hawk Explorer in gravimeter units. These readings were used to establish the gravimeter drift for the survey and tie the meter to an absolute gravity base station.

and all readings were corrected for this trend. While ideally the port readings would have been performed in the same location, this was obviously not possible. Subsequent analysis of the internal consistency of the gravity dataset validated the drift trend established by these readings.

4.6.2 Data reduction

These gravity readings were reduced to free-air gravity anomalies via the methods outlined in Section 4.4. As this is a marine gravity survey utilising a beam type gravimeter, both Eötvös and cross coupling errors need to be considered.

The errors associated with the Eötvös effect were calculated using the ships recorded heading and speed in the gravity log file. These corrections reached a maximum of $\sim 80\ mGal$ during an easterly leg in which the ship's speed was in excess of 12 $knots$. These errors were added to the computed free-air anomaly to correct for this effect.

Cross-coupling errors were calculated automatically, and listed in the gravity data log. We also calculated them independently using the supplied acceleration data in the gravity log. In general cross coupling errors were small ($< 5mGal$), as the seas of the

Arabian Gulf and Gulf of Oman are generally relatively calm. Erratic cross coupling errors of several tens of *mGal* were also noted in several places however. These errors were subtracted from the Eötvös corrected free-air anomalies to correct for this effect.

While the filter applied to the raw gravity readings meant that they were relatively consistent and stable, the cross-coupling corrections could be erratic, particularly when the ship was changing course. A cosine-arch convolution filter was therefore applied to these corrections before their application to smooth out short period noise. Our filter had the form

$$\frac{1}{2}(1 + \cos(t\frac{2\pi}{t_{max}} - \pi)) \tag{4.28}$$

where t_{max} is the filter length. Several filter lengths were tested with our data to find a good balance between effective damping and resolution, and a filter with $t_{max} = 1200\ s$ was eventually selected.

A sample of 8 hours worth of data from the 20^{th} of July 2014 is shown in Figure 4.10, with the satellite altimetry derived free-air anomaly of Sandwell & Smith included for comparison (*Sandwell et al.*, 2014). The importance of the Eötvös correction is evident, with large positive and negative swings as the ship changes heading eliminated. The cross coupling errors increase dramatically in several places along this leg but as they oscillate between positive and negative contributions at relatively high frequency, their effect largely averages to zero when a long period convolution filter is applied. A regional correction is also applied, but at $\sim -1.5\ mGal$ its effect is minimal.

Quality control

The broad agreement between our dataset and the Sandwell & Smith data is encouraging, and validates the data reduction process so far. The shorter wavelength discrepancies also highlight the advantage of marine gravity data over satellite altimetry derived data in resolving shorter wavelength gravity anomalies to a high resolution.

The internal consistency of marine gravity datasets can be further checked by analysing repeated measurements at points where the ships track crosses over itself

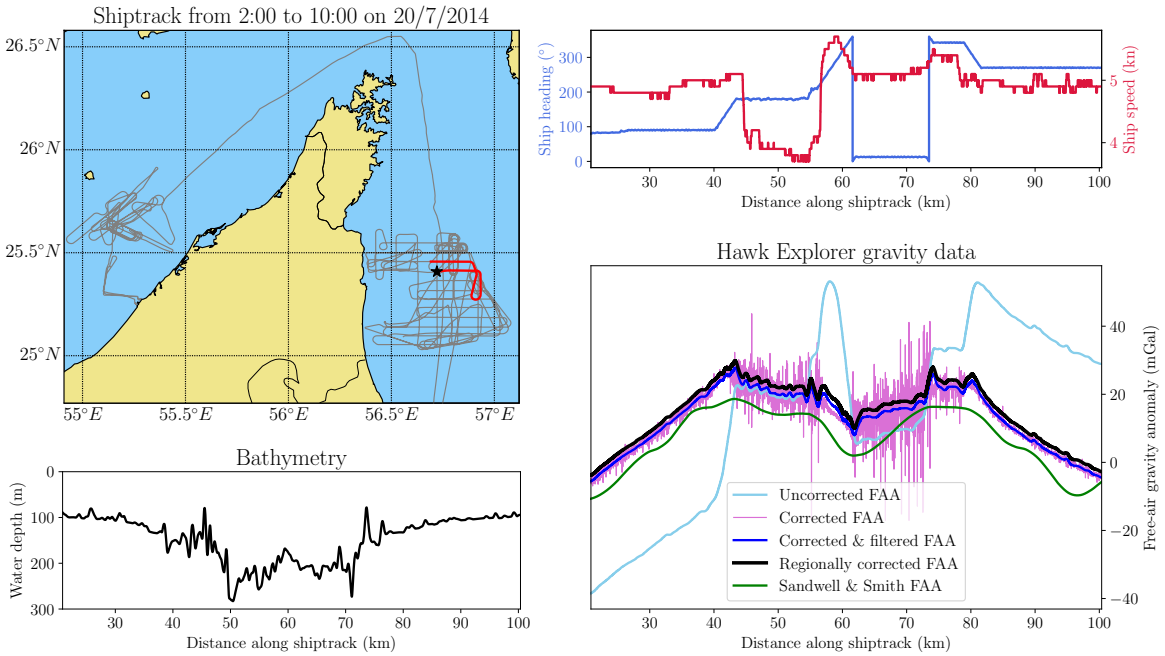


Figure 4.10: A sample of 8 hours worth of gravity data from the Hawk Explorer. The map on the top left shows the ship track of the day in question in red, with the starting point marked by the star. Bottom left displays the water depth during that time, as recorded by a Simrad Ea 400 Echosounder. Top right shows the ship heading and speed. Bottom right shows the gravity data recorded on this portion of the cruise. The uncorrected free-air anomaly (FAA) shows the calculated anomaly in the absence of Eötvös and cross-coupling corrections. The corrected FAA shows the anomaly with these corrections applied. The corrected and filtered FAA shows the anomaly with filtered corrections applied (the filter used was a 1200 s cosine arch filter). The regionally corrected FAA shows the corrected and filtered anomaly with the long wavelength component removed. Satellite altimetry derived free-air anomaly of Sandwell & Smith is included for reference.

(*Wessel and Watts*, 1988). In the case of this cruise, an abundance of such data is available as the ship often backtracked and crossed over previous paths.

Cross-over errors were computed and analysed with the aid of *GMT*'s *x2sys* modules. Over 100, 000 cross-overs were recorded for our gravity data (Figure 4.11). With a mean cross-over error of 0.22 *mGal* and a standard deviation of 1.02 our dataset appears to be highly self consistent, with no clear spatial or temporal trend.

Gridding the data

The processed offshore free-air gravity dataset was converted to a grid using *GMT*'s *nearneighbor* algorithm. The algorithm searches the space surrounding each node and

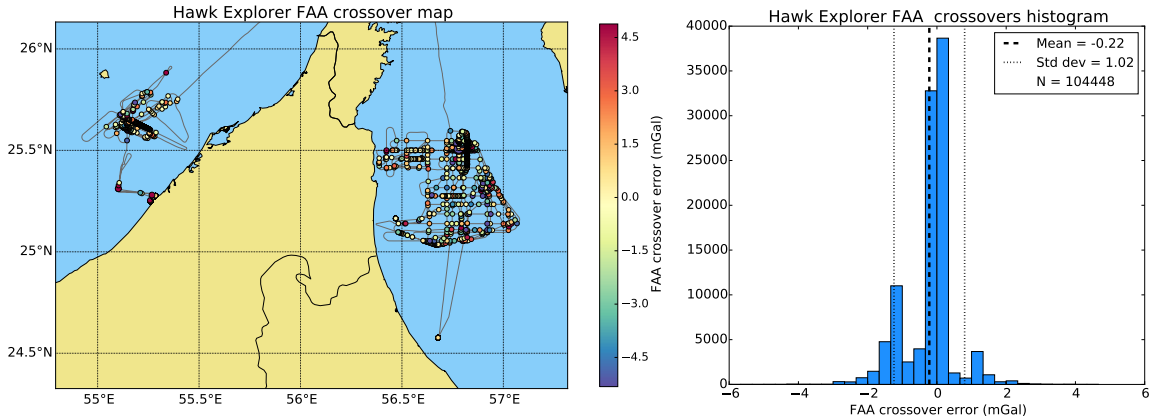


Figure 4.11: Cross-over errors for the processed Hawk Explorer gravity data in map (left) and histogram (right) form. Our dataset was highly consistent, with a mean cross-over error of 0.22 *mGal* and a standard deviation of 1.02.

computes a distance weighted average value. We computed our grid at 1 *minute* resolution, using a 2 *minute* search radius and requiring data points in at least 2 of the 4 sectors surrounding each node. The resulting grid is displayed in Figure 4.12. It shows a relatively constant ~ -80 *mGal* low within the Arabian Gulf. In the Gulf of Oman the anomaly remained close to zero offshore, but increases rapidly at a rate of $\sim 7\ mGal\, km^{-1}$ towards the coastline to reach a maximum of around 170 *mGal*.

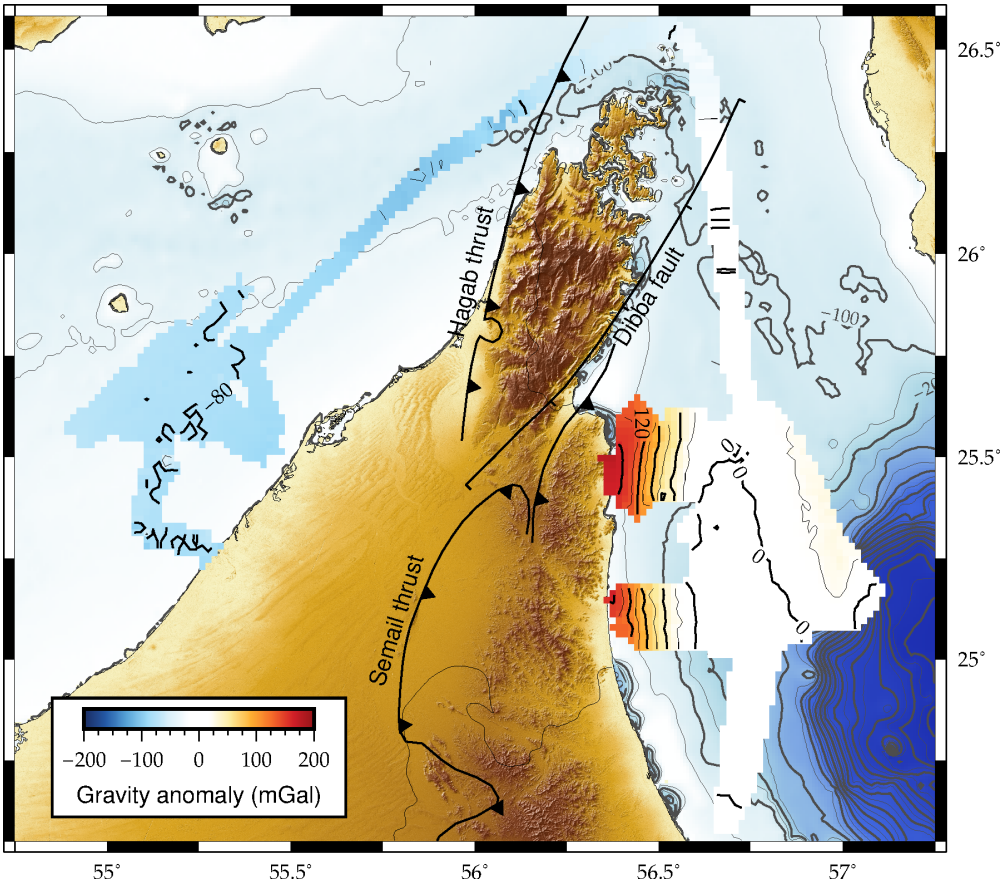


Figure 4.12: Free-air gravity anomaly grid derived from the Hawk Explorer data. Computed at 1 *minute* resolution using *GMT*'s *nearneighbor* algorithm, with 2 *minute* search radius.

4.7 Terrestrial gravity dataset

Terrestrial gravity data for this project were acquired across two profiles, over three field campaigns in early 2016. The two profiles were designed to be coincident with the D1 and D4 vibroseis reflection profiles acquired by the UAE's Ministry of Energy in 2003-2004 (*Ellison and Styles*, 2006), as well as our own seismometer deployments and refraction profiles, and have therefore been given the same names (Figure 4.13).

The data were acquired using a Scintrex CG-5 Autograv gravimeter provided by the Petroleum Institute. This is a relative gravimeter based on the zero-length spring concept described in Section 4.3. The gravimeter included a GPS attachment for measuring the latitude, longitude, and elevation of each measurement. The elevation accuracy on such GPS devices is known to be relatively poor, and this uncertainty

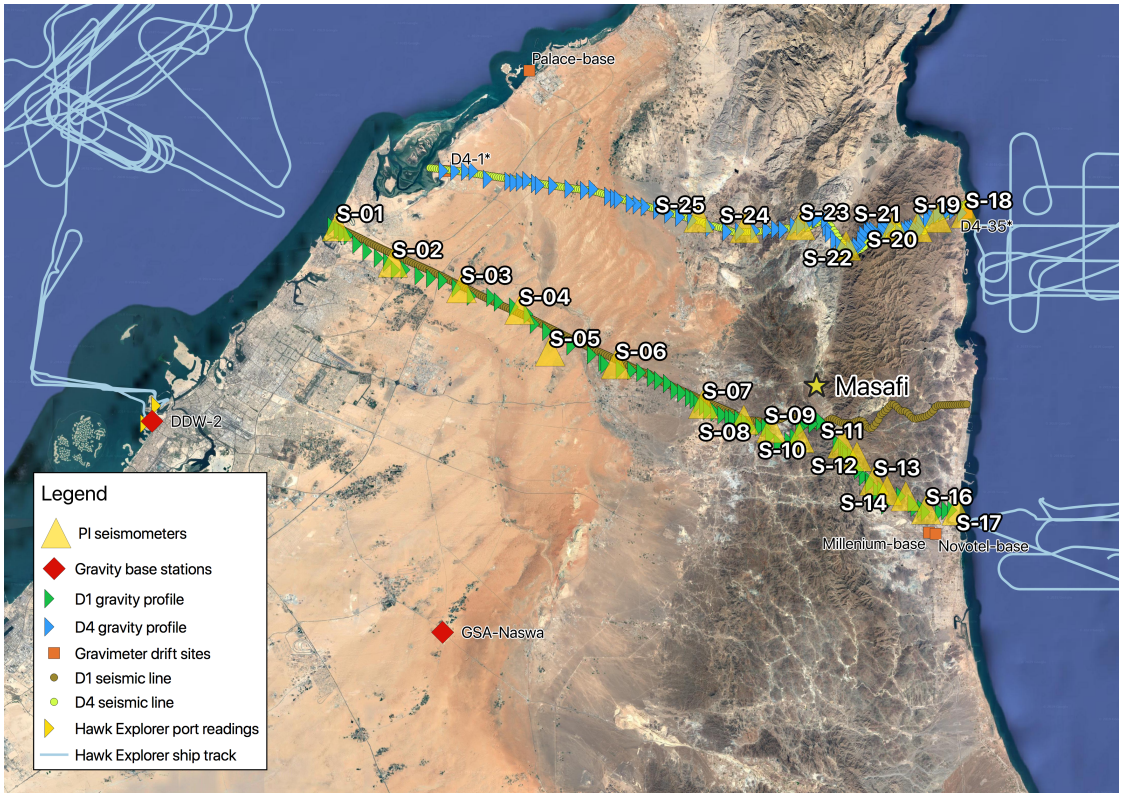


Figure 4.13: Map of the two onshore gravity profiles, D1 and D4, with the location of the D1 and D4 vibroseis seismic lines shown for reference. Gravimeter drift measurement sites and absolute gravity base stations used in this project are shown, along with the PI seismic network.

in elevation feeds through into the gravity measurement itself via the free-air and Bouguer corrections. Additional elevation measurements were therefore made using a mobile phone and a dedicated Garmin GPS device (though the latter was not available for the entirety of the survey) to obtain more accurate data, and to estimate the error.

Elevation measurements from all three devices were compared to elevations recorded in the ASTER30m DEM to estimate the reliability of each dataset (Figures 4.14, 4.18, 4.19). The gravimeter's GPS showed the largest standard deviation of the three ($\sigma = 19.75$), with a significant number of large outliers. GPS elevations from the phone and Garmin GPS were much more consistent with the DEM, with the Garmin device showing slightly tighter grouping ($\sigma = 10.35$, compared to $\sigma = 13.89$, see Figure 4.14).

Due to the variance and uncertainty associated with the GPS elevation measurements, we elected to use the ASTER30m DEM elevation dataset as our elevation data

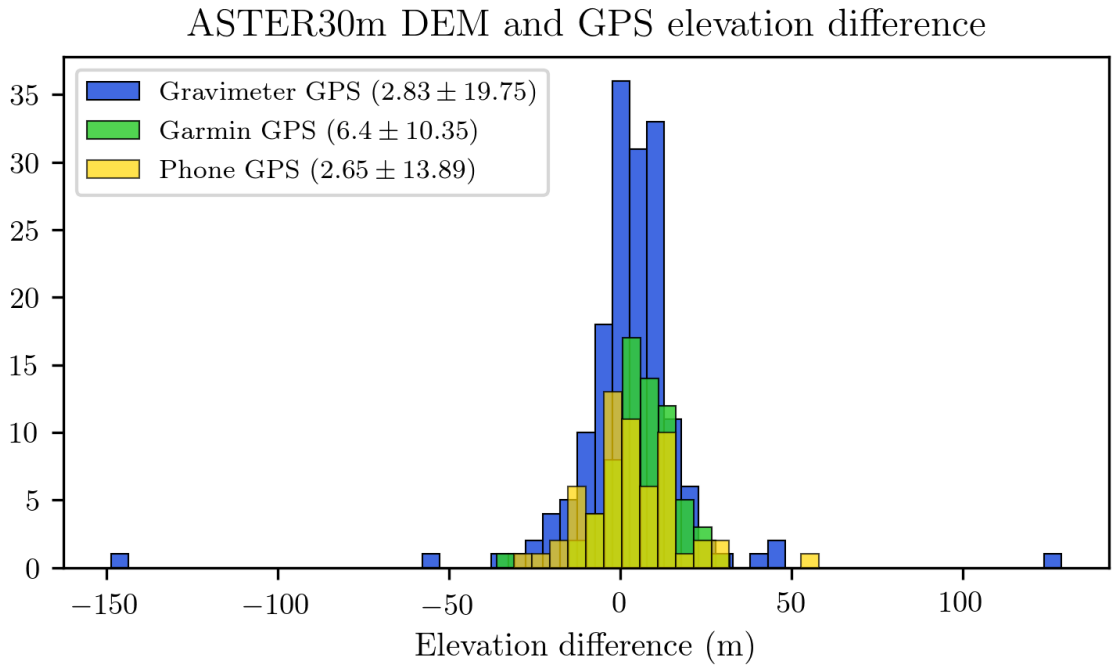


Figure 4.14: GPS elevations compared to the ASTER30m DEM. The mean difference for each dataset, with 1 standard deviation error is listed in the legend.

for our terrestrial gravity data reduction. While the spatial resolution of the dataset limits its accuracy in areas of steep topography, this was mitigated by our endeavours to locate each observation in a relatively flat location to simplify and minimise the inner terrain correction. We estimate the mean error for this elevation estimate to be $\sim 3\ m$ on average, translating to a Bouguer anomaly error of $\sim 0.57\ mGal$.

4.7.1 Base station tie

The Scintrex CG-5 is a relative gravimeter, meaning its measurements need to be tied to a base station to convert them to absolute gravity. Fortunately a series of absolute gravity base stations were established in the Emirate of Dubai in 2003. One of these base stations is located in the desert near the town of Naswa, approximately $\sim 30\ km$ west of the UAE-Oman mountains and $\sim 40\ km$ south of our southern profile D1 (see Figures 4.13 and 4.15). This base station was located near our usual route from Abu Dhabi out to our survey area, and several measurements were made here with the



Figure 4.15: Naswa absolute gravity station in the Emirate of Dubai. The value of gravity here is listed as 978846.767 *mGal*. Access to the building was not available, so our base station ties were made out front.

Station	Latitude	Longitude	Elevation (m)	Gravity (mGal)
GSA-Naswa	24.995561	55.660248	152.63	978846.767

Table 4.1: Naswa absolute gravity station from a geodetic survey of Dubai in 2003 (Mohammed Ali, pers. comm., 2015). This station was used as our absolute gravity tie for our onshore gravity surveys.

Scintrex CG-5 to tie its readings to an absolute gravity value before and after each survey.

The details of this gravity station were provided by Mohammed Ali, and are listed in Table 4.1. The mean gravimeter reading before each survey was tied to this absolute gravity value.

4.7.2 Drift correction

Relative gravimeters such as the CG-5 are based on the concept of a zero length spring, and their readings have a tendency to drift over time. It is therefore normal practice to make repeated measurements in a single location throughout the course of a survey

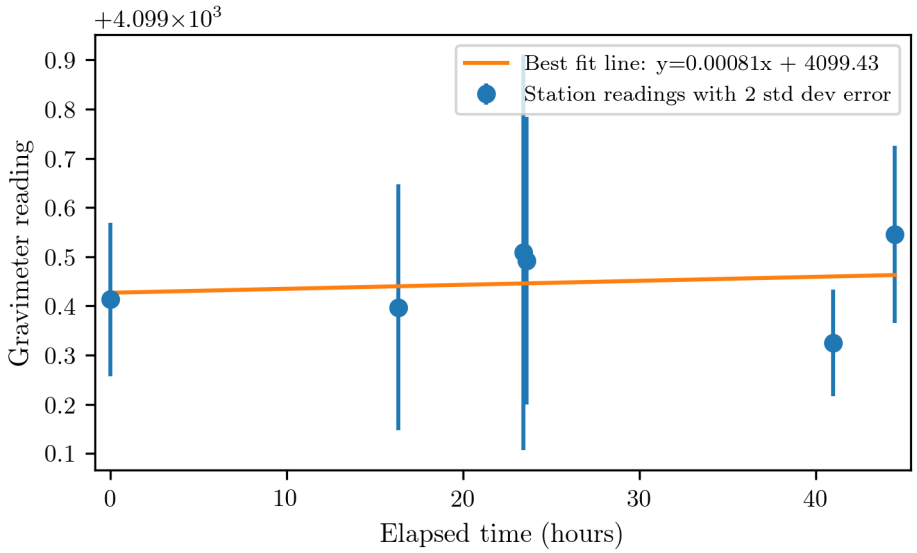
to record this drift. As our field area was quite large and our base of operations shifted several times throughout each survey this was not practicable. Repeated measurements were instead taken in several locations and their results analysed to identify a drift trend during the survey.

Analysis of these measurements revealed that the drift remained within measurement error for the majority of gravimeter drift measurement sites (Figures 4.13, 4.16a). A few sites did record some drift however, such as the Millenium hotel base station in Fujairah (Figure 4.16b). Where drift did occur it was typically small ($\sim 0.5\ mGal$ over 50-100 hours) and no consistent trend was observed throughout a survey. It was therefore deemed acceptable to neglect the drift correction, and consider the gravimeter as stable for the duration of each survey.

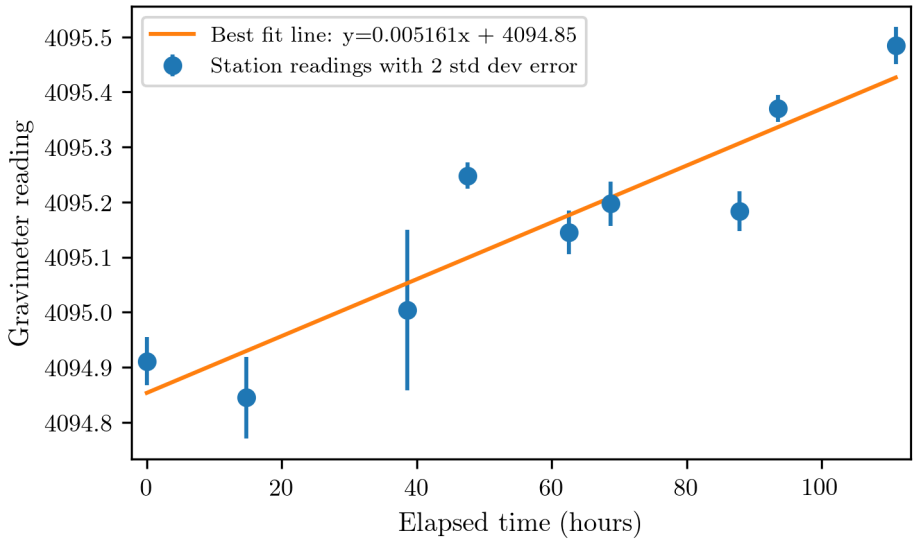
4.7.3 Terrain correction

We computed terrain corrections for the innermost zone ($0 - 20\ m$) during the survey using the built in function of the Scintrex CG-5 gravimeter. The remainder of the correction (including the *Bullard B* correction) was calculated using the *GTeC* MATLAB routine of *Cella* (2015) and the ASTER GDEMv2 1 $arc - second$ ($\sim$ 30 m) and GEBCO2014 30 $arc - second$ ($\sim$ 900 m) global DEM's for the topography and bathymetry respectively. GTeC calculates the terrain correction by dividing the region around the observation point into a series of zones, and progressively sampling a DEM at higher resolutions closer to the station. Far from the station each sampling point is considered as a flat topped, rectangular prism, while in the zones closer to the station tessellation can be used to create angular topped prisms to better approximate the true topography.

The terrain corrections for both profiles are shown in Figures 4.18 and 4.19. Their contributions are typically small compared to the Bouguer correction, reaching a maximum of $\sim 7\ mGal$ in particularly steep section of the mountains along line D4.



(a) Gravimeter drift at Novotel base station.

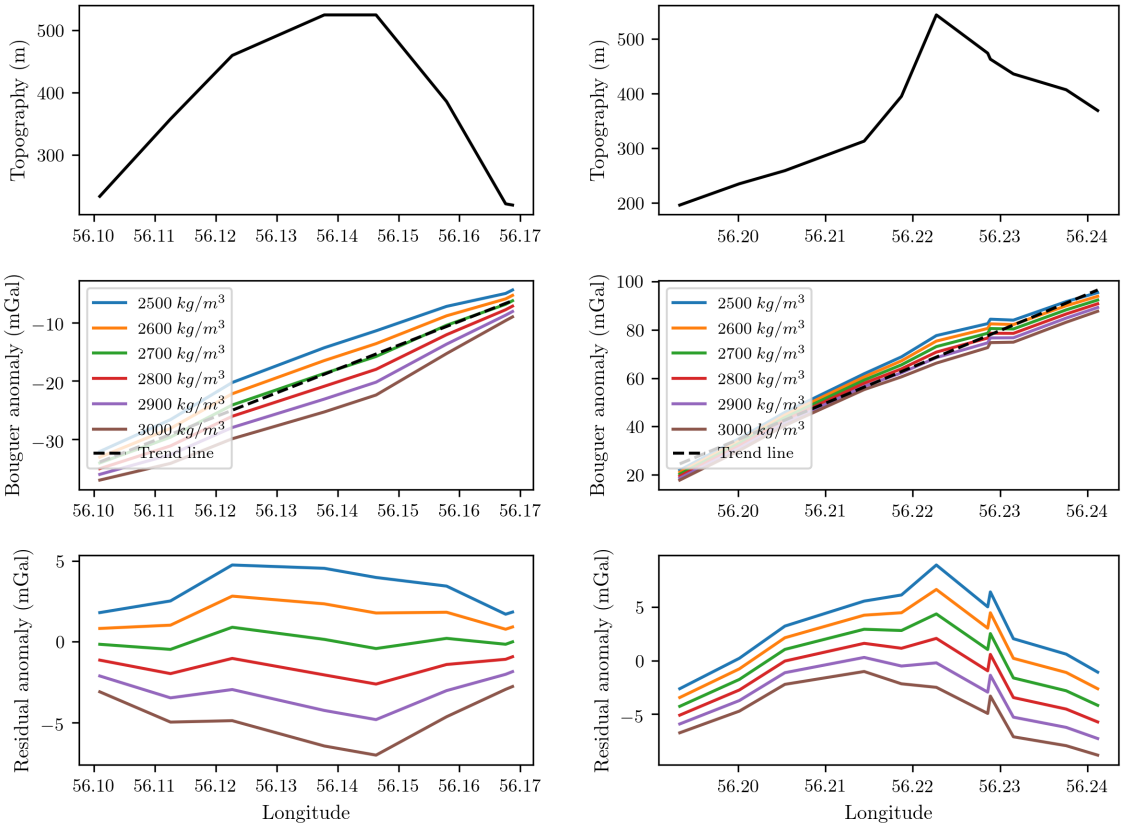


(b) Gravimeter drift at Millenium base station.

Figure 4.16: Gravimeter drift the Novotel hotel base station (**a**) and the Millenium hotel base station (**b**). The majority of base stations recorded did not record any drift outside of measurement error, as in **a**. Where drift did occur, it was typically less than ~ 0.5 *mGal*.

4.7.4 Reduction density

Determining the reduction density to use when computing Bouguer corrections is not always simple, especially in a region of complex geology containing many lithologies. A straightforward approach is Nettleton's method (*Linsser*, 1965; *Lowrie*, 2007). Bouguer



(a) Obducted margin. **(b)** Ophiolite.

Figure 4.17: Determination of reduction density across the obducted margin **(a)** and ophiolite **(b)** along profile D4. Reduction densities from $2500 - 3000\ kg\,m^{-3}$ are tested. A linear trend line is subtracted from the gravity data and the residual anomaly compared with topography. A value of 2700 $kg\,m^{-3}$ produced the smallest correlation to topography across the obducted margin. Across the ophiolite the picture was more complicated, and all values tested may have been too low. A value of 2900 $kg\,m^{-3}$ flattened the topographic peak most effectively.

corrections are designed to remove the effect of gravity associated with topographic deviations from the geoid. In Nettleton's method we compute Bouguer corrections for a range of possible reduction densities to find the value that produces the lowest correlation to topography.

Extracting a reduction density via this method proved to be complicated due to the wide range of Bouguer anomalies observed (-110 to 170 $mGal$), and the steep gravity gradients involved. In general no correlation was obvious but, two segments of the northern profile D4 provided reasonable results (Figure 4.17). The first across

a 7 km mountainous stretch of obducted margin west of the Masafi window, and the second across a 5 km segment of peridotite just east of the Semail thrust. A linear trend was removed from the Bouguer anomalies of both segments and the resulting residual anomaly provided a minor correlation with topography. Across the obducted margin the density that provided the smallest correlation was 2700 $kg\,m^{-3}$. Across the ophiolite the picture was more complicated, and the densities tested may have been too low, but a value of 2900 $kg\,m^{-3}$ flattened the topographic peak most effectively.

4.7.5 Gravity profiles

The data acquired during these surveys was processed to a complete Bouguer anomaly, and the regional trend removed with the methods outlined above. A relatively high reduction density of 2800 $kg\,m^{-3}m$ was selected based on the analysis in Section 4.7.4. While this value is likely too high for measurements in the foreland, the low elevations here minimise any potential errors.

The onshore gravity profiles D1 and D4 are displayed in Figures 4.18 and 4.19. D1 comprises 78 unique observations (not including base station measurements) across a ~ 130 km east-southeast profile, extending from the coast of the Arabian gulf in the west to the Gulf of Oman in the east. The gravity anomaly starts with a -110 $mGal$ low in the western foreland. As we move east and approach the mountains (and the ophiolite) this gives way to a steep ~ 6 $mGal\,km^{-1}$ gradient that continues for some 20 km. It then eases slightly, before a brief reversal in trend near Masafi, after which it climbs rapidly again to reach a peak of 160 $mGal$ at the Gulf of Oman coastline in the east.

D4 comprises 71 unique observations across a ~ 100 km east-west profile. It originates on the coast of the Arabian gulf some 15 km north of the western end of D1 and ends on the coast of the Gulf of Oman 40 km north of the eastern end of D1. The gravity anomaly along D4 starts out in much the same way as D1, with a -110 $mGal$ low in the western foreland. As we approach the mountains it increases by ~ 50 $mGal$ at a rate of ~ 2.5 $mGal\,km^{-1}$ as we move through the obducted blocks of the former

passive margin. The gradient increases dramatically to $\sim 12\ mGal\,km^{-1}$ as soon we reach the Semail thrust and its associated peridotite outcrops, before tapering off to a peak of 160 $mGal$ near the Gulf of Oman coastline again.

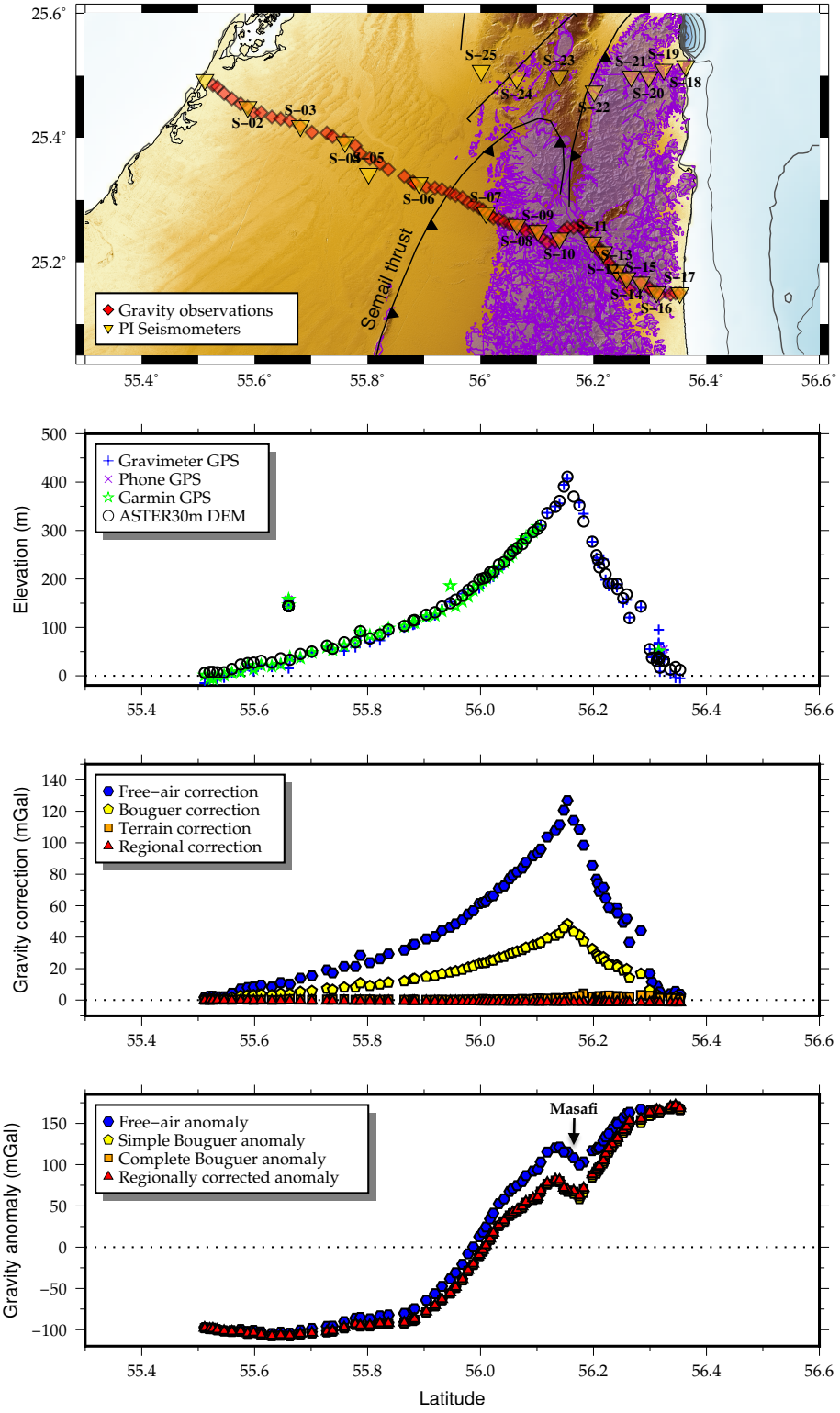


Figure 4.18: Gravity and topography data from the D1 survey. Free-air and Bouguer gravity corrections are derived from the DEM elevations using a density of 2800 $kg\,m^{-3}$. The terrain and regional corrections are also shown, with the resulting gravity anomalies plotted bottom. The PI seismic network is also included, peridotite outcrops are highlighted in purple.

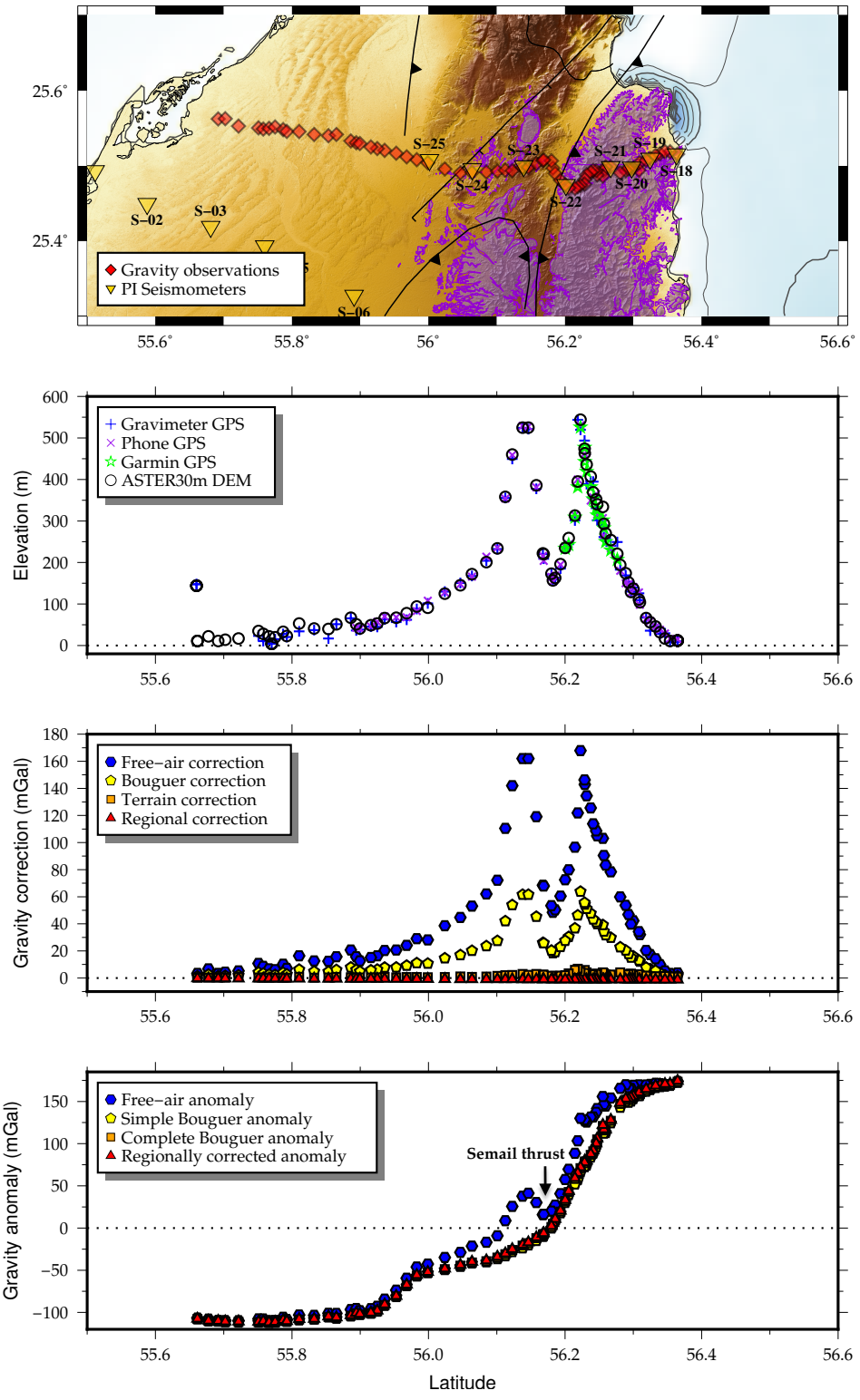
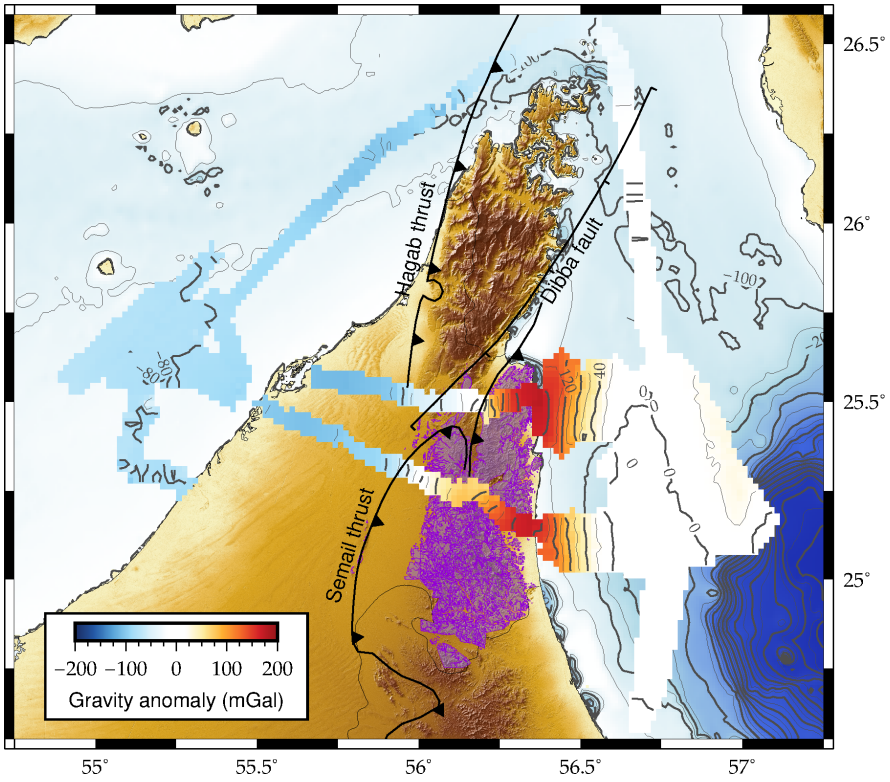


Figure 4.19: Gravity and topography data from the D4 survey. Free-air and Bouguer gravity corrections are derived from the DEM elevations using a density of 2800 $kg\,m^{-3}$. The terrain and regional corrections are also shown, with the resulting gravity anomalies plotted bottom. The PI seismic network is also included, and peridotite outcrops are highlighted in purple.

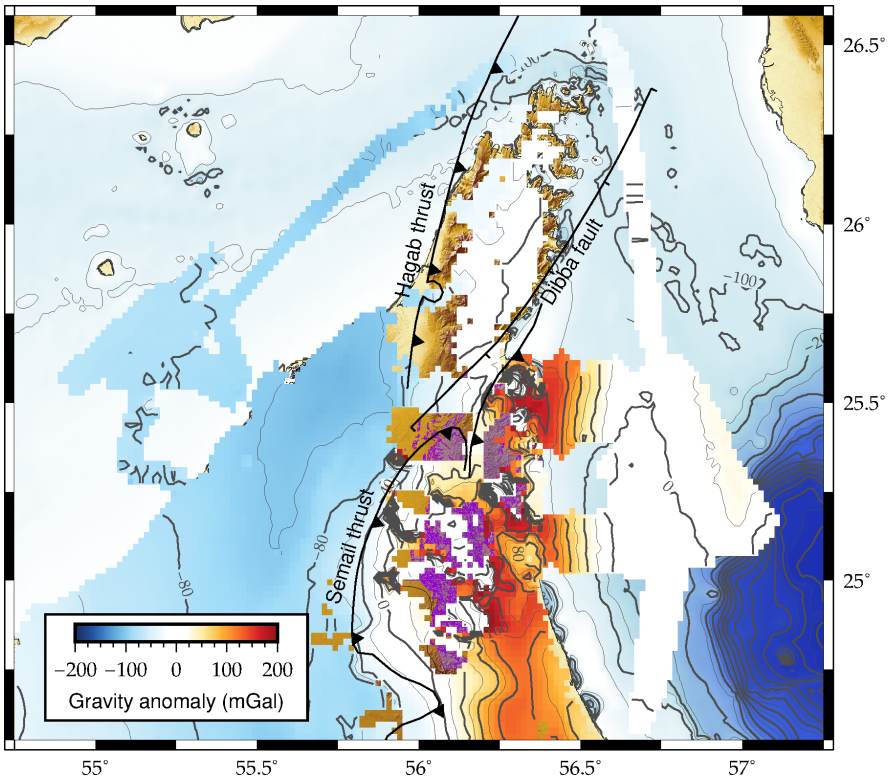
4.8 Merged dataset

The onshore and offshore datasets were merged into a single grid at 1 *minute* resolution, with free-air gravity anomalies offshore and Bouguer anomalies onshore. Both datasets matched up very closely near the Gulf of Oman coastline so no bulk shift was required during the merge. This merged dataset is shown in Figure 4.20a.

We also attempted to combine the our newly acquired data with the collated dataset of *Ali et al.* (2014) (Figure 4.20b). In the foreland these datasets were in very good agreement. Their data is sparse across the mountains however and the Bouguer anomalies recorded here vary significantly. They typically underestimated the values obtained during our surveys along D1 and D4, but several anomalously high data points with Bouguer anomalies up to 460 *mGal* were also noted. This made combining these datasets into a single grid difficult, and a weighting factor of 0.25 for existing data compared to 1 for newly acquired data was therefore applied. Even with this weighting, dramatic spatial variations in Bouguer anomalies across the ophiolite are evident, with neutral anomalies intertwined with large gravity highs. We therefore decided to rely solely on our own dataset for subsequent interpretations across the ophiolite.



(a) Newly acquired data.



(b) All data.

Figure 4.20: Merged gravity grid containing Bouguer anomaly data (onshore) and free-air anomaly data (offshore) acquired during this project (**a**), and integrating the collated dataset of *Ali et al.* (2014) (**b**). Data from *Ali et al.* (2014) is weighted at 0.25 compared to newly acquired data. Ophiolite outcrops in the UAE are highlighted in purple, and the major faults associated with emplacement marked.

4.9 Ophiolite mass

We can compute the effective mass excess (ΔM) associated with ophiolite loading across both our profiles using Gauss's law for gravity and free-air anomalies from our offshore and onshore dataset. Gauss's law states

$$\Delta M = \frac{1}{2\pi G} \oint_S g_{FA} dS \tag{4.29}$$

where S is a closed surface.

Positive Bouguer anomalies correlate with the first peridotite outcrops on both profiles. If we assume that this positive anomaly is entirely due to ophiolite loading and include the offshore data, we obtain a two-dimensional mass of $1.586 \times 10^{11}\ kg\,m^{-1}$ and $1.359 \times 10^{10}\ kg\,m^{-1}$ along D1 and D4 respectively. If these profiles are taken as representative of the the Aswad and Khor Fakkan massifs respectively (the names given to the ophiolite nappes south and north of Masafi, e.g. *Nicolas et al.* (2000)), and taking the width of these blocks to be 45 km and 40 km, the estimated mass of their load is $7.137 \times 10^{15}\ kg$ and $5.436 \times 10^{14}\ kg$ for each respective block.

4.10 Discussion

The gravity data acquired for and during this project has been processed to free-air anomaly data offshore and Bouguer anomaly data onshore. A higher than average reduction density of 2800 $kg\,m^{-3}$ was deemed appropriate in calculating Bouguer anomalies based on the analysis using Nettleton's method. This gives a high quality dataset that is both internally and externally consistent upon which to build our models and interpretations.

The gravity anomalies recorded in our study area span some 280 $mGal$, and exhibit the classic positive-negative couple typical of mountain and foreland basin complexes (*Karner and Watts*, 1983). Bouguer anomalies range from -110 $mGal$ in the foreland of the UAE to $\sim$ 160 $mGal$ along the Gulf of Oman coastline. The anomalies are

correlated with the various tectonic regimes, with the -110 $mGal$ gravity low in the west delineating the UAE foreland basin, the steep gradients and 160 $mGal$ high on the Gulf of Oman coastline associated with peridotite and gabbro outcrops of the obducted ophiolite, and the decrease back down to a neutral anomaly offshore representing the hinterland basin and a potential transition from a continental to oceanic tectonic setting. There is no evidence of the edge-effect in the free-air anomaly that is typically associated with the transition from continental to oceanic crust at continental margins however (*Worzel and Shurbet*, 1955; *Watts and Fairhead*, 1999). This is somewhat surprising as the presence of the obducted ophiolite suggests the transition zone is near the coastline, as their transportation ~ 50 km inland seems unlikely. Water depths off the coast of the UAE are shallow (< 250 m), and the present day slope begins further offshore than the eastern edge of our marine dataset. It is therefore possible that either the edge-effect of the transition is obscured by the gravity signal of the ophiolite, or the transition is further offshore and the hinterland basin lies on extended continental crust.

The gravity anomaly associated with the ophiolite extends down the length of the UAE-Oman mountains into Oman. The anomaly observed in the UAE differs from what is observed in Oman in two respects: firstly, the amplitude of the anomaly appears to be higher in the UAE, suggesting a greater ophiolite thickness, a greater proportion of denser mantle materials, or a lower degree of serpentinisation; secondly, the anomaly extends some way offshore in the UAE, suggesting some kind of offshore continuation of the ophiolite in the UAE is likely. This offshore continuation in the UAE has been noted by previous authors (e.g. *Khattab* (1993); *Ali and Watts* (2009); *Ali et al.* (2014)), and has been modelled at the south-eastern end of the ophiolite, offshore Muscat (*Manghnani and Coleman*, 1981). All previous authors have argued against an ophiolite rooted in the mantle ((*Manghnani and Coleman*, 1981; *Shelton*, 1990; *Ravaut et al.*, 1997)), however the unique nature of the gravity anomalies observed in the UAE may require a different geometry to be adequately modelled. We look to address these questions in the next chapter.

4.11 Chapter summary

In this chapter we have introduced the force of gravity, as it relates to geophysical exploration, and described how gravity measurements are reduced to gravity anomalies. We reduce the marine gravity data acquired by the M/V *Hawk Explorer* to a free-air anomaly, and grid it at 1 *minute* resolution. The onshore gravity data acquired along profiles D1 and D4 is reduced to terrain corrected Bouguer anomalies, and merged with the marine gravity to create a unified gravity dataset. The gravity anomalies along these east-west profiles exhibit the classic high-low couple typical of foreland basins, and range from -110 *mGal* in the foreland to the west, to $\sim$ 160 *mGal* across the ophiolite, to a neutral anomaly offshore in the Gulf of Oman. It is clear the ophiolite extends some way offshore in the UAE, but no edge-effect marking the end of the continental margin is evident, leaving the nature of the underlying crust unclear.

.

Chapter 5

Modelling

5.1 Introduction

In this chapter we will introduce and discuss gravity modelling methods, with a focus on the line integral method for 2D gravity models. We summarise all of our data constraints (density data, reflection and refraction seismic data, receiver functions, and surface geology), and build two 2D gravity models along our two passive seismic/gravity profiles D1 and D4. We finish by discussing the geological implications of these models, and summarise our key conclusions.

5.2 Modelling gravity

Early approaches to modelling gravity anomalies compared the shape of an observed anomaly to the anomaly produced by some simple geometries. The gravity anomaly of a buried sphere for example can be computed as though all of its mass were located at its centre (see Section 4.2.2), with a gravitational acceleration of

$$\mathbf{g} = -\frac{GM}{r^2}\hat{\mathbf{r}} \tag{5.1}$$

where G is the gravitational constant, M is the mass excess of the sphere relative to its host rock, and r is the distance to its centre of mass. As gravity observations

only measure the component of gravity normal to the geoid, it is only the vertical component of **g** that contributes to the observed gravity anomaly

$$g_z = |\mathbf{g}| \sin\theta = \frac{GM}{r^2}\frac{z}{r} \tag{5.2}$$

where z is the depth to the sphere. M and r are given by

$$M = \frac{4}{3}\pi R^3 \Delta\rho \quad \text{and} \quad r^2 = x^2 + z^2 \tag{5.3}$$

so the vertical contribution to gravity from the buried sphere can be written as

$$g_z = \frac{4}{3}\pi G R^3 \Delta\rho \frac{z}{(z^2 + x^2)^{\frac{3}{2}}} \tag{5.4}$$

The gravity anomalies observed on a profile across the top of such a buried sphere is shown in Figure 5.1. This example illustrates two key points when it comes to modelling gravity anomalies: The first is that the wavelength and amplitude of the anomaly are related to the burial depth z. A common rule of thumb to use is the "half-width" method, in which the width of the gravity anomaly at half of the maximum amplitude (w_h) is related to depth by $z \approx 1.3 w_h$. The second is that gravity anomalies are non-unique, and it is not possible to determine both the volume and density contrast of a buried body from the gravity anomaly alone. For a given depth z, any number of combinations $\Delta\rho$ and R could produce the same gravity anomaly at the surface.

Mathematical formula's for the gravity anomalies of numerous other basic shapes have also been derived. This allowed the gravity anomalies associated with more complex geometries to be approximated by breaking them down into a series of basic shapes for which the gravity anomaly was already established. Such methods could be tedious, and computationally demanding when large numbers of such shapes were required however, and a method to compute the anomaly associated with arbitrary shaped bodies was therefore required.

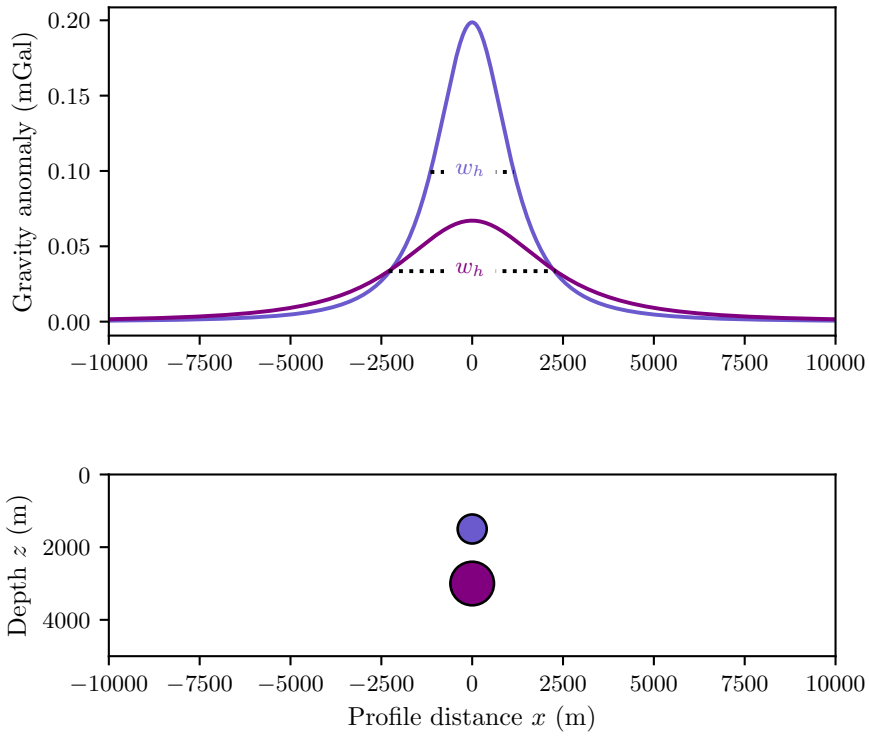


Figure 5.1: Gravity anomaly produced by two spheres buried at 1500 m and 3000 m. The shallow sphere has a radius of 400 m, and a density contrast of 250 $kg\,m^{-3}$ relative to the surrounding rock. The deeper sphere has a radius of 600 m and a density contrast of 100 $kg\,m^{-3}$.

5.2.1 Line integral method

Hubbert (1948) presented two methods for computing the gravity anomalies of arbitrary shaped polygons in two dimensions. The first he termed the *areal* method, in which the gravity anomaly of an arbitrary shaped body could be computed at the origin by

$$\Delta g = 2G \sum_{i=0}^{n} \Delta\rho_i \Delta\theta \Delta z \tag{5.5}$$

where $\Delta\rho_i$ is the density contrast of a polygon defined by θ, $\Delta\theta$, z, and Δz. This method was limited in that it could not deal with infinite shapes, or mass situated too near the $z = 0$ plane. He presented a second method to handle these circumstances

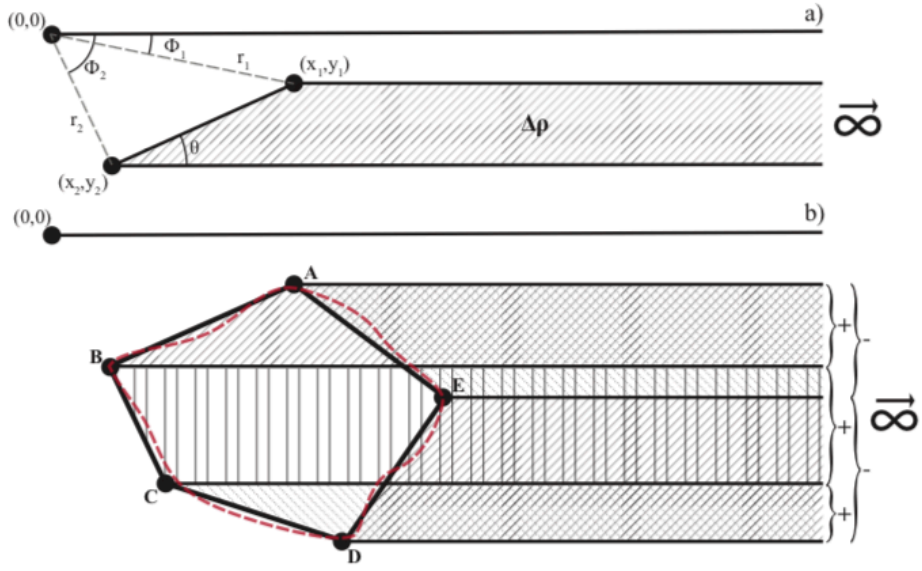


Figure 5.2: An illustration of the line-integral method for an one sided infinite slab (**a**), highlighting the variables necessary for the computation of Equation 5.6. For finite shapes the gravity effect can be calculated by approximating its shape with an n-sided polygon and computing the line integral along each side (**b**) Figure from *Tozer et al.* (2017).

that he termed the *line-integral* method. This method computes the gravity anomaly at the origin of a cartesian coordinate system by integrating around the periphery of a polygon. This method was able to handle infinite shapes, but was restricted to integration along paths where either θ or z was constant. Subsequent authors modified the method to address this deficiency (e.g. *Talwani et al.* (1959); *Bott* (1969)), allowing the method to be applied to n-sided arbitrary shaped polygons. The method used by the gravity modelling software employed in this project (*GMG*, see Section 5.3.7) is based on the analytic solution of *Heiland* (1940) for the gravity anomaly produced by an arbitrary side of a polygon

$$\Delta g_i = 2G\Delta\rho \left\{ -(x_1 \sin\theta + y_1 \cos\theta) \left[\sin\theta \log_e \frac{r_2}{r_1} + \cos\theta(\phi_2 - \phi_1) \right] + y_2\phi_2 - y_1\phi_1 \right\} \tag{5.6}$$

where (x_1, y_1) and (x_2, y_2) are the coordinates of the points defining the polygon side, r_1 and r_2 are the distance from these points to the origin, ϕ_i are the angle between r_i and the x-axis, and θ is the angle between the polygon side and the horizontal (see

Figure 5.2). All other symbols have the same meaning as above.

The total gravity anomaly is computed by moving counter-clockwise around the polygon and summing the contribution from each side.

$$\Delta g = \sum_{i=0}^{n} \Delta g_i \tag{5.7}$$

Δg_i is positive when $z_2 > z_1$ and negative when $z_1 > z_2$ so the contributions outside of the polygon cancel in the summation, leaving only the anomaly produced by the shape itself.

5.3 Object oriented modelling

Object oriented gravity modelling is the standard method of modelling gravity anomalies. In this approach observed gravity anomalies are forward modelled by constructing a series of static polygons designed to represent the geological units thought to be present within the subsurface. This is usually done in two dimensions by constructing profiles normal to the strike of the major geological features to be modelled. 2D models assume the modelled polygons extend infinitely out of the modelling plane. This assumption may not always be appropriate however, and a modification known as 2.5D modelling allows the out of plane extent to be defined. We utilise 2D modelling for this thesis as the primary target of study is the Semail ophiolite, which is sufficiently laterally continuous and normal to our gravity profiles.

Due to the non-unique nature of gravity models, there is no guarantee that a model that successfully reproduces all of the features of an observed gravity anomaly represents a true picture of the subsurface (e.g. *Skeels* (1947)). It is therefore important to incorporate as many independent constraints into a model as possible to ensure it is a genuine approximation of the subsurface structure.

The two primary model parameters that can be adjusted to fit a given gravity anomaly are the geometry and density of the constituent polygons. A large amount of geophysical data was collected as part of this project, and numerous other studies

in the region have been published. We draw on these sources to obtain constraints for these parameters.

5.3.1 Density

Density data for the geological units within our model comes primarily from the literature, as no direct density measurements were made for this project. Laboratory density measurements are available from field samples acquired during several previous studies however (e.g. *Manghnani and Coleman* (1981); *Christensen and Smewing* (1981); *Ali et al.* (2008, 2009)). These represent the most reliable density data available, and provide valuable constraints on our models (providing these surface samples are representative of their respective units at depth). This is particularly relevant for the ophiolite peridotites, as extensive serpentinisation has been observed in surface samples. However it is not clear whether this serpentinisation represents bulk alteration of the ophiolite, or is just related to surficial processes.

Other density data comes from seismic studies (*Naville et al.*, 2013), and previous gravity studies (*Searle and Ali*, 2009; *Ali and Watts*, 2009; *Ali et al.*, 2014). The available data is summarised in Table 5.1

5.3.2 Reflection seismic

Ministry of Energy surveys

The WesternGeco acquired four onshore vibroseis profiles on behalf of the Ministry of Energy of the UAE in 2003-2004 (*Ellison and Styles*, 2006). Two of these profiles extended east-west across the ophiolite (D1 and D4), while the other two linked these profiles together in two shorter north-south profiles (D2 and D3). While we do not have access to the data itself, we did obtain high resolution PDF files of the time-migrated and interpreted east west profiles.

Several papers have also been published that utilise these surveys. *Naville et al.* (2013) utilised the data along the southern profile D1 to perform a near-critical angle

Geological unit	**Density ($kg\,m^{-3}$)**	**Reference**
Ophiolite:		
Pillow lavas	$2540 - 2770$	*Christensen and Smewing* (1981)
Basalt	2600	*Manghnani and Coleman* (1981)
Dolerite	$2670 - 2830$	*Manghnani and Coleman* (1981); *Christensen and Smewing* (1981)
Gabbro	$2830 - 3070$	*Manghnani and Coleman* (1981); *Christensen and Smewing* (1981)
Peridotite (serpentinized)	$2750 - 2980$	*Manghnani and Coleman* (1981); *Ali et al.* (2008)
Peridotite (unserpentinized)	$3200 - 3330$	*Manghnani and Coleman* (1981); *Christensen and Smewing* (1981)
Obducted sediments:		
Hawasina	$2420 - 2770$	*Manghnani and Coleman* (1981); *Ali et al.* (2008)
Continental crust:		
Melange	2420	*Manghnani and Coleman* (1981)
Shelf carbonates	$2600 - 2700$	*Naville et al.* (2013); *Manghnani and Coleman* (1981)
Basement	$2750 - 2900$	*Manghnani and Coleman* (1981); *Ali et al.* (2008, 2009, 2014)
Foreland basin:		
Upper foreland	$2300 - 2500$	*Searle and Ali* (2009); *Ali et al.* (2014)
Lower foreland	$2400 - 2720$	*Ali et al.* (2009, 2014)
Hinterland basin:		
Water	1030	-
Top sediments	1950	*Manghnani and Coleman* (1981)
Deeper sediments	$2100 - 2300$	*Manghnani and Coleman* (1981)

Table 5.1: Summary of density data available for the various geological units present in our study area.

refraction study with the aim of illuminating the base of the ophiolite. Their results showed the base of the ophiolite gently dipping westwards of Masafi to a depth of $\sim 2.5\ km$, they did not attempt to process far offset data east of Masafi however, so their data provides no constraints for this section. *Tarapoanca et al.* (2013) model the kinematic evolution along line D4 and present models based on the vibroseis data. Their models covers the upper 10 km of the crust and extends from the foreland in the west to the Gulf of Oman coastline. Their model suggests the obducted sedimentary

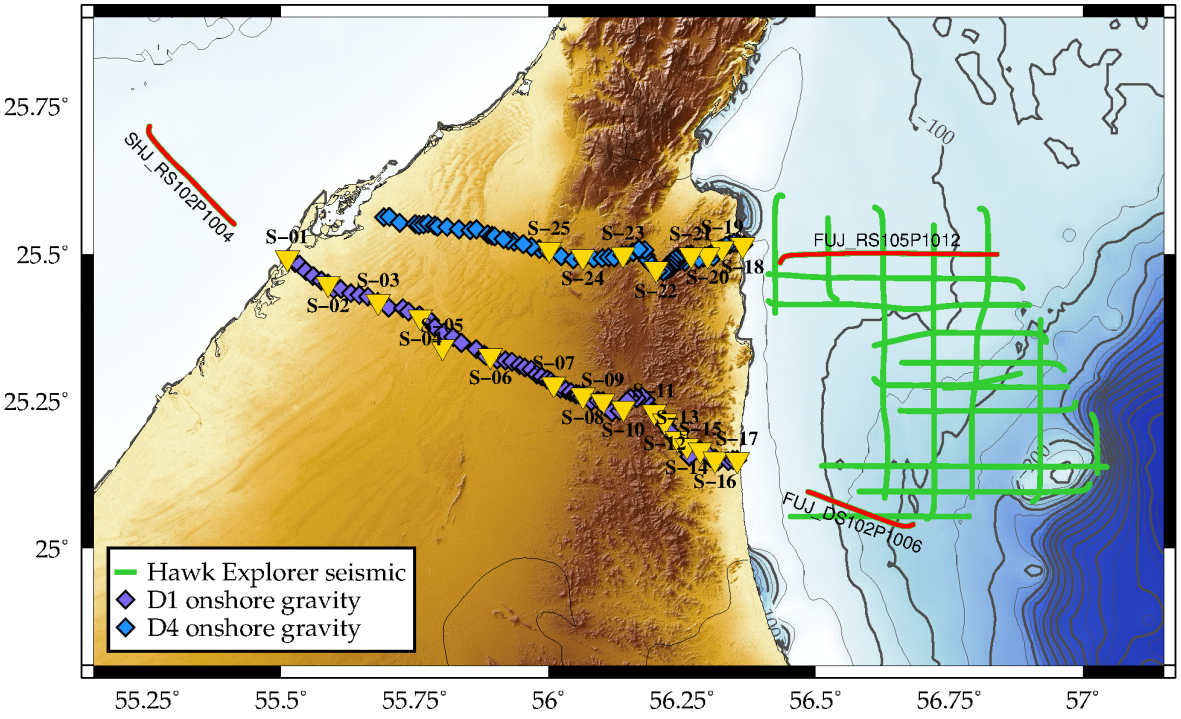


Figure 5.3: Map showing the reflection seismic data acquired by the M/V *Hawk Explorer*. Lines relevant to the D1 and D4 gravity profiles and highlighted in red, with the data from these lines shown in Figures 5.4, 5.5, and 5.6.

units of the Hawasina formation and the ophiolite itself occupy the upper ~ 5 *km* of the crust in a series of thrust sheets, with the ophiolite dippping gently eastwards.

Inspection of the high resolution PDF's shows that the upper 10 *km* of the crust is imaged in good detail, particularly in the foreland basin. Across the ophiolite a high degree of scattering is evident however, and we would treat any interpretation of structure within the ophiolite based on this data with caution.

M/V *Hawk Explorer* data

The M/V *Hawk Explorer* acquired around 925 *km* of reflection seismic data as part of this project, primarily offshore in the Gulf of Oman (Figure 5.3). This data was processed to depth-migrated seismic sections by WesternGeco and interpreted with the aid of three wells from previous surveys (F-1, FM-A1, and F-2) by Mohammed Ali. The sections were processed down to 25 *km* depth, but coherent reflections are difficult to trace below ~ 10 *km*.

The data showed a thick (up to 10 km) sedimentary sequence, deposited post ophiolite obduction in the late Cretaceous. The Upper Miocene and younger sediments are relatively un-deformed, but significant transpressional deformation is evident from the mid Miocene sequences onwards. A clear basement horizon was generally not evident, and Moho was also not definitively imaged.

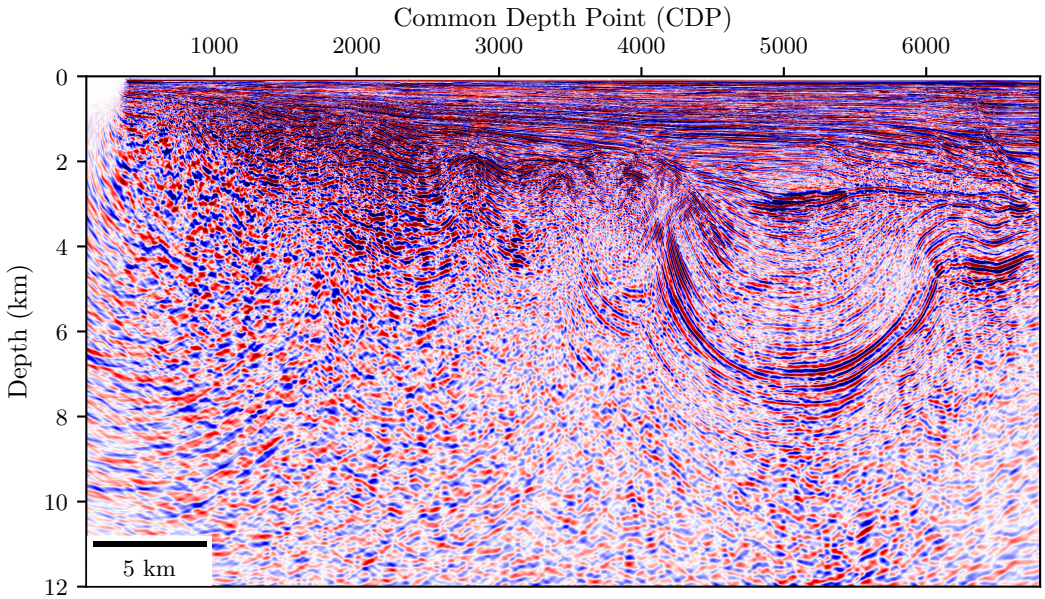
Three of these lines were ideally positioned constrain the upper crustal structure offshore from our onshore gravity profiles: *FUJ_RS105P1012* as an offshore extension of D4 in the Gulf of Oman (Figure 5.4); *FUJ_DS102P1006* as an offshore extension of D1 in the Gulf of Oman (Figure 5.5); and *SHJ_RS102P1004* as an offshore extension of D1 in the Arabian Gulf (Figure 5.6).

The ophiolite is imaged on the western end of line FUJ_RS105P1012 as a steeply dipping ($\sim 45°$) zone of diffuse reflectivity, and can be traced down to ~ 6 km depth. The interpretation of this line provided by Mohammed Ali shows at least 9 km of sediments. Line specific interpretation was not available for the other two lines discussed in this section, but the general structure can still be inferred. The ophiolite is not evident on line FUJ_102P1006, though it was interpreted to be present closer to the coastline on the southern-most east-west line (FUJ_RS100P1025) just to the south. The shallow sediments are again relatively un-deformed however, while the deformation of the deeper sediments is less intense. Line SHJ_RS102P1004 in the Arabian Gulf shows remarkably little deformation, with strong reflectivity down to ~ 5 km and several more coherent horizons evident down to ~ 12 km.

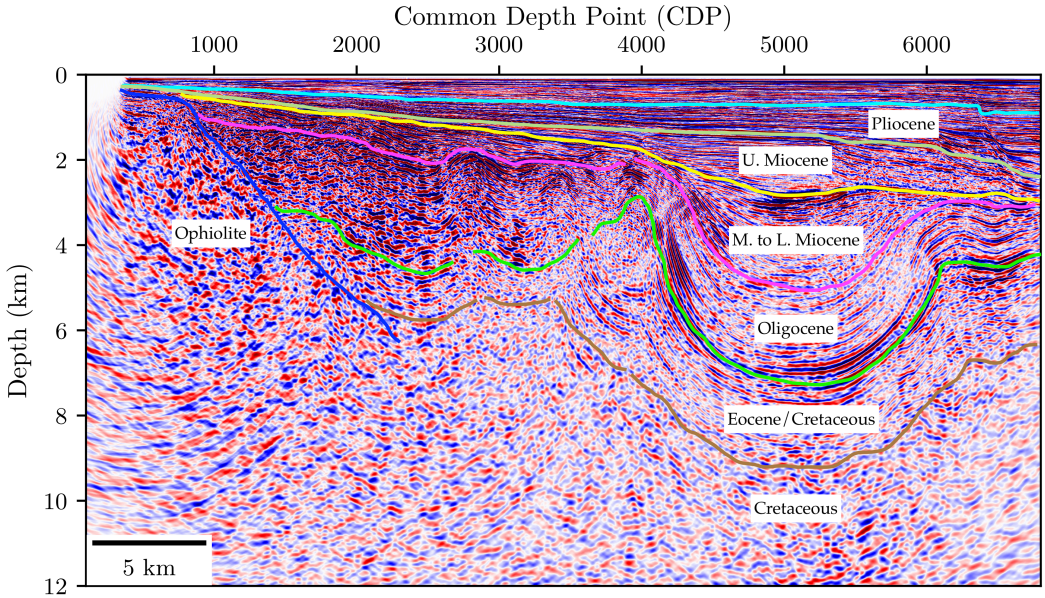
5.3.3 Refraction seismic

The M/V *Hawk Explorer* also acquired two onshore-offshore refraction profiles during its cruise in 2014, shooting into a network of seismometers deployed along two profiles. This data was processed and analysed by Simone Pilia using *rayinvr*.

The northern refraction profile D4 was generated from the recordings of airgun shots in an east-west profile offshore on the northern seismometer profile (S-18 - S-25). No shots were reliably recorded beyond S-23 however so the model extends 78 km



(a) Depth migrated section.



(b) Interpreted section.

Figure 5.4: The depth migrated seismic line FUJ_RS105P1012 (**a**), with the interpretation of Mohammed Ali (**b**). This line represents the offshore continuation of the northern line D4 into the Gulf of Oman, with the ophiolite imaged on the left hand side as steeply dipping zone of diffuse reflectivity.

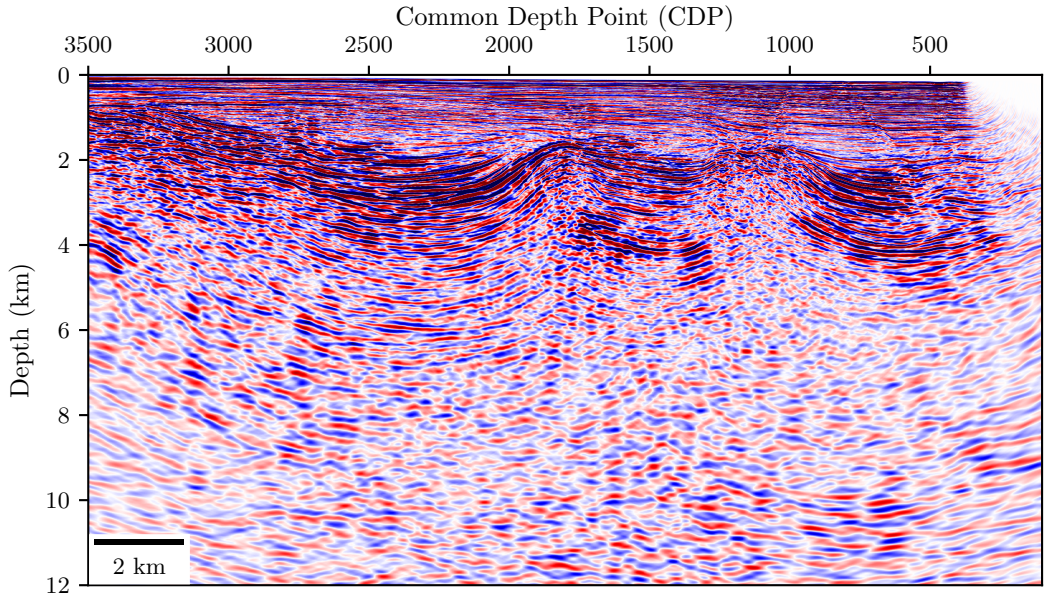


Figure 5.5: The depth migrated seismic line FUJ_DS102P1006. This line represents an offshore continuation of the southern line D1 into the Gulf of Oman. No interpretation was available at the time of writing.

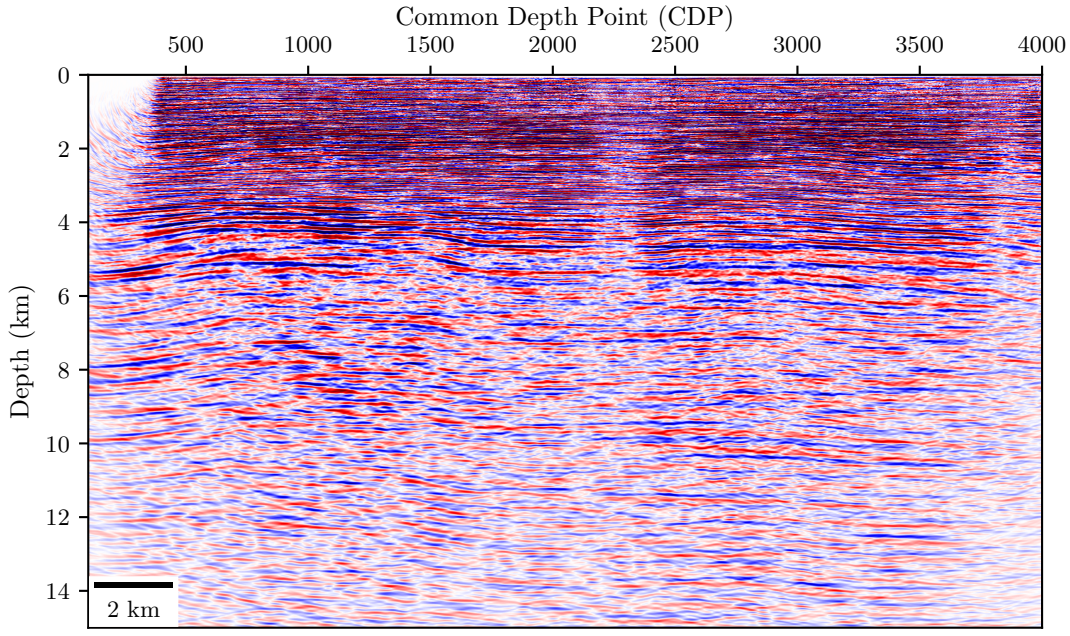


Figure 5.6: The depth migrated seismic line SHJ_RS102P1004. This line represents an offshore continuation of the southern line D1 into the Arabian Gulf. No interpretation was available at the time of writing.

eastwards from here and covers the western side of the UAE-Oman mountains and the hinterland basin offshore. The offshore sedimentary sequence was constrained with the aid of M/V *Hawk Explorer* seismic reflection data.

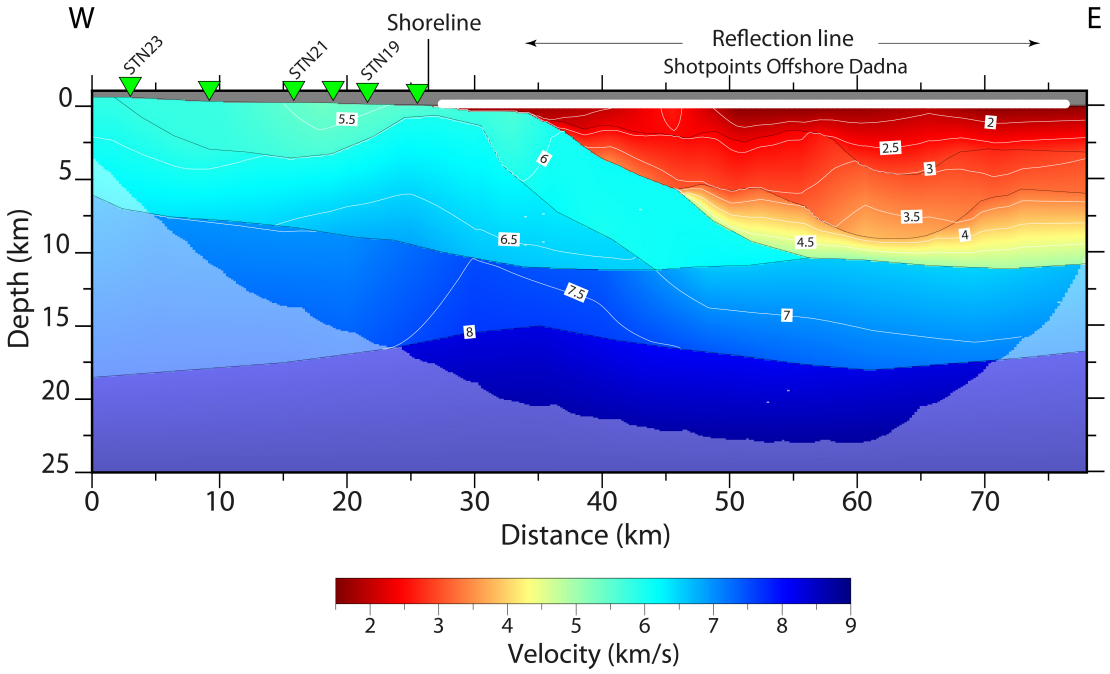
The model, and its associated ray coverage is shown in Figure 5.7a. The rayhits map (Figure 5.7b) shows the model is well covered down to $\sim$ 18 km offshore, and down to $\sim$ 5 km onshore. The hinterland basin is modelled with slow velocities down to $\sim$ 10 km, and show a sharp jump up to $\sim$ 6 $km\,s^{-1}$ into a slanted block that is likely an offshore continuation of the ophiolite as we move onshore. Velocity analysis of the sub-sedimentary section of the model is consistent with typical oceanic crust offshore (Figure 5.8). The contour lines follow the shape of the ophiolite however, and do not show the crust thickening to continental levels. This suggests the sub-ophiolite structure is not imaged by this data.

5.3.4 Receiver functions

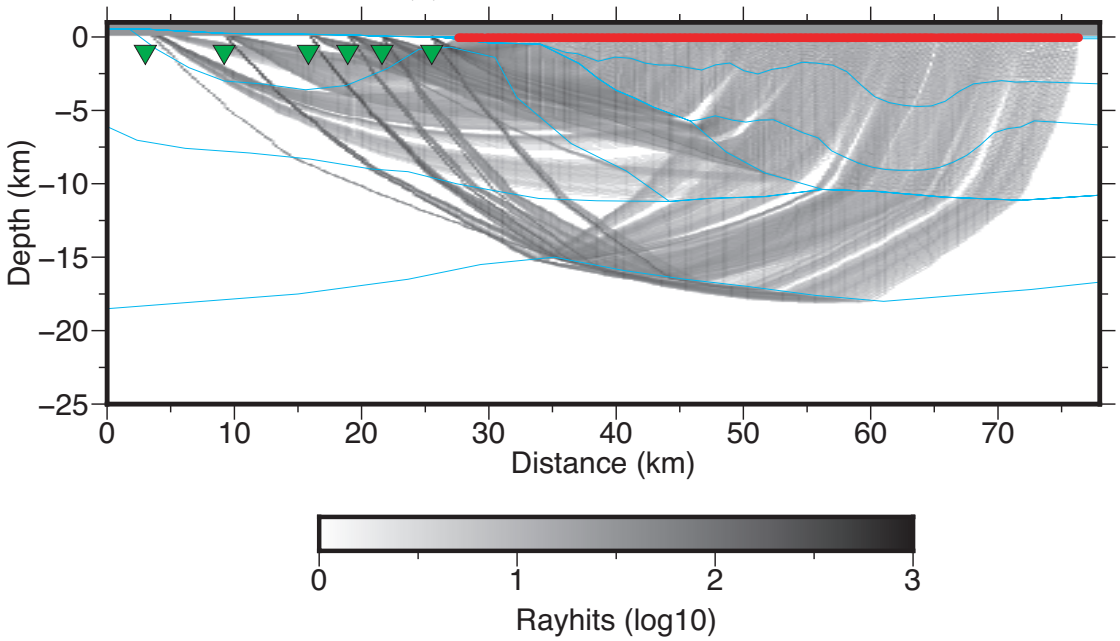
Constraints on the mid to lower crustal structure were obtained via a receiver function study that forms part of this thesis (see Chapter 3). We use the depth points obtained via $H - k$ stacking, and the geometries highlighted in our receiver function profiles as guidance in the creation of our models, and to constrain the depths and spatial extent of key units within our model. The Moho and base ophiolite conversions in particular proved to be very useful constraints.

5.3.5 Surface geology

Surface geology has been mapped extensively in the UAE. The most recent comprehensive geological maps were produced by the British Geology Survey (BGS) in a project undertaken for the Ministry of Energy in the UAE (*Ellison and Styles*, 2006). More recent field mapping by *Ambrose and Searle* (2019) called into question some of their interpretations, in particular their suggestions of mantle rooted shear zones, and late stage magmatism.



(a) D4 refraction model.



(b) D4 refraction model rayhits.

Figure 5.7: The D4 refraction model generated from onshore recordings of airgun shots offshore in the Gulf of Oman (**a**). The ray coverage is shown below (**b**). Figures provided by Simone Pilia.

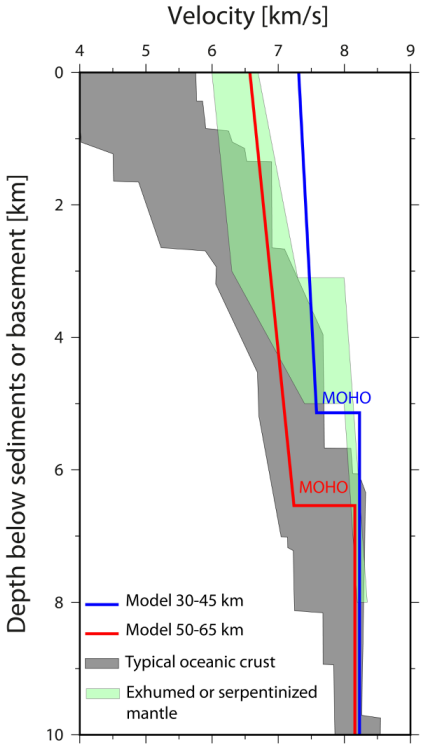


Figure 5.8: Sub-sedimentary velocity profile of two sections of the refraction model shown in Figure 5.7a. Offshore the velocity structure compares favourably with typical oceanic crust. Figure provided by Simone Pilia.

A simplified geological map, based on the work of *Ambrose and Searle* (2019), is presented in Figure 5.9. This map shows the surface extent of obducted oceanic crust (primarily gabbros, displayed in light green) and mantle (primarily hazburgites, displayed in pink) rocks, with their mapped surface extent being used as a key constraint in building our gravity models.

5.3.6 Reference model

In gravity modelling we calculate anomalies based on relative rather than absolute densities. A polygon produces a positive gravity anomaly when its relative density is greater than the the reference density and vice versa. The reference section against which gravity anomalies are computed can therefore have a significant impact on the modelled gravity anomalies. A reference section is defined by three key parameters: The thickness of the crustal column (T_c), the density of the crustal column (ρ_c), and

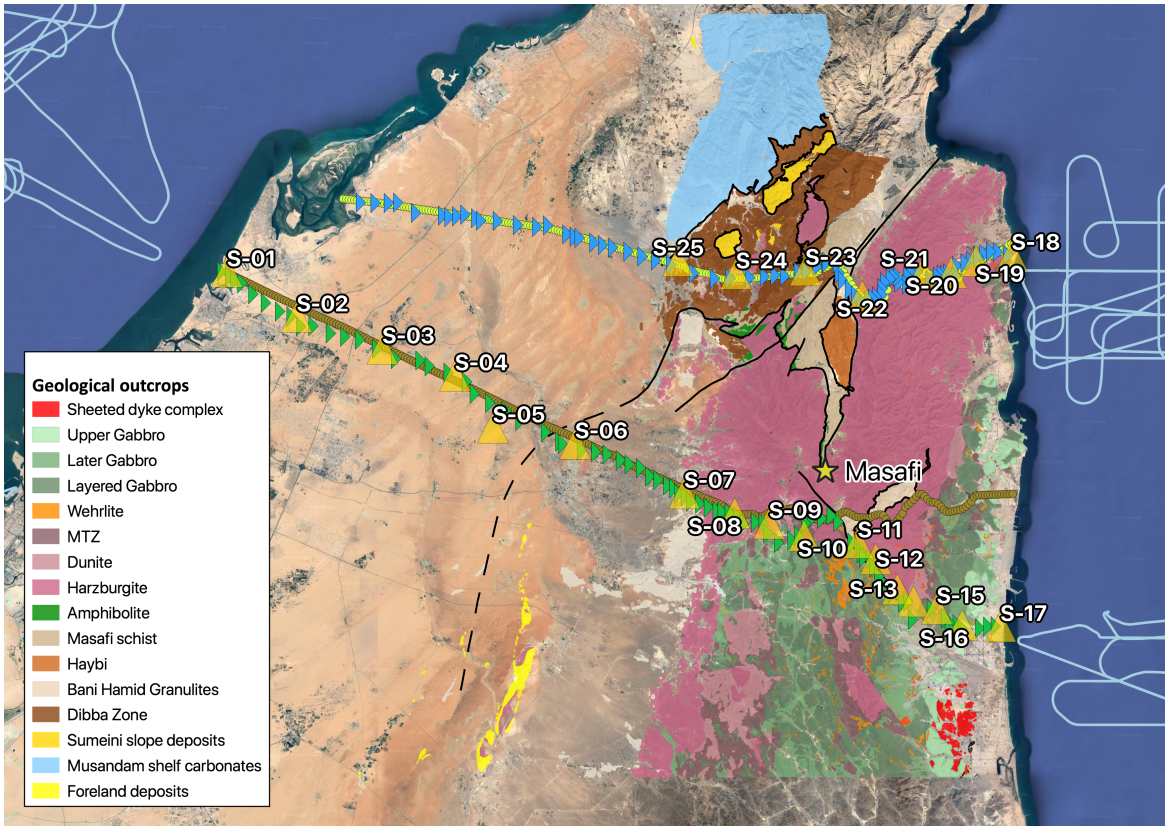


Figure 5.9: Simplified geology of the UAE. Based on the field mapping undertaken by the BGS (*Ellison and Styles*, 2006), and simplified and reinterpreted by *Ambrose and Searle* (2019). The PI seismic network is displayed as golden triangles, and the D1 and D4 seismic and gravity profiles are displayed as small circles and sideways triangles respectively.

the density of the underlying mantle (ρ_m). Care must be taken when determining these parameters to ensure that they are geologically reasonable and appropriate for the tectonic setting. The reference section should also be in isostatic equilibrium, as the gravity anomaly it produces is assumed to be zero.

In this study we incorporate terrestrial and marine gravity datasets, with our profiles extending offshore to potentially include the transition from continental to oceanic crust. It is therefore important that our reference section be appropriate for both continental and oceanic tectonic settings.

We follow the approach of *Cochran* (1981, 1983) and determine our reference section by balancing pressures of a continental lithospheric column against a lithospheric column at a mid-ocean ridge (MOR), as the latter is known to be in isostatic equilibrium.

Parameter	Symbol	Value
Lithospheric thickness	t_L	125 km
Continental crust thickness	t_c	31.2 km
Water column thickness	t_c	2.5 km
Oceanic crust thickness	t_c	5 km
Continental crustal density*	ρ_c	2770 $kg\,m^{-3}$
Oceanic crustal density*	ρ_c	2800 $kg\,m^{-3}$
Mantle density*	ρ_m	3330 $kg\,m^{-3}$
Water density	ρ_w	1030 $kg\,m^{-3}$
Asthenosphere temperature	T_a	1333 $°C$
Coefficient of thermal expansion	α	3.4×10^{-5} $°C^{-1}$
Specific heat capacity of the asthenosphere	c_p	1000 $J\,K^{-1}$
Gravitational acceleration	g	9.81 $m\,s^{-2}$

Table 5.2: Values of parameters used in computing our reference section. The * indicates the value at 0°C, the actual value will decrease with depth due to thermal expansion and the geothermal gradient.

The parameters used in computing our reference section are shown in Table 5.2, and the columns shown in Figure 5.10. The parameters were selected so as to produce equivalent pressures at compensation depth for both the continental and MOR columns to ensure isostatic equilibrium.

The reference section accounts for thermal expansion with a linear geothermal gradient from the top of the crust to the asthenosphere. The temperature at the base of the asthenospheric column of the MOR section is computed with the equation for adiabatic compression in *McKenzie and Bickle* (1988) and a linear gradient again assumed. The density in both sections will therefore decrease with depth.

The reference value that we compute gravity anomalies against will be the mean crustal density (2754 $kg\,m^{-3}$), and the upper mantle density (3290 $kg\,m^{-3}$) of the continental reference section.

5.3.7 GMG

Object oriented gravity modelling for this project was undertaken using a graphical user interface (GUI) developed by Brook Tozer as part of his D.Phil (*Tozer et al.*, 2017). The program is called *GMG*, shorthand for Geophysical Modelling GUI, and is intended

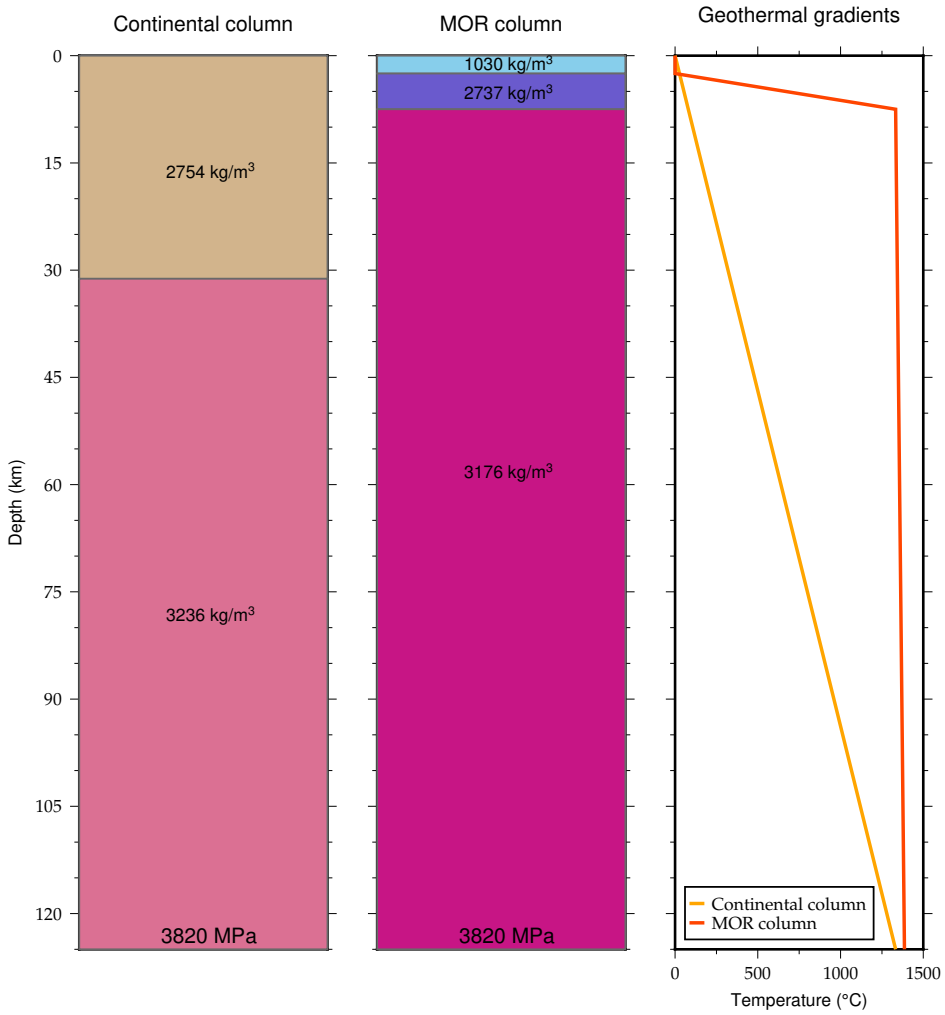


Figure 5.10: Continental reference section used for our gravity model. The continental column produces the same pressure at compensation depth as the mid-ocean ridge (MOR) column (3820 MPa), and can therefore be considered to be in isostatic equilibrium. The geothermal gradient of each column is shown to the right. Densities listed are mean values for each respective section.

to be open source, collaboratively developed geophysical modelling project. It is being developed in *python*, a flexible cross-platform programming language, and was in the *beta* stages of development at the time of writing. Its development can be followed, and a free copy downloaded at `https://github.com/btozer/gmg`. GMG computes 2D gravity anomalies using the line integral method described in Section 5.2.1.

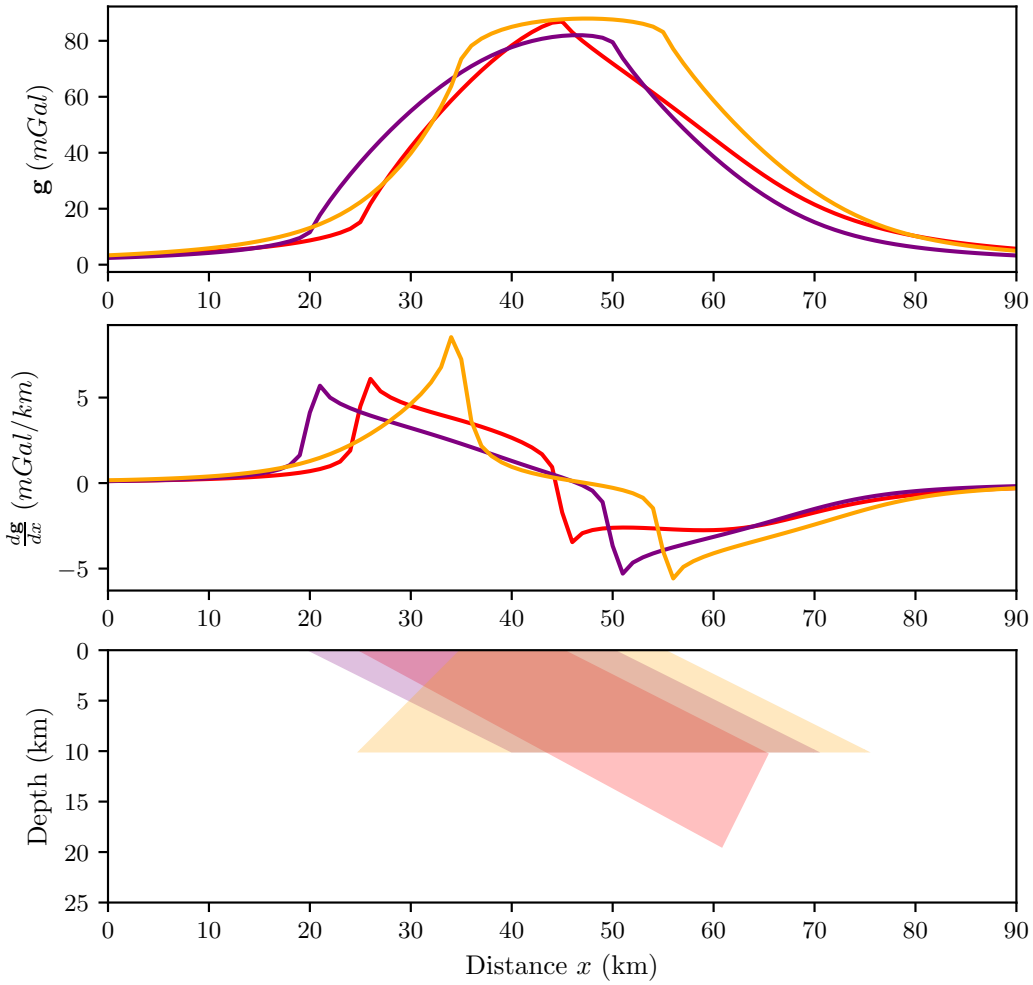


Figure 5.11: The gravity anomalies (**g**) that would be produced if the ophiolite were modelled as an acute trapezoid (yellow), a parallelogram (purple), and a tilted block (red) with $\Delta\rho = +250\ kg\,m^{-3}$. The horizontal gravity gradient ($\frac{d\mathbf{g}}{dx}$) of each geometry is shown to further highlight the key differences between each model.

5.3.8 Simple models

While we have a comprehensive dataset upon which to build a detailed gravity model, it can be helpful to begin by modelling some basic geometries and comparing them to the observed gravity anomaly (e.g. *Bott* (1956, 1967)).

The anomaly that would be produced if the ophiolite were modelled by some basic

geometries (an acute trapezoid, a parallelogram, and a tilted block), and a density contrast of $\Delta\rho = +250\ kg\,m^{-3}$ are shown in Figure 5.11:

- The example of an acute trapezoid (yellow in Figure 5.11) shows that if the western margin of the ophiolite were sloped outwards the associated gravity anomaly would be flat topped, with convex build ups on either side. The horizontal gradient gradually builds up to a peak where surface outcrops begin, and follows the reverse trend on the opposite side.

- The example of a parallelogram (purple in Figure 5.11) shows the more likely configuration of eastward sloping sides at both ends. This results in a concave build up and a shallow convex drop-off in gravity. The horizontal gradient shows rapid build-up to a peak where outcrops begin and gradual drop-off back to zero, before repeating the pattern with opposite polarity as the contact drops off on the other side.

- The example of a truncated tilted block (red in Figure 5.11) results in a more triangular peak in the gravity anomaly and an almost linear drop-off as the ophiolite drops away to the east. The horizontal gradient shows a similar pattern to the parallelogram on its western edge, but is notably different on its eastern margin. Here a constant negative gradient persists until the edge of the buried ophiolite, after which it gradually returns to zero as in the other examples.

Comparing the gravity signature of these shapes to our data can give us an idea as to the rough geometry of the obducted ophiolite block. The gravity anomalies and horizontal gradients of the combined onshore-offshore gravity dataset along two 120 km profiles coincident with D1 and D4 are shown in Figure 5.12. Of the shapes tested, the parallelogram most closely approximates the observed gravity anomalies. The sharp onsets in the horizontal gradient at $\sim 45\ km$ along both profiles suggest an eastward sloping contact on the western side. The slower decline and recovery as we move offshore suggests an eastward sloping contact here as well without the deeper root of the tilted block.

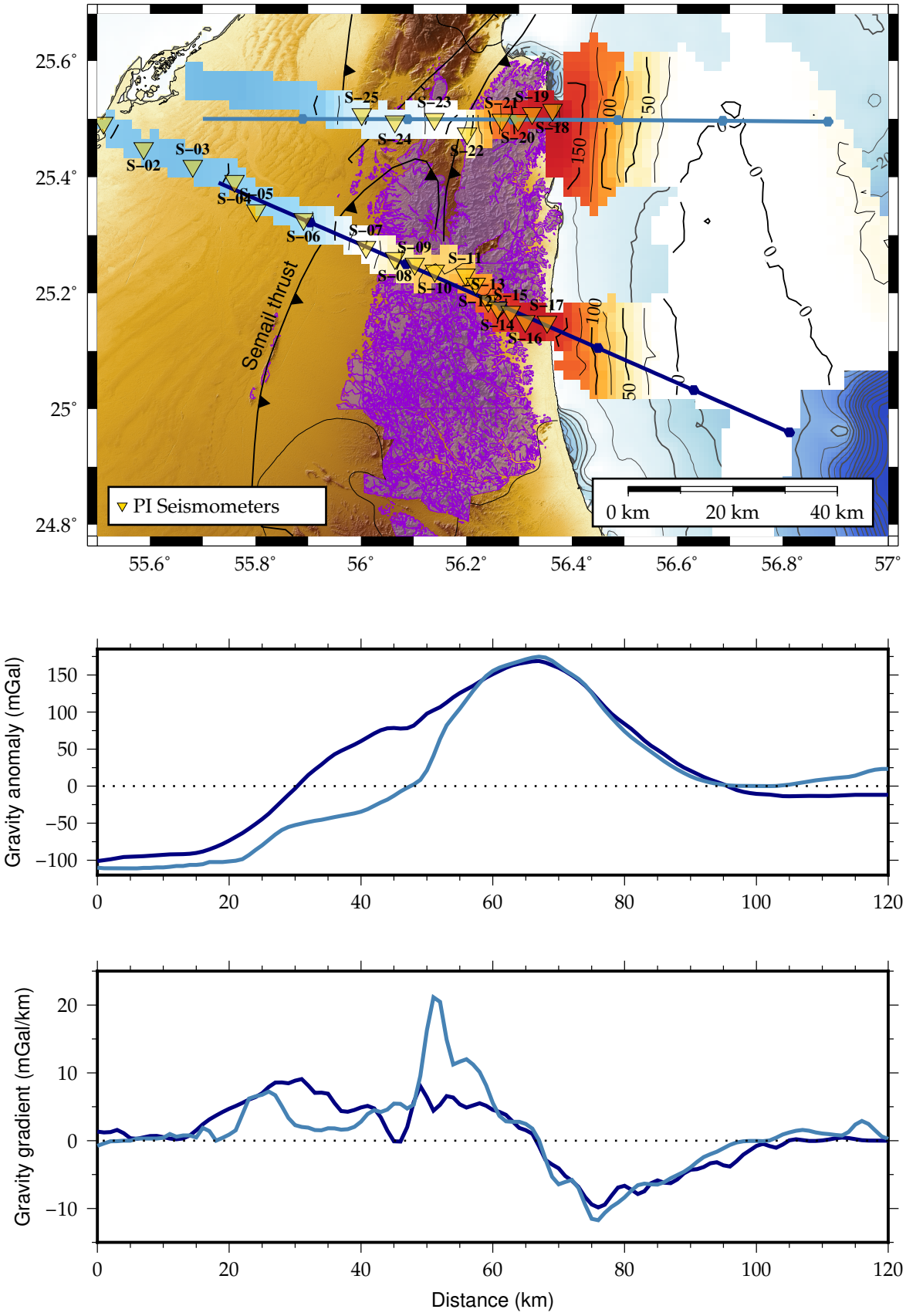


Figure 5.12: The gravity anomalies and horizontal gradients (Bouguer onshore and free-air offshore) of the combined gravity dataset are projected along two 120 km profiles coincident with D1 (dark blue) and D4 (light blue). Notches on the profiles mark 20 *km* intervals.

The observed data is of course the superposition of the gravity signature of all the geological units in the crust and upper mantle along both profiles, and we will model these sources in more detail in the next section. It is however interesting to note that at a density contrast of $\Delta\rho = +250\ kg\,m^{-3}$ and thickness of 10 km, our modelled geometries are still well short of reproducing the $\sim 160\ mGal$ gravity anomalies observed across the ophiolite. This implies that both the thickness and/or bulk density of the obducted ophiolite block must be significantly higher than these values.

5.3.9 D1 gravity model

The D1 gravity profile extends 160 km east - southeast from offshore in the Arabian gulf, across the foreland basin and UAE-Oman mountains to extend $\sim 30\ km$ offshore in the Gulf of Oman (Figure 5.13). Data from our combined onshore-offshore gravity dataset (see Section 4.8) is projected onto this profile using the *GMT project* and *grdtrack* functions. Note that a kink is present at 30 km in this projected profile. This is an artifact arising from a gap in data between our onshore and offshore gravity datasets in this part of the profile, and we do not attempt to reproduce it in our model.

This profile follows the original D1 seismic line across the foreland, but deviates at Masafi to follow our seismometer network and gravity profile down to Fujairah city. This seismic line, and the models based upon it (i.e. *Naville et al.* (2013)), provide key constraints for the shallow crustal structure of the foreland basin.

Across the ophiolite surface geology provides a key clues to the subsurface structure, as it delineates the transitions from foreland sediments, to obducted passive margin units, upper mantle peridotites, and massive and layered gabbro of the obducted oceanic crust. This geological data is of only limited use when it comes to inferring the subsurface structures though, and we turn to geophysical data to fill in some of this knowledge gap.

Offshore in the Arabian Gulf the shallow crustal structure is constrained by the seismic line *SHJ_RS102P1004* (Figure 5.6), which is offset to the north from our 2D profile. The structure here appears to be sufficiently homogenous for this offset not

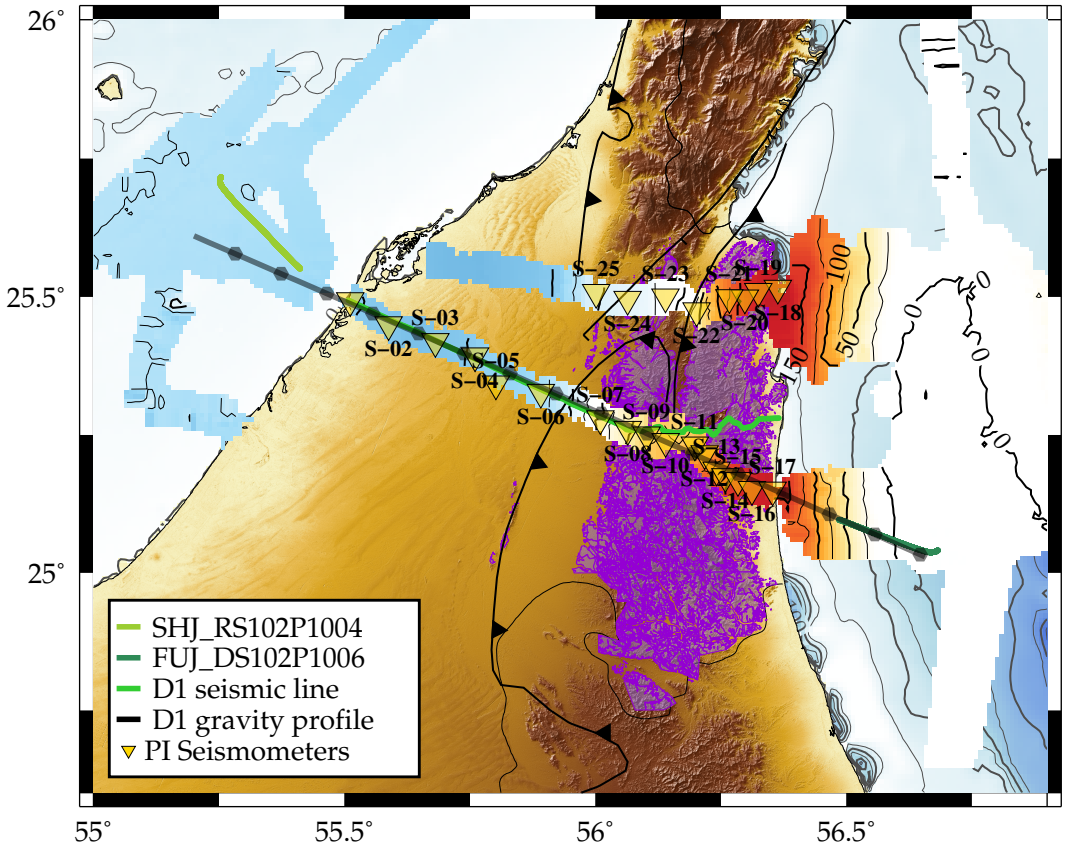


Figure 5.13: Map showing the location of the D1 gravity profile, marked at 10 *km* intervals. Locations of the PI seismic network and the relevant offshore seismic lines are marked, along with the original D1 seismic profile on which our profile is based. Ophiolite outcrops are marked in purple.

to matter though. At the other end of the gravity profile the line *FUJ_DS102P1006* (Figure 5.5) again provides constraints on the shallow structure offshore in the Arabian Gulf.

Receiver function results and their $H - k$ stacking depths from 17 onshore seismic stations provide the only constraints on mid to lower crustal structure across the foreland basin and ophiolite. We interpret the deeper of the potential Moho results below the UAE-Oman mountains as the Moho, and the eastward dipping set of reverse polarity results as our base ophiolite interface. The other scattered results were more difficult to interpret, and matching these to associated interfaces was of secondary importance.

Our model is displayed in Figure 5.14.

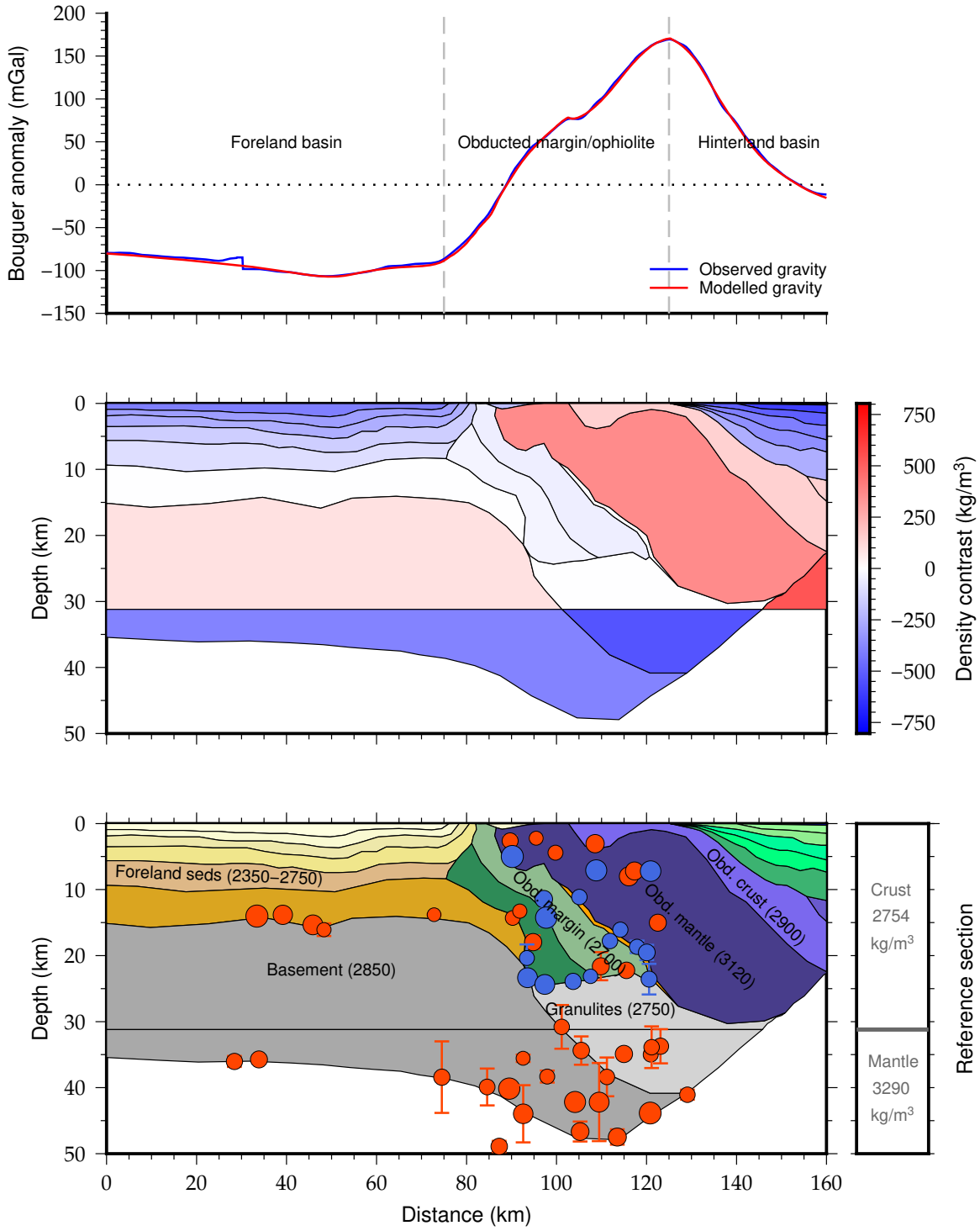


Figure 5.14: The 2D gravity model for the southern profile D1. The observed and modelled gravity data is shown top, with dotted lines dividing the tectonic regimes. Note that the kink in the observed gravity anomaly at $\sim 30\ km$ is an artifact of the projection, and we do not attempt to reproduce it. The mass distribution relative to our reference model (bottom right) is shown middle, with red indicating polygons with a mass excess and blue a mass deficit. A geological interpretation of the model is shown bottom, with the obducted (obd.) and sedimentary (seds) units labelled, and normal (red) and reverse polarity (blue) receiver function depth points from $H - k$ stacking overlain.

Building a model that satisfied all of these constraints and accurately reproduced the observed gravity anomaly was challenging, and required many iterations.

We reproduce the large $\sim -110\ mGal$ negative anomaly observed in the foreland with a combination of a $\sim 15\ km$ thick, low density sedimentary sequence ($2200 - 2700\ kg\,m^{-3}$) and a Moho some $\sim 5\ km$ deeper than our reference section at $\sim 36\ km$.

From $75\ km$ the observed gravity anomaly increases rapidly to a peak of $\sim 160\ mGal$ at $125\ km$, with a slight kink at $105\ km$ near Masafi. This portion of the profile was the most difficult to model, with surface geology providing hard constraints on outcrop extent and rock type (and therefore density) near the surface and receiver functions constraining the Moho and base ophiolite surface. A root, that is interpreted to be flexural in origin, extends down $\sim 12\ km$ to $\sim 48\ km$ depth at $110\ km$ before rapidly shallowing eastwards, provides a large mass deficit. The expected densities of the obducted margin and metamorphic sole ($\sim 2700\ kg\,m^{-3}$), and the inferred presence of granulites below the ophiolite both also provide neutral to slightly negative contributions to the modelled gravity anomaly. A thick, dense ($3120\ kg\,m^{-3}$) body of peridotites is therefore required to counteract these negative contributions. This unit is slightly folded at its western end, and dips eastwards at $\sim 35°$ past $90\ km$. The reverse polarity receiver function results in this region from $10-20\ km$ provide support for the thickness and geometry of this unit. A lower density ($2900\ kg\,m^{-3}$) crustal layer was modelled separately to match surface outcrops of gabbro, and a shallower density contrast helped reproduce some features of the observed anomaly (e.g. the kink near Masafi).

The observed gravity anomaly decreases rapidly again from $125\ km$ as we approach the eastern coastline and the Gulf of Oman. Reflection and refraction seismic provide constraints on the shallow structures, and point to the presence of a rapidly dipping ophiolite contact and thick ($\sim 10\ km$) sedimentary sequence. Pairing these features with typical sedimentary densities ($2150 - 2500\ kg\,m^{-3}$) accurately reproduces both the shape and magnitude of the observed gravity anomaly in this part of the model. However a large mass excess is required to bulk shift the signal upwards to match the

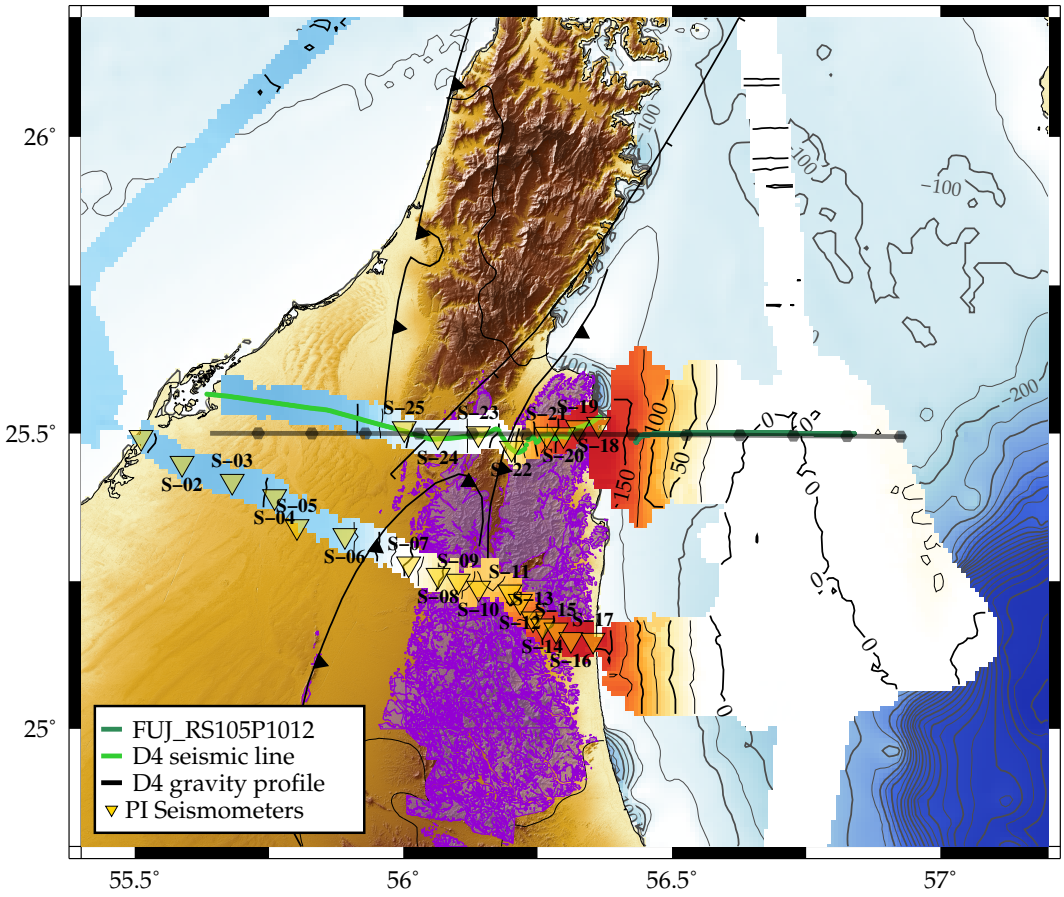


Figure 5.15: Map showing the location of the D4 gravity profile, marked at 10 *km* intervals. Locations of the PI seismic network and the relevant offshore seismic lines are marked, along with the original D4 seismic profile on which our profile is based. Ophiolite outcrops are marked in purple.

near zero gravity signal observed further offshore however, and this is achieved with a layer of in situ oceanic crust below the sediments and a shallow ~ 20 *km* Moho.

5.3.10 D4 gravity model

The D4 gravity profile extends 130 *km* due east, starting from a point $\sim$ 10 *km* inland from the Arabian Gulf coastline and $\sim$ 6 *km* north of the southern profile D1, and finishing $\sim$ 55 *km* offshore in the Gulf of Oman (see Figure 5.15). Data from our combined onshore-offshore gravity dataset (see Section 4.8) is projected onto this profile using the *GMT project* and *grdtrack* functions.

The profile follows the D4 seismic line on land (though it deviates to the south

slightly in the foreland to keep the line straight), and extends offshore in the Gulf of Oman to the edge of our marine dataset. This seismic line, and the models based upon it (i.e. *Tarapoanca et al.* (2013)) provide key constraints in the foreland and western mountains.

Surface geology again provides hard constraints for several units across the ophiolite, with the obducted sediments of the Haybi and Hawasina exposed west of the Semail thrust, and peridotites exposed to the east. Near the Gulf of Oman coastline gabbros and granites of the obducted crust appear sporadically, marking a transition from the obducted mantle to the crust.

Offshore in the Gulf of Oman the upper crustal structure is well constrained by the seismic line *FUJ_RS105P1012* (see Figure 5.4), and the refraction model of Simone Pilia (see 5.3.3).

Receiver functions from 8 seismic stations again provide some constraints on the deeper structure across the ophiolite, but our network did not extend into the Foreland basin to the west on this profile so we infer similar deep structure here to that observed from receiver function results to the south on line D1. We again interpret the deeper of the potential Moho results below the UAE-Oman mountains as the Moho, and the eastward dipping set of reverse polarity results east of the Semail thrust as our base ophiolite interface. The other scattered results were also difficult to interpret on this line, and matching these to associated interfaces was again of secondary importance.

Our model is displayed in Figure 5.16. It shares many features with our D1 gravity model, but differs significantly in some places.

The large amplitude $\sim -110\,mGal$ negative anomaly in the foreland is again reproduced in much the same way to line D1, with a $\sim 15\ km$ thick, low density sedimentary sequence ($2200 - 2700\ kg\,m^{-3}$) and a deep Moho at $\sim 35\ km$ depth.

Ophiolite outcrops are almost entirely absent west of the Semail thrust, so the western half of our mountains are modelled with the thick slightly negative relative density units of the obducted Haybi ($2670\ kg\,m^{-3}$) and Hawasina ($2700\ kg\,m^{-3}$) blocks from $\sim 35 - 55\ km$ to give us the step from ~ -110 to $\sim -40\ mGal$ with a gradual

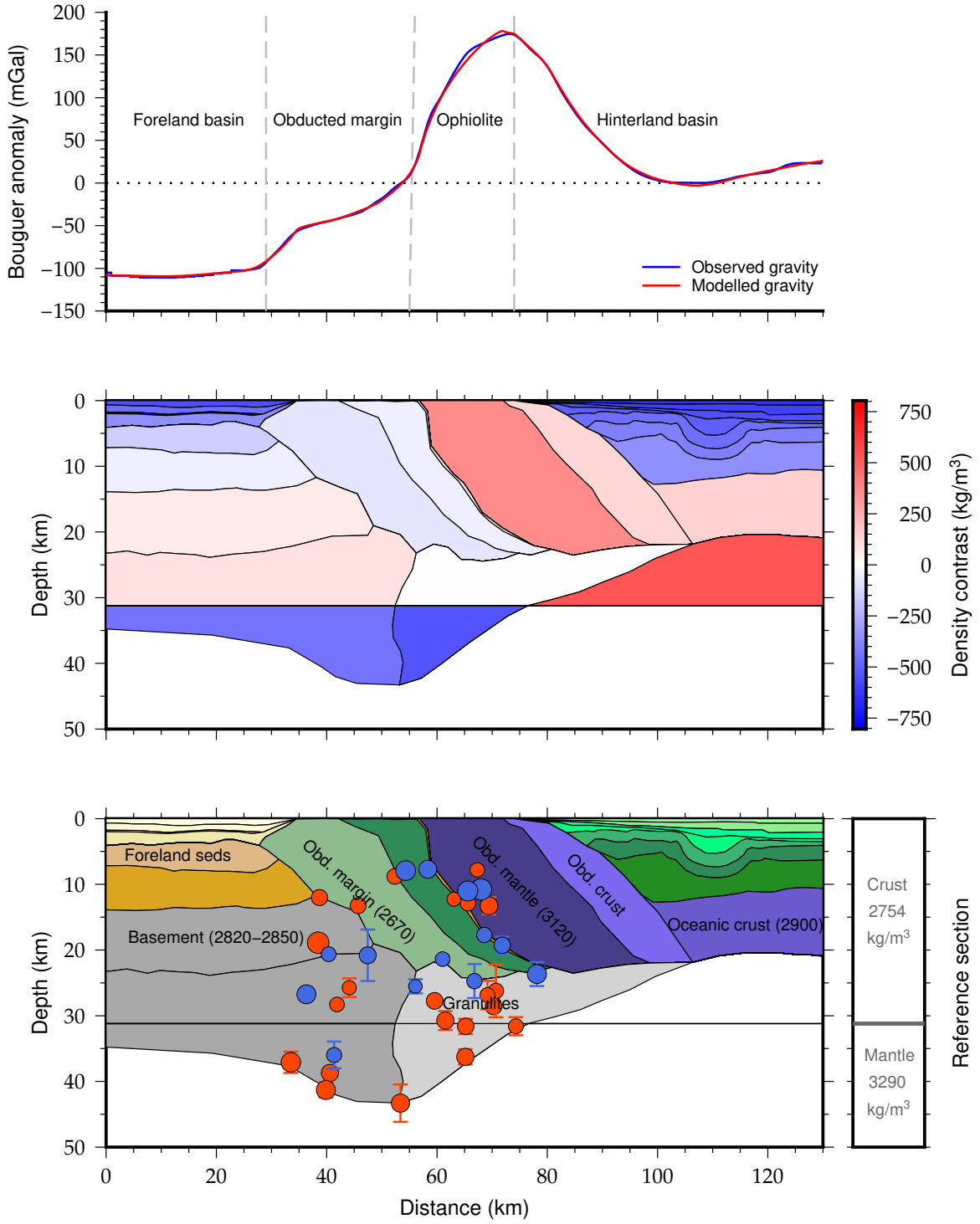


Figure 5.16: The 2D gravity model for the southern profile D4. The observed and modelled gravity data is shown top, with dotted lines dividing the tectonic regimes. The mass distribution relative to our reference model (bottom right) is shown middle, with red indicating polygons with a mass excess and blue a mass deficit. A geological interpretation of the model is shown bottom, with the obducted (obd.) and sedimentary (seds) units labelled, and normal (red) and reverse polarity (blue) receiver function depth points from $H - k$ stacking overlain.

gradient eastwards. Receiver functions suggest the Moho flexes down $\sim$ 10 km to $\sim$ 45 km depth here, which increases the long wavelength low in this part of the model.

The Semail thrust marks the start of bulk peridotite outcrops, and a dramatic increase in the gradient of the gravity anomaly. We reproduce this with an almost vertically dipping, dense obducted mantle unit (3120 $kg\,m^{-3}$) that slopes eastward below 10 km depth at $\sim 50^{\circ}$ to reach a maximum depth of $\sim$ 25 km near the coastline at $\sim$ 75 km. An eastward shallowing mantle in this part of the model helps us reach the maximum observed gravity anomaly of $\sim$ 160 $mGal$ at 72 km.

In the hinterland basin offshore in the Gulf of Oman the gravity anomaly drops down rapidly from its peak to 0 $mGal$ at 105 km before increasing slightly to $\sim$ 20 $mGal$. The seismic data imaged a thicker sedimentary sequence here than the offshore part of the D1 model, with coherent reflections down to $\sim$ 10 km. The observed gravity anomalies were similar however, so our basin depth here is only slightly deeper than on the D1 model. A rapidly shallowing Moho again counteracts the gravity low these sediments would otherwise produce, to give us the neutral anomaly observed.

The slight decrease in gravity gradient between $64 - 72$ km was the only aspect of the observed gravity anomaly that we were not able to satisfactorily reproduce. The mapped surface geology precludes any kind of facies change and the receiver function results put the lower surface of the obducted mantle unit too deep to produce the wavelength required. It may represent a buried inclusion. The terrain is also particularly inaccessible here so it is possible that there are some previously unmapped facies changes. Receiver functions results also suggested that the base ophiolite contact was relatively flat inland, before dropping off sharply near the coastline. We were unable to reproduce this in our gravity model, as the western-most receiver function depth points for the flat portion of this interface were west of the Semail thrust, and a flat base with a sharp dropoff did not reproduce the steep gradient needed east of this marker.

5.4 Discussion

Building the gravity models shown in Figures 5.14 and 5.16 has been a long process, and they have gone through many iterations. The first versions were built along the northern profile D4 using just the marine gravity data, with onshore segments filled in by global gravity data sets. These were progressively updated as the onshore gravity surveys were completed, reflection seismic data results became available, refraction models were completed, and receiver function results added and progressively refined.

The refraction models in particular proved to be a real challenge to incorporate. In an ideal world a refraction and a gravity model should be complementary, with the contours and velocities of the refraction model informing the geometries and densities of the gravity model and vice versa. For this project this only proved to be partially true, and significant problems were encountered when we tried to convert the modelled velocities across the ophiolite to densities, and vice versa.

The relationship between density and seismic velocity is well established (e.g. Birch's law, or Gardner's rule). It is perhaps best known, and most widely applicable, as the Nafe-Drake curve/relation (*Ludwig et al.*, 1970), shown in Figure 5.17. *Brocher* (2005) formalised this relation in the polynomial

$$\rho = 1.6612v_p - 0.4721v_p^2 + 0.0671v_p^3 - 0.0043v_p^4 + 0.000106v_p^5 \tag{5.8}$$

where v_p is compressional seismic velocity and ρ is density. While the predictive relationship between these two properties is not perfect, experimental results generally plot within $\pm 10\%$ of the curve described by this equation (see Figure 5.17).

A direct gravity conversion of the D4 refraction model displayed in Section 5.3.3 is shown in Figure 5.18. This was created by extracting the velocities contours of the refraction model, importing these polygons into our gravity modelling software, and converting the velocity of each polygon to density using the Nafe-Drake relationship defined in Equation 5.8. This Figure shows that the relatively low velocities used to model the ophiolite in the refraction model ($5.5 - 6.5\ km\,s^{-1}$) do not translate into the

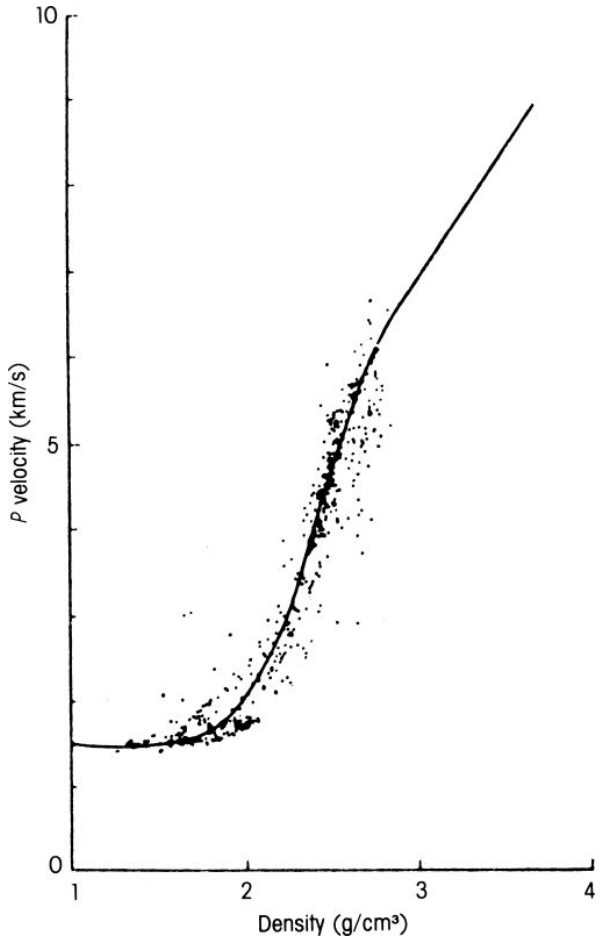


Figure 5.17: The Nafe-Drake curve, illustrating the relationship between density and seismic velocity. Figure taken from the SEG wiki page (`https://wiki.seg.org/wiki/Dictionary:Nafe-Drake_relation`).

densities required to produce the large gravity anomaly observed across the ophiolite in the gravity model, and in fact result in a slightly negative gravity contribution. A secondary problem was that the shallow westward dipping Moho of the refraction model results in too great a mass excess from the shallow mantle, and results in a $\sim 100\ mGal$ bulk shift between of modelled and observed gravity anomalies.

The problem is partially related to the lack of ray coverage in the refraction model below $\sim 15\ km$ depth, as well as the limited coverage onshore. Testing end member scenarios suggested the minimum bulk density at which the ophiolite could be feasibly modelled was $\sim 2950\ kg\,m^{-3}$, in which case it would occupy the entire crust. According to Equation 5.8, such a density would translate into a seismic velocity $\sim 7.10\ km\,s^{-1}$,

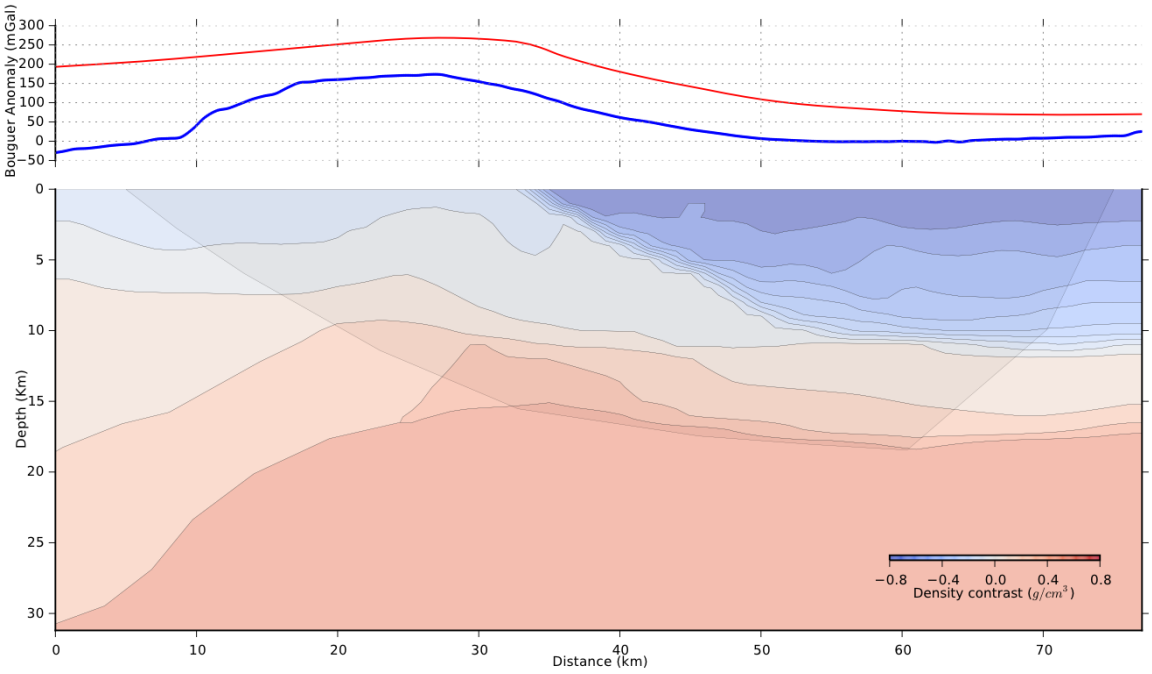


Figure 5.18: A direct conversion of the D4 refraction model to gravity using the Nafe-Drake relationship (Equation 5.8). The shaded area indicates the ray coverage of the refraction model. The observed gravity anomaly is displayed top in blue, with the modelled anomaly in red.

significantly faster than the velocities used for the ophiolite in both this, and previous refraction models (e.g. *Naville et al.* (2013)).

Significant time and effort was put into trying to resolve this discrepancy, and while we managed to find good agreement in our models offshore in the Gulf of Oman, we could not find a way around the velocity - density problem.

Christensen and Smewing (1981) obtained direct measurements of both density and seismic velocity from ophiolite samples in the north of Oman, to the south of our study area. They obtained mean compressional velocities of $6.7 - 7.5\ km\,s^{-1}$ for gabbroic samples, and $7.8 - 8.5\ km\,s^{-1}$ for un-serpentinised ultramafic samples. This suggests bulk velocities should be much higher than the $5.5 - 6.5\ km\,s^{-1}$ used in these refraction models, especially since the majority of the ophiolite body is expected to be ultramafic dunites and hazburgites.

Two possible mechanisms for explaining the lower modelled seismic velocities within the ophiolite are serpentinisation and fracturing. *Miller and Christensen* (1997) have

described the effects of both these mechanisms on gabbroic and ultramafic samples collected south of the Kane transform at the mid-Atlantic ridge. Their results show that serpentinisation has a dramatic effect on seismic velocity, and bulk serpentinisation fractions of $60-100\%$ would bring the velocities down to the values presented in the refraction models. Their work also shows that serpentinisation has a dramatic effect on bulk density though, with values from $2500-2800\ kg\,m^{-3}$ for $60-100\%$ alteration, too low to reproduce the large gravity anomalies observed across the ophiolite. The bulk density favoured for ultramafic rocks in our gravity model ($3120\ kg\,m^{-3}$) suggests bulk serpentinisation is relatively minor, at around 30%.

Fracturing and de-pressurisation are a more likely explanation for the discrepency. *Miller and Christensen* (1997) found measured compressional velocities dropped by $\sim 10\%$ when measured at low versus high pressures for both gabbros and serpentinised peridotites. *Christensen and Smewing* (1981) measured compressional velocity as a function of porosity for a number of Oman ophiolite samples and found a similar effect, with measured velocities dropping by up to 17% for a $\sim 5\%$ increase in porosity. Large scale fracturing, and small scale micro-fractures within the ophiolite could therefore account for the lower velocities favoured by the refraction models, without significantly impacting the density. A 5% decrease in the density of unaltered peridotite would reduce it from $3290\ kg\,m^{-3}$ to $3125.5\ kg\,m^{-3}$, similar to the values used in our models. A 5% porosity value across the whole ophiolite is probably unrealistic however, and serpentinisation is still likely to play a role.

The choice of reference section employed for full crustal gravity models can also have a significant impact on the resulting model. Our model covers both continental and oceanic domains so it was important to have a reference section that could work for both. A thicker reference section can be favoured for continental models, and this would have reduced the impact of the thickened foreland and flexural root, but it would have also increased the mass excess associated with the shallow Moho offshore in the Gulf of Oman. An intermediate choice was therefore deemed more appropriate.

Our models accurately reproduce the gravity anomalies observed along both profiles

D1 and D4, but there is undoubtedly a great deal of complexity that these models do not capture. This is evidenced by the number of $H - k$ stacking depth points that do not correspond to any particular interface in our model, and by the high degree of scattering observed at many stations in our receiver function study. There is also an inherent trade off in any gravity model between geometry and relative density, so the geometries presented in this model should be treated as approximations (especially in the absence of external constraints). We have also ignored out-of-plane effects in generating these 2D models. While both profiles are broadly orthogonal to the strike of the obducted crust and mantle blocks, making a 2D assumption reasonable, the ophiolite is also observed to be tilted slightly to the south in this region (e.g. *Ambrose and Searle* (2019)), and this is not captured in our models.

5.5 Chapter Summary

In this chapter we have introduced and described 2D gravity modelling methods. We then described the key external constraints on our gravity models (density data, reflection and refraction seismic data, receiver functions, and surface geology), and constructed two 2D gravity profiles along the passive seismic/gravity profiles D1 and D4. Our models showed that:

1. The large ~ -110 $mGal$ Bouguer anomalies observed in the western foreland basin could be explained by a combination of a $\sim$ 15 km thick sedimentary sequence, and a thickened (relative to our reference section) 36 km crust.

2. The steep gravity gradients, and large ~ 160 $mGal$ Bouguer anomalies observed across the UAE-Oman mountains could be explained by a series of thick, tilted, thrust sheets representing the obducted passive margin and ophiolite.

3. The obducted ophiolite needed to be both thick ($\sim$ 20 km), and dense ($\sim$ 3120 $kg\,m^{-3}$) in order to reproduce the ~ 160 $mGal$ observed Bouguer anomalies.

4. The large mass deficit associated with the thick hinterland sedimentary basin is counteracted by a large mass excess associated with a rapidly thinning Moho as we transition from continental to oceanic crust offshore in the Gulf of Oman.

5. The high density required to model the ophiolite (3120 $kg\,m^{-3}$) suggests bulk serpentinisation of obducted peridotites is minimal ($< 30\%$), and the relatively low velocities implied by refraction modelling are likely are result of large and small scale fracturing generated during the obduction process.

Chapter 6

Discussion, conclusions, and future work

6.1 Discussion

In this thesis we set out to constrain the thickness and subsurface geometry of the Semail ophiolite complex, investigate its offshore extent, examine the nature of the underlying Arabian margin by obtaining Moho depths, and investigate the transition from continental to oceanic crust further offshore in the Gulf of Oman.

To achieve this we primarily relied on two geophysical datasets: A passive seismic dataset acquired across a network of 25 seismometers arranged in two profiles over 2.4 years, and a gravity dataset consisting of marine gravity data acquired during a cruise in 2014, and 149 unique new land gravity measurements acquired across two profiles coincident with our seismic network. These datasets provided the basis for two new 2D gravity models across the foreland basin, Semail ophiolite complex and hinterland basin, and provide new insights into the crustal structure in the region.

6.1.1 Ophiolite thickness and geometry

The thickness of the ophiolite has previously been estimated to be $20 - 25\ km$ based upon field mapping of surface outcrops (e.g. *Searle* (2007); *Searle et al.* (2014)). Direct

measurements of its thickness were limited though, with its base only weakly imaged in a few localities by reflection seismic data (i.e. *Naville et al.* (2013); *Tarapoanca et al.* (2013)). We have interpreted the negative polarity 'slow to fast' receiver functions obtained along the east of the UAE-Oman mountains to mark the base of the ophiolites obducted upper mantle, and we believe these results provide the best constraints yet on its in situ thickness.

On the southern profile, D1, results dip linearly eastwards at $\sim 30°$ from $\sim 10\ km$ depth near Masafi, to $\sim 25\ km$ near the Gulf of Oman coastline. On the northern profile, D4, there appears to be a step in ophiolite thickness near the Gulf of Oman coastline, as depths based on receiver functions are relatively flat at $\sim 10\ km$ eastwards of S-20, before stepping down rapidly to $\sim 25\ km$ near the Gulf of Oman coast again.

Gravity modelling confirmed a $\sim 20\ km$ thick, dense ($\sim 3120\ kg\,m^{-3}$) ophiolite was required to reproduce the $\sim 160\ mGal$ Bouguer anomalies observed across the ophiolite. These modelling results also raised the possibility that the ophiolite may be rooted in the mantle offshore in the Gulf of Oman. Previous authors have argued against such a model (e.g. *Manghnani and Coleman* (1981); *Shelton* (1990); *Ravaut et al.* (1997)). However our work suggests the ophiolite in the UAE may be at least double the thickness suggested by previous models, and can feasibly extend down $\sim 25\ km$ depth to link up with the shallowing Moho below the Gulf of Oman hinterland basin.

6.1.2 Offshore extent

An offshore continuation of the ophiolite in the UAE has been suggested by previous authors (e.g. *Khattab* (1993); *Ali and Watts* (2009); *Ali et al.* (2014)), and has been modelled at the south-eastern end of the ophiolite, offshore Muscat by *Manghnani and Coleman* (1981). The gravity data we have acquired, with a peak anomaly at the Gulf of Oman coastline and high values continuing offshore supports this conclusion.

Reflection seismic data acquired for this project reveals a diffuse reflector dipping eastwards at $\sim 45°$ that has been interpreted as a major normal fault marking the

top of the ophiolite offshore (e.g. Figure 5.4, *Ali et al.* (2019)). Seismic refraction modelling also supports this conclusion, as a strong velocity contrast is required here to successfully trace rays from the hinterland basin to our seismic stations onshore (see Section 5.3.3).

Considering these results, we can say with some confidence that the ophiolite extends offshore into the Gulf of Oman beneath sediments of the hinterland basin, terminating in a steep normal fault. This fault marks the suture zone between the obducted oceanic crust of the Semail ophiolote and the present day oceanic crust of the Gulf of Oman, and created the accommodation space for the formation of the hinterland basin (*Ali et al.*, 2019).

6.1.3 The Arabian continental crust

Prior to this study, no direct estimates of crustal thickness in the north-east of Arabia could be found in the literature. Receiver functions computed as part of this thesis show a consistent Moho depth of $\sim 36\ km$ in the foreland basin west of the UAE-Oman mountains. This is in very good agreement with Moho depths inferred from rifting and subsidence by *Ali et al.* (2017).

These receiver functions also show a mid crustal conversion at $\sim 15\ km$ depth that we interpret to be the base of the foreland sediments. This is deeper than previously published values of $7 - 11\ km$ for this basin (e.g. *Stern and Johnson* (2010); *Naville et al.* (2013); *Tarapoanca et al.* (2013); *Ali et al.* (2014, 2017)). If we assume the Arabian margin was originally at typical continental thickness ($31.2\ km$), this would imply rifting has thinned it to $21\ km$, giving a stretching factor(β) of ~ 1.49, higher than the backstripping estimates obtained by *Ali et al.* (2017) ($\beta \approx 1.2$), but similar to the value obtained by *Tiberi et al.* (2007) in the Gulf of Aden ($\beta = 1.38 - 1.54$).

Moho depths appear to increase eastwards across the foreland to $\sim 40\ km$ at the foothills of the UAE-Oman mountains. East of the Semail thrust clear Moho conversions were replaced with weak candidates from a range of depths, but a root could be made out by tracing the deeper results. This root reached a maximum depth

of $\sim 48\ km$ below Masafi on profile D1, and $\sim 44\ km$ below the Masafi window to the north on D4. In both cases this root is offset westwards from the primary ophiolite load by $\sim 20\ km$.

6.1.4 Continental-oceanic transition

Receiver function results suggest the Moho thins rapidly east of Masafi, and the Masafi window on D1 and D4 respectively. These results end near the Gulf of Oman coastline however, so we are reliant on our gravity models to inform us of Moho structure offshore below the hinterland basin. Gravity modelling supports a rapidly thinning Moho, as a large mass excess is required to counteract the low densities of the hinterland sediments. These models (Figures 5.14 and 5.16) suggest it thins to $\sim 20\ km$ depth around 30 km offshore, with $10-12\ km$ of sediments overlying $\sim 8\ km$ of Gulf of Oman oceanic crust. This suggests the transition from continental to oceanic crust takes place $20-30\ km$ offshore in the Gulf of Oman, below the hinterland sediments.

6.1.5 Flexure and isostasy

Our receiver function results point to the presence of a mantle root below the UAE-Oman mountains, offset $\sim 20\ km$ inland from the primary ophiolite load. This root extends down $\sim 10\ km$ deeper than the $\sim 36\ km$ Moho observed in the foreland basin the west, reaching $\sim 48\ km$ beneath Masafi, and $\sim 44\ km$ beneath the Masafi window to the north.

Topography across the UAE-Oman mountains is generally moderate in the UAE, peaking at $400-500\ m$ along our gravity profiles D1 and D4 (see Figures 4.18 and 4.19), and generally remaining below 1000 m. Airy isostasy (see Section 4.4.8) predicts a $\sim 5\ km$ root from 1 km of topography using crust and mantle densities of 2750 $kg\,m^{-3}$ and 3290 $kg\,m^{-3}$ respectively. Less than half of the $\sim 10\ km$ required to reproduce the roots suggested by our receiver function results. The WGM2012 global isostatic gravity anomaly dataset of *Balmino et al.* (2011) also shows large positive isostatic anomalies across the UAE-Oman mountain range (see Figure 4.6), suggesting the topography is

significantly undercompensated at present. An alternative explanation, such as buried loads, is therefore required to account for the flexure observed beneath the UAE-Oman mountains, and the high isostatic gravity anomalies.

Buried loads have been proposed to explain excessive flexure or subsidence, and gravity anomalies that cannot be explained by the topographic load observed at the surface by several authors (e.g. *Karner and Watts* (1983); *Lin and Watts* (2002)). The source of these loads could be overthrusting of crustal blocks, mafic intrusions into the lower crust, or a number of other mechanisms.

The Semail ophiolite complex represents a significant buried load upon the continental margin, with up to 25 km of of obducted material and a density contrast of around $+370\ kg\,m^{-3}$ relative to the continental margin. We estimated this load constitutes a two-dimensional mass excess on the order of $\sim 10^{11}\ kg\,m^{-1}$ (see Section 4.9).

This load has resulted in significant flexure in the rifted Arabian continental margin (*Robertson*, 1987; *Ravaut et al.*, 1997; *Ali and Watts*, 2009), with backstripping models by *Ali and Watts* (2009); *Ali et al.* (2017) suggesting up to $\sim 6\ km$ of tectonic subsidence. Process oriented gravity modelling by *Ali et al.* (2019) suggested ophiolite loading could comfortably produce $\sim 10\ km$ of subsidence in a rifted margin, with the maximum flexure offset landwards from the driving load, and a gravity anomaly roughly similar to that observed.

This root therefore likely formed as a result of flexure caused by ophiolite loading of the rifted Arabian continental margin in the late Cretaceous.

6.1.6 Geological model of the Arabian margin

The data acquired in this project, and the receiver function and gravity modelling results presented in this thesis, form the basis for a new geological model of the north-eastern margin of the Arabian plate presented by (*Ali et al.*, 2019). This model is shown in Figure 6.1. It shows a thick passive margin and foreland sedimentary sequence overlying a rifted continental margin. A series of stacked thrust sheets, representing the Semail ophiolite complex, have been obducted onto the edge of this margin, and

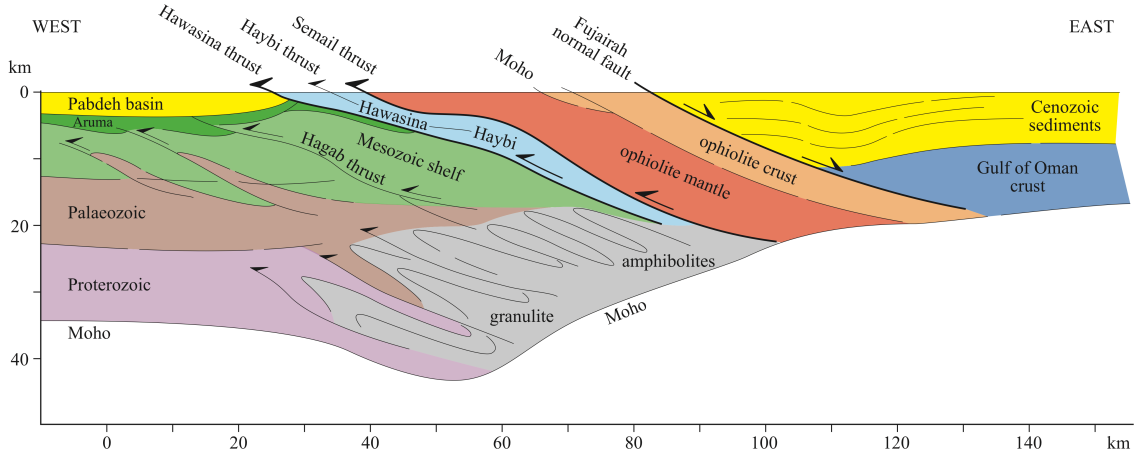


Figure 6.1: A geological cross-section of the Arabian margin based on the data acquired during this project. Figure provided by Mike Searle, and is from *Searle et al.* (2014); *Ali et al.* (2019).

overlie a lower crust metamorphosed during its attempted subduction. The ophiolite terminates offshore in a steep normal fault, creating the accomodation space for a thick hinterland sedimentary sequence above the suture linking the ophiolite to the present day oceanic crust of the Gulf of Oman.

6.2 Conclusions

The results presented in this thesis represent key new constraints on the crustal structure of the UAE-Oman mountains, and their flanking basins in the United Arab Emirates (UAE).

In the foreland basin to the west of these mountains, our receiver functions revealed a $\sim 15\ km$ thick sedimentary sequence, and a $\sim 36\ km$ deep Moho. This implies a stretching factor for the rifted Arabian margin of $\beta \approx 1.49$.

Across the UAE-Oman mountains our receiver functions suggest Moho depths increase to $44 - 48\ km$ in a $\sim 10\ km$ thick flexural root, offset $\sim 20\ km$ landwards from the primary ophiolite load. They also image the base of the ophiolite east of Masafi for the first time, where it is shown to be dipping eastwards at $\sim 30°$, from $5 - 10\ km$

depth to $\sim 25\ km$ depth near the Gulf of Oman coastline. Gravity modelling of the crust across these mountains showed that the ophiolite must be both thick ($\sim 20\ km$), and dense ($\sim 3120\ kg\,m^{-3}$) in order to reproduce the $\sim 160\ mGal$ Bouguer anomalies observed near the Gulf of Oman coastline. This implies that bulk serpentinisation of the obducted peridotites must be minimal ($< 30\%$).

Offshore in the Gulf of Oman new seismic reflection data reveals a $\sim 10\ km$ thick sedimentary sequence, and images the surface of the ophiolite dropping off below these sediments in a steep ($\sim 45°$) normal fault. Gravity modelling suggests the Moho must thin rapidly east of Masafi. We estimate that it reduces from $44-48\ km$ depth beneath thinned continental crust at Masafi to $\sim 20\ km$ depth beneath oceanic crust around $30\ km$ offshore. This implies that the continental-oceanic transition lies beneath these sediments offshore in the Gulf of Oman.

6.3 Future work

One of the biggest challenges encountered in this project was resolving the discrepancies between the gravity, and seismic refraction models across the ophiolite. Our gravity models required a high ophiolite density ($\rho > 2950\ kg\,m^{-3}$) in order to reproduce the $\sim 160\ mGal$ Bouguer anomalies observed across the ophiolite. However the refraction model favoured velocities of $5.5 - 6.5\ km\,s^{-1}$ within the ophiolite, implying a density of $\sim 2700\ kg\,m^{-3}$, which is too low to produce a positive density contrast and contribute to the observed gravity anomaly. While a highly fractured, and mildly serpentinised ophiolite could explain this discrepancy, further investigation is warranted. Further direct measurements of both density and seismic velocity of Semail ophiolite rock samples, and targeted seismic refraction experiments across the ophiolite are therefore encouraged. The vibroseis refraction survey undertaken along D1 in late 2016 (see Section 2.4.2) has the potential to provide some further insight into this problem, with several shot points and receivers located across the ophiolite.

The Oman drilling project (`https://www.omandrilling.ac.uk`) is currently un-

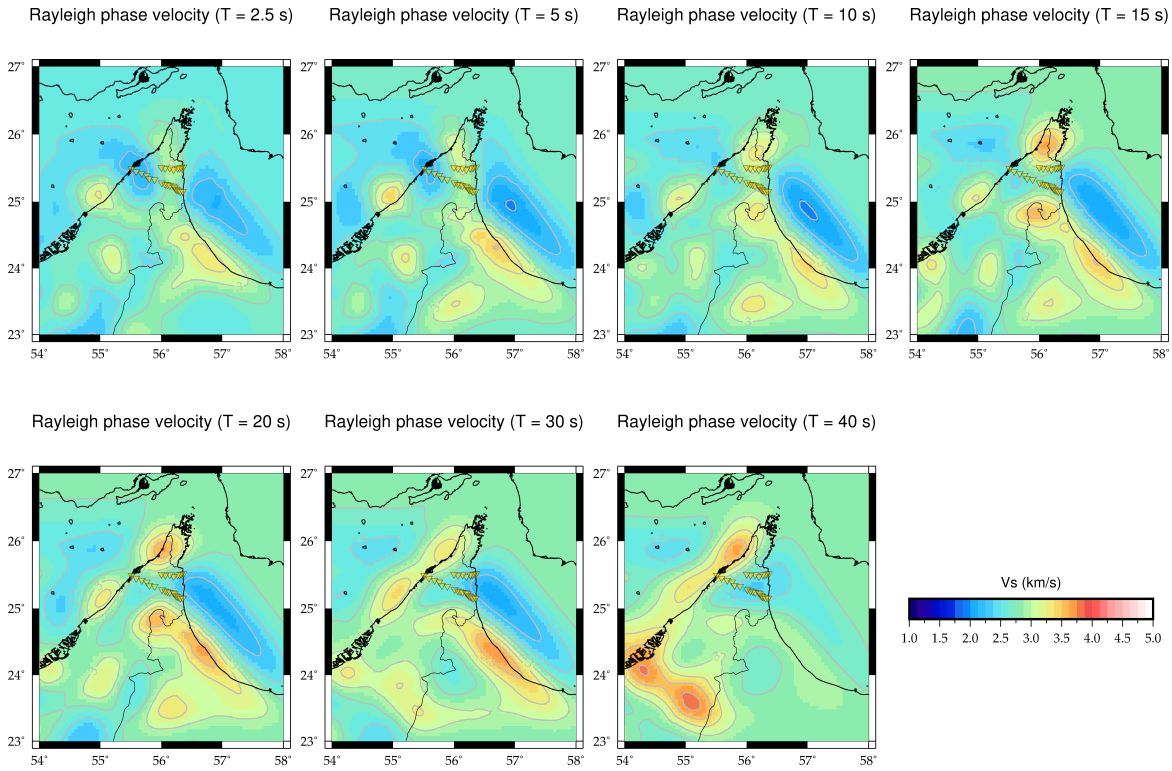


Figure 6.2: Rayleigh wave dispersion curves computed by Simone Pilia from our passive seismic dataset. Inverted golden triangles mark the seismometers of the PI/Oxford network. Note the anomalously low velocities at high period beneath our study area in the north of the UAE.

derway, drilling several deep wells into the Semail ophiolite south of Muscat. While no results have been published at the time of writing, it will be interesting to see whether their cores confirm the in situ fracturing and mild serpentinisation inferred from our gravity and refractions models.

Our gravity models suggest the crust below the hinterland basin in the Gulf of Oman transitions from continental to oceanic $20 - 30\ km$ offshore. However no estimates of Moho depth were obtained, and no wells have penetrated basement in this region. Further investigation is therefore required.

The large passive seismic dataset acquired during this project holds significant potential for further work. Possible uses include tomographic, or ambient noise investigations into crust and upper mantle structure, or building a more detailed earthquake catalogue in the region to map natural and induced seismicity.

One promising new method for imaging crustal velocity structures is the joint in-

version of receiver functions and surface wave dispersion curves (*Julià et al.*, 2000; *Tkalcic et al.*, 2006; *Bodin et al.*, 2012). These datasets are complementary, as receiver functions can provide information on impedance contrast interfaces, but require accurate crustal velocities to map their depth. Surface wave dispersion curves on the other hand provide an approximate velocity profile, but cannot accurately pin down specific interfaces.

We obtained inversion codes from Jordi Julia and Thomas Bodin, and Simone Pilia computed Rayleigh wave dispersion curves with our passive seismic dataset (see Figure 6.2). However this dispersion dataset exhibited a velocity inversion (lower velocities at higher periods), and anomalously low velocities at high periods below our study area in the north of the UAE. This impacted the inversion algorithms, and prevented them from settling on a sensible velocity structure. Recomputing these dispersion curves to investigate whether these low velocities are real, or an artifact arising from the inversion process or station distribution could be an interesting future project. Joint inversion of receiver functions and surface wave dispersion curves could then be re-attempted.

Bibliography

Abers, G. A., X. Hu, and L. R. Sykes (1995), Source scaling of earthquakes in the shumagin region, Alaska: timedomain inversions of regional waveforms, *Geophysical Journal International*, *123*(1), 41–58, doi:10.1111/j.1365-246X.1995.tb06660.x.

Abt, D. L., K. M. Fischer, S. W. French, H. A. Ford, H. Yuan, and B. Romanowicz (2010), North American lithospheric discontinuity structure imaged by Ps and Sp receiver functions, *Journal of Geophysical Research: Solid Earth*, *115*(9), 1–24, doi: 10.1029/2009JB006914.

Airy, G. B. (1855), On the computation of the effect of the attraction of mountain-masses, as disturbing the apparent astronomical latitude of stations in geodetic surveys, *Philosophical Transactions of the Royal Society of London*, (145), 101–104.

Al-Damegh, K., E. Sandvol, and M. Barazangi (2005), Crustal structure of the Arabian plate: New constraints from the analysis of teleseismic receiver functions, *Earth and Planetary Science Letters*, *231*, 177–196, doi:10.1016/j.epsl.2004.12.020.

Al-Husseini, M. I. (2000), Origin of the Arabian plate structures: Amar Collision and Najd Rift, *GeoArabia*, *5*(4), 527–542.

Al-Husseini, M. I. (2004), Pre-Unayzah unconformity , Saudi Arabia, *GeoArabia Special Publication*, (3).

Al-Lazki, A. I., D. Seber, E. Sandvol, and M. Barazangi (2002), A crustal transect across the Oman Mountains on the eastern margin of Arabia, *GeoArabia*, *7*(1), 47–78.

Alabaster, T., J. A. Pearce, and J. Malpas (1982), The volcanic stratigraphy and petrogenesis of the Oman ophiolite complex, *Contributions to Mineralogy and Petrology*, *81*(3), 168–183, doi:10.1007/BF00371294.

Ali, M., M. Sirat, and J. Small (2009), Seismic Investigation Over the Jabal Hafit Structure: Implications for Basement Configuration of the Frontal FoldandThrust, *Journal of Petroleum Geology*, *32*(January), 21–37.

Ali, M. Y., and A. B. Watts (2009), Subsidence history, gravity anomalies and flexure of the United Arab Emirates (UAE) foreland basin, *GeoArabia*, *14*(2), 17–44.

Ali, M. Y., M. Sirat, and J. Small (2008), Geophysical investigation of Al Jaww Plain, eastern Abu Dhabi: Implications for structure and evolution of the frontal fold belts of the Oman Mountains, *GeoArabia*, *13*(2), 91–118.

Ali, M. Y., A. B. Watts, and A. Farid (2014), Gravity anomalies of the United Arab Emirates: Implications for basement structures and infra-Cambrian salt distribution, *GeoArabia, Journal of the Middle East Petroleum Geosciences*, *19*(1), 85–112.

Ali, M. Y., S. Aidarbayev, M. P. Searle, and A. B. Watts (2017), Subsidence History and Seismic Stratigraphy of the Western Musandam Peninsula, Oman-United Arab Emirates Mountains, *Tectonics*, pp. 1–28, doi:10.1002/2017TC004777.

Ali, M. Y., A. B. Watts, M. P. Searle, B. S. Keats, S. Pilia, and T. Ambrose (2019), Crustal structure, ophiolites and flexure beneath the Oman-UAE mountains, *Manuscript submitted for publication*.

Amante, C., and B. W. Eakins (2009), ETOPO1 arc-minute global relief model: procedures, data sources and analysis.

Ambrose, T. K., and M. P. Searle (2019), 3-D Structure of the Northern Oman-UAE Ophiolite: Widespread, Short-Lived, Suprasubduction Zone Magmatism, *Tectonics*, *38*(1), 233–252, doi:10.1029/2018TC005038.

Ammon, C. J. (1991), the Isolation of Receiver Effects From Teleseismic P Waveforms, *Bulletin of the Seismological Society of America*, *81*(6), 2504–2510, doi:10.1029/2005JB004161.

Baker, G. E., J. B. Minster, G. Zandt, and H. Gurrola (1996), Constraints on crustal structure and complex moho topography beneath Piñon Flat, California, from teleseismic receiver functions, *Bulletin of the Seismological Society of America*, *86*(6), 1830–1844, doi:10.1161/circulationaha.108.815944.

Balmino, G., N. Vales, A. Bonvalot, and S. Briais (2011), Spherical harmonic modelling to ultra-high degree of Bouguer and isostatic anomalies, *Journal of Geodesy*, doi:10.1007/s00190-011-0533-4.

Bayer, R., J. Chery, M. Tatar, P. Vernant, M. Abbassi, F. Masson, F. Nilforoushan, E. Doerflinger, V. Regard, and O. Bellier (2006), Active deformation in Zagros-Makran transition zone inferred from GPS measurements, *Geophysical Journal International*, *165*(1), 373–381, doi:10.1111/j.1365-246X.2006.02879.x.

Beyreuther, M., R. Barsch, L. Krischer, T. Megies, Y. Behr, and J. Wassermann (2010), ObsPy: A Python Toolbox for Seismology, *Seismological Research Letters*, *81*(3), 530–533, doi:10.1785/gssrl.81.3.530.

Bodin, T., M. Sambridge, H. Tkalćić, P. Arroucau, K. Gallagher, and N. Rawlinson (2012), Transdimensional inversion of receiver functions and surface wave dispersion, *Journal of Geophysical Research: Solid Earth*, *117*(2), 1–24, doi:10.1029/2011JB008560.

Boote, D. R., D. Mou, and R. I. Waite (1990), Structural evolution of the Suneinah Foreland, Central Oman Mountains, *Geological Society Special Publication*, *49*(49), 397–418, doi:10.1144/GSL.SP.1992.049.01.25.

Bott, M. H. P. (1956), A geophysical study of the granite problem, *Quarterly Journal of the Geological Society*, *112*, 45–67.

Bott, M. H. P. (1959), The use of electronic digital computers for the evaluation of gravimetric terrain corrections, *Geophysical Prospecting*, *7*(1), 45 – 54.

Bott, M. H. P. (1967), Geophysical investigations of the Northern Pennine basement rocks, *Proceeding of the Yorkshore Geological Society*, *36*, 139–168.

Bott, M. H. P. (1969), GRAVN. Durham geophysical computer specification.

Boudier, F., G. Ceuleneer, and A. Nicolas (1988), Shear zones, thrusts and related magmatism in the Oman ophiolite: Initiation of thrusting on an oceanic ridge, *Tectonophysics*, *151*(1-4), 275–296, doi:10.1016/0040-1951(88)90249-1.

Boudier, F., A. Nicolas, B. Ildefonseand, and D. Jousselin (1997), EPR microplates, a model for the Oman Ophiolite, *Terra Nova*, *9*(2), 79–82, doi:10.1111/j.1365-3121.1997.tb00007.x.

Bouguer, P. (1749), *LA FIGURE DE LA TERRE, Déterminée par les Observations de Messieurs BOUGUER, & DE LA CONDAMINE, de l'Academie Royale des Sciences, envoyés par ordre du Roy au Pérou, pour observer aux environs de l'Equateur: Avec une Relation abregee de ce Voyage, qui con*, Charles-Antoine Jombert.

Brocher, T. M. (2005), Empirical relations between elastic wavespeeds and density in the Earth's crust, *Bulletin of the Seismological Society of America*, *95*(6), 2081–2092, doi:10.1785/0120050077.

Bullard, E. C. (1936), Gravity measurements in East Africa, *Philosophical Transactions of the Royal Society of London*, *235*(757), 445–531.

Burdick, L. J., and C. A. Langston (1977), Modeling crustal structure through the use of converted phases in teleseismic body-wave forms, *Bulletin of the Seismological Society of America*, *67*(3), 677–691.

Cella, F. (2015), GTeC-A versatile MATLAB tool for a detailed computation of the terrain correction and Bouguer gravity anomalies, *Computers and Geosciences*, *84*, 72–85, doi:10.1016/j.cageo.2015.07.015.

Christensen, N. I. (1996), Poisson's ration and crustal seismology, *Journal of Geophysical Research*, *101*(B2), 3139–3156.

Christensen, N. I., and W. D. Mooney (1995), Seismic velocity structure and composition of the continental crust: A global view, *Journal of Geophysical Research: Solid Earth (19782012)*, *100*(B6), 9761–9788, doi:10.1029/95JB00259.

Christensen, N. I., and M. H. Salisbury (1975), Structure and constitution of the lower oceanic crust, *Reviews of Geophysics*, *13*(1), 57–86, doi:10.1029/RG013i001p00057.

Christensen, N. I., and J. D. Smewing (1981), Geology and seismic structure of the northern section of the Oman ophiolite, *Journal of Geophysical Research: Solid Earth*, *86*(B4), 2545–2555, doi:10.1029/JB086iB04p02545.

Clairaut, A. C. (1743), *Théorie de la figure de la terre, tirée des principes de l'hydrostatique*, chez David fils, libraire, ruë Saint-Jacques à la plume d'or.

Clayton, R. W., and R. A. Wiggins (1976), Source shape estimation and deconvolution of teleseismic bodywaves, *Geophysical Journal of the Royal Astronomical Society*, *47*, 151–177.

Cochran, J. R. (1981), Simple models of diffuse extension and the pre-seafloor spreading development of the continental margin of the northwestern Gulf of Alden, *Oceanologica Acta*, *26*, 155–165.

Cochran, J. R. (1983), Effects of finite rifting times on the development of sedimentary basins, *Earth and Planetary Science Letters*, *66*(C), 289–302, doi:10.1016/0012-821X(83)90142-5.

Coleman, R. G., and E. H. Bailey (1974), Mineral deposits and Geology of Northern Oman as of 1974, *Tech. rep.*

Cowan, R. J., M. P. Searle, and D. J. Waters (2014), Structure of the metamorphic sole to the Oman Ophiolite, Sumeini Window and Wadi Tayyin: Implications for ophiolite obduction processes, *Geological Society Special Publication*, *392*(1), 155–175, doi:10.1144/SP392.8.

Crotwell, H. P., T. J. Owens, and J. Ritsema (1999), The TauP Toolkit: Flexible Seismic Travel-time and Ray-path Utilities, *Seismological Research Letters*, *70*(2), 154–160, doi:10.1785/gssrl.70.2.154.

Dehghani, G. A., and J. Makris (1984), The gravity field and crustal structure of Iran, *Neues Jahrbuch für Geologie und Paläontologie-Abhandlungen*, pp. 215–229.

Dueker, K. G., and A. F. Sheehan (1997), Mantle discontinuity structure from midpoint stacks of converted P to S waves across the Yellowstone hotspot track, *Journal of Geophysical Research: Solid Earth*, *102*(B4), 8313–8327, doi:10.1029/96JB03857.

Effron, B., and R. J. Tibshirani (1991), Statistical data analysis in the computer age, *Science*, *253*(x), 390–395.

Ellison, R. A., and M. T. Styles (2006), *The Geology and Geophysics of the United Arab Emirates. Volume 1: Executive Summary.*, United Arab Emirates, Ministry of Energy, Petroleum and Minerals Sector.

Ernewein, M., C. Pflumio, and H. Whitechurch (1988), The death of an accretion zone as evidenced by the magmatic history of the Sumail ophiolite (Oman), *Tectonophysics*, *151*(1-4), 247–274, doi:10.1016/0040-1951(88)90248-X.

Everest, G. (1859), Rectification of logarithmic errors in the measurements of two sections of the meridional arc of India, *Proceedings of the Royal Society of London*, (9), 620–626.

Faqira, M., M. Rademakers, and A. K. M. Afifi (2009), New insights into the Hercynian Orogeny, and their implications for the Paleozoic Hydrocarbon System in the Arabian plate, *GeoArabia*, *14*(3), 199–228.

Farra, V., and L. Vinnik (2000), Upper mantle stratification by P and S receiver functions, *Physics*, (November).

Frizon De Lamotte, D., S. Tavakoli-Shirazi, P. Leturmy, O. Averbuch, N. Mouchot, C. Raulin, F. Leparmentier, C. Blanpied, and J. C. Ringenbach (2013), Evidence for Late Devonian vertical movements and extensional deformation in northern Africa and Arabia: Integration in the geodynamics of the Devonian world, *Tectonics*, *32*(2), 107–122, doi:10.1002/tect.20007.

Glennie, K. W., M. G. A. Boeuf, M. W. Hughes Clarke, M. Moody-Stuart, W. F. H. Pilaar, and B. M. Reinhardt (1973), Late Cretaceous Nappes in Oman Mountains and Their Geologic Evolution, *AAPG Bulletin*, *58*(5), 895–898.

Gnos, E. (1998), Peak metamorphic conditions of garnet amphibolites beneath the semail ophiolite: Implications for an inverted pressure gradient, *International Geology Review*, *40*(4), 281–304, doi:10.1080/00206819809465210.

Goodenough, K. M., M. T. Styles, D. Schofield, R. J. Thomas, Q. C. Crowley, R. M. Lilly, J. McKervey, D. Stephenson, and J. N. Carney (2013), Architecture of the Oman-UAE ophiolite: Evidence for a multi-phase magmatic history, *Frontiers in Earth Sciences*, *5*, 23–42, doi:10.1007/978-3-642-30609-9_2.

Gurrola, H., G. E. Baker, and J. B. Minster (1995), Simultaneous time-domain deconvolution with application to the computationof receiver function, *Geophys. J. Int.*, *120*, 537–543.

Hamilton, E. L. (1979), Vp/Vs and Poisson's Ratios In Marine Sediments And Rocks, *Journal of the Acoustical Society of America*, *66*(4), 1093–1101, doi:10.1121/1.383344.

Hammer, S. (1939), Terrain corrections for gravimeter stations, *293*(1936), 292–293.

Hansen, S. E., A. J. Rodgers, S. Y. Schwartz, and A. M. S. Al-Amri (2007), Imaging ruptured lithosphere beneath the Red Sea and Arabian Peninsula, *Earth and Planetary Science Letters*, *259*, 256–265, doi:10.1016/j.epsl.2007.04.035.

Hayford, J. F., and W. Bowie (1912), The Effect of Topography and Isostatic Compensation upon the Intensity of Gravity, *Bulletin of the American Geographical Society*, *44*(6), 464–465.

Heiland, C. A. (1940), *Geophysical exploration*, Prentice-Hall, Incorporated.

Helffrich, G. (2006), Extended-time multitaper frequency domain cross-correlation receiver-function estimation, *Bulletin of the Seismological Society of America*, *96*(1), 344–347, doi:10.1785/0120050098.

Hirt, C., and M. Rexer (2015), Earth2014: 1 arc-min shape, topography, bedrock and ice-sheet models - Available as gridded data and degree-10,800 spherical harmonics, *International Journal of Applied Earth Observation and Geoinformation*, *39*, 103–112, doi:10.1016/j.jag.2015.03.001.

Hubbert, M. K. (1948), A line-integral method of computing the gravimetric effects of two-dimensional masses, *Geophysics*, *13*(2), 215–225.

Jordan, T. (2007), Gravity Anomalies, Flexure, and the Long-term Rigidity of the Continental Lithosphere, Ph.D. thesis, University of Oxford.

Julià, J. (2007), Constraining velocity and density contrasts across the crust mantle boundary with receiver function amplitudes, pp. 286–301, doi:10.1111/j.1365-2966.2007.3502.x.

Julià, J., C. J. Ammon, R. B. Herrmann, and A. M. Correig (2000), Joint inversion of receiver function and surface wave dispersion observations, *Geophysical Journal International*, *143*(1), 99–112.

Julià, J., C. J. Ammon, and R. B. Herrmann (2003), Lithospheric structure of the Arabian Shield from the joint inversion of receiver functions and surface-wave group velocities, *Tectonophysics*, *371*(1-4), 1–21, doi:10.1016/S0040-1951(03)00196-3.

Kane, M. F. (1962), A comprehensive system of terrain corrections using a digital computer, *Geophysics*, *27*(4), 455–462.

Karner, G. D., and A. B. Watts (1983), Gravity anomalies and flexure of the lithosphere at mountain ranges., *Journal of Geophysical Research*, *88*(B12), 10,449–10,477, doi:10.1029/JB088iB12p10449.

Kennett, B. L. N., and E. R. Engdahl (1991), Travel times for global earthquake location and phase identification, *Geophysical Journal International*, *105*(2), 429–465, doi:10.1111/j.1365-246X.1991.tb06724.x.

Khattab, M. M. (1993), Interpretation of recent gravity profiles over the ophiolite belt, Northern Oman Mountains, United Arab Emirates, *Journal of African Earth Sciences*, *16*(3), 319–327.

Kumar, M. R., D. S. Ramesh, J. Saul, D. Sarkar, and R. Kind (2002), Crustal structure and upper mantle stratigraphy of the Arabian shield, *Geophysical Research Letters*, *29*(8), 1242–1245, doi:10.1029/2001GL014530.

Kumar, P., R. Kind, and X. Yuan (2010), Receiver function summation without deconvolution, *Geophysical Journal International*, *180*(3), 1223–1230, doi:10.1111/j.1365-246X.2009.04469.x.

Kuo, C., C. Lindberg, and D. J. Thomson (1990), Coherence established between atmospheric carbon dioxide and global temperature, *Nature*, *343*(6260), 709–714, doi:10.1038/343709a0.

Lacoste, L. J. B. (1967), Measurement of Gravity at Sea and in the Air, *Reviews of Geophysics*, *5*(4), 477–526, doi:10.1029/TR002i001p00003.

LaFehr, T. R. (1991), An exact solution for the gravity curvature (Bullard B) correction, *Geophysics*, *56*(8), 1179–1184, doi:10.1190/1.1443138.

Langston, C. A. (1979), Structure under Mount Rainier, Washington, inferred from teleseismic body waves, *Journal of Geophysical Research*, *84*(B9), 4749, doi:10.1029/JB084iB09p04749.

Leahy, G. M., J. A. Collins, C. J. Wolfe, G. Laske, and S. C. Solomon (2010), Underplating of the Hawaiian Swell: Evidence from teleseismic receiver functions, *Geophysical Journal International*, *183*(1), 313–329, doi:10.1111/j.1365-246X.2010.04720.x.

Lee, C. W. (1990), A review of platform sedimentation in the Early and Late Permian of Oman, with particular reference to the Oman Mountains, *Geological Society Special Publication*, *49*(49), 39–47, doi:10.1144/GSL.SP.1992.049.01.04.

Lee, D. (2008), Gravity constraints on the western limit of the Semail Ophiolite in the northwestern Oman Mountains, Masters thesis, University of Oxford.

Levin, V., and J. Park (2000), Shear zones in the Proterozoic lithosphere of the Arabian shield and the nature of the Hales discontinuity, *Tectonophysics*, *323*(3-4), 131–148, doi:10.1016/S0040-1951(00)00105-0.

Ligorría, J. P., and C. J. Ammon (1999), Iterative deconvolution and receiver function estimation, *Bulletin of the Seismological Society of America*, *89*(October), 1395–1400.

Lin, A. T., and A. B. Watts (2002), Origin of the West Taiwan basin by orogenic loading and flexure of a rifted continental margin, *Journal of Geophysical Research*, *107*(B9), doi:10.1029/2001JB000669.

Linsser, H. (1965), A generalized form of Nettleton's density determination, *Geophysical Prospecting*, *13*(2), 247–258.

Lippard, S. J., and A. W. Shelton (1986), The Ophiolite Of Northern Oman, *Geological Society, London*, *11*.

Longman, I. M. (1959), Formulas for computing the tidal accelerations due to the moon and the sun, *Journal of Geophysical Research*, *64*(12), 2351, doi:10.1029/JZ064i012p02351.

Lowrie, W. (2007), *Fundamentals of geophysics*, Cambridge University Press.

Ludwig, W. J., J. E. Nafe, and C. L. Drake (1970), Seismic refraction, The Sea, 4 (1), 5384, *VViley-Intersci., NY*.

MacLeod, C. J., C. Johan Lissenberg, and L. E. Bibby (2013), "Moist MORB" axial magmatism in the Oman ophiolite: The evidence against a mid-ocean ridge origin, *Geology*, *41*(4), 459–462, doi:10.1130/G33904.1.

Manghnani, M. H., and R. G. Coleman (1981), Gravity profiles across the Samail Ophiolite, Oman, *Journal of Geophysical Research: Solid Earth*, *86*(B4), 2509–2525, doi:10.1029/JB086iB04p02509.

McKenzie, D., and M. J. Bickle (1988), The Volume and Composition of Melt Generated by Extension of the Lithosphere, *Journal of Petrology*, *29*(3), 625–679.

Miller, D. J., and N. I. Christensen (1997), Seismic velocities of lower crustal and upper mantle rocks from the slow-spreading Mid-Atlantic Ridge, south of the Kane Fracture Transform Zone (MARK), *Proceedings of the Ocean Drilling Program, Scientific Results*, *153*, 437–454.

Mohr, P. J., D. B. Newell, and B. N. Taylor (2016), CODATA Recommended Values of the Fundamental Physical Constants : 2014, *Journal of Physical and Chemical Reference Data*, doi:10.1063/1.4954402.

Mooney, W. D., M. E. Gettings, H. R. Blank, and J. H. Healy (1985), Saudi Arabian seismic-refraction profile: A traveltime interpretation of crustal and upper mantle structure, *Tectonophysics*, *111*(3-4), doi:10.1016/0040-1951(85)90287-2.

Musacchio, G., W. D. Mooney, J. H. Luetgert, and N. I. Christensen (1997), Composition of the crust in the Grenville and Appalachian Provinces of North America inferred from V P /V S ratios , *Journal of Geophysical Research: Solid Earth*, *102*(B7), 15,225–15,241, doi:10.1029/96jb03737.

Muttoni, G., M. Gaetani, D. V. Kent, D. Sciunnach, L. Angiolini, F. Berra, E. Garzanti, M. Mattei, and A. Zanchi (2009), Opening of the Neo-Tethys Ocean and the Pangea B to Pangea A transformation during the Permian, *GeoArabia*, *14*(4), 17–48.

Naville, C., M. Ancel, P. Andriessen, P. Ricarte, and F. Roure (2013), New constrains on the thickness of the semail ophiolite in the Northern Emirates, *Frontiers in Earth Sciences*, *5*, 43–59, doi:10.1007/978-3-642-30609-9_3.

Nicolas, A., and F. Boudier (2017), Emplacement of Semail Emirates ophiolite at ridge trench collision, *Terra Nova*, *29*(2), 127–134, doi:10.1111/ter.12256.

Nicolas, A., F. Boudier, B. Ildefonse, and E. Ball (2000), Accretion of Oman and United Arab Emirates ophiolite–Discussion of a new structural map, *Mar. Geophys. Res.*, *21*(3), 147–180, doi:10.1023/A:1026769727917.

Park, J., and V. Levin (2000), Receiver functions from multiple-taper spectral correlation Estimates, *Bulletin of the Seismological Society of America*, *90*(6), 1507–1520, doi:10.1785/0119990122.

Park, J., C. R. Lindberg, and F. L. Vernon (1987), Multitaper spectral analysis of high-frequency seismograms, *Journal of Geophysical Research: Solid Earth*, *92*(B12), 12,675–12,684, doi:10.1029/JB092iB12p12675.

Patton, T. L., and S. J. O'Connor (1988), Cretaceous flexural history of northern Oman mountain foredeep, United Arab Emirates, *AAPG Bulletin*, *72*(7), 797–809.

Pavlis, N. K., S. a. Holmes, S. C. Kenyon, and J. K. Factor (2012), The development and evaluation of the Earth Gravitational Model 2008 (EGM2008), *Journal of Geophysical Research: Solid Earth*, *117*, doi:10.1002/jgrb.50167,2013.

Pearce, J. A., T. Alabaster, A. W. Shelton, and M. P. Searle (1981), The Oman Ophiolite as a Cretaceous Arc-Basin Complex: Evidence and Implications, *300*(1454), 299–317, doi:10.1098/rsta.1981.0066.

Phinney, R. A. (1964), Structure of the Earth's crust from spectral behavior of long-period body waves, *Journal of Geophysical Research*, *69*(14), 2997–3017, doi:10.1029/JZ069i014p02997.

Pratt, J. H. (1855), On the attraction of the Himalaya Mountains, and of the elevated regions beyond them, upon the plumb-line in India, *Philosophical Transactions of the Royal Society of London*, (145), 53–100.

Pratt, J. H. (1859), On the deflection of the plumb-line in India, caused by the attraction of the Himmalaya mountains and of the elevated regions beyond; and its modification by the compensating effect of a deficiency of matter below the mountain mass, *Philosophical Transactions of the Royal Society of London*, (149), 745–778.

Rabu, D., P. Nehlig, J. Roger, F. Béchennec, M. Beurrier, J. Le Métour, C. H. Bourdillon-De-Grissac, M. Tegyey, J.-J. Chauvel, C. Cavelier, H. Al Azri, T. Juteau, D. Janjou, B. Lemière, M. Villey, and R. Wyns (1993), Stratigraphy and structure of the Oman mountains, *Documents - B.R.G.M.*, (221), 300.

Ramesh, D. S., R. Kind, and X. Yuan (2002), Receiver function analysis of the North American crust and upper mantle, *Geophysical Journal International*, *150*(1), 91–108, doi:10.1046/j.1365-246X.2002.01697.x.

Ravaut, P., R. Bayer, R. Hassani, D. Rousset, and A. Yahya'ey (1997), Structure and evolution of the northern Oman margin: gravity and seismic constraints over the Zagros-Makran-Oman collision zone, *Tectonophysics*, *279*(1-4), 253–280, doi:10.1016/S0040-1951(97)00125-X.

Rioux, M., S. Bowring, P. Kelemen, S. Gordon, F. Dudás, and R. Miller (2012), Rapid crustal accretion and magma assimilation in the Oman-U.A.E. ophiolite: High precision U-Pb zircon geochronology of the gabbroic crust, *Journal of Geophysical Research: Solid Earth*, *117*(7), 1–12, doi:10.1029/2012JB009273.

Rioux, M., S. Bowring, P. Kelemen, S. Gordon, R. Miller, and F. Dudás (2013), Tectonic development of the Samail ophiolite: High-precision U-Pb zircon geochronology and Sm-Nd isotopic constraints on crustal growth and emplacement, *Journal of Geophysical Research: Solid Earth*, *118*(5), 2085–2101, doi:10.1002/jgrb.50139.

Rioux, M., J. Garber, A. Bauer, S. Bowring, M. P. Searle, P. Kelemen, and B. Hacker (2016), Synchronous formation of the metamorphic sole and igneous crust of the Semail ophiolite: New constraints on the tectonic evolution during ophiolite formation from high-precision U-Pb zircon geochronology, *Earth and Planetary Science Letters*, *451*, 185–195, doi:10.1016/j.epsl.2016.06.051.

Robertson, A. (1987), The transition from a passive margin to an Upper Cretaceous foreland basin related to ophiolite emplacement in the Oman Mountains, *Bulletin of the Geological Society of America*, *99*(5), 633–653, doi:10.1130/0016-7606(1987)99⟨633:TTFAPM⟩2.0.CO;2.

Ruban, D. A., M. I. Al-Husseini, and Y. Iwasaki (2007), Review of Middle East Paleozoic plate tectonics, *GeoArabia*, *12*(3), 35–56.

Sandvol, E., D. Seber, M. Barazangri, F. Vernon, R. Mellors, and A. Al-Amri (1998), Lithospheric seismic velocity discontinuities beneath the Arabian Shield, *25*(15), 2873–2876.

Sandwell, D. T. (1992), Global marine gravity from ERS-1. Geosat and Seasat Revell New Tectonic Fabrics, *EOS Transations of the American Geophysical Union*, *73*, 133.

Sandwell, D. T., R. D. Müller, W. H. F. Smith, E. Garcia, and R. Francis (2014), Marine geophysics. New global marine gravity model from CryoSat-2 and Jason-1 reveals buried tectonic structure., *Science (New York, N.Y.)*, *346*(6205), 65–7, doi:10.1126/science.1258213.

Savage, M. K., J. Park, and H. Todd (2007), Velocity and anisotropy structure at the Hikurangi subduction margin, New Zealand from receiver functions, *Geophysical Journal International*, *168*(3), 1034–1050, doi:10.1111/j.1365-246X.2006.03086.x.

Searle, M. P. (1988), Structure of the Musandam culmination (Sultanate of Oman and United Arab Emirates) and the Straits of Hormuz syntaxis, *Journal of the Geological Society*, *145*(5), 831–845, doi:10.1144/gsjgs.145.5.0831.

Searle, M. P. (2007), Structural geometry, style and timing of deformation in the Hawasina Window, Al Jabal al Akhdar and Saih Hatat culminations, Oman Mountains, *GeoArabia*, *12*(2), 99–130.

Searle, M. P., and M. Y. Ali (2009), Structural and tectonic evolution of the Jabal Sumeini Al Ain Buraimi region , northern Oman and eastern United Arab Emirates, *GeoArabia*, *14*(1), 115–142.

Searle, M. P., and J. Cox (1999), Tectonic setting, origin, and obduction of the Oman ophiolite, *Bulletin of the Geological Society of America*, *111*(1), 104–122, doi:10.1130/0016-7606(1999)111⟨0104:TSOAOO⟩2.3.CO;2.

Searle, M. P., and J. Malpas (1980), Structure and metamorphism of rocks beneath the Semail ophiolite of Oman and their significance in ophiolite obduction, *Transactions of the Royal Society of Edinburgh: Earth Sciences*, *71*(4), 247–262, doi:10.1017/S0263593300013614.

Searle, M. P., and J. Malpas (1982), Petrochemistry and origin of sub-ophiolitic metamorphic and related rocks in the Oman Mountains., *Journal of the Geological Society*, *139*(3), 235–248, doi:10.1144/gsjgs.139.3.0235.

Searle, M. P., A. G. Cherry, M. Y. Ali, and D. J. W. Cooper (2014), Tectonics of the Musandam Peninsula and northern Oman Mountains : From ophiolite obduction to continental collision, *GeoArabia*, *19*(2), 135–174.

Searle, M. P., D. Waters, J. Garber, M. Rioux, A. Cherry, and T. Ambrose (2015), Structure and metamorphism beneath the obducting Oman ophiolite: Evidence from the Bani Hamid granulites, northern Oman mountains, *Geosphere*, *11*(6), GES01,199.1, doi:10.1130/GES01199.1.

Segre, M. (1989), Galileo, Viviani and the tower of Pisa, *Studies in History and Philosophy of Science*, *20*(4), 435–451.

Shelton, A. W. (1990), The interpretation of gravity data in Oman: constraints on the ophiolite emplacement mechanism, *The Geology and Tectonics of the Oman Region*, *49*(1), 459–471, doi:10.1144/gsl.sp.1992.049.01.29.

Skeels, D. C. (1947), Ambiguity in gravity interpretation, *Geophysics*, *12*(1), 43–56, doi:10.1190/1.1437295.

Somigliana, C. (1929), Teoria generale del campo gravitazionale dell'ellissoide di rotazione, *Memorie della società astronomica italiana*, *4*, 425.

Stern, R. J., and P. Johnson (2010), Continental lithosphere of the Arabian Plate: A geologic, petrologic, and geophysical synthesis, *Earth-Science Reviews*, *101*(1-2), 29–67, doi:10.1016/j.earscirev.2010.01.002.

Talwani, M., J. L. Worzel, and M. Landisman (1959), Rapid gravity computations for two-dimensional bodies with application to the Mendocino submarine fracture zone, *Journal of Geophysical Research*, *64*(1), 49, doi:10.1029/JZ064i001p00049.

Tarapoanca, M., P. Andriessen, K. Broto, L. Chérel, N. Ellouz-Zimmermann, J. L. Faure, A. Jardin, C. Naville, and F. Roure (2013), Forward kinematic modelling of a regional transect in the northern emirates using geological and apatite fission track age constraints on paleo-burial history, *Frontiers in Earth Sciences*, *5*, 159–175, doi:10.1007/978-3-642-30609-9_8.

Thomson, D. J. (1982), Spectrum Estimation and Harmonic Analysis, *Proceedings of the IEEE*, *70*(9), 1055–1096, doi:10.1109/PROC.1982.12433.

Tiberi, C., S. Leroy, E. D'Acremont, N. Bellahsen, C. Ebinger, A. Al-lazki, and A. Pointu (2007), Crustal geometry of the northeastern Gulf of Aden passive margin: Localization of the deformation inferred from receiver function analysis, *Geophysical Journal International*, *168*(3), 1247–1260, doi:10.1111/j.1365-246X.2006.03294.x.

Tilton, G. R., C. A. Hopson, and J. E. Wright (1981), Uranium-lead isotopic ages of the Samail ophiolite, Oman, with applications to Tethyan ocean ridge tectonics., *Journal of Geophysical Research*, *86*(B4), 2763–2775, doi:10.1029/JB086iB04p02763.

Tkalcic, H., M. E. Pasyanos, A. J. Rodgers, R. Gok, W. R. Walter, and A. Al-Amri (2006), A multistep approach for joint modeling of surface wave dispersion and teleseismic receiver functions: Implications for lithospheric structure of the Arabian Peninsula, *Journal of Geophysical Research: Solid Earth*, *111*(11), 1–25, doi:10.1029/2005JB004130.

Tozer, B., A. B. Watts, and M. C. Daly (2017), Crustal structure, gravity anomalies, and subsidence history of the Parnaíba cratonic basin, Northeast Brazil, *Journal of Geophysical Research: Solid Earth*, *122*(7), 5591–5621, doi:10.1002/2017JB014348.

Vernon, L., J. Fletcher, L. Carrol, A. Chave, and E. Sembera (1991), Coherence of Seismic Body Waves From Local Events as Measured by a Small-Aperture Array, *96*(91).

Warburton, J., T. J. Burnhill, R. H. Graham, and K. P. Isaac (1990), The evolution of the Oman Mountains Foreland Basin, *Geological Society, London, Special Publications*, (49), 419–427.

Warren, C. J., R. R. Parrish, D. J. Waters, and M. P. Searle (2005), Dating the geologic history of Oman's Semail ophiolite: Insights from U-Pb geochronology, *Contributions to Mineralogy and Petrology*, *150*(4), 403–422, doi:10.1007/s00410-005-0028-5.

Watts, A. B. (2001), *Isostasy and Flexure of the Lithosphere*, Cambridge University Press.

Watts, A. B., and J. D. Fairhead (1999), A process-oriented approach to modeling the gravity signature of continental margins, *The Leading Edge*, *18*(2), 258, doi:10.1190/1.1438270.

Watts, A. B., and J. D. P. Moore (2017), Flexural Isostasy : Constraints From Gravity, *Journal of Geophysical Research: Solid Earth*, *112*, 8417–8430, doi:10.1002/2017JB014571.

Wessel, P., and A. B. Watts (1988), On the accuracy of marine gravity measurements, *Journal of Geophysical Research*, *93*(B1), 393, doi:10.1029/JB093iB01p00393.

White, R. S., and K. Klitgord (1976), Sediment deformation and plate tectonics in the Gulf of Oman, *Earth and Planetary Science Letters*, *32*, 199–209, doi:10.1016/0012-821X(76)90059-5.

White, R. S., and D. A. Ross (1979), Tectonics of the Western Gulf of Oman, *Journal of Geophysical Research*, *84*(Nb7), 3479–3489, doi:Doi10.1029/Jb084ib07p03479.

Whitman, W. W. (1991), A microgal approximation for the Bullard B - Earth's curvature - gravity correction, *Geophysics*, *56*(12), 1980–1985.

Worzel, J. L., and G. L. Shurbet (1955), Gravity anomalies at continental margins, *Geology*, *41*, 458–469.

Zhu, L., and H. Kanamori (2000), Moho depth variation in southern California from teleseismic receiver functions, *Journal of Geophysical Research*, *105*, 2969–2980, doi:10.1029/1999JB900322.

Appendix A

Onshore gravity survey data

A.1 Introduction

This appendix contains the gravity data acquired along the profiles D1 and D4 during my field season in 2016. Data was acquired with a Scintrex CG-5 Autograv gravimeter, and meter readings listed in the tables below are in counter units (CU). These can be converted to absolute gravity by equating meter readings at GSA-Naswa to the reported absolute gravity value at that site (978846.767 $mGal$, see Section 4.7.1). Elevation data is from the gravimeters GPS dongle and is in meters. However the vertical resolution on such GPS devices is known to be poor, and we extracted elevation data from the ASTER30m digital elevation model for our data reduction instead.

Further details relating to these the surveys can be found in the main text in Sections 2.4.1 and 4.7.

A.2 D1 gravity survey data

Table A.1: D1 gravity survey data. Elevation data is in meters and meter readings are in CU. A *-base* suffix indicates that this site was utilised as a base station for estimating instrument drift.

D1 gravity survey table						
Station	**Date**	**Time**	**Latitude**	**Longitude**	**Elevation**	**Reading**
GSA-Naswa	05/04/2016	12:25	24.99558	55.66019	157.30	3820.57
D1-1	05/04/2016	14:11	25.49319	55.51158	-15.10	3865.40
D1-2	05/04/2016	14:28	25.48881	55.52031	-6.80	3863.60
D1-3	05/04/2016	14:42	25.48464	55.52606	-3.20	3863.36
D1-4	05/04/2016	15:00	25.48186	55.53386	-8.20	3861.92
D1-5	05/04/2016	15:14	25.47117	55.54589	-3.80	3859.79
D1-6	05/04/2016	15:31	25.46269	55.55961	5.50	3857.15
D1-7	05/04/2016	15:45	25.45453	55.57508	9.00	3855.15
D1-8	05/04/2016	16:04	25.44961	55.58758	20.80	3851.62

D1 gravity survey table						
Station	**Date**	**Time**	**Latitude**	**Longitude**	**Elevation**	**Reading**
D1-9	05/04/2016	16:21	25.43997	55.59814	10.00	3851.81
D1-10	05/04/2016	17:21	25.44053	55.61144	22.60	3848.68
D1-11	05/04/2016	17:36	25.43342	55.63044	18.40	3847.51
D1-12	05/04/2016	17:48	25.43036	55.64614	25.30	3846.15
Millenium-base	05/04/2016	19:26	25.12253	56.31553	46.10	4094.91
Millenium-base	06/04/2016	10:10	25.12256	56.31556	45.50	4094.84
Millenium-base	07/04/2016	10:00	25.12247	56.31561	49.50	4095.00
D1-13	07/04/2016	11:35	25.42753	55.66217	33.00	3845.74
D1-14	07/04/2016	11:51	25.41878	55.68086	38.70	3845.03
D1-15	07/04/2016	12:06	25.40889	55.70131	47.10	3844.76
D1-16	07/04/2016	12:28	25.40767	55.72797	60.90	3843.58
D1-17	07/04/2016	12:50	25.40203	55.73808	56.30	3845.32
D1-18	07/04/2016	13:11	25.39600	55.75861	51.40	3846.34
D1-19	07/04/2016	13:36	25.38728	55.77847	58.90	3849.86
D1-20	07/04/2016	13:51	25.37533	55.78714	82.20	3842.81
D1-21	07/04/2016	14:11	25.36644	55.80392	69.00	3845.26
D1-22	07/04/2016	14:26	25.35883	55.82175	73.00	3845.78
D1-23	07/04/2016	14:42	25.34900	55.83697	89.80	3843.19
D1-24	07/04/2016	15:17	25.33814	55.86481	99.60	3841.74
D1-25	07/04/2016	15:33	25.32889	55.88036	105.30	3842.07
D1-26	07/04/2016	15:57	25.32664	55.88322	106.40	3842.93
D1-27	07/04/2016	16:23	25.32050	55.90375	122.60	3849.30
D1-28	07/04/2016	16:41	25.31917	55.91942	124.80	3855.68
D1-29	07/04/2016	16:54	25.31689	55.93178	137.20	3860.65
Millenium-base	07/04/2016	18:55	25.12250	56.31564	54.50	4095.25
Millenium-base	08/04/2016	09:56	25.12250	56.31561	44.60	4095.14
Millenium-base	08/04/2016	16:09	25.12256	56.31556	55.70	4095.20
Millenium-base	09/04/2016	11:16	25.12250	56.31547	94.80	4095.18
D1-30	09/04/2016	12:22	25.31114	55.94617	152.70	3867.12
D1-31	09/04/2016	12:31	25.30722	55.95583	-	3872.22
D1-32	09/04/2016	12:40	25.30367	55.96789	169.30	3879.65
D1-33	09/04/2016	12:49	25.29550	55.97814	179.10	3888.02
D1-34	09/04/2016	12:58	25.29214	55.98714	179.20	3893.96
D1-35	09/04/2016	13:14	25.28692	55.99775	180.70	3901.38
D1-36	09/04/2016	13:24	25.28400	56.00422	192.60	3906.20
D1-37	09/04/2016	13:35	25.27906	56.00953	200.50	3911.45
D1-38	09/04/2016	14:00	25.27600	56.01675	201.40	3917.57
D1-39	09/04/2016	14:08	25.27097	56.02272	204.40	3923.99
D1-40	09/04/2016	14:18	25.26906	56.03247	219.50	3930.61
D1-41	09/04/2016	14:29	25.26544	56.04186	229.30	3934.68
D1-42	09/04/2016	14:39	25.26189	56.05144	244.00	3938.73
D1-43	09/04/2016	14:51	25.26117	56.05664	254.30	3939.96
D1-44	09/04/2016	15:02	25.26019	56.06453	264.20	3941.46

D1 gravity survey table						
Station	**Date**	**Time**	**Latitude**	**Longitude**	**Elevation**	**Reading**
D1-45	09/04/2016	15:27	25.25631	56.07392	276.20	3943.52
D1-46	09/04/2016	15:36	25.24972	56.08033	285.60	3946.73
D1-47	09/04/2016	15:42	25.25106	56.09300	295.60	3948.24
D1-48	09/04/2016	15:50	25.25025	56.10136	305.40	3948.09
Millenium-base	09/04/2016	17:00	25.12258	56.31564	68.10	4095.37
Millenium-base	10/04/2016	10:24	25.12261	56.31542	65.60	4095.48
GSA-Naswa	10/04/2016	14:43	24.99564	55.66017	156.30	3820.84
GSA-Naswa	10/04/2016	14:47	24.99564	55.66017	-	3820.85
GSA-Naswa	10/04/2016	14:49	24.99564	55.66017	-	3820.86
GSA-Naswa	17/04/2016	16:27	24.99561	55.66014	152.30	3822.09
GSA-Naswa	17/04/2016	16:32	24.99561	55.66014	152.30	3822.09
GSA-Naswa	17/04/2016	16:34	24.99561	55.66014	15.20	3822.08
Novotel-base	17/04/2016	17:58	25.12106	56.32469	37.50	4099.41
Novotel-base	18/04/2016	10:18	25.12108	56.32456	34.00	4099.40
D1-49	18/04/2016	11:46	25.24019	56.10661	309.80	3954.07
D1-50	18/04/2016	11:58	25.23117	56.11817	336.60	3957.91
D1-51	18/04/2016	12:10	25.23344	56.13258	349.80	3959.10
D1-52	18/04/2016	12:22	25.23822	56.13978	356.00	3956.62
D1-53	18/04/2016	13:13	25.23164	56.19781	277.00	3977.86
D1-54	18/04/2016	13:35	25.22683	56.20528	243.60	3987.61
D1-55	18/04/2016	14:03	25.22156	56.20781	232.80	3992.61
D1-56	18/04/2016	14:12	25.21717	56.21047	231.30	3996.60
D1-57	18/04/2016	14:33	25.21586	56.21764	240.10	4002.45
D1-58	18/04/2016	14:47	25.20728	56.22144	198.40	4013.52
D1-59	18/04/2016	15:00	25.19108	56.23344	184.90	4028.18
D1-60	18/04/2016	15:20	25.18619	56.24147	183.20	4035.75
D1-61	18/04/2016	15:33	25.18242	56.24242	189.10	4036.90
D1-62	18/04/2016	15:47	25.19867	56.22708	185.40	4022.47
D1-63	18/04/2016	16:06	25.17308	56.25275	151.50	4049.65
D1-64	18/04/2016	16:27	25.17433	56.25875	156.80	4052.28
D1-65	18/04/2016	16:40	25.15606	56.26372	120.30	4067.79
D1-66	18/04/2016	17:04	25.16717	56.28394	141.50	4065.03
Novotel-base	18/04/2016	17:24	25.12100	56.32464	37.40	4099.51
Novotel-base	18/04/2016	17:35	25.12100	56.32464	37.40	4099.49
Novotel-base	19/04/2016	10:57	25.12100	56.32464	53.30	4099.32
D1-67	19/04/2016	11:23	25.15194	56.31211	29.30	4098.17
D1-68	19/04/2016	11:37	25.15339	56.30367	37.90	4094.31
D1-69	19/04/2016	11:50	25.15800	56.29953	55.00	4089.82
D1-70	19/04/2016	12:07	25.14781	56.31747	8.70	4099.72
D1-71	19/04/2016	12:25	25.14794	56.33644	3.30	4105.28
D1-72	19/04/2016	12:37	25.14989	56.34525	-4.10	4106.05
D1-73	19/04/2016	12:51	25.15017	56.35336	-5.40	4104.46
Novotel-base	19/04/2016	14:28	25.12097	56.32469	39.40	4099.55

D1 gravity survey table						
Station	**Date**	**Time**	**Latitude**	**Longitude**	**Elevation**	**Reading**
D1-74	19/04/2016	15:03	25.25194	56.18250	334.70	3952.61
D1-75	19/04/2016	15:15	25.25797	56.17500	358.00	3939.26
D1-76	19/04/2016	15:34	25.25517	56.16478	-	3942.03
D1-77	19/04/2016	15:43	25.25511	56.15386	406.90	3936.58
D1-78	19/04/2016	15:52	25.25036	56.14750	394.60	3942.21
GSA-Naswa	19/04/2016	17:49	24.99564	55.66014	143.60	3822.10
End of D1 data table						

A.3 D4 gravity survey data

Table A.2: D4 gravity survey data. Elevation data is in meters and meter readings are in *CU*. A *-base* suffix, or an asterisk, indicates that this site was utilised as a base station for estimating instrument drift.

D4 gravity survey table						
Station	**Date**	**Time**	**Latitude**	**Longitude**	**Elevation**	**Reading**
GSA-Naswa	17/02/2016	13:37	24.99564	55.66017	-	3797.57
GSA-Naswa	17/02/2016	13:44	24.99564	55.66017	-	3797.53
GSA-Naswa	17/02/2016	13:47	24.99564	55.66017	-	3797.51
GSA-Naswa	17/02/2016	13:58	24.99564	55.66017	-	3797.46
D4-1*	17/02/2016	17:38	25.56234	55.66153	-	3835.39
D4-1*	17/02/2016	17:46	25.56234	55.66153	-	3835.39
D4-2	17/02/2016	17:58	25.56203	55.67756	-	3830.81
D4-3	17/02/2016	18:08	25.56228	55.69197	-	3832.64
D4-4	17/02/2016	18:16	25.56269	55.70219	-	3831.48
D4-5	17/02/2016	18:33	25.55278	55.72164	-	3829.74
D4-1*	17/02/2016	18:50	25.56234	55.66153	-	3835.28
Palace-base	18/02/2016	09:12	25.68667	55.77019	-	3848.82
Palace-base	18/02/2016	09:16	25.68667	55.77019	-	3848.81
D4-6	18/02/2016	12:11	25.55042	55.75097	23.10	3826.17
D4-7	18/02/2016	12:30	25.54894	55.75797	10.70	3828.17
D4-8	18/02/2016	12:50	25.54975	55.76636	14.00	3828.12
D4-9	18/02/2016	13:08	25.55156	55.77519	15.30	3828.99
D4-10	18/02/2016	14:06	25.54817	55.78700	27.80	3828.56
D4-11	18/02/2016	14:44	25.54572	55.79233	20.60	3828.91
D4-12	18/02/2016	15:38	25.54558	55.81047	34.20	3824.94
D4-13	18/02/2016	16:25	25.54172	55.83242	37.20	3827.84
D4-14	18/02/2016	17:06	25.53997	55.85344	16.80	3830.55
D4-15	18/02/2016	17:45	25.54167	55.86508	51.40	3827.09
D4-16	18/02/2016	18:28	25.53311	55.88619	65.60	3826.12
Palace-base	18/02/2016	20:45	25.68667	55.77019	-	3848.81
Palace-base	19/02/2016	09:59	25.68667	55.77019	4.40	3848.87

D4 gravity survey table continued						
Station	**Date**	**Time**	**Latitude**	**Longitude**	**Elevation**	**Reading**
D4-17	19/02/2016	11:45	25.53067	55.89422	36.30	3832.05
D4-18	19/02/2016	12:04	25.52958	55.89944	38.20	3832.54
D4-19	19/02/2016	12:22	25.52056	55.93581	62.80	3837.89
D4-20	19/02/2016	13:00	25.50814	55.98272	88.10	3866.53
D4-21	19/02/2016	13:36	25.50408	55.99900	101.40	3870.65
D4-22	19/02/2016	14:10	25.49581	56.02386	129.90	3867.40
D4-23	19/02/2016	14:47	25.49069	56.04661	150.60	3866.92
D4-24	19/02/2016	15:03	25.49103	56.06361	167.60	3865.90
D4-25	19/02/2016	15:17	25.49189	56.08475	204.20	3861.68
D4-26	19/02/2016	15:32	25.49292	56.10094	232.40	3859.21
D4-27	19/02/2016	16:00	25.49414	56.11256	355.40	3838.98
D4-28	19/02/2016	17:20	25.49353	56.12269	449.40	3824.33
D4-29	19/02/2016	17:43	25.49789	56.13781	524.40	3816.64
D4-30	19/02/2016	17:54	25.49808	56.14631	521.30	3820.18
D4-31	19/02/2016	18:08	25.50303	56.15789	377.60	3852.39
D4-32	19/02/2016	18:19	25.50689	56.16758	220.40	3888.86
D4-33	19/02/2016	18:34	25.49694	56.18214	158.70	3914.22
D4-34	19/02/2016	18:47	25.48983	56.18556	163.20	3917.27
D4-35*	20/02/2016	10:39	25.51547	56.36486	8.20	4112.16
D4-35*	20/02/2016	10:45	25.51547	56.36486	-	4112.16
D4-35*	20/02/2016	11:07	25.51547	56.36486	-	4112.15
D4-36	20/02/2016	11:30	25.51867	56.35378	9.30	4109.01
D4-37	20/02/2016	11:46	25.51619	56.33922	28.00	4103.44
D4-38	20/02/2016	11:57	25.50975	56.32467	35.70	4094.79
D4-39	20/02/2016	12:27	25.50444	56.30956	109.00	4078.25
D4-40	20/02/2016	12:48	25.49428	56.30831	125.80	4076.16
D4-41	20/02/2016	13:16	25.49706	56.29994	140.00	4067.72
D4-42	20/02/2016	13:28	25.49567	56.29661	130.00	4066.36
D4-43	20/02/2016	13:46	25.49564	56.29289	153.50	4060.39
D4-44	20/02/2016	14:00	25.49367	56.28875	169.00	4056.72
D4-45	20/02/2016	14:44	25.49064	56.28089	183.00	4046.12
D4-35*	20/02/2016	17:23	25.51547	56.36486	-	4112.48
D4-35*	20/02/2016	17:28	25.51547	56.36486	-	4112.49
D4-35*	21/02/2016	13:46	25.51544	56.36481	10.00	4112.29
D4-46	21/02/2016	14:30	25.51897	56.34642	29.50	4107.05
D4-47	21/02/2016	14:39	25.51383	56.33247	46.50	4099.51
D4-48	21/02/2016	14:48	25.50742	56.31881	67.30	4090.80
D4-49	21/02/2016	15:45	25.50661	56.18006	171.10	3908.11
D4-50	21/02/2016	15:53	25.50781	56.16872	209.20	3890.01
D4-51	21/02/2016	16:11	25.48078	56.19328	185.40	3919.93
D4-52	21/02/2016	16:55	25.51197	55.96797	61.90	3858.38
D4-53	21/02/2016	17:07	25.51669	55.95272	56.50	3847.95
D4-54	21/02/2016	17:19	25.52289	55.92500	44.70	3833.60

D4 gravity survey table continued						
Station	**Date**	**Time**	**Latitude**	**Longitude**	**Elevation**	**Reading**
D4-55	21/02/2016	17:30	25.52506	55.91556	45.70	3832.21
D4-35*	21/02/2016	18:30	25.51547	56.36486	-	4112.68
D4-35*	22/02/2016	09:00	25.51547	56.36486	-	4112.67
D4-56	22/02/2016	09:40	25.49700	56.27656	249.20	4034.13
D4-57	22/02/2016	09:57	25.49864	56.26697	240.20	4016.75
D4-58	22/02/2016	10:54	25.49847	56.25961	258.20	4002.20
D4-59	22/02/2016	11:15	25.49356	56.25683	261.20	3996.78
D4-60	22/02/2016	11:45	25.48639	56.25533	289.40	3992.88
D4-61	22/02/2016	12:08	25.48800	56.24708	301.90	3976.97
D4-62	22/02/2016	12:34	25.49339	56.24561	331.10	3969.16
D4-63	22/02/2016	13:25	25.49375	56.24119	394.70	3958.47
D4-64	22/02/2016	14:02	25.49156	56.23758	395.70	3946.38
D4-65	22/02/2016	14:58	25.48808	56.23153	388.80	3931.26
D4-66	22/02/2016	15:23	25.48194	56.22889	-	3923.91
D4-67	22/02/2016	15:52	25.47572	56.22858	493.60	3921.58
D4-68	22/02/2016	16:21	25.47383	56.22269	519.60	3901.35
D4-69	22/02/2016	16:55	25.47206	56.21869	543.70	3920.59
D4-70	22/02/2016	17:23	25.47003	56.21442	301.30	3931.03
D4-71	22/02/2016	17:47	25.47050	56.20533	244.00	3928.67
D4-72	22/02/2016	18:00	25.47472	56.20011	236.70	3924.31
D4-35*	22/02/2016	19:15	25.51547	56.36486	-	4112.75
GSA-Naswa	22/02/2016	21:50	24.99564	55.66014	147.50	3797.24
GSA-Naswa	22/02/2016	21:54	24.99564	55.66014	147.50	3797.23
End of D4 data table						

Appendix B

H - *k* stacking results

B.1 Introduction

This appendix contains the $H-k$ stacking results obtained from receiver functions across the PI/Oxford network (see Chapter 3). These results were computed using the time domain deconvolution method, with a 1 Hz low pass filter applied to the raw data, and weights of 0.6, 0.3, and 0.1 were used for w_1, w_2, and w_3. Some results were computed using a narrowed search frame to exclude the influence of a nearby phase. Uncertainties are calculated using the bootstrap method, with a B-value of 50.

B.2 PI/Oxford network

Table B.1: $H-k$ stacking results from receiver functions on the PI/Oxford network. Distance and back azimuth (Baz) are in units of degrees, N represents the number of receiver functions used, and v_p is the average velocity of the overlying crustal column.

H – k stacking results table							
Station	**v_p**	**Baz**	**Distance**	**N**	**Polarity**	**H (km)**	**k**
S-01	6	0-360	30-98	43	P	14.02 ± 0.08	1.878 ± 0.008
S-01	6.5	114-360	30-98	13	P	36.03 ± 0.83	1.693 ± 0.021
S-02	6	0-180	30-98	3	P	15.35 ± 0.9	1.809 ± 0.05
S-02	6	180-360	30-98	4	P	13.82 ± 0.22	1.798 ± 0.022
S-02	6.5	180-360	30-98	4	P	35.72 ± 0.24	1.725 ± 0.019
S-03	6	230-360	30-98	4	P	16.08 ± 0.96	1.62 ± 0.041
S-05	6.5	0-180	30-98	6	P	38.41 ± 5.42	1.696 ± 0.103
S-06	6.5	0-180	30-98	3	P	39.89 ± 2.79	1.678 ± 0.057
S-06	6	180-360	30-98	5	P	13.81 ± 0.12	1.603 ± 0.006
S-07	6	40-60	65-80	6	P	14.31 ± 0.27	1.638 ± 0.045
S-07	6.5	40-60	65-80	6	P	35.55 ± 0.56	1.615 ± 0.011
S-07	5.5	80-120	60-98	11	P	3.13 ± 0.13	1.606 ± 0.01
S-07	6	80-120	60-98	11	N	5 ± 0.03	1.882 ± 0.005

H – k stacking results table continued							
Station	**v_p**	**Back az**	**Distance**	**N**	**Polarity**	**H (km)**	**k**
S-07	6	80-120	60-98	11	P	13.26 ± 0.22	1.622 ± 0.021
S-07	6	80-120	60-98	11	N	20.36 ± 2.06	1.649 ± 0.089
S-07	6.5	80-120	60-98	11	P	38.32 ± 0.91	1.646 ± 0.016
S-07	5.5	80-120	30-60	6	P	2.63 ± 0.72	1.684 ± 0.078
S-08	5.5	0-180	40-65	11	P	2.23 ± 0.14	1.614 ± 0.039
S-08	6	0-180	40-65	11	N	11.45 ± 0.21	1.736 ± 0.011
S-08	6.5	0-180	40-65	11	P	46.65 ± 1.51	1.745 ± 0.031
S-08	6	0-180	75-98	7	N	14.25 ± 1.37	1.856 ± 0.055
S-08	6.5	0-180	75-98	7	P	30.8 ± 3.31	1.671 ± 0.061
S-08	6.5	0-180	75-98	7	P	42.16 ± 1	1.847 ± 0.018
S-09	5.5	0-180	50-98	32	P	4.41 ± 0.12	1.652 ± 0.051
S-09	6.5	0-180	50-98	32	N	23.91 ± 0.69	1.694 ± 0.02
S-09	6.5	0-180	50-98	32	P	34.38 ± 2.15	1.707 ± 0.048
S-09	6	180-360	30-98	5	P	17.96 ± 1.03	1.728 ± 0.035
S-09	6.5	180-360	30-98	5	N	23.34 ± 0.88	1.809 ± 0.029
S-09	6.5	180-360	30-98	5	P	40.15 ± 0.66	1.858 ± 0.044
S-09	6.5	180-360	30-98	5	P	48.9 ± 0.85	1.705 ± 0.022
S-10	6	0-180	50-98	22	N	11.13 ± 0.25	1.672 ± 0.029
S-10	6	0-180	50-98	22	N	23.14 ± 0.19	1.635 ± 0.009
S-10	6.5	0-180	50-98	22	P	38.37 ± 2.93	1.671 ± 0.05
S-10	6.5	0-180	50-98	22	P	47.47 ± 1.17	1.754 ± 0.027
S-10	6.5	180-360	30-98	5	N	24.36 ± 0.92	1.815 ± 0.039
S-10	6.5	180-360	30-98	5	P	43.95 ± 4.33	1.803 ± 0.078
S-11	5.5	0-85	71-98	15	P	3.04 ± 0.34	1.762 ± 0.062
S-11	6	0-85	71-98	15	N	7.08 ± 0.77	1.851 ± 0.074
S-11	6.5	0-85	71-98	15	P	21.61 ± 2.12	1.721 ± 0.073
S-11	6	100-180	30-98	18	N	17.78 ± 0.3	1.668 ± 0.016
S-11	6.5	100-180	30-98	18	P	34.89 ± 0.69	1.73 ± 0.017
S-12	6	0-180	40-98	15	N	16.08 ± 0.28	1.657 ± 0.027
S-12	6.5	0-180	40-98	15	P	22.24 ± 0.22	1.705 ± 0.012
S-12	6.5	0-180	40-98	15	P	43.84 ± 1.09	1.872 ± 0.024
S-13	6	0-180	70-98	21	P	7.99 ± 0.31	1.789 ± 0.099
S-13	6	0-180	70-98	21	N	18.68 ± 0.94	1.66 ± 0.031
S-13	6.5	0-180	70-98	21	P	34.99 ± 0.43	1.654 ± 0.011
S-14	6	0-180	30-98	10	N	19.52 ± 1.15	1.715 ± 0.058
S-14	6.5	0-180	30-98	10	P	33.73 ± 2.59	1.693 ± 0.064
S-15	6	180-360	30-98	4	P	7.18 ± 0.28	1.758 ± 0.066
S-15	6.5	180-360	30-98	4	P	42.18 ± 5.92	1.813 ± 0.096
S-15	6.5	0-80	30-98	10	N	23.57 ± 2.32	1.691 ± 0.058
S-15	6.5	0-80	30-98	10	P	33.88 ± 3.16	1.67 ± 0.044
S-15	6	97-150	30-98	8	P	15.01 ± 0.27	1.719 ± 0.021
S-15	6	97-150	30-98	8	N	7.2 ± 0.23	1.831 ± 0.008
S-15	6.5	97-150	30-98	8	P	41.07 ± 0.76	1.67 ± 0.014

H – k stacking results table continued							
Station	**v_p**	**Back az**	**Distance**	**N**	**Polarity**	**H (km)**	**k**
S-18	6.5	0-180	70-98	13	N	23.66 ± 1.82	1.791 ± 0.055
S-18	6	180-360	30-98	4	P	13.26 ± 1.31	1.747 ± 0.064
S-18	6.5	180-360	30-98	4	N	24.73 ± 2.59	1.67 ± 0.063
S-18	6.5	180-360	30-98	4	P	31.63 ± 1.16	1.704 ± 0.043
S-19	6	180-360	60-98	3	P	12.88 ± 0.36	1.672 ± 0.017
S-19	6.5	180-360	60-98	3	P	30.74 ± 1.45	1.728 ± 0.027
S-19	6.5	0-100	72-98	8	N	19.27 ± 1.3	1.708 ± 0.055
S-19	6.5	0-100	72-98	8	P	31.6 ± 1.38	1.648 ± 0.028
S-20	6	0-80	60-98	11	P	7.8 ± 0.16	1.63 ± 0.029
S-20	6.5	0-80	60-98	11	N	17.72 ± 0.29	1.668 ± 0.029
S-20	6.5	0-80	60-98	11	P	28.59 ± 0.61	1.715 ± 0.022
S-20	6.5	80-180	60-98	12	N	10.78 ± 0.89	1.859 ± 0.052
S-20	6.5	80-180	60-98	12	P	26.22 ± 4.01	1.671 ± 0.098
S-20	6	180-360	60-98	3	P	12.27 ± 0.11	1.617 ± 0.011
S-20	6.5	180-360	60-98	3	N	21.39 ± 0.5	1.637 ± 0.017
S-20	6.5	180-360	60-98	3	P	27.74 ± 0.64	1.715 ± 0.017
S-21	6.5	0-180	30-98	28	N	11.01 ± 0.14	1.817 ± 0.018
S-21	6.5	0-180	30-98	28	P	26.86 ± 2.17	1.65 ± 0.053
S-22	6	180-360	30-98	4	N	7.92 ± 0.93	1.815 ± 0.074
S-22	6	0-180	30-98	16	N	7.71 ± 0.6	1.752 ± 0.11
S-22	6.5	0-180	30-98	16	P	36.27 ± 1.16	1.733 ± 0.043
S-23	6	0-180	60-98	20	P	8.8 ± 0.27	1.678 ± 0.047
S-23	6.5	0-180	68-98	16	P	33.77 ± 1.71	1.721 ± 0.048
S-23	6.5	0-180	68-98	16	N	25.52 ± 1.08	1.605 ± 0.036
S-23	6.5	180-360	30-98	3	P	25.73 ± 1.42	1.622 ± 0.029
S-23	6.5	180-360	30-98	3	N	35.99 ± 2.05	1.662 ± 0.043
S-23	6.5	180-360	30-98	3	P	38.7 ± 0.49	1.731 ± 0.029
S-23	6.5	180-360	30-98	3	P	41.3 ± 1.13	1.785 ± 0.079
S-24	6.5	0-180	68-98	25	P	13.24 ± 0.04	1.687 ± 0.008
S-24	6.5	0-180	68-98	25	N	20.8 ± 3.91	1.72 ± 0.139
S-24	6.5	0-180	68-98	25	P	43.3 ± 2.85	1.763 ± 0.046
S-24	6.5	180-360	30-98	4	P	18.89 ± 0.63	1.864 ± 0.029
S-24	6.5	180-360	30-98	4	N	26.73 ± 0.24	1.786 ± 0.019
S-24	6.5	180-360	30-98	4	P	37.09 ± 1.61	1.806 ± 0.044
S-25	6	70-180	30-80	31	P	12.01 ± 0.28	1.698 ± 0.03
S-25	6.5	70-180	30-80	31	N	20.63 ± 0.14	1.651 ± 0.01
S-25	6.5	70-180	30-80	31	P	28.3 ± 0.37	1.639 ± 0.012
End of H – k stacking results table							